DOCTORAL THESIS

Flow-induced vibrations of twin cylinders in the post-critical regime

Author:
Raphaël DUBOIS

Supervisors:
Dr. Thomas ANDRIANNE
Prof. Greg DIMITRIADIS

A thesis submitted in fulfillment of the requirements for the degree of Doctor of Philosophy

in the

Wind Tunnel Laboratory
Department of Aerospace and Mechanical Engineering
University of Liège

January 2024

Members of the examination committee

Prof. **B. Dewals** (Committee President)	University of Liège, Belgium
Dr. Ir. **T. Andrianne** (Supervisor)	University of Liège, Belgium
Prof. **G. Dimitriadis** (Co-supervisor)	University of Liège, Belgium
Prof. **V. Denoël**	University of Liège, Belgium
Prof. **V. E. Terrapon**	University of Liège, Belgium
Prof. **C. Mannini**	University of Florence, Italy
Dr. Ir. **F. Lupi**	Niemann Ingenieure, Germany

Declaration of Authorship

I, Raphaël DUBOIS, declare that this thesis titled, "Flow-induced vibrations of twin cylinders in the post-critical regime" and the work presented in it are my own. I confirm that:

- This work was done wholly or mainly while in candidature for a research degree at this University.
- Where any part of this thesis has previously been submitted for a degree or any other qualification at this University or any other institution, this has been clearly stated.
- Where I have consulted the published work of others, this is always clearly attributed.
- Where I have quoted from the work of others, the source is always given. With the exception of such quotations, this thesis is entirely my own work.
- I have acknowledged all main sources of help.
- Where the thesis is based on work done by myself jointly with others, I have made clear exactly what was done by others and what I have contributed myself.

Signed: 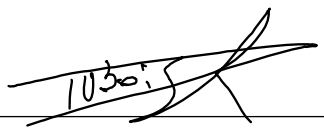

Date: 01/01/2024

"I seem to have been only like a boy playing on the seashore, and diverting myself in now and then finding a smoother pebble or a prettier shell than ordinary, whilst the great ocean of truth lay all undiscovered before me."

Isaac Newton

Abstract

Flow-induced vibrations of twin cylinders in the post-critical regime

by Raphaël DUBOIS

Cylinder-like structures can be found in various engineering applications. Therefore, fluid flows around a circular cylinder have been extensively studied in the past and correspond to canonical problems in fluid mechanics. In many cases, the structure is in a multiple-body form, which leads to flow interference between the cylinders. Fluid-structure interactions may result from flow interference because of the high fluctuating forces. Hence, a complete understanding of the flow is needed to avoid any critical situation for structural integrity, e.g. failure. Because of the continuous increase in size of the civil engineering structure, the flow around the structure often lies in the post-critical regime. The boundary layers developing around the bodies are fully turbulent before separation in this specific regime.

This thesis investigates the flow around twin cylinders at low incidences and their potential flow-induced vibrations in the post-critical regime. In that sense, extensive experimental studies are performed in the wind tunnel of the University of Liège.

The first part of the work consists in triggering the post-critical flow regime at lower Reynolds numbers because of the limitations in size and flow velocity inside the wind tunnel. It is performed by applying appropriate surface roughness on the cylinders, which promotes the transition from the laminar to turbulent state of flow.

The second part analyses in detail the flow around static twin rough cylinders. The main outcome of this analysis is the sensitivity and complexity of the flow dynamics around the two cylinders. Hence, the aerodynamic quantities are highly dependent on different parameters such as the Reynolds number, the spacing ratio and the flow incidence.

An experimental aeroelastic test campaign is then carried out using springs and elastomers to allow one degree of freedom to each cylinder. The free responses are measured and analysed for different configurations.

Finally, the possibility of mathematically modelling the flow-induced vibrations is assessed. The investigation demonstrates that the classical approaches fail to reproduce the large vibrations observed experimentally and, hence, supports the need for more research on this subject.

Acknowledgements

I would like to acknowledge my supervisor, Dr. Ir. Thomas Andrianne, for his guidance and confidence over the past four years. I valued a lot the interesting discussions we had related to either my project or other topics. I am truly grateful to him for giving me the opportunity to work on such a rich and varied research project, allowing me to improve my technical knowledge.

I also wish to thank all the people who contributed to this project. A special thanks goes to Professor Vincent Denoël, who helped me with the mathematical modelling aspects in the project. I wish to thank the other members of my thesis committee, Professor Vincent E. Terrapon, and my co-supervisor, Professor Greg Dimitriadis, for the valuable advice they gave me throughout the years.
Experimental work cannot be conducted without the precious support of a technical team. Hence, I would like to express my gratitude to Antonio Martinez, Mathieu Torfs and Antoine Désiron, who spent a lot of time in the wind tunnel with me for the design and installation of the setup.
I would like to extend my thanks to my colleagues and friends, François Piron, Vincent Schmitz and Nayan Levaux, for their contributions to my work through the discussions we had around good meals at lunchtime and for their friendly support.

Finally, I wish to thank my family for all their kind support and encouragement. Without them, it would not have been possible...

Contents

List of Figures

List of Tables

List of Abbreviations

BL	**B**oundary **L**ayer
CFD	**C**omputational **F**luid **D**ynamics
FIV	**F**low-**I**nduced **V**ibrations
FFT	**F**ast **F**ourier **T**ransform
FRF	**F**requency **R**esponse **F**unction
L	**L**aminar
PIV	**P**article **I**mage **V**elocimetry
PSD	**P**ower **S**pectral **D**ensity
SC	**S**ingle **C**ylinder
SL	**S**hear **L**ayer
Tr	**Tr**ansition (laminar to turbulent state of flow)
TrW	**Tr**ansition-in-**W**ake
TrSL	**Tr**ansition-in-**S**hear-**L**ayers
TrBL	**Tr**ansition-in-**B**oundary-**L**ayers
T	**T**urbulent
VIV	**V**ortex-**I**nduced **V**ibrations

Nomenclature

Roman

A_i	amplitude of vibration of ith cylinder	m
b	width of bars in turbulence grid	m
B	width of wind tunnel test section	m
c_d	2D drag coefficient	-
c_l	2D lift coefficient	-
c_f	skin friction coefficient	-
$c_{f_{ai}}$	2D aeroelastic force coefficient on ith cylinder	-
C_p	pressure coefficient	-
D	external diameter	m
f_{ai}	2D aeroelastic force on ith cylinder	$\mathrm{kg\,s^{-2}}$
f	frequency variable	Hz
f_0	natural frequency of the structure	Hz
f_s	structural frequency	Hz
f_{vs}	eddy shedding frequency	Hz
F_L	2D drag force	$\mathrm{kg\,s^{-2}}$
F_L	2D lift force	$\mathrm{kg\,s^{-2}}$
f_m	parameter related to Magnus effect	-
h	depth of wake lamina	m
h^*	dimensionless depth of wake lamina	-
k	roughness mean size	m
l	characteristic length	m
$\bar{l}$	mean half-length of wake lamina	m
l^*	dimensionless mean half-length of wake lamina	-
L	centre-to-centre spacing	m
L_f	length of eddy formation	m
L_u	integral length scale	m
M	mesh size in turbulence grid	m
m_f	mass per unit length of displaced fluid	kg/m
m_r	mass ratio	-
m_s	structural mass per unit length	kg/m
p	local pressure	$\mathrm{kg\,m^{-1}\,s^{-2}}$

p_∞	free-stream pressure	$\mathrm{kg\,m^{-1}\,s^{-2}}$
r_i	reference radius in quasi-steady modelling	m
Re	Reynolds number	-
S	span length	m
Sc	Scruton number	-
St	Strouhal number	-
t	time variable	s
T	period of shedding cycle	s
T_i	turbulence intensity	-
T_L	turbulence length scale	m
U_∞	free-stream velocity	$\mathrm{m\,s^{-1}}$
U	local velocity	$\mathrm{m\,s^{-1}}$
U_r	reduced velocity	-
u	streamwise component of flow velocity	m/s
v	crosswise component of flow velocity	m/s
w	spanwise component of flow velocity	m/s
y_i	transverse displacement of ith cylinder	m
Y_i	dimensionless transverse displacement	-
y_s	twin-cylinder transverse displacement	m

Greek

α	flow incidence	rad or °
α_{a_i}	apparent flow incidence of ith cylinder	rad or °
α_s	flow incidence induced by the relative motion	rad or °
$\alpha_{eff,i}$	effective flow incidence of ith cylinder	rad or °
β	wake lamina angle	rad or °
δ	logarithmic decrement	-
ζ	structural damping ratio	-
η	damping parameter in wake oscillator	-
θ	angular location on cylinder	rad or °
λ	body-acceleration parameter in wake oscillator	-
μ	fluid dynamic viscosity	$\mathrm{kg\,m^{-1}\,s^{-1}}$
μ_i	time delay parameter of ith cylinder	-
ν	dimensionless velocity in wake oscillator	-
ρ	fluid density	$\mathrm{kg\,m^{-3}}$
τ	dimensionless time	-
τ_i	time delay of ith cylinder	s
τ_w	local wall shear stress	$\mathrm{kg\,m^{-1}\,s^{-2}}$

ϕ	phase lag between motions of the cylinders	rad or °
φ_i	coordinate related to ith structural mode	m
ω	radial frequency	rad/s

Operators

$\overline{(.)}$	time-averaged value
$(.)'$	standard deviation value
$\dot{(.)}$	time derivative
$(.)'$	dimensionless time derivative (in model)

Chapter 1

Introduction

1.1 Context

Cylinder-like structures are found in various engineering applications and might be, in some cases, submitted to air or water flows. In general, the flow around any flexible structure – whatever its shape – generates steady and unsteady fluid-dynamic forces on the latter, which may consequently lead to *fluid-structure interactions*. Therefore, it is of paramount importance to consider the effects of the flow on the body(ies) of interest in the design phase. The objective consists in minimising or controlling those effects in order to avoid any critical situation for the structure's integrity (e.g. failure). In that sense, a thorough understanding of the flow is needed.

Because of its common occurrence in various applications, the flow around a circular[1] cylinder has been extensively studied in the past and corresponds to a canonical problem in fluid mechanics and fluid-structure interaction. Several comprehensive reviews of the flow around a single, isolated cylinder exist in the literature and

[1]The term "circular" refers to the sectional shape. Since the present work only deals with this particular sectional shape, this term will not be used anymore.

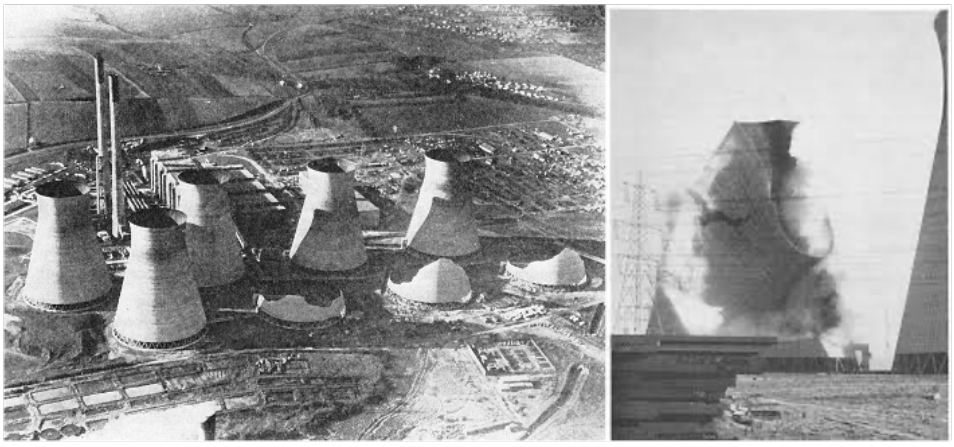

FIGURE 1.1: Collapse of three cooling towers in Ferrybridge, 1965.

are mostly summarised in the work of Zdravkovich (1997). The fundamental flow features around a cylinder consist of boundary layers, separation, free shear layers, re-attachment, formation and shedding of eddies (or vortices) in the wake.

In many applications, the cylinder-like structure appears in a multiple-body form such as tubes in heat exchangers, for example. The flow around multiple cylinders and its effects on them become more complex and have been investigated to a lesser extent. The proximity of two (or more) bodies induces a flow interference which can result in different types of fluid-structure interactions. A famous example of interference effects leading to a catastrophic failure is the collapse of cooling towers in Ferrybridge in 1965 (Figure 1.1). After this incident, engineers around the world recognised that the group effect and the environment have to be taken into account in the design phase (e.g. in wind tunnel tests).

A pair of cylinders in various arrangements corresponds to the simplest case of structures in a group. This particular case can be found in various engineering applications, e.g. twin chimney stacks, twin-conductor power lines, cooling towers, landing gears, main cables of bridge, etc (Figure 1.2). Fluid-structure interactions are often reported in real applications for twin-cylinder structures. For example, twin chimneys started to vibrate in the wind in Cornwall in 2015 (Figure 1.3).

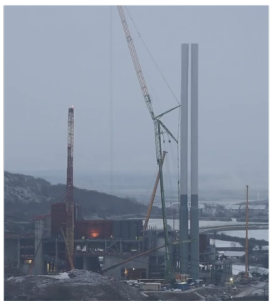

(a) Twin chimneys

(b) Cooling towers

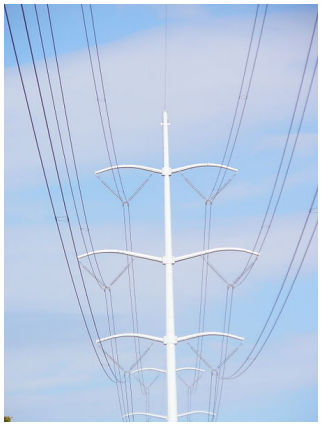

(c) Transmission lines

(d) Landing gears

(e) Bridge cables

FIGURE 1.2: Examples of twin-cylinder structures in engineering applications.

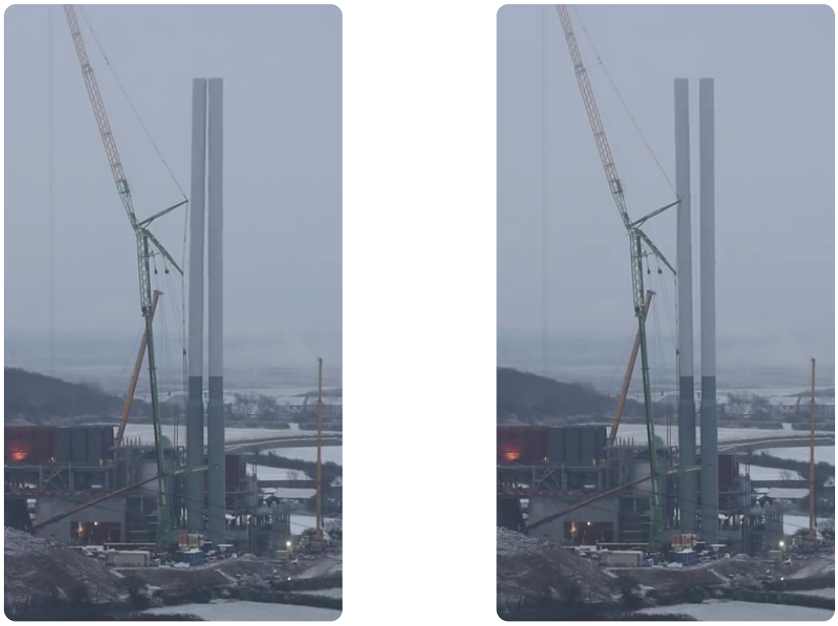

FIGURE 1.3: Flow-induced vibrations of twin chimneys in Cornwall, 2015.

The twin-tube structures of the Hyperloop and submerged-floating tube bridge concepts (Figure 1.4) represent particular illustrations of a two-cylinder configuration submitted to the wind and water stream, respectively. In these new transportation projects, the two cylinders are placed in close proximity and they are almost aligned with the incoming flow (or one behind the other). For such structures, fluid-structure interactions must be avoided or minimised because the slightest static or dynamic deflection may lead to an unsafe situation.

(a) (b)

FIGURE 1.4: New transportation concepts: (a) Hyperloop and (b) submerged-floating tube bridge.

Different fluid-structure interactions (or *aeroelastic phenomena*) can occur in twin-cylinder engineering applications:

- ***Static deflection or deformation***: it corresponds to the simplest consideration when designing a structure submitted to a flow and is induced by the time-averaged aerodynamic forces which results in static deflection and/or deformation of the structure.

- ***Vortex-Induced Vibrations (VIV)***: in bluff-body aerodynamics, a large separated-flow region is found behind the structure. At sufficiently high Reynolds numbers, this flow region is unstable and leads to an alternate shedding of eddies in the wake. As a result, the aerodynamic forces acting on the structure fluctuate at the eddy shedding frequency and may cause a resonance phenomenon if the latter frequency matches one of the modal frequencies. The resulting low amplitude vibrations are denoted Vortex-Induced Vibrations (VIV).

- ***Galloping***: the motion of the structure induces changes in the flow around it. In some cases, these modifications generate an aerodynamic excitation on the structure. It is common to represent it as an aerodynamic damping and stiffness added to the structural system. When the aerodynamic damping is negative and counterbalances the structural damping, the total damping of the system decreases to zero and an aeroelastic instability occurs: energy is fed by the flow to the structure which is not able to completely dissipate it. This damping-controlled instability is called *galloping* in bluff-body aeroelasticity. It must be noted that galloping cannot be observed in the case of an axisymmetric body (single cylinder) because its motion does not lead to an energy transfer from the flow to the structure. The situation is different in the case of two cylinders in proximity, for which two types of galloping instabilities have been reported in the past. The first type is referred to as the *wake galloping*: the rear (or downstream) cylinder vibrates while the front (or upstream) cylinder remains static. The motion of the rear cylinder together with the incoming wake from the front cylinder generate an aerodynamic excitation on the rear cylinder while the front cylinder is unaffected. The wake galloping instability is observed when the spacing between the cylinders is large. The second type of galloping instability for twin cylinders is the *interference galloping*: vibrations of both cylinders are observed. The close proximity of the two cylinders induces large interference effects on the aerodynamic forces acting on both of them. The motion of either cylinder can therefore trigger an aeroelastic instability. The interference galloping instability is observed when the cylinders are in close proximity.

- ***Buffeting***: in general, the structures are submitted to turbulent incoming free stream (e.g. civil structures in an atmospheric boundary layer). Buffeting is the structural response to the turbulent excitation characterised by a broad band frequency spectrum. The resulting vibrations are mostly observed in the stream-wise direction. For a constant level of turbulence, the variation of the buffeting energy is quadratic with the flow velocity.

A generic response curve of the dynamic fluid-structure interactions described above is schematically reported in Figure 1.5. Note that all phenomena do not necessarily arise for any given configuration of the two cylinders.

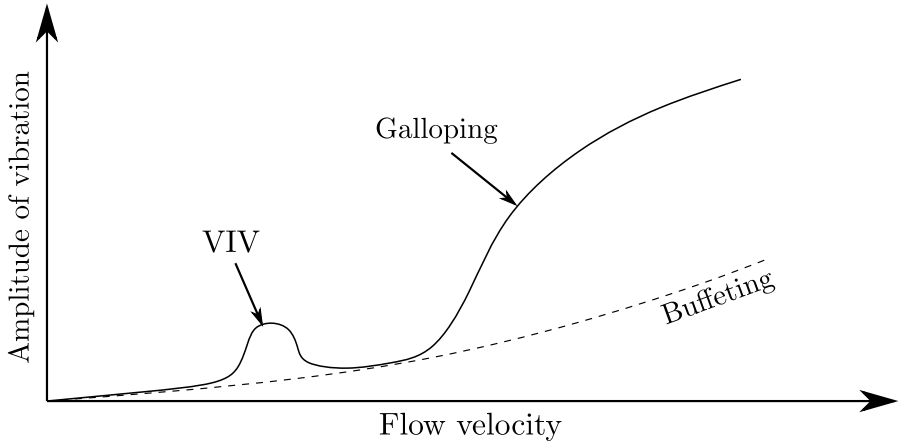

FIGURE 1.5: Schematic diagram showing the possible occurrence of VIV, galloping and buffeting with increasing the flow velocity.

The flow around cylinder-like structures is mainly driven by the value of the corresponding *Reynolds number*. This dimensionless number appears in the Navier-Stokes equations and represents the ratio of inertial to viscous forces. For a cylinder, it is defined as

$$Re = \frac{\rho U_\infty D}{\mu}, \tag{1.1}$$

where ρ is the fluid density, U_∞ is the free-stream velocity, D is the external diameter and μ is the fluid dynamic viscosity.

Figure 1.6 shows the variation of the drag coefficient of a single cylinder with the Reynolds number. It illustrates the importance of viscous effects through the Reynolds number where different main flow regimes are defined. The differences between them lie in the state of flow of the boundary layers, i.e. whether they are laminar, transitional or turbulent.

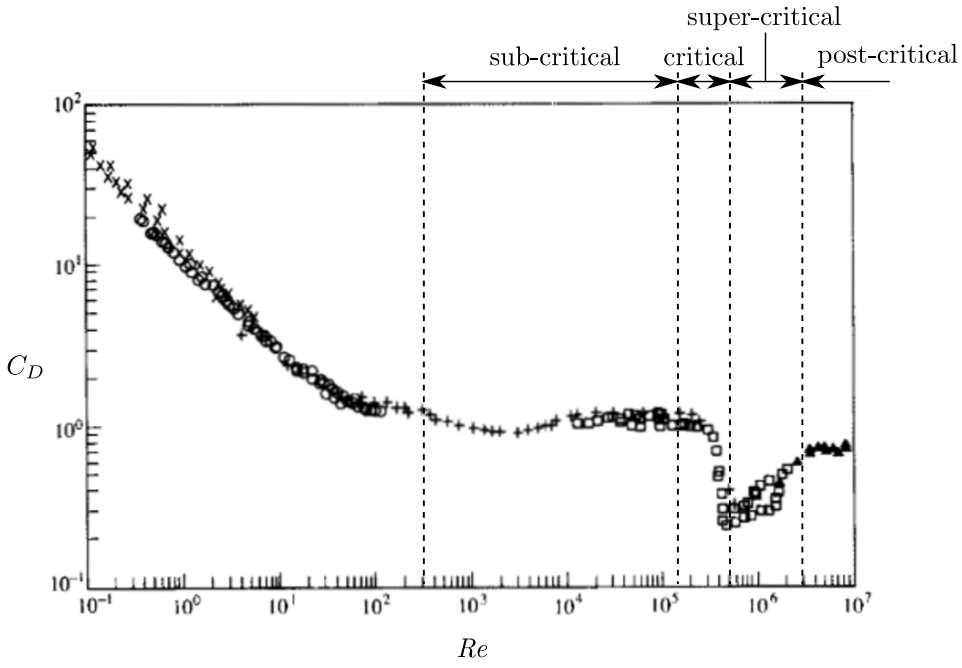

FIGURE 1.6: Definition of the main flow regimes around a cylinder (from Panton, 1984).

The Reynolds number becomes very high in case of large structures, such as in the new transportation concepts introduced above in Figure 1.4. For the Hyperloop structure, if one considers a typical external diameter of 4 meters and a windspeed of 30 m/s, the resulting Reynolds number is around 8×10^6. The same Reynolds number is reached for the Submerged-Floating Tube Bridge application with an external diameter of 8 meters and by considering a water-flow velocity around 1 m/s. Figure 1.6 shows that those two engineering applications lie in the last flow regime, denoted post-critical regime. In this regime, the boundary layers on the cylinder(s) are fully turbulent before separation.

Because of the continuous increase in size of civil engineering structures, the flow around these structures often lies in the post-critical regime. Nevertheless, only few investigations in the literature have been performed on two static cylinders in this regime. The literature is even sparser on the topic of flow-induced vibrations of twin cylinders at high *Re*. In this case, no research was published to the author's knowledge. Although it was not their intention, Schewe and Jacobs (2019) observed vibrations of twin cylinders in the post-critical flow regime during aerodynamic force measurements in a high-pressure wind tunnel. This observation supports the fact that the flow-induced vibrations of twin cylinders are not well understood, especially in the post-critical regime. This thesis aims at providing new experimental results in this field.

1.2 Objectives of the thesis

The discussion above highlights the need to investigate the flow characteristics and the resulting flow-induced vibrations of twin flexible cylinders in the post-critical regime. Therefore, the objective of this doctoral thesis is to develop and apply appropriate techniques to analyse and characterise the flow-induced vibrations of two cylinders in a cross-flow. It must be pointed out that an infinite number of possible arrangements between two cylinders exists (combinations of diameters, spacing, flow incidence, orientation, etc). In this thesis, two parallel and identical cylinders are considered. Furthermore, the research is focused on slightly staggered cylinders in close proximity. This specific arrangement corresponds to the configurations of the new transportation concepts presented in Figure 1.4, where two cylinders are almost aligned with the incoming free-stream.

The different objectives of the thesis are:

- **Experimental investigation on static cylinder(s)**:
  An extensive experimental investigation on static cylinders is performed with the following objectives:
  - Design of an experimental set-up able to trigger the post-critical flow regime within the accessible Reynolds numbers in the atmospheric wind tunnel. It is done by applying appropriate surface roughness on the cylinder(s) (Chapter 3).
  - A thorough analysis is then carried out on the flow around twin static cylinders by means of pressure field measurements to characterise the unsteady aerodynamics as a function of different parameters (Reynolds number, spacing between the cylinders, flow incidence, etc). The final objective is to propose a classification of the flow patterns around the twin cylinders (Chapters 4 and 5).

- **Experimental investigation on aeroelastic cylinders**:
  An experimental aeroelastic set-up has been designed to measure and analyse the free vibrations of twin cylinders in the post-critical flow regime (Chapter 6). Physical explanations are given for the different types of aeroelastic instabilities on the basis of the resulting type of motions and the unsteady flow dynamics identified from static measurements.

- **Mathematical modelling**:
  The possibilities to mathematically model the identified aeroelastic instabilities

will be investigated by following classical modelling techniques (VIV and galloping) in Chapter 6.

Chapter 2

Flow around cylinder(s)

This chapter introduces the theoretical background and state-of-the-art concerning the flow around static circular cylinder(s). This type of fluid flows corresponds to a canonical problem in fluid mechanics because of the geometrical simplicity, while the flow itself is complex. Hence, a large amount of experimental works exists in the literature. The chapter focuses on the specific aspects of flow regimes and influencing parameters.

2.1 Single cylinder

Before describing and analysing the flow around multiple cylinders, it is important to introduce the flow around a single cylinder. First, the different flow features are defined. They correspond to the different regions of the flow field and the parameters of interest. The different disturbances influencing the flow around a cylinder are then listed and discussed. Finally, the distinct flow regimes are introduced and thoroughly described. The state-of-the-art presented in this section is mainly inspired by the work of Zdravkovich (1997).

2.1.1 Definition of flow features

When a fluid flows around a stationary body, it forms an altered region of the flow field around the body with respect to the free stream. The extent of the altered flow region is dependent on the problem of interest : the geometry of the body, the fluid properties and the flow velocity. Moreover, it may be influenced by a wide variety of small disturbances. The latter will be introduced and discussed later in this section.

For bluff (or "non-streamlined") bodies, a particularly large and unsteady separated flow is generated behind them. A bluff body may have sharp edges, e.g. prismatic body or a flat plate at large incidence. In this particular case, separation of the flow is generally located at the sharp edges. But if the sharpness of the edges is decreased and they become more rounded, the flow separation location is not fixed but

moves on the surface of the body depending on the state of flow in different regions around it. Because of this dependency, flow around cylinder-like bluff bodies is more complex to understand or model in comparison with the case of sharp edges, which is almost unaffected by the state of the flow. The flow around cylinder(s) is therefore more interesting and challenging from a fundamental point of view.

A region of the flow is characterised by the variation of the local flow velocity U in magnitude, direction and time. In case of a single cylinder, four different regions of the flow are identified in Figure 2.1:

(i) a small region of retarded flow, which can be termed *stagnation region*;

(ii) two *boundary layers* attached to the surface of the cylinder;

(iii) two sidewise regions of displaced and accelerated flow;

(iv) one wide downstream region of separated flow, which is called the *wake*.

The incoming free-stream is decelerated by the presence of the body in the first region and a stagnation point appears on the upstream surface of the cylinder. Two boundary layers develop on the surface of the cylinder on both sides of the stagnation point. The boundary layers around the cylinder are first subjected to a favourable pressure gradient which accelerates the flow. It is then followed by a small region of adverse pressure gradient which leads to separation. The separated boundary layers continue to develop downstream as *free shear layers*. These free shear layers basically separate

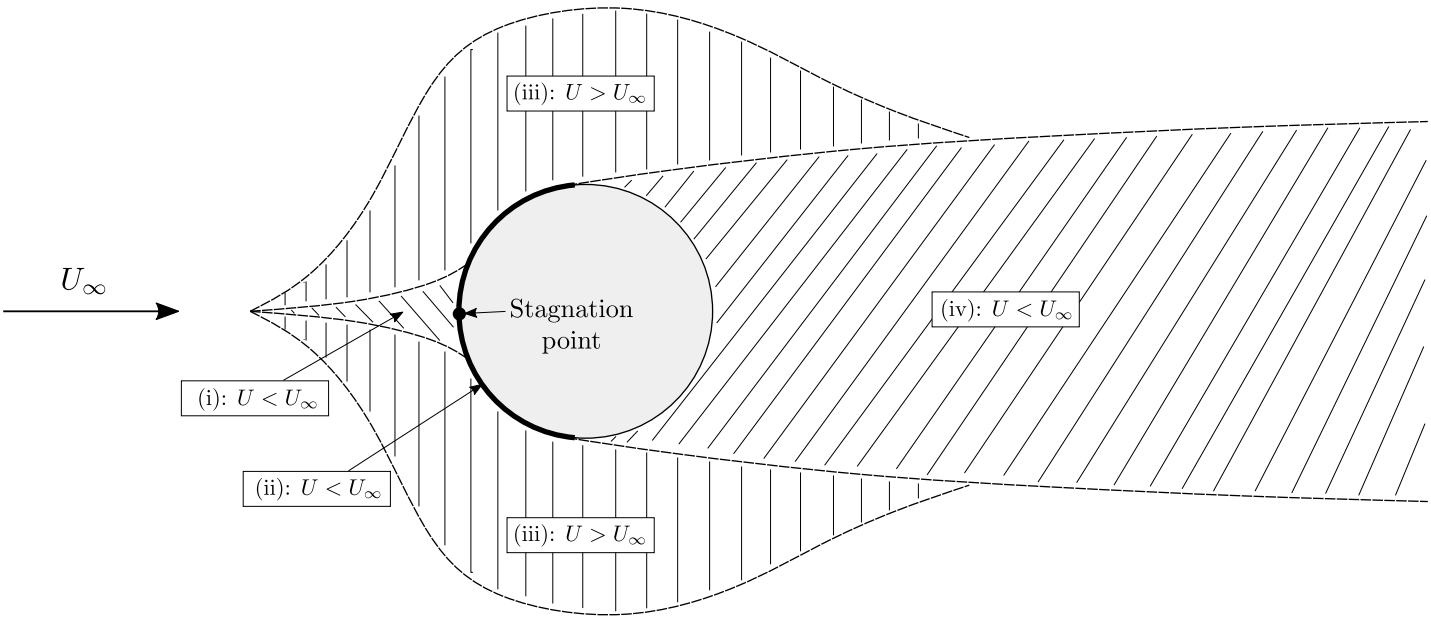

FIGURE 2.1: Distinct regions of flow field around a single cylinder (adapted from Zdravkovich, 1997).

the two sidewise regions of accelerated flow and the wake. They initially border what is called the *near-wake*. Large flow structures are formed in the near-wake and gradually decay along the wake. The different mechanisms involved in the formation and decay of those structures are largely dependent on the state of the flow in the different regions of the flow around the body which may be laminar, transitional or turbulent.

A very important concept in fluid mechanics is therefore the transition from the laminar state of flow to the turbulent one. Reynolds (1883) discovered that transition from laminar to turbulent flow in a smooth pipe depends on the fluid density ρ, the viscosity of the fluid μ, the flow velocity U_∞ and a characteristic length l (the internal diameter of the pipe in his case). The resulting dimensionless parameter is the well-known *Reynolds number*, which is defined as follows

$$Re = \frac{\rho U_\infty l}{\mu}, \tag{2.1}$$

and represents the ratio of inertial to viscous forces. The Reynolds number can also be interpreted as the ratio of destabilising to stabilising forces in the flow. In other words, the flow is more prone to become turbulent as the Reynolds number increases. Transition from laminar to turbulent flow occurs within a range of Re. This particular range may depend on additional influencing parameters. For a cylinder in a cross-flow, the external diameter D is conveniently taken as the characteristic length to define the Reynolds number with Equation (2.1).

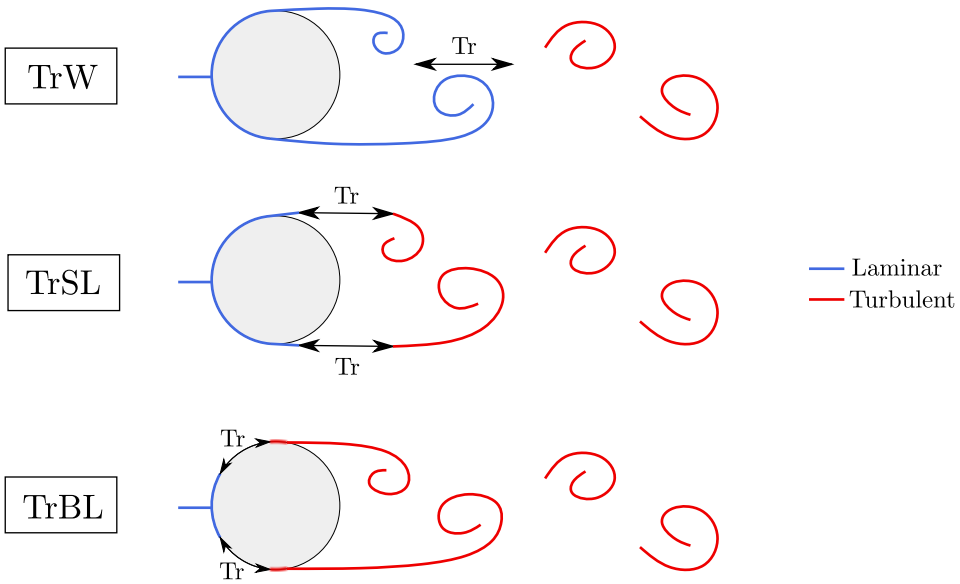

FIGURE 2.2: Transition from laminar to turbulent state of flow in various disturbed regions (adapted from Zdravkovich, 1997).

A particular feature of the flow around bluff bodies is the succession of transition in the different regions of the flow when *Re* increases, as shown in Figure 2.2. The transition may occur in the wake (TrW), in the separated shear layers (TrSL) or in the boundary layers (TrBL) depending on *Re* and influencing parameters. The region where the transition from laminar to turbulence takes place has a significant effect on the flow behaviour around the cylinder, and hence on the fluid forces that apply on the latter.

2.1.2 Influencing parameters

From the discussion above, it appears evident that the Reynolds number *Re* is considered as the *governing* parameter for an idealised or *disturbance-free* flow around a two-dimensional cylinder. In practice, real flows around a cylinder are subjected to different types of disturbances that may have a significant effect on the flow behaviour. These disturbances can be quantified through the definition of *influencing* parameters. Moreover, they can be divided into three families: (i) flow disturbances, (ii) geometric disturbances and (iii) motion disturbances.

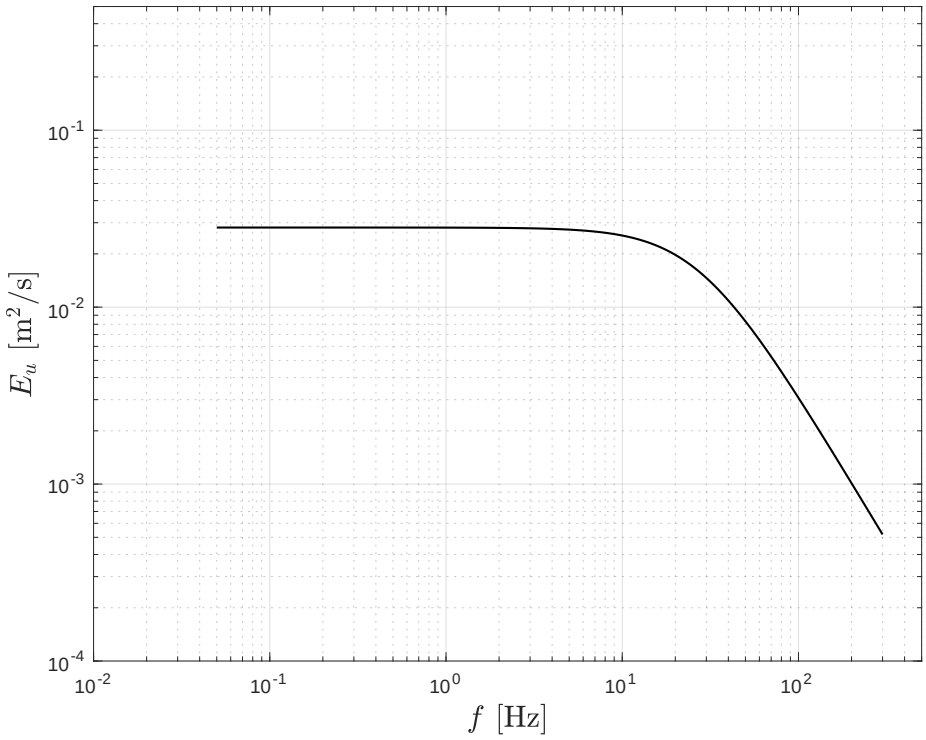

FIGURE 2.3: Typical frequency spectrum of the free-stream turbulence (from von Karman model with T_i = 8.5%, L_u = 0.065 m and $U_\infty = 15$ m/s).

For an incompressible uniform flow, the first family is simply reduced to the free-stream turbulence which corresponds to the fluctuations in time of the incoming flow velocity. The turbulence is defined by its frequency spectrum, as shown in Figure 2.3. The latter is classically characterised by the following parameters:

- *turbulence intensity* T_i,
- *integral length scale* L_u.

The free-stream turbulence strongly affects the transition from laminar to turbulent state of flow in the different regions since it has a destabilising effect on the flow. Note that the free-stream turbulence which is composed of a broad band of frequencies (Figure 2.3) is responsible for the buffeting response of flexible structure, as introduced in the previous chapter.

The geometric disturbances associated with the second family are shown in Figure 2.4 and are the following ones:

(a) *surface roughness* which can be characterised by two influencing parameters: the relative size of roughness k/D and its texture. The surface roughness acts as a destabilising force inside the boundary layers attached to the body. Indeed, the excrescences on the surface generate coherent structures with a characteristic length of the same order of k. These coherent structures produce turbulent energy and destabilise the boundary layer. This particular disturbance will be of paramount importance in this work. It will be shown that it has a non-negligible effect on the post-critical flow: the separation points move upstream with k/D, leading to an increase in drag coefficient. In practice, rough surfaces are due to corrosion (metal), erosion (cavitation, sand), manufacture (concrete), machining (knurling for heat transfer purposes), marine fouling on offshore structures (mussels, seaweed), etc.

(b) *wall blockage ratio* D/B (where B is the width of test section): this disturbance is mainly observed in confined flows, as encountered in heat exchangers or when performing wind (or water) tunnel tests. The presence of the walls has a significant effect on the flow around the cylinder if the blockage ratio is large. In a confined flow, the cylinder reduces the cross-sectional area locally which causes an increase in velocity around the cylinder. Moreover, the side walls affect the widening of the wake (known as the *wake blockage*). An increase in drag coefficient is associated with an increase in blockage ratio. It is common practice in wind tunnel tests to minimise the effect of wall blockage by keeping D/B below 10%.

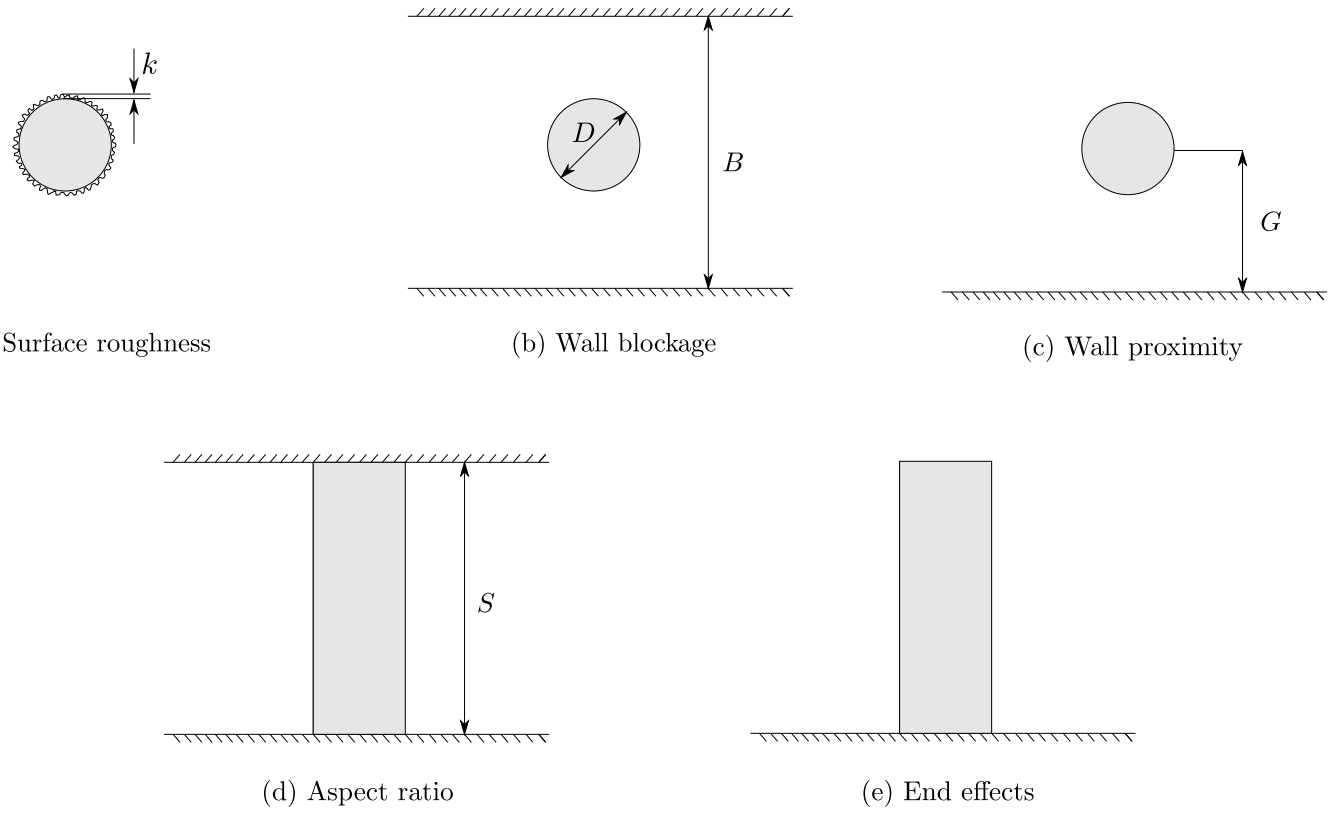

(a) Surface roughness (b) Wall blockage (c) Wall proximity

(d) Aspect ratio (e) End effects

FIGURE 2.4: Typical geometric disturbances on the flow around a cylinder (adapted from Zdravkovich, 1997).

(c) *wall proximity* G/D (where G is the distance from the wall): it corresponds to an asymmetric "blockage" which is induced by the proximity of a single wall or boundary. In the Hyperloop concept (Figure 1.4(a)), the effect of this particular disturbance should be investigated since the two cylinders might be close to the ground at some locations.

(d) *aspect ratio* S/D (where S is the span length): it is one of the most important influencing parameter when it comes to simulate (experimentally or numerically) a flow around a two-dimensional cylinder. When the aspect ratio is rather small, three-dimensional effects cannot be neglected anymore.

(e) *end effects* : the cylinder might have one or both ends free (without the use of *end-plates*) which has a significant three-dimensional effect on the flow along the span. Cylinders with one free end can be found in civil engineering applications such as chimneys or cooling towers. An example of end effects is the well-known wing tip vortex observed for aircrafts which induces a spanwise component in the flow field around the wing.

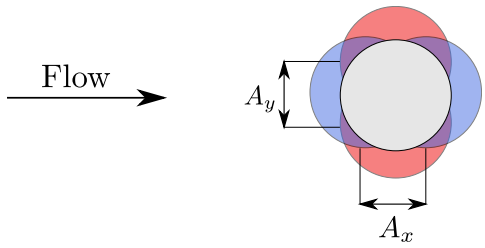

FIGURE 2.5: Motion disturbances on the flow around a cylinder (adapted from Zdravkovich, 1997).

Finally, the motion disturbances associated with the third family correspond to forced *structural vibrations* A_x/D and A_y/D in the streamwise and crosswise directions, respectively (see Figure 2.5). This is a powerful disturbance which can eliminate the effects of other disturbances beyond a threshold amplitude A/D.

It should be noted that, more generally, when a given disturbance becomes large, it reduces or even cancels the effects of other disturbances on the flow around the cylinder. For example, a sufficiently high turbulence level in the free-stream significantly reduces the effect of the surface roughness or even Reynolds number. In that case, the parameters related to this disturbance may become governing ones.

2.1.3 Flow regimes

Experimental works in the literature revealed the existence of several flow features around the cylinder depending on the Reynolds number and influencing parameters. The occurrence of these flow features and their variation, which persist over specific ranges of Re, can be used to define *flow regimes*. The flow regimes are expected to be observed within fixed ranges of Re for given values of the influencing parameters. The distinct flow regimes that can be identified for a disturbance-free flow around a cylinder are introduced hereafter. Nonetheless, the reader should keep in mind that the disturbances – presented above and characterised by the influencing parameters – can lead to the obliteration of some flow regimes or the displacement of their corresponding range of Re.

Laminar state of flow, L

For very low Reynolds numbers, the flow around the cylinder remains fully laminar in all regions. The vorticity generated at the surface of the cylinder is dissipated by the viscous forces and the flow remains stable. The laminar state of flow can be subdivided into three basic flow regimes (Figure 2.6):

- L1, *"creeping" or Stokes flow* ($Re < 4$ to 5):
  The flow remains fully attached to the surface of the cylinder. The flow is steady and symmetric around the body and no wake is visible behind it because there is no separation of the boundary layers.

- L2, *steady separation regime* (4 to 5 $< Re <$ 30 to 48):
  When *Re* reaches 4 to 5, separation initiates and forms a steady and symmetric closed near-wake bordered by the free shear layers which meet at the end of it. A pair of recirculation regions symmetrically disposed around the centreline of the wake can be observed in the near-wake. Within this regime, the length of the near-wake increases with *Re*.

- L3, *periodic laminar regime* (30 to 48 $< Re <$ 180 to 200):
  As *Re* increases, the elongated near-wake becomes unstable and the trail starts to oscillate. The trail oscillation increases with *Re* and the free shear layers eventually roll up to form laminar eddies. Bénard (1908) was the first to sketch the alternate procession of laminar eddies behind a cylinder. Kármán (1912) theoretically investigated the stability of two rows of vortices and his work triggered a great interest on the flow around a single cylinder. Based on that, the procession of laminar eddies observed in this flow regime is often referred to as the *Kármán-Bénard eddy street*.

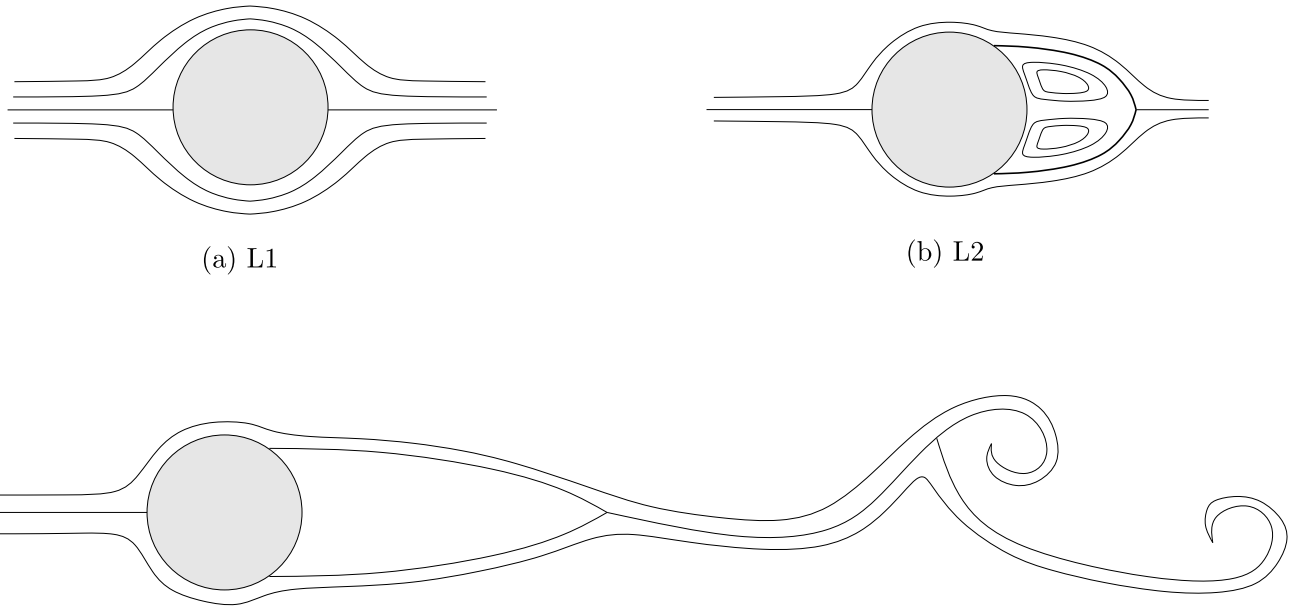

(a) L1 (b) L2

(c) L3

FIGURE 2.6: Schematics of flow around a cylinder in the laminar state.

Transition-in-wake state of flow, TrW

The Kármán-Bénard eddy street eventually undergoes transition to turbulence when *Re* increases. The viscous forces decrease and cannot dissipate all the flow instabilities anymore. The onset of transition from laminar to turbulent state of flow is located far downstream in the wake at first and moves upstream with *Re*. The transition-in-wake state of flow can be subdivided into two flow regimes (Figure 2.7):

- TrW1, *lower transition regime* (180 to 200 $< Re <$ 220 to 250):
  The transition is initiated in the Kármán-Bénard eddy street. It means that the eddies are formed laminar and regular and become turbulent further downstream.

- TrW2, *upper transition regime* (220 to 250 $< Re <$ 350 to 400):
  The transition takes place during the formation of the eddy and the latter becomes turbulent before being shed and carried downstream in the wake.

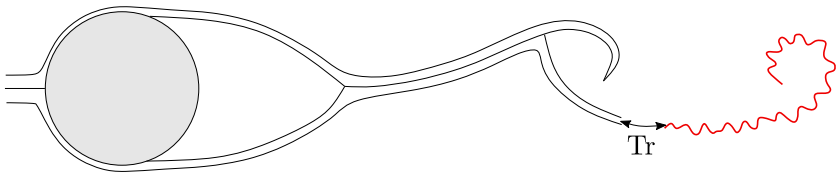

(a) TrW1

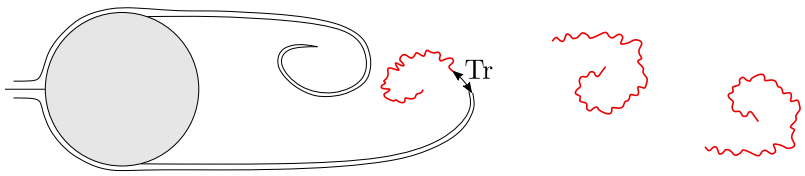

(b) TrW2

FIGURE 2.7: Schematics of flow around a cylinder in the TrW state.

An interesting phenomenon occurs between the flow regimes TrW1 and TrW2: a change of eddy shedding mode can be observed. It is reflected by a discontinuous variation in shedding frequency f_{vs} expressed by the dimensionless Strouhal number:

$$St = \frac{f_{vs} D}{U_\infty}. \tag{2.2}$$

Transition-in-shear-layers state of flow, TrSL (sub-critical)

The transition reaches the separated shear layers while the boundary layers remain fully laminar. This state of flow is commonly called *sub-critical* in the literature because it precedes the one where the onset of the transition takes place in the boundary layers and which is considered as *critical*. Wieselberger (1921) originally used the terms sub-critical and super-critical to refer to the states of flow below and above the "crisis" in drag force. The transition-in-shear-layers state of flow can be subdivided into three flow regimes (Figure 2.8):

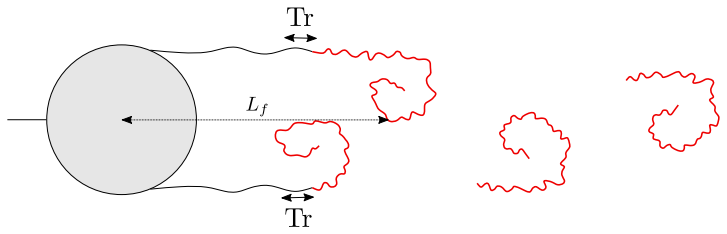

(a) TrSL1

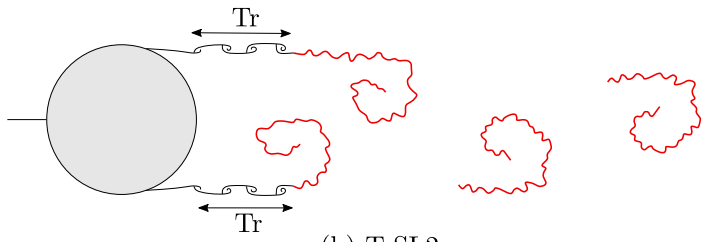

(b) TrSL2

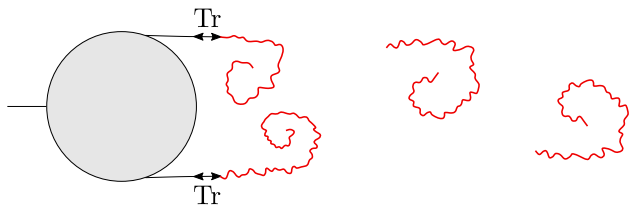

(c) TrSL3

FIGURE 2.8: Schematics of flow around a cylinder in the TrSL state.

- TrSL1, *lower sub-critical regime* (350 to 400 $< Re <$ 1k[1] to 2k):
  Transition waves appear as undulations along the separated shear layers. Those are called the *Gerrard-Bloor transition waves* in the literature. It is interesting to note that the length of eddy formation L_f increases with Re in this particular flow regime.

[1] k stands for "thousand" in this manuscript

- TrSL2, *intermediate sub-critical regime* (1k to 2k $< Re <$ 20k to 40k):
  The transition waves roll up to form transition eddies along the separated shear layers. They were first observed by Couregelongue (1929). As *Re* increases, the onset of transition to turbulence moves towards the separation of the boundary layers from the cylinder and it is accompanied by the shortening of the length of eddy formation L_f.

- TrSL3, *upper sub-critical regime* (20k to 40k $< Re <$ 100k to 200k):
  When the shortening of the eddy formation is completed at the end of TrSL2, the transition eddies suddenly disappear in the separated shear layers. The transition to turbulence is reduced to a location of a sudden burst in the shear layers close to the cylinder. In this flow regime, the transition region seems to be reluctant to move upstream with *Re*. This particular feature leads to a *quasi-invariable* flow with *Re*. For this reason, this flow regime has attracted a lot of attention in the past and has been thoroughly investigated. It must be mentioned that the fluctuations induced by the eddy shedding are the largest in this regime.

Transition-in-boundary-layers state of flow, TrBL

The onset of transition from laminar to turbulent state of flow finally reaches the separation lines and therefore the boundary layers. An intricate interaction between separation, transition and re-attachment is initiated. The transition-in-boundary-layers can be subdivided into four distinct flow regimes (Figure 2.9):

- TrBL0, *pre-critical regime* (100k to 200k$< Re <$ 300 to 340k):
  It is characterised by the first onset of transition in the separated shear layers along the separation lines. The inherent three-dimensional flow along the span disturbs the near-wake and thus delays the eddy formation. It results in an initial decrease in the drag coefficient while the eddy shedding frequency remains almost constant.

- TrBL1, *one-bubble regime* (300k to 340k $< Re <$ 380k to 400k):
  Bearman (1969) found that on one side of the cylinder the separated shear layers undergoes sufficient transition to turbulence to re-attach onto the surface of the cylinder. It forms what is called a laminar *separation bubble*. The subsequent turbulent separation is considerably delayed because it is more stable to separation. This leads to an asymmetric flow around the cylinder and a discontinuous drop in the drag coefficient is observed at the same time.

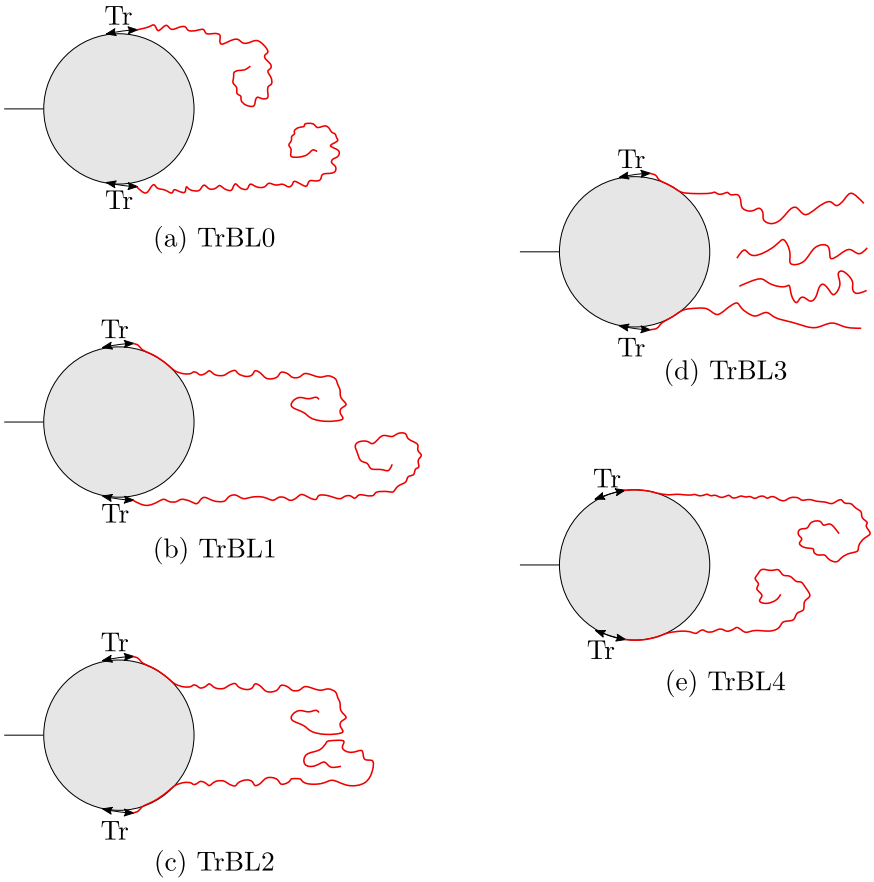

FIGURE 2.9: Schematics of flow around a cylinder in the TrBL state.

- TrBL2, *two-bubble regime* (380k to 400k $< Re <$ 500k to 1M[2]):
  A second discontinuous drop in the drag coefficient is observed and corresponds to the appearance of a second separation bubble on the other side of the cylinder.

- TrBL3, *super-critical regime* (500k to 1M $< Re <$ 3.4M to 6M):
  The transition reaches the initial laminar separation of the boundary layers and disrupts the separation bubbles along the span. This disruption prevents a periodic eddy shedding and it results in a chaotic wake behind the cylinder.

- TrBL4, *post-critical regime* (3.4M to 6M $< Re <$?):
  Regular eddy shedding re-appears when the boundary layers become fully turbulent before separation all along the span. This flow regime is thus characterised by a transition occurring in the boundary layers somewhere between the stagnation and separation lines. As Re increases, the transition region moves upstream towards the stagnation line. Nonetheless, the upper end of this regime is not quantitatively defined in the literature.

[2]M stands for "million" in this manuscript

It should be pointed out that the single and two-bubble regimes, TrBL1 and TrBL2, are highly sensitive to disturbances and may be obliterated in some cases, e.g. sufficiently rough surface or turbulence in the free-stream.

Fully turbulent state of flow, T

The fully turbulent state of flow is reached when all regions of the flow around the cylinder are turbulent. As stated above for the end of TrBL4 regime, the start of the T-state is not known. However, it can be stated that the end of this state of flow is theoretically $Re \rightarrow \infty$. Because of the difficulty to identify the distinction between TrBL4 and T regimes, it is chosen to only refer to the post-critical flow regime TrBL4 in this work. This choice is supported by the fact that the boundary layers are fully turbulent before separation in both flow regimes.

Comment on the three-dimensionality of the flow

As described above, a nominally two-dimensional cylinder generates a flow with inherent three-dimensionality in most flow regimes. Williamson (1996) defined two kinds of three-dimensionality of the flow around a cylinder: (i) "extrinsic", from the end effects for example; (ii) "intrinsic" from natural instabilities of the flow. The second kind is present in this work focusing on the flow around nominally two-dimensional bodies. The unsteady wake behind the cylinder leads to three-dimensional coherent structures (eddies). The three-dimensionality of the flow becomes even more important when laminar flow breaks down to turbulence since the latter is characterised by three-dimensional vorticity. Nevertheless, most research dealing with aeroelastic systems relies on the investigation of two-dimensional flows. It is supported by the fact that the large coherent structures of the flow responsible for the aeroelastic instabilities display a two-dimensionality, at least to a first approximation. Hence, all experimental investigations and quantities presented in this thesis are based on the two-dimensional flow assumption.

2.1.4 Aerodynamic forces

The distinct flow regimes and their variation – described in the previous section – can explain the variation of the aerodynamic forces with Re. As stated just above, the present work focuses on two-dimensional flow quantities even though the flow is inherently three-dimensional. Hence, the two-dimensional aerodynamic forces are the drag $F_D(t)$ and lift $F_L(t)$ acting in the streamwise and crosswise directions, respectively, as shown in Figure 2.10. The forces are classically expressed in their dimensionless form using the notion of aerodynamic force coefficients:

- drag coefficient:

$$c_d(t) = \frac{F_D(t)}{1/2\rho U_\infty^2 D}, \tag{2.3}$$

- lift coefficient:

$$c_l(t) = \frac{F_L(t)}{1/2\rho U_\infty^2 D}. \tag{2.4}$$

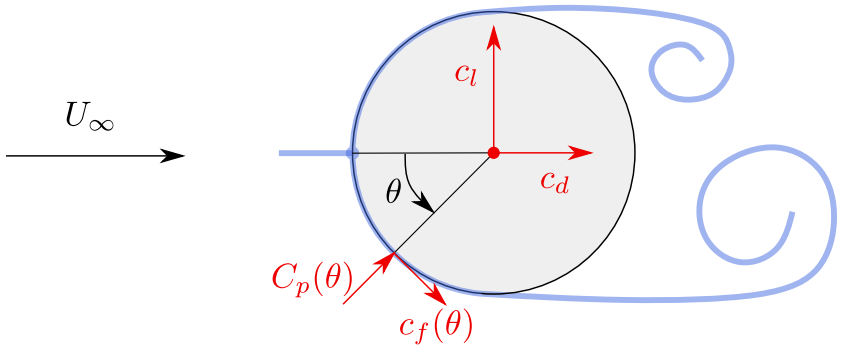

FIGURE 2.10: Definition of the aerodynamic forces acting on a cylinder.

The lift and drag forces are due to the pressure distribution $p(\theta, t)$ and the wall shear stress distribution $\tau_w(\theta, t)$ over the surface of the cylinder in the normal and tangential direction, respectively. Similarly to the aerodynamic forces, the pressure and wall shear stress are conveniently reduced to their dimensionless form:

- pressure coefficient:

$$C_p(\theta, t) = \frac{p(\theta, t) - p_\infty}{1/2\rho U_\infty^2}, \tag{2.5}$$

- skin friction coefficient:

$$c_f(\theta, t) = \frac{\tau_w(\theta, t)}{1/2\rho U_\infty^2}, \tag{2.6}$$

with p_∞ being the reference pressure in the free-stream. The aerodynamic forces can be computed by integrating the two contributions over the surface of the cylinder. Hence, an aerodynamic force coefficient can be decomposed as follows

$$C_F = C_{Fp} + C_{Ff}, \tag{2.7}$$

where C_F is a force coefficient, C_{Fp} the contribution produced by the pressure distribution and C_{Ff} the contribution resulting from the viscous friction along the surface. For a cylinder, it will be shown that the viscous friction contribution C_{Ff} drastically decreases with Re and becomes negligible beyond a particular value of Re.

Because of the inherent unsteady nature of the flow around the cylinder (except in L1 and L2 regimes), the aerodynamic coefficients fluctuate in time. Therefore, an aerodynamic coefficient C_a is conveniently decomposed in a time-averaged value $\overline{C}_a$ and fluctuating one $\widetilde{C_a}$:

$$C_a(t) = \overline{C}_a + \widetilde{C_a}(t). \tag{2.8}$$

Moreover, the fluctuating part is usually reduced to and reported as its root-mean-square (r.m.s.) value $\sqrt{\overline{\widetilde{C_a}(t)^2}}$ in the literature. For the sake of clarity, the r.m.s. fluctuating coefficient is denoted C'_a in this manuscript.

Figure 2.11 shows the variation of the time-averaged and fluctuating force coefficients with Re for a disturbance-free flow around a cylinder. Zdravkovich (1990) summarised in this figure the effects of the different flow regimes on the aerodynamic force coefficients. One of the most important feature is the sudden drop in the time-averaged drag coefficient at the beginning of TrBL1 with the appearance of a non-zero time-averaged value for the lift coefficient. It is associated with the appearance of a laminar separation bubble on one side of the cylinder leading to a narrower wake and asymmetric flow. It is followed by a second drop in the time-averaged drag coefficient at the beginning of TrBL2 regime associated with the appearance of a second laminar separation bubble on the other side of the cylinder which narrows even more the wake. At the same time, the time-averaged lift coefficient takes a zero

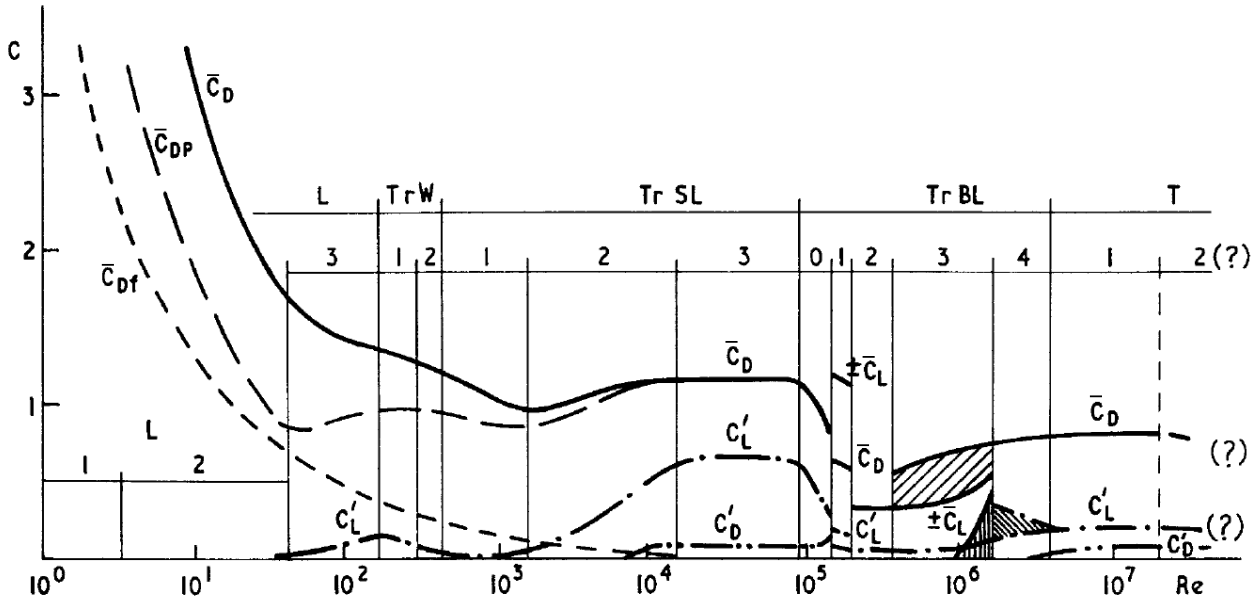

FIGURE 2.11: Variation of the aerodynamic force coefficients with Re in a disturbance-free flow (from Zdravkovich, 1990).

value since the flow becomes symmetric again. The fluctuating lift coefficient C'_L appears when the Kármán-Bénard eddy street develops at the beginning of L3 regime. It is interesting to notice that C'_L reaches local maxima between L3 and TrW1 regimes or in TrSL3 regime, which correspond to ranges of Re where the formation length of eddy reaches local minimum values. The eddies are formed closer to the base of the cylinder and therefore lead to larger fluctuations of the aerodynamic forces.

The contributions of the pressure and viscous friction in the time-averaged drag coefficient are also reported in Figure 2.11. It is observed that the viscous friction contribution $\overline{C}_{Df}$ monotonically decreases with Re and becomes negligible at the end of TrSL2 regime. Viscous forces can therefore be neglected for high Reynolds number flow regimes. Nevertheless, it should be stressed out that viscosity effects are not neglected.

The description of the flow regimes and variation of the aerodynamic forces with Re highlights the complexity of the flow around a single cylinder, which is strongly dependent on the Reynolds number. Furthermore, it was described for a disturbance-free flow, and the influencing parameters may also have significant effects.

2.2 Twin cylinders

A single cylinder has been considered up to now, but in practice many engineering applications involve the use of multiple cylinders. As stated in the introduction, the present thesis is devoted to the particular case of twin cylinders in close proximity. The flow around twin cylinders has been investigated to a lesser extent than around a single cylinder. Nonetheless, many studies exist in the literature and revealed flow interference between the two cylinders which strongly depends on their arrangement.

An infinite number of arrangements between two cylinders exist. The present work is focused on two parallel circular cylinders with equal diameter in a cross-flow. Nonetheless, the reader should be aware that some researchers also investigated the flow around non-parallel tandem cylinders (e.g. Younis, Alam, and Zhou, 2016 or Alam et al., 2022) or around tandem cylinders with different diameters (e.g. Igarashi, 1982 or Wang, Alam, and Zhou, 2018). But these specific arrangements go beyond the scope of this doctoral thesis.

The possible arrangements of two parallel cylinders of equal diameter in a cross-flow are shown in Figure 2.12 and are the following ones:

(a) *tandem arrangement*: one cylinder is located behind the other with respect to the incoming free-stream;

(b) *side-by-side arrangement*: the cylinders are placed side-by-side, facing the incoming free-stream;

(c) *staggered arrangement*: it corresponds to the most general arrangement which is in between the tandem and side-by-side arrangements.

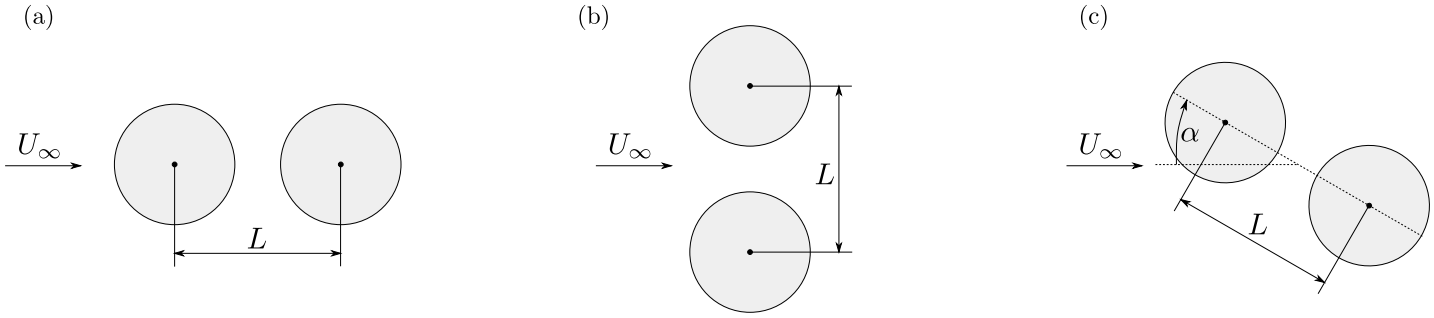

FIGURE 2.12: Possible arrangements of two parallel cylinders of equal diameter in a cross-flow: (a) tandem, (b) side-by-side and (c) staggered.

Two additional geometric parameters are introduced for the flow around two cylinders: (i) the centre-to-centre spacing ratio L/D and (ii) the flow incidence or stagger angle α, as defined in Figure 2.12. It is easy to conceive that those two geometric parameters have a strong effect on the flow developing around the two cylinders.

2.2.1 Interference flow regions

Zdravkovich (1987) classified the flow interference between two parallel cylinders into four particular kinds (see Figure 2.13) :

(i) *proximity interference*: the cylinders are close to each other but none of them is found in the wake of the other (e.g. side-by-side configuration);

(ii) *wake interference*: the rear cylinder is near to or submerged into the wake of the front cylinder and the flow around the latter is unaffected by the presence of the other cylinder (e.g. tandem configuration with large spacing ratio);

(iii) *proximity and wake interference*: a combination of both proximity and wake interferences occurs;

(iv) *no interference*: the interference is considered negligible and the flow around each cylinder is similar as for the single cylinder.

This basic qualitative classification is nonetheless insufficient to describe all distinct flow patterns that can be observed around twin cylinders. For example, Sumner,

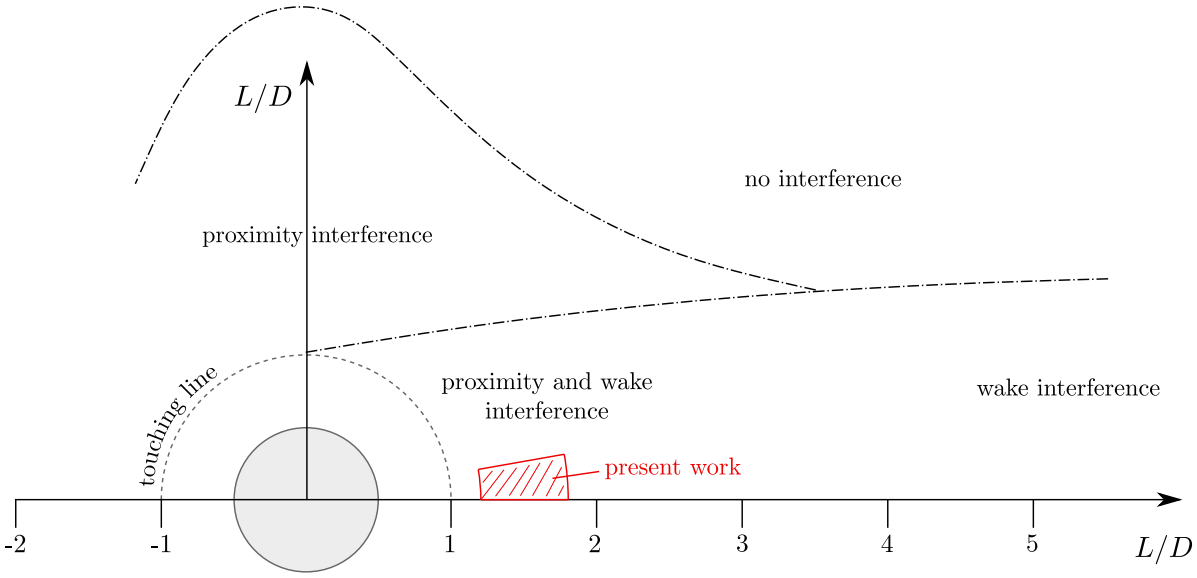

FIGURE 2.13: Interference flow regions around two cylinders (adapted from Zdravkovich, 1987).

Price, and Païdoussis (2000) identified nine distinct flow patterns by means of flow visualisation, depending on the spacing ratio L/D and the flow incidence α. Further subdivisions of the flow interference shown in Figure 2.13 were suggested by Zdravkovich (1987), resulting in 12 interference flow patterns which represent a tentative overview based on the existing literature at that moment. More recently, Alam and Meyer (2011) identified up to 19 distinct interference flow patterns based on the aerodynamic forces, Strouhal number St and flow structures. This large number of flow patterns clearly highlights the complexity of the flow around twin cylinders.

The present work focuses on closely spaced cylinders in tandem and slightly staggered arrangements which implies that proximity and wake interference is expected, as highlighted by the red dashed zone in Figure 2.13. The tandem and staggered arrangements are now discussed in separate sections for deeper physical insights.

2.2.2 Tandem arrangement

One of the earliest experimental studies on tandem cylinders was carried on by Biermann and Herrnstein (1933) who investigated the interference of airplane struts. They noticed that the presence of a cylinder in the wake of another slightly affects the drag of the front cylinder (upstream) while the drag of the rear cylinder (downstream) is significantly reduced in comparison with the one acting on a single cylinder. For small spacing ratio, a negative drag force is observed which indicates a thrust force acting on the rear cylinder.

The measurements of the drag forces performed by Biermann and Herrnstein (1933) were then completed with the identification of different flow patterns by different authors. Hori (1959) was the first to measure and report the time-averaged pressure distribution around tandem cylinders. His work shows that the pressure distribution around the front cylinder is similar to the one of a single cylinder. The interference affects only the minimum and base pressure values. On the other hand, the pressure distribution around the rear cylinder is strongly affected. For small spacing ratios, the pressure in the gap between the cylinder is lower than the base pressure of the rear cylinder. This particular feature explains the observation of a negative drag force acting on the rear cylinder.

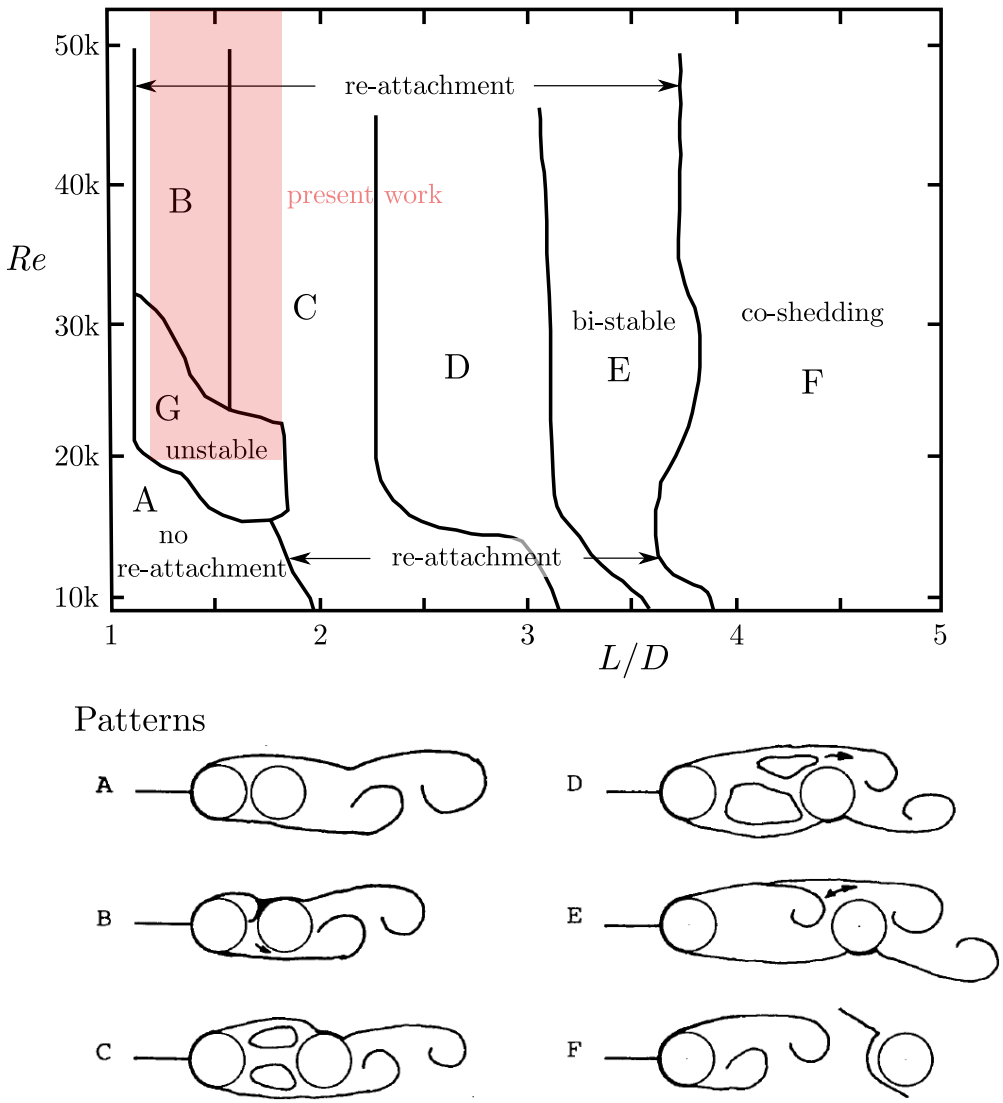

FIGURE 2.14: Classification and definition of the flow patterns around tandem cylinders (from Igarashi, 1981).

Ishigai et al. (1972) used the Schlieren method to visualise the flow around the two cylinders. The flow visualisation revealed different behaviours of the separated shear layers from the front cylinder depending on the spacing ratio. Igarashi (1981, 1984) carried out extensive measurements of the fluctuating pressure distribution together with flow visualisation (using smoke) and he classified flow patterns as a function of the spacing ratio L/D and Reynolds number Re. The classification is shown in Figure 2.14.

The identified flow patterns reported in Figure 2.14 are briefly described below:

- A : the shear layers from the front cylinder do not re-attach onto the rear cylinder. Eddies are formed and shed behind the rear cylinder.
- B : the shear layers alternately re-attach onto the rear cylinder.
- C : the shear layers re-attach onto the rear cylinder and quasi-stationary eddies are formed between the cylinders.
- D : the quasi-stationary eddies become unstable and their shedding is detected intermittently.
- E : the shear layers from the front cylinder roll up intermittently in front of the rear cylinder. It corresponds to a bi-stable flow in the transition region between flow patterns D and F.
- F : the shear layers from the front cylinder roll up between the cylinders.
- G : it corresponds to an unstable flow in the transition region between flow patterns A, B and C.

Based on these flow patterns, Zdravkovich (1987) defined three main behaviours of the separated shear layers from the front cylinder:

(i) *extended-body* (or *no re-attachment*) behaviour: the shear layers do not re-attach onto the rear cylinder and they form an single eddy street behind the tandem arrangement (flow pattern A);

(ii) *re-attachment* behaviour: the shear layers re-attach onto the rear cylinder and an eddy street is formed only behind the latter (flow patterns B, C and D);

(iii) *co-shedding* behaviour: the shear layers roll up and form an eddy street between the front and rear cylinders and hence both cylinders shed eddies (flow pattern F).

These main behaviours are reported in Figure 2.14. It is observed that the spacing ratio corresponding to the transition from one behaviour (or one flow pattern) to the other depends on the Reynolds number, as the boundaries vary with Re. Ljungkrona, Norberg, and Sunden (1991) also showed that these boundaries vary with the turbulence level in the incoming flow. Therefore, the occurrence of one specific flow pattern or the other around two tandem cylinders depends on the Reynolds number, the spacing ratio L/D and the different influencing parameters introduced in section 2.1.2.

In Figure 2.14, the red zone shows the range of L/D investigated in the present work. Moreover, it will be shown later in this manuscript that the experimental tests are performed for a Reynolds number ranging from 21k to 395k. Hence, it is expected to observe the flow patterns B, C and G in the present investigation (for $Re < 50$k at least).

2.2.3 Slightly staggered arrangement

Although staggered arrangement is perhaps the most commonly found in engineering applications, numerous investigations on the flow around two cylinders have been performed in tandem or side-by-side arrangement, while only relatively few studies focused on the staggered arrangement.

Time-averaged aerodynamic forces acting on two staggered cylinders were measured or reported by Hori (1959), Zdravkovich and Pridden (1977), Gu and Sun (1999), Sumner, Richards, and Akosile (2005) or Schewe and Jacobs (2019), among others. A common observation in the different studies concerns the so-called "inner" and "outer" lift peaks, which correspond to local maximum values of the lift coefficient in the $(L/D - \alpha)$ plane. The inner lift peak is observed for small spacing ratios. It is explained by the establishment of a strong gap flow between the two cylinders when the flow incidence becomes sufficiently large. The outer lift peak is observed for larger spacing ratios. It is produced by the displacement of the fully formed wake of the front cylinder by the flow around the rear cylinder. The outer lift reaches a maximum value near the edge of the wake boundary and diminishes gradually to zero when the flow incidence is decreased.

Systematic measurements of the time-averaged pressure and wake velocities for two staggered cylinders in the upper sub-critical flow regime were made by Gu and Sun (1999). They identified flow patterns based on the time-averaged pressure distribution. They found two switching flow processes and three distinct pressure-distribution patterns (I_B, II_B, III_B) on the rear cylinder. The associated flow patterns are shown in Figure 2.15, in which the flow incidence α is denoted β. For the first

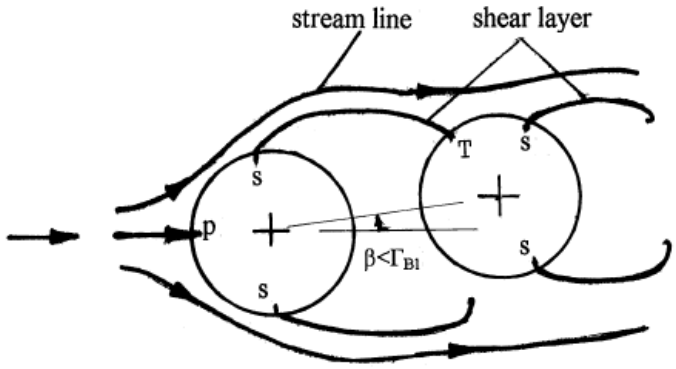

(1) The interference of wake
($\beta<\Gamma_{B1}$, the pressure pattern I_B on the downstream cylinder)

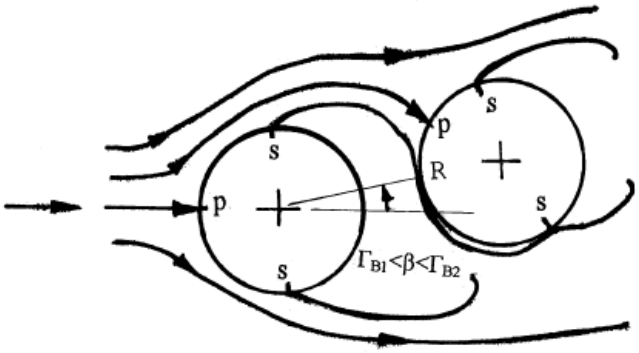

(2) The interference of shear layer
($\Gamma_{B1}<\beta<\Gamma_{B2}$, the pressure pattern II_B on the downstream cylinder)

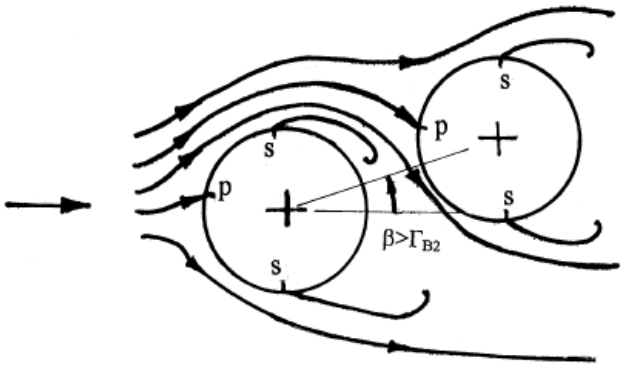

(3) The interference of neighborhood
($\beta>\Gamma_{B2}$, the pressure pattern III_B on the downstream cylinder)

FIGURE 2.15: Sketches of flow patterns of two cylinders in staggered arrangement from Gu and Sun (1999) (S: separation point; P: stagnation point; R: re-attachment point; T: shear layer touch point).

pattern, the shear layer re-attaches onto the rear cylinder and the latter is almost completely submerged in the wake of the front cylinder. In that case, no stagnation point associated with $\overline{C}_p = 1$ is found on the surface of the rear cylinder. For the

second pattern, the shear layer completely goes through the gap between the cylinders and re-attaches onto the forward surface of the rear cylinder. A stagnation point with $\overline{C}_p = 1$ is observed on the rear cylinder in this flow pattern. For the third flow pattern, a sufficient amount of the free-stream goes through the gap between the cylinders and prevents the shear layer from re-attaching onto the rear cylinder. For $L/D = 1.7$, the flow patterns I_B, II_B and III_B were respectively identified in the ranges $\alpha = 0°$–$9.65°$, $9.7°$–$15°$ and $16°$–$90°$ at $Re = 220$k. Gu and Sun (1999) also examined the switching processes between the distinct flow patterns and pointed out that the corresponding critical flow incidences depend on the spacing ratio and the Reynolds number. Moreover, they emphasised that the switching process of flow pattern from one to the other is not just an abrupt change but it may be randomly changed back and forth at the critical flow incidences, leading to a bi-stable nature of the flow.

Alam, Sakamoto, and Zhou (2005) measured the unsteady forces and pressures acting on twin cylinders for different flow incidences and spacing ratios. The flow patterns were identified using surface-oil visualisations. For some arrangements (e.g. $L/D = 1.1$ and $\alpha = 10°$), a bi-stability of the flow was also observed. This bi-stability concerned the behaviour of the flow along the forward face of the rear cylinder when a gap flow is established. The location of separation point of the forward boundary layer intermittently switches from the upstream face to the downstream face of the rear cylinder. The bi-stability resulted in jumps of the time-averaged lift coefficients applied on both cylinders.

2.2.4 Flow regimes

As the flow pattern boundaries of Igarashi (1981) indicate (Figure 2.14), the flow around two cylinders is particularly sensitive to the Reynolds number. Consequently, the flow patterns and their extent in the $(L/D - \alpha)$ plane are expected to depend on the distinct flow regimes which were introduced in section 2.1.3 for a single cylinder.

In the past, several experimental studies considered the effect of the Reynolds number on the flow around two cylinders. For example, Zhou et al. (2009) investigated the effect of the Reynolds number on the Strouhal number of staggered cylinders, but their work is limited to the sub-critical flow regimes (TrSL). In the same regime, Alam (2014) classified the flow patterns around tandem cylinders as a function of the Reynolds number and spacing ratio.

Sumner (2010) reviewed the works on two identical cylinders in a cross-flow. He showed that most of the previous studies on twin cylinders have been performed in the sub-critical flow regimes (TrSL) and highlighted the need for more research in the super and post-critical regimes.

Okajima (1979) was the first to experimentally simulate the post-critical flow regime around two cylinders in tandem arrangement by means of surface roughness. He investigated the variation of the time-averaged drag coefficients and Strouhal numbers of both individual cylinders with the Reynolds number and spacing ratio. Sun et al. (1992) examined the fluctuating pressure on staggered cylinders in the super-critical flow regime. A recent investigation on the flow around twin smooth cylinders from sub- to post-critical regimes was conducted by Schewe and Jacobs (2019) in a high-pressure wind tunnel. It consists in a parametric analysis of time-averaged flow quantities for a given spacing ratio ($L/D = 1.56$). As already stated in the introduction, they reported vibrations of the cylinders, which were supposed to be static, in the post-critical regime. Schewe and Jacobs (2019) concluded that the strong non-linearity of the aerodynamic force and moment coefficients is heavily dependent on the Reynolds number and is responsible for the difficulty to identify the source(s) of excitation of the flow-induced vibrations. Furthermore, they supported the need to measure unsteady forces in order to better understand the different types of flow-induced vibrations.

To summarise this brief literature review, there is clearly a lack of investigation on the unsteady flow around twin cylinders in the post-critical regime. Hence, it supports the present research work which aims at providing new experimental results in this flow regime.

2.3 Terminology

Based on the literature presented above, different flow features around twin cylinders are defined and shown in Figure 2.16. This terminology is used through the manuscript.

- *Stagnation point*: Point on the surface of the cylinder where the flow velocity is zero and is associated with $\overline{C}_p = 1$. A stagnation point is always found on the upstream face of the front cylinder and is found on the rear cylinder when a gap flow is established between the cylinders.

- *Separation point*: Point on the surface of the cylinder where the boundary layer separates from the surface.

- *Re-attachment point*: Point on the surface of the cylinder where one of the shear layers re-attaches. A local maximum value in the pressure distribution ($\overline{C}_p < 1$) is associated with the re-attachment point.

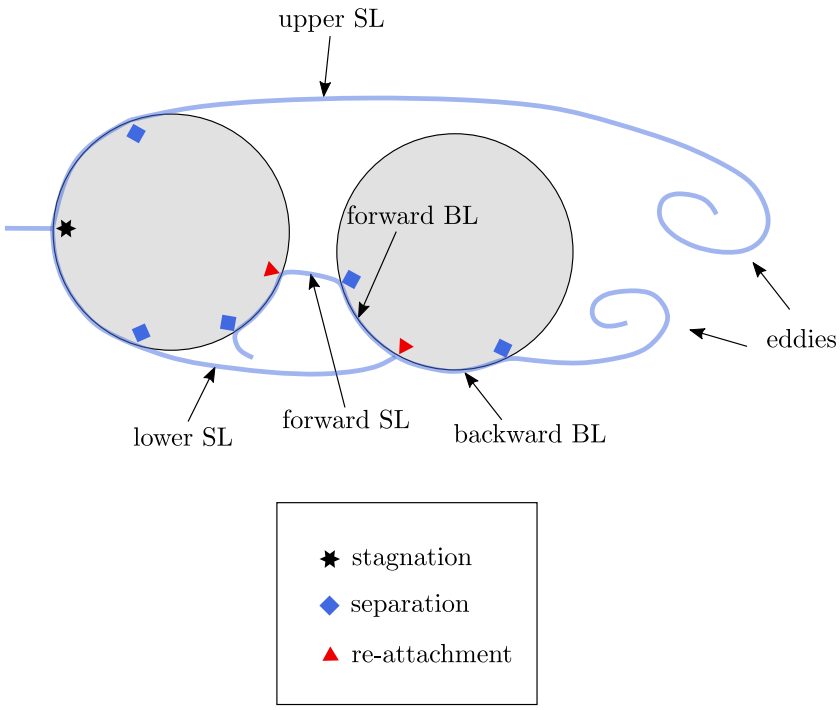

FIGURE 2.16: Definition of the flow features around two slightly staggered cylinders (BL: boundary layer; SL: shear layer).

From a stagnation or re-attachment point, two boundary layers develop on both sides. Concerning the front cylinder, the resulting boundary and shear layers from the stagnation point on the upstream face are denoted as upper and lower layers, as shown in Figure 2.16. For the rear cylinder, the terms backward and forward boundary layers are used to denote the boundary layers flowing in the downstream or upstream direction, respectively (see Figure 2.16). Note that the forward boundary layer may separate and re-attach onto the back face of the front cylinder in some arrangement (small spacing ratio), as shown in Figure 2.16.

Flow schematics (similar to Figure 2.16) will be used to support and facilitate the discussions throughout this manuscript. The objective is to give the reader a qualitative understanding of the flow physics. In some existing literature (in the sub-criticial flow regime), these schematics are extracted from surface pressure and flow visualisation. In this work, only pressure measurements on the surface of the cylinders are used. The schematics presented here in the post-critical regime are based on the combination of pressure measurements and existing literature. For this reason, it remains an approximation of the reality, which could be verified and improved via flow visualisation.

Because of their use in various works, it is also necessary to clearly define some other terms in order to avoid any misunderstanding throughout the manuscript:

- *State of flow*: it refers to whether the flow is laminar, transitional or turbulent in the different regions around the cylinder.
- *Flow regime*: it corresponds to a sub-division of the state of flow and is characterised by the occurrence of specific flow features and a particular variation of fluid forces with the Reynolds number.
- *Main behaviour of shear layers*: it refers to the time-averaged behaviour of the shear layers from the front cylinder with respect to the rear cylinder.
- *Flow pattern*: it completely describes the unsteady flow and the different flow features that can be observed around the two cylinders. It is worth noting that a unique flow pattern is defined in a specific flow regime for a single cylinder. On the other hand, several flow patterns can be identified in a flow regime around twin cylinders as a function of the spacing ratio L/D and flow incidence α.

This chapter has introduced the important features and state-of-the-art concerning the flow around static cylinder(s). The main outcome of this chapter is the strong sensitivity of the flow to the Reynolds number, which leads to the existence of distinct flow regimes. The flow patterns that are observed around two cylinders depend not only on the spacing ratio L/D and the flow incidence α, but also on the flow regime and other influencing parameters (e.g., free-stream turbulence, surface roughness). The literature review has revealed that most studies have been performed in the sub-critical flow regime. It supports the need for more research in the post-critical flow regime, which is the subject of this thesis.

Chapter 3

Triggering the post-critical flow regime

As stated in the introduction, the present work focuses on the flow and potential aeroelastic phenomena in the post-critical regime, where the different regions of the flow around the cylinders are turbulent. In the previous chapter, it has been shown that this particular flow regime occurs at high Reynolds numbers in a disturbance-free flow ($Re > 3.4$M to 6M). Because of the limitations in size and flow velocity, such high Reynolds numbers cannot be reached in the atmospheric wind tunnel of the University of Liège. Hence, the post-critical flow regime has to be triggered at lower Reynolds numbers. To do so, a common practice in wind tunnel tests consists in applying appropriate surface roughness on the body of interest. The same approach is followed in this work. This disturbance has already been mentioned when defining the influencing parameters earlier. A review of the effect of the surface roughness on the flow around a single cylinder is first presented. A careful preliminary investigation is then performed on a single cylinder in order to validate the use of surface roughness to access the critical and post-critical flow regimes in the wind tunnel tests.

3.1 Use of surface roughness

The effect of the surface roughness on the flow around a single cylinder have been investigated in the past (Fage and Warsap, 1929; Achenbach, 1971; Szechenyi, 1975; Güven, Farell, and Patel, 1980; Adachi, 1997; Hinsberg, 2015). It has been mostly analysed through the parameter k which corresponds to the mean size of the excrescences on the surface, as defined in the previous chapter.

The surface roughness introduces small disturbances in the flow along the surface of the cylinder which promotes the transition from laminar to turbulence. Fage and Warsap (1929) were the first to note that the surface roughness produces turbulence within the boundary layers and affects the flow in a similar manner as the free-stream turbulence. The difference is that the free-stream and roughness-generated turbulences act on the boundary layers from "outside" and "inside", respectively. The

complete mechanism details of the production of roughness turbulence have not yet been investigated. But it can be stated that the roughness turbulence is related to:

(i) the *relative roughness*, k/D;

(ii) the *texture*, Te.

The texture, Te, of the surface roughness is a combination of the shape of the excrescences (most frequently occurring shape) and their distribution (irregular, regular, partial, etc). It is assumed that the parameter Te has a lesser effect on the production of roughness turbulence than k/D, but it appears important in determining the turbulent scale and turbulence dissipation. Therefore, it seems that both k/D and Te are required to define the surface roughness. Nonetheless, the texture parameter has been investigated to a lesser extent than the relative roughness in the literature.

Fage and Warsap (1929) carried out pioneering experiments to assess the effect of surface roughness on the drag coefficient of a single cylinder. They obtained rough surfaces by carefully applying different glass papers around the cylinder. It is observed that the critical Reynolds number Re_c associated with the sudden drop in time-averaged drag coefficient decreases as the surface is roughened. This observation was subsequently also made by many researchers after them (Achenbach, 1971

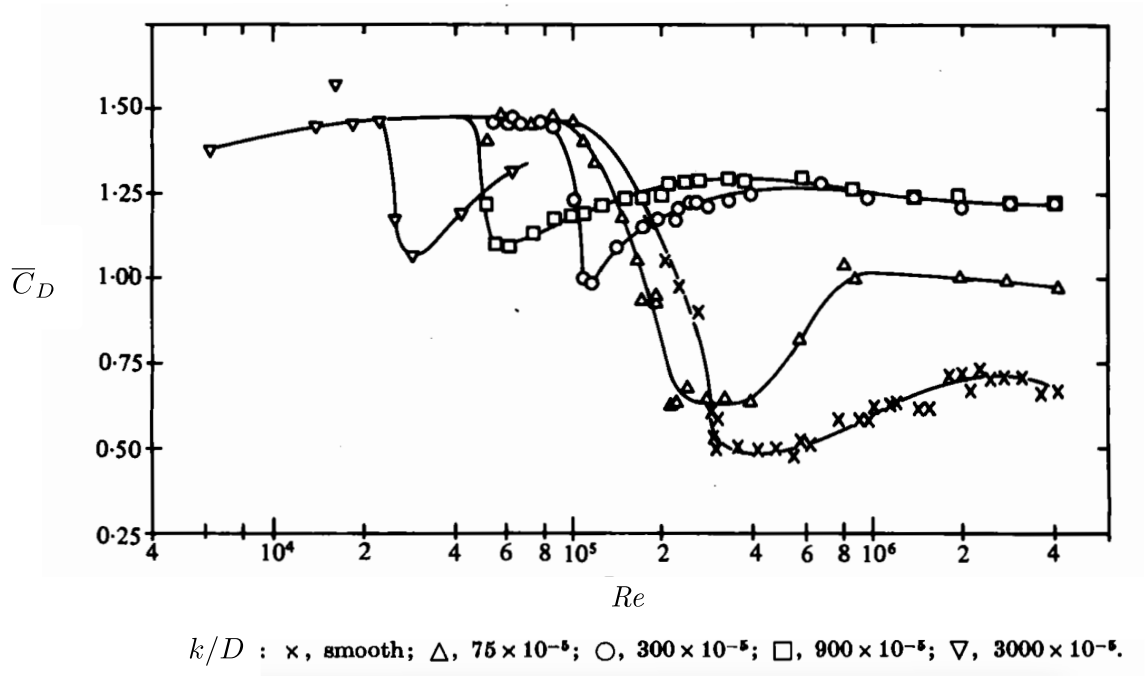

FIGURE 3.1: Drag coefficient of a single cylinder for various surface roughness levels (Achenbach and Heinecke, 1981).

or Buresti, 1981, among others). Figure 3.1 shows the time-averaged drag coefficient of a single cylinder for different surface roughness levels. It clearly illustrates the previous statement, i.e., the critical Reynolds number Re_c decreases with k/D. Achenbach and Heinecke (1981) suggested the following empirical equation based on literature results:

$$Re_{(\overline{C}_{D\min})} = \frac{6000}{(k/D)^{1/2}} \tag{3.1}$$

which relates the value of Re at which $\overline{C}_D$ is minimum – just after the drag crisis – to the relative roughness k/D. In the previous chapter, it was pointed out that the drag crisis is associated with the beginning of the TrBL state of flow. Hence, the decrease in Re_c with k/D implies that the onset of transition from laminar to turbulence reaches the boundary layers at lower Reynolds numbers when the surface of the cylinder is roughened. Consequently, it allows to go beyond the critical flow regime and reach the post-critical one at lower Reynolds numbers.

Buresti (1981) reported a tentative mapping of the occurring flow regimes in the (k/D-Re) plane, as shown in Figure 3.2. It must be pointed out that his experiments

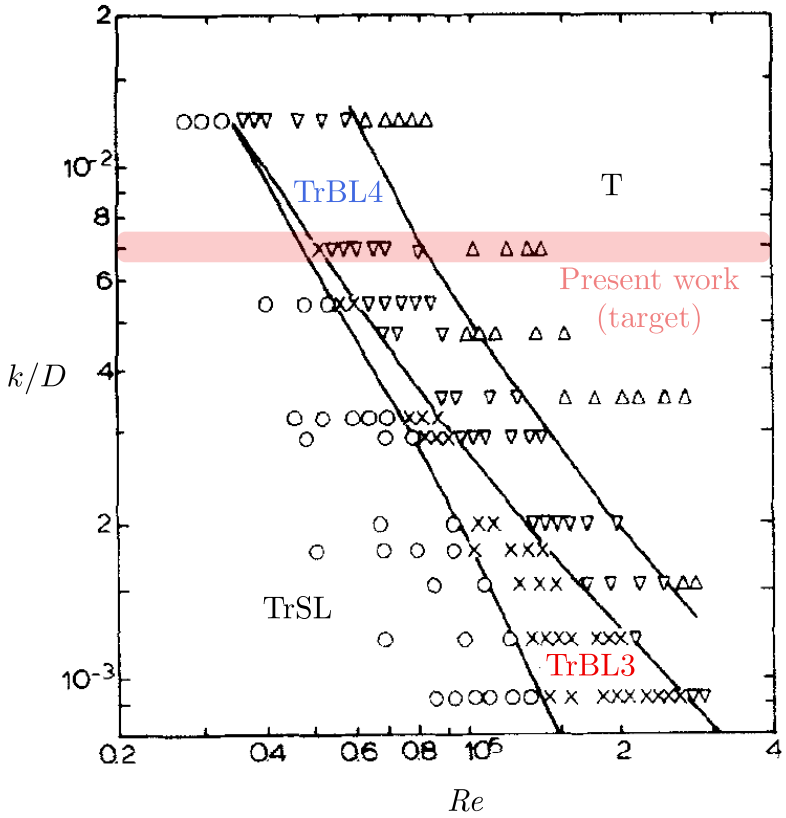

FIGURE 3.2: Mapping of the occurring flow regimes in the (k/D-Re) plane (Buresti, 1981).

were performed with a free-stream turbulence intensity of 1%, which cannot be totally neglected and may have an effect on the flow around the cylinder. Nonetheless, it is interesting to notice that the one-bubble and two-bubble flow regimes (TrBL1 and TrBL2) are not reported in this figure. It was mentioned earlier that those regimes are very sensitive to disturbances. Hence, they are obliterated by the presence of surface roughness on the cylinder. In Figure 3.2, it is also observed that the super-critical regime, TrBL3, shrinks as k/D increases and even disappears beyond a certain roughness level. The main outcome of Figure 3.2 is that the post-critical flow regime, TrBL4, can be reached with the appropriate surface roughness parameter k/D. The design and choice of the surface roughness was supported by this outcome and the retained value of k/D around 7×10^{-3} is shown by the red window in Figure 3.2. Using Equation (3.1), the Reynolds number associated with the minimum value of time-averaged drag coefficient is estimated at $Re \approx 72$k.

3.2 Experimental set-up

A detailed description of the experimental apparatus used in the present work to investigate the flow around static cylinder(s) is given in this section.

3.2.1 Wind tunnel facility

The experimental campaign is performed in the wind tunnel facility of the University of Liège. This facility consists in a closed-loop low-subsonic wind tunnel. It operates in atmospheric conditions, which means that it is not possible to pressurise the wind tunnel test section and hence to modify the density of air giving access to larger Reynolds numbers. The aeronautical test section in which the model is mounted is 2 m in width and 1.5 m in height. The flow velocity can be varied from 2 m/s to 65 m/s and the flow is characterised by a low level of turbulence (maximum turbulence intensity of 0.2%).

3.2.2 Model

The experimental model is shown in Figure 3.3. It consists of a cylinder with an external diameter D of 0.125 m and a span length S equal to 1.25 m. This leads to an aspect ratio S/D and a geometric blockage ratio D/B equal to 10 and 6.25%, respectively. The value of the blockage ratio being lower than 10%, no correction is applied as it is common practice in similar wind tunnel tests. The flow velocity is varied from 2.5 m/s to 47 m/s. The tested Reynolds number Re based on the external

FIGURE 3.3: Picture of the experimental model of a single cylinder in the wind tunnel of Uliège.

diameter D is therefore ranging from 21k to 395k. The cylinder is clamped on both ends using end-plates (with diameter of $4.4D$) to minimise the three-dimensional effects on the flow. The cylinder is composed of three parts: an instrumented central part obtained by means of a 3D printing technique, which allows controlling the geometry and texture of the surface roughness near the measurement locations, and two steel parts on the extremities covered by sandpapers. The set-up is mounted vertically on a turn-table, allowing to adjust accurately the orientation of the cylinder with respect to the incoming flow. The experimental model is intended to be static and was designed in order to minimise the structural vibrations. This is ensured by using steel tubes with large stiffness. All static tests performed in this thesis showed no vibration.

3.2.3 Instrumentation

The cylinder is instrumented by 48 pressure taps of 1.37 mm inner diameter, equally spaced on an instrumented section at mid-span, as shown in Figure 3.4. The pressure is measured during 60 s at a sampling frequency of 600 Hz using a pressure scanner (from Turbulent Flow Instrumentation Pty Ltd) with a range of ± 2.7 kPa and accuracy of $\pm 0.1\%$ of the full-scale. Dynamic effects of the pressure lines are corrected using the analytical model by Bergh and Tijdeman (1965).

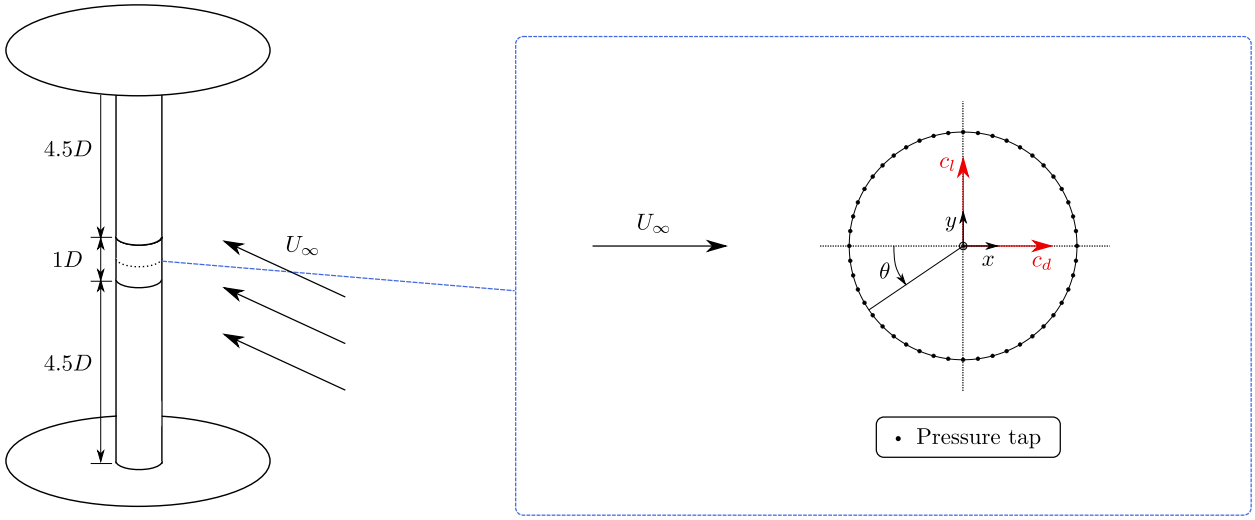

FIGURE 3.4: Schematic of the set-up and definition of the variables.

The pressure coefficient C_p is calculated using

$$C_p(\theta, t) = \frac{p(\theta, t) - p_\infty}{1/2\rho U_\infty^2} \tag{3.2}$$

where $p(\theta, t)$ is the cylinder surface pressure measured by the pressure scanner and p_∞ is the static pressure measured by a Pitot tube at the free-stream reference which is located at $x/D = -4.36$, $y/D = -2.64$ and slightly above the instrumented section. The origin of xy-coordinates is located in the centre of the cylinder, as shown in Figure 3.4. The Pitot tube also provides the dynamic pressure ($1/2\rho U_\infty^2$), allowing to extract the flow velocity U_∞ inside the tunnel.

The time-dependent pressure components of two-dimensional lift coefficient c_l and drag coefficient c_d are obtained by integrating the surface pressure,

$$c_l(t) = \frac{1}{2}\int_0^{2\pi} C_p(\theta, t)\sin(\theta)d\theta, \tag{3.3}$$

$$c_d(t) = \frac{1}{2}\int_0^{2\pi} C_p(\theta, t)\cos(\theta)d\theta. \tag{3.4}$$

Note that the viscous components of the aerodynamic force coefficients are not taken into account because their respective contribution is negligible in comparison with the one from the pressure distribution when $Re > 10$k, as already pointed out in Figure 2.11. All experimental measurement are prone to errors (e.g., from pressure scanner or misalignment). For this reason, the quantities presented above are characterised by uncertainties. This specific aspect is investigated in details in Appendix B. In this manuscript, the error bars are not superimposed in the figures for clarity.

3.3 Validation of surface roughness

A particular care is given to the validation of the surface roughness applied on the cylinder to trigger the post-critical flow regime at lower Reynolds numbers. It is particularly important in the present experimental investigation because two different kinds of surface roughnesses are used along the span of the cylinder. Indeed, the instrumented central part is roughened with very regular excrescences by means of a 3D-printing technique, while the other parts are roughened by sandpapers which present a less regular distribution of the excrescences on the surface. The texture parameter *Te* is therefore not the same and it must be ensured that the same equivalent surface roughness is applied all along the span of the cylinder to avoid potential three-dimensional effect on the flow.

3.3.1 Effect of the central roughness

Four different surface roughnesses for the instrumented central part of the cylinder are investigated. The parameters characterising the generated surface roughnesses are given in Table 3.1 and defined in Figure 3.5. Three different regular patterns of cubic excrescences are considered, as shown in Figure 3.6. The effect of roughness pattern, which somehow defines the texture parameter, on the aerodynamic force coefficients is therefore analysed.

Name	k/D	Pattern	c_{lx_r}/D	Density (2D)	S_q/D
A1	7.2×10^{-3}	A	1.6×10^{-2}	25%	3.1×10^{-3}
A2	1.1×10^{-2}	A	1.6×10^{-2}	25%	4.9×10^{-3}
B	7.2×10^{-3}	B	1.6×10^{-2}	50%	3.6×10^{-3}
C	7.2×10^{-3}	C	1.6×10^{-2}	25%	3.1×10^{-3}

TABLE 3.1: Parameters of the different generated surface roughnesses of the central part (see Figures 3.5 and 3.6).

Pattern A corresponds to cubic excrescences aligned with the free-stream with a two-dimensional surface density equal to 25%. This density is increased to 50% to obtain pattern B (chessboard-like pattern). Finally, the cubic excrescences from the first pattern are rotated by an angle of 45° to obtain pattern C. The relative roughness k/D is kept the same for all surface roughnesses, except for A2 where it is slightly increased. The relative periodicity length in the streamwise direction c_{lx_r}/D remains the same for each surface roughness. The parameter S_q in Table 3.1 corresponds to

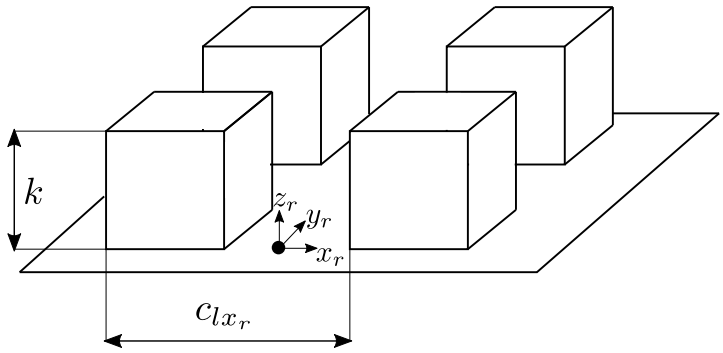

FIGURE 3.5: Definition of the parameters of the printed surface roughnesses on the central part of the cylinder (Pattern A is shown here).

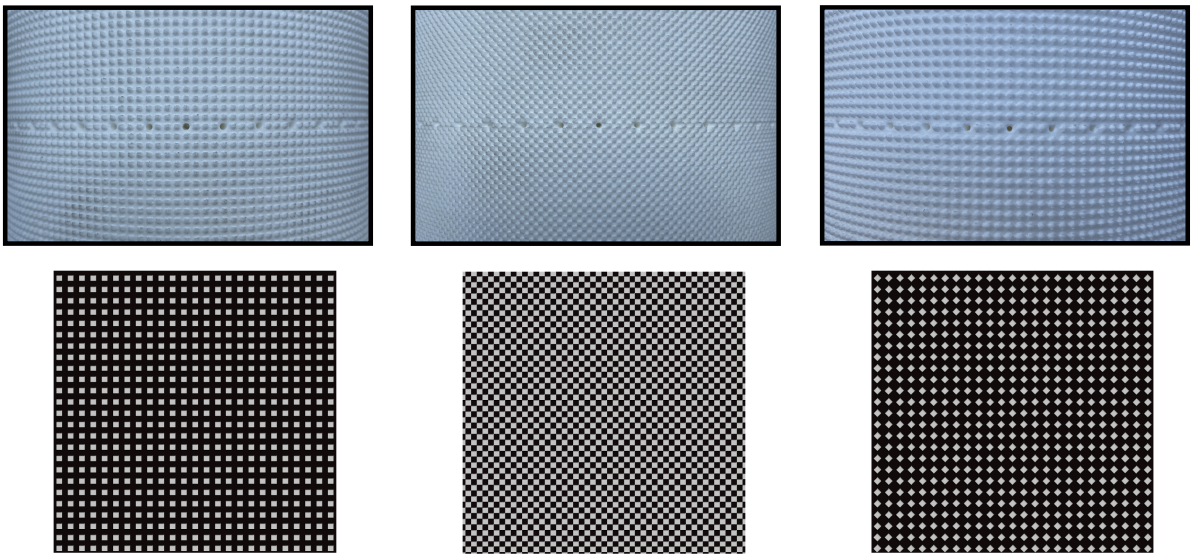

(a) Pattern A (b) Pattern B (c) Pattern C

FIGURE 3.6: Description of the different roughness patterns printed on the central part of the cylinder.

the two-dimensional standard deviation of the surface defined by

$$S_q = \sqrt{\frac{1}{A}\iint_A z_r^2(x_r, y_r)\, dx_r\, dy_r}. \tag{3.5}$$

In this expression, z_r denotes the height-coordinate of the surface from its averaged value. Hence, parameter S_q depends on both k/D and the pattern.

Figure 3.7 shows the variation of the time-averaged drag coefficient $\overline{c}_d$ and lift coefficient $\overline{c}_l$ of a single cylinder with the Reynolds number for the different surface

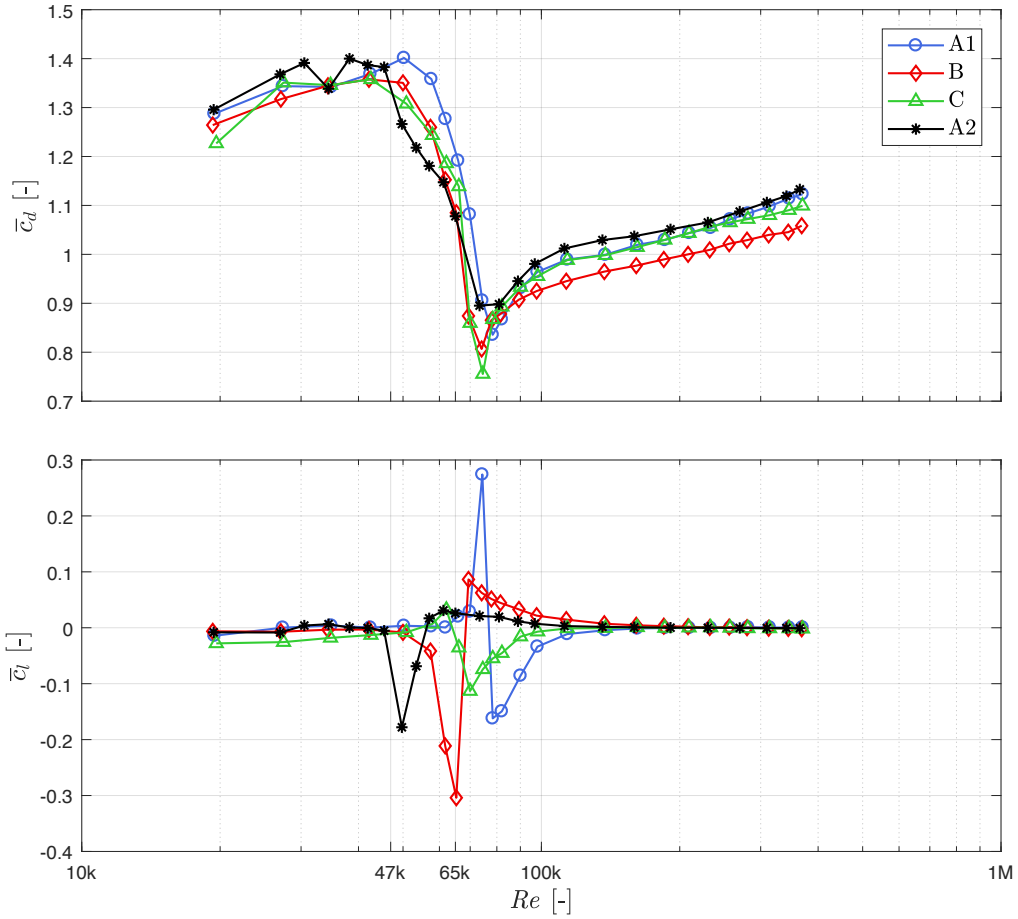

FIGURE 3.7: Variation of the time-averaged drag coefficient $\overline{c}_d$ and lift coefficient $\overline{c}_l$ of a single cylinder with Re for different printed surface roughnesses and sandpaper P40 applied on the extremities of the cylinder.

roughnesses generated on the instrumented central part and described above. Sandpaper P40 (ISO/FEPA) is applied on the rest of the cylinder for each tested central surface roughness. Surface roughness A1 is taken as the reference. Its relative roughness k/D is intentionally high ($k/D = 7.2 \times 10^{-3}$) in order to reach the post-critical flow regime within the accessible Reynolds numbers of the wind tunnel. This choice was made based on literature data, as previously discussed and shown in Figure 3.2.

For roughness B, the two-dimensional surface density is increased to 50% and the time-averaged drag coefficient curve remains similar to roughness A1. The critical flow regime, which is characterised by the drag crisis and a non-zero lift coefficient, is slightly shifted to lower Reynolds numbers. The critical regime with roughness A1 begins at $Re \approx 65$k, while it begins at $Re \approx 60$k with roughness B. Beyond that critical regime, i.e., at Reynolds number above 80k, the time-averaged drag coefficient with roughness B is found to be slightly smaller than with roughness A1, but this

difference is lower than 10%.

For roughness C, the cubic excrescences are rotated by 45° and the time-averaged drag coefficient curve still remains similar to the ones with roughness A1 or B. Similarly to roughness B, the critical regime is slightly shifted to lower Reynolds numbers in comparison with roughness A1 and it begins at $Re \approx 60$k. When the Reynolds number is increased ($Re > 80$k), the time-averaged drag coefficient with roughness C is found to be equal to the one with roughness A1. Hence, a rotation of 45° of the cubic excrescences has a negligible effect on the flow around the rough cylinder.

The time-averaged drag coefficient curve is rather different with roughness A2 which is characterised by a larger relative roughness ($k/D = 1.1 \times 10^{-2}$). The occurrence of the drag crisis and non-zero lift coefficient is observed at a significantly lower Reynolds number. The critical regime begins at $Re \approx 47$k. Based on the literature, this observation is expected from an increase in relative roughness. Nonetheless, it is observed that the time-averaged drag coefficient decreases in two steps with roughness A2 in the critical regime: a first step between $Re \approx 47$k and 60k and a second one between $Re \approx 60$k and 75k. It is attributed to spanwise effects which will be discussed in more details in the next section. At higher Reynolds numbers (Re > 80k), the time-averaged drag coefficient is nearly the same as, even though slightly larger than, with roughness A1.

Based on the observations made above, it is concluded that the pattern of the central roughness has a very limited influence on the flow at the measurement section. Therefore, the pattern A is retained for the rest of the work. As expected, the parameter k/D has a strong effect: the drag crisis occurs at lower Reynolds number for larger k/D. However, the results with the roughness A2 reveal spanwise effects. The surface roughness A1 is selected to investigate the spanwise effect in the next section.

3.3.2 Effect of the spanwise roughness

The effect of the spanwise roughness, which corresponds to the sandpaper applied on the rest of the cylinder, is investigated by keeping roughness A1 for the instrumented central part. Three different roughness levels are considered: no sandpaper ($k/D \approx 10^{-4}$), sandpaper P24 ($k/D = 1.2 \times 10^{-2}$) and sandpaper P40 ($k/D = 6.7 \times 10^{-3}$).

The variation of the time-averaged aerodynamic force coefficients of a single cylinder with the Reynolds number for the different spanwise roughnesses is shown in Figure 3.8.

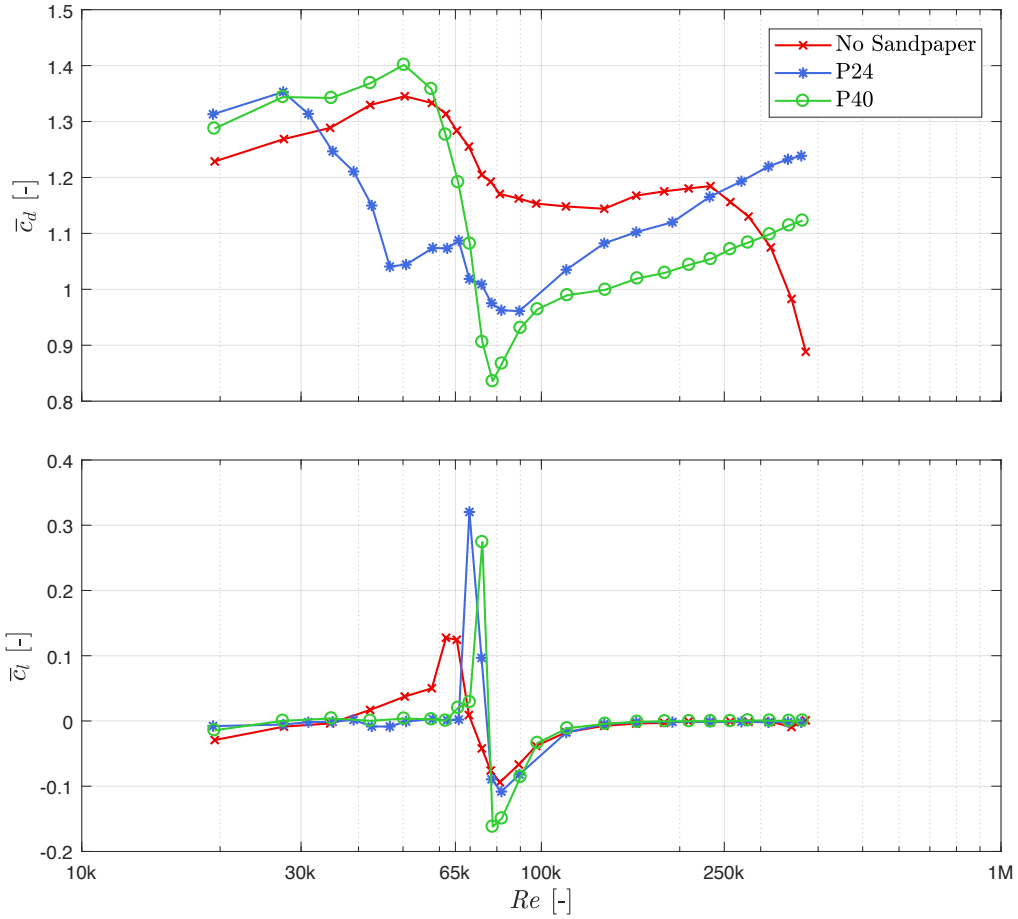

FIGURE 3.8: Variation of the time-averaged drag coefficient $\overline{c}_d$ and lift coefficient $\overline{c}_l$ of a single cylinder with Re for the surface roughness A1 and different roughnesses applied on the extremities of the cylinder.

A unique drag crisis is observed when applying sandpaper P40. It is interesting to notice that a drag crisis begins at $Re \approx 65$k for each configuration. From this observation, it is inferred that this drag crisis corresponds to the critical flow regime on the central part of the cylinder with roughness A1. It is corroborated by the simultaneous occurrence of a non-zero lift coefficient which characterises the critical regime.

Without sandpaper or with sandpaper P24, two drag crises are observed in the time-averaged drag coefficient curve. The second drag crisis observed in these cases corresponds to the occurrence of the critical flow regime on the extremities of the cylinder (on both sides of the instrumented central part). Without sandpaper, it begins at a larger Reynolds number ($Re \approx 250$k) because the relative roughness of the steel is much lower than roughness A1. The roughness of sandpaper P24 is, conversely, larger than the roughness A1 and hence the second drag crisis begins at a lower Reynolds number ($Re \approx 30$k).

It is concluded that the spanwise roughness has a strong effect on the flow at the measurement section. Non-equivalent surface roughnesses between the central part and the rest of the cylinder give rise to undesired spanwise effects, e.g., the occurrence of two drag crises. Based on this, it is stated that the double drag crisis, previously observed for roughness A2 in Figure 3.7, is due to the fact that roughness A2 and sandpaper P40 are not exactly equivalent. The unique drag crisis obtained with the combination of sandpaper P40 and roughness A1 indicates that their roughness is equivalent. Hence, this specific configuration (P40 + roughness A1) is retained to perform the experiments on twin cylinders.

3.4 Post-critical flow regime

It is important to note that the surface roughness level has a non-negligible effect on the resulting post-critical flow. As a matter of fact, it is observed that the drag coefficient increases with the relative roughness k/D in the post-critical flow regime (see Figure 3.1). This observation was already made by Fage and Warsap (1929). They stated that as the surface of the cylinder is roughened the boundary layer is retarded, so that the separation region moves upstream and leads to an increase in the drag coefficient. Their statement was verified thanks to skin friction distributions measured by Achenbach (1971), as the upstream movement of the angular location of separation with the relative roughness could be observed. Güven, Farell, and Patel (1980) completed the physical explanation by stating that larger relative roughness leads to a thicker boundary layer with larger momentum deficit. Hence, it becomes less stable to separation and leaves the surface earlier.

Niemann and Hölscher (1990) compiled a few comparable data from the literature of the critical and post-critical values of the time-averaged drag coefficient for a wide range of k/D. Figure 3.9 shows the variation of those values with k/D, together with literature data (Achenbach, 1971; Schewe, 1983; Hinsberg, 2015). It highlights the previous observation – the drag coefficient increases with k/D – and how the present results compare to existing data.

The time-averaged drag coefficients obtained in the present work are slightly above the curves suggested by Niemann and Hölscher (1990). But they stated themselves that the curves represent a tentative illustration of the variation of the drag coefficients with k/D. Moreover, the measurement technique may have an effect on the results. In the present work, the drag coefficient is obtained through the integration of pressure distribution at mid-span and hence is a two-dimensional quantity.

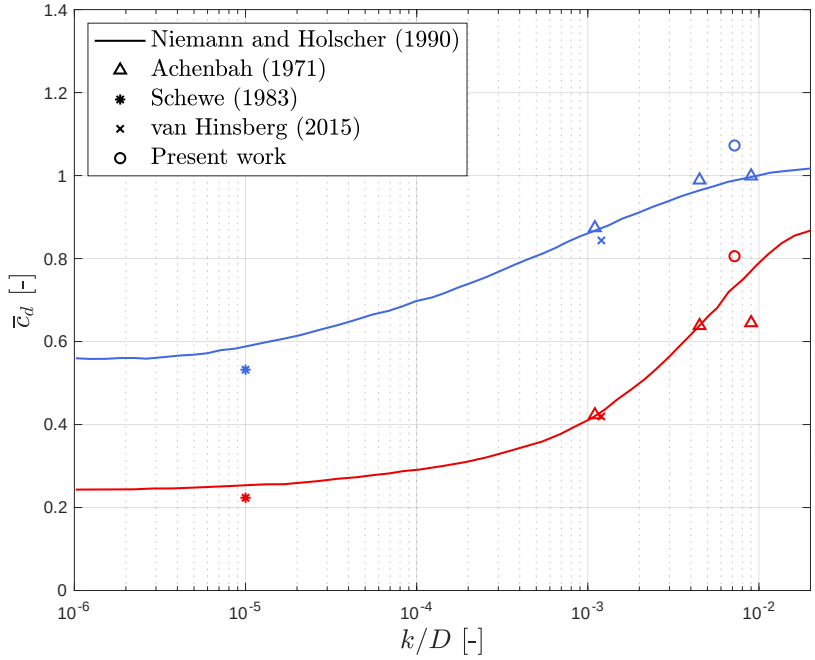

FIGURE 3.9: Variation of the critical (in red) and post-critical (in blue) values of the drag coefficient $\overline{c}_d$ of a single cylinder with k/D.

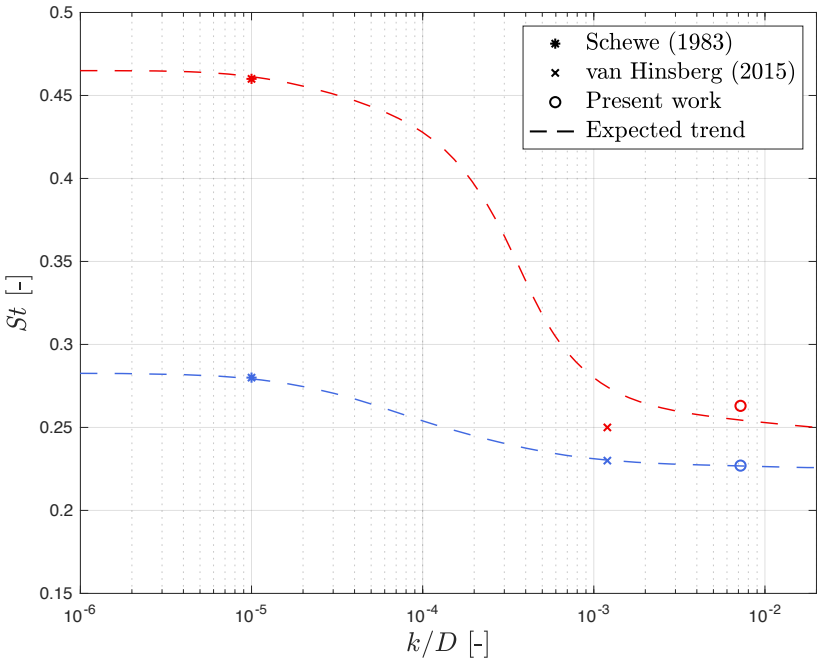

FIGURE 3.10: Variation of the critical (in red) and post-critical (in blue) values of the Strouhal number St of a single cylinder with k/D.

Schewe (1983) or Hinsberg (2015) meanwhile measured the drag with a force balance, in which three-dimensional effects may be present. Nevertheless, Figure 3.9 shows that the trend is respected.

In conclusion, the flow around a single cylinder reached in the post-critical regime depends on the relative roughness k/D. An increase in the latter leads to a larger separated region behind the cylinder and, therefore, an increase in the drag coefficient. It must be mentioned and emphasised that it has an effect on the Strouhal number as well, as shown in Figure 3.10. Indeed, the eddy shedding frequency is intimately related to the width of the wake. When the latter widens, the Strouhal number decreases. Hence, an increase in k/D results in a smaller Strouhal number in the post-critical flow regime.
It is important to understand that the effect of the surface roughness on the flow in the post-critical regime may lead to different flow patterns or potential aeroelastic instabilities in case of two cylinders. Indeed, the flow interference is expected to vary with the width of the wake from the front cylinder.

Chapter 4

Two cylinders in tandem arrangement

By using the appropriate roughness level, it has been shown that the post-critical flow regime is triggered for a single cylinder within the accessible Reynolds number range of the wind tunnel. Therefore, the experimental test campaign is now extended to two rough cylinders. In this chapter, the tandem arrangement is analysed for different spacing ratios between the cylinders. Particular attention is given to the identification of the distinct flow regimes that occur within the tested Reynolds number range. The flow patterns are then classified as a function of the spacing ratio in the main flow regimes (sub-critical, critical and post-critical). It is the main subject of the first published article related to this thesis (Dubois and Andrianne, 2022). At last, the effect of free-stream turbulence is investigated for a particular spacing ratio.

4.1 Experimental set-up

The experimental set-up used to perform static tests on twin cylinders is shown in Figure 4.2. It is the same apparatus as for a single cylinder presented in the previous chapter, with the addition of an identical cylinder in its wake. The cylinder centre-to-centre spacing ratio L/D can be varied by moving forwards or backwards the rear

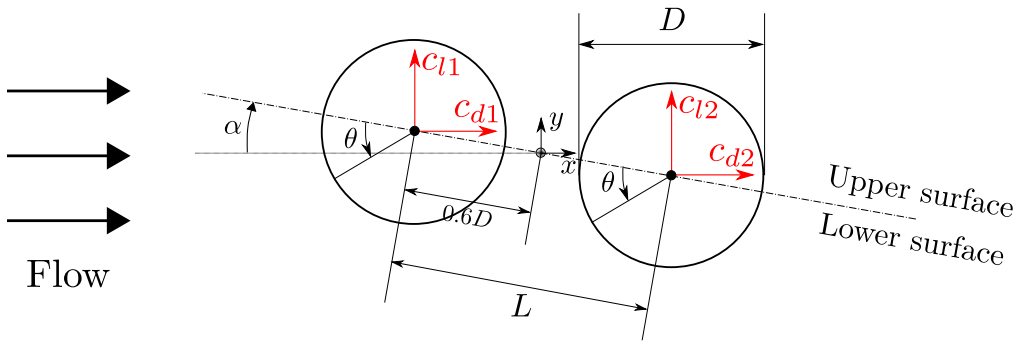

FIGURE 4.1: Staggered configuration of twin cylinders in cross-flow.

FIGURE 4.2: Picture of the experimental model of twin cylinders in the wind tunnel of Uliège.

cylinder using pre-defined holes drilled on the end plates. It leads to investigated spacing ratios of 1.2, 1.4, 1.56 and 1.8. The spacing ratio of 1.56 (instead of 1.6) is used to compare the present results with the ones of Schewe and Jacobs (2019). The set-up is mounted on a turn-table, allowing to accurately adjust the incidence of the cylinders to the incoming flow. In this chapter, the flow incidence α is set to 0° for all configurations to investigate the tandem arrangement.

4.2 Flow regimes and spacing effect

The distinct flow regimes are first identified as a function of the Reynolds number based on the aerodynamic force coefficients. The terminology used to define the flow regimes around the tandem arrangement follows the one suggested by Zdravkovich (1997) for the flow around a single cylinder presented in Chapter 2. In that sense, this section consists of the extension of the flow regimes around tandem rough cylinders.

4.2.1 Time-averaged aerodynamic force coefficients

The time-averaged drag and lift coefficients for both individual cylinders arranged in tandem are plotted against the Reynolds number in Figure 4.3. The results from the single cylinder are superimposed on the ones of the front cylinder to assess the interference effect due to the presence of a cylinder in its wake.

As stated above, in previous works of the literature the variation of the time-averaged drag coefficient of the front cylinder is very similar to the one of a single cylinder (see Figure 4.3(a)). Hence, the flow regimes around the tandem arrangement are identified in the same way as for a single cylinder. Based on the state of flow around the front cylinder, five distinct flow regimes are observed within the tested Reynolds number range. The identification of those flow regimes allows to explain

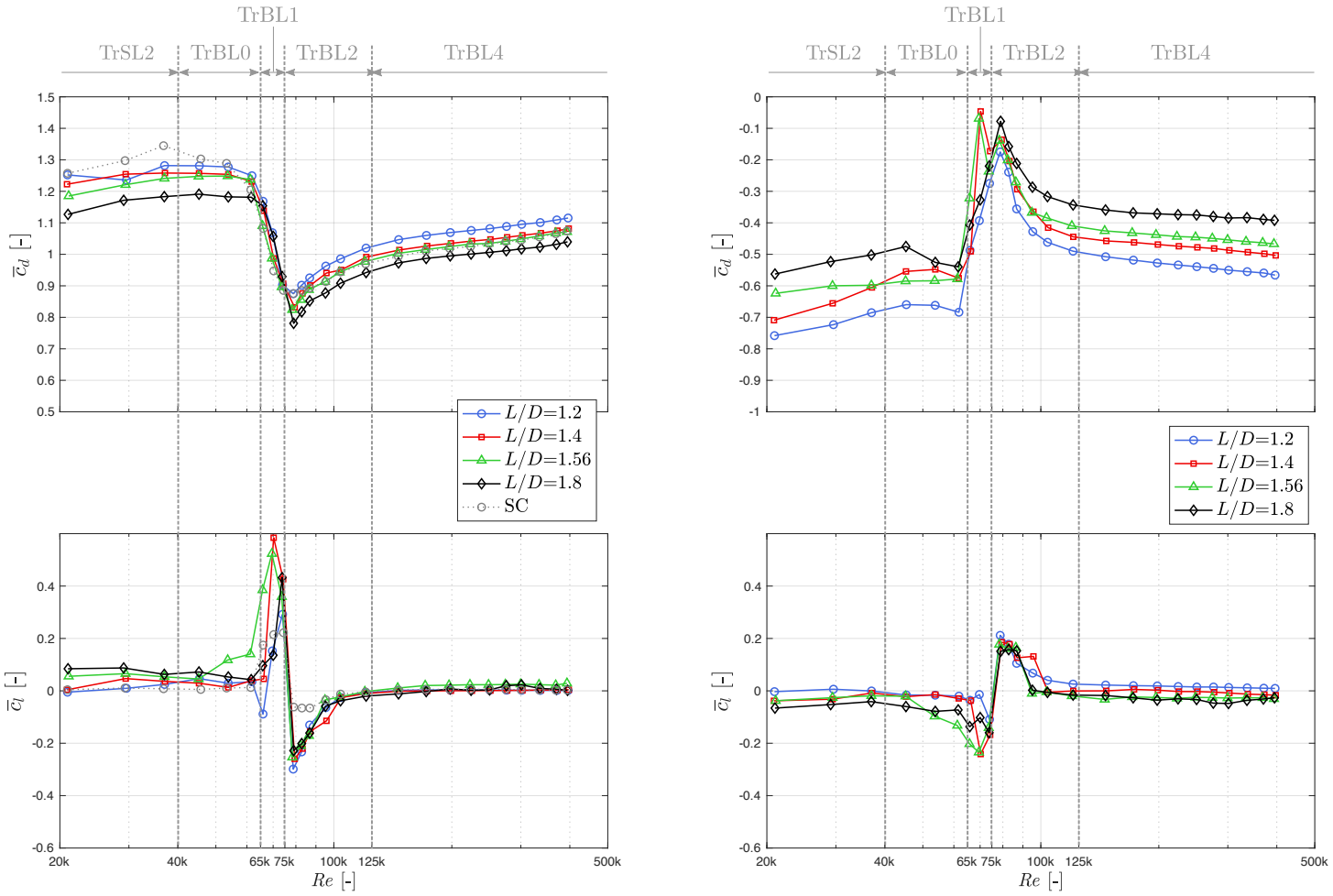

(a) Front cylinder

(b) Rear cylinder

FIGURE 4.3: Variation of the time-averaged drag coefficient $\overline{c}_d$ and lift coefficient $\overline{c}_l$ with Re for different spacing ratios L/D.

the variation of the aerodynamic quantities of the rear cylinder as a function of the Reynolds number. Hence, the flow regimes are also applicable to the rear cylinder.

Figure 4.3(b) shows that the time-averaged drag coefficient of the rear cylinder remains negative within the entire tested Reynolds number range for each spacing ratio L/D. These negative values indicate that the investigated spacing ratios are all below the critical spacing ratio: the flow behaviour either belongs to the extended-body or re-attachment one, as defined by Zdravkovich (1987). It implies that no eddy is shed between the two cylinders. Since it is located in the near-wake of the front cylinder, the rear cylinder is pushed towards the former one. This negative drag force was observed by Okajima (1979) and Schewe and Jacobs (2019), among others. It is also worth noting that the time-averaged drag coefficient of the rear cylinder increases with L/D.

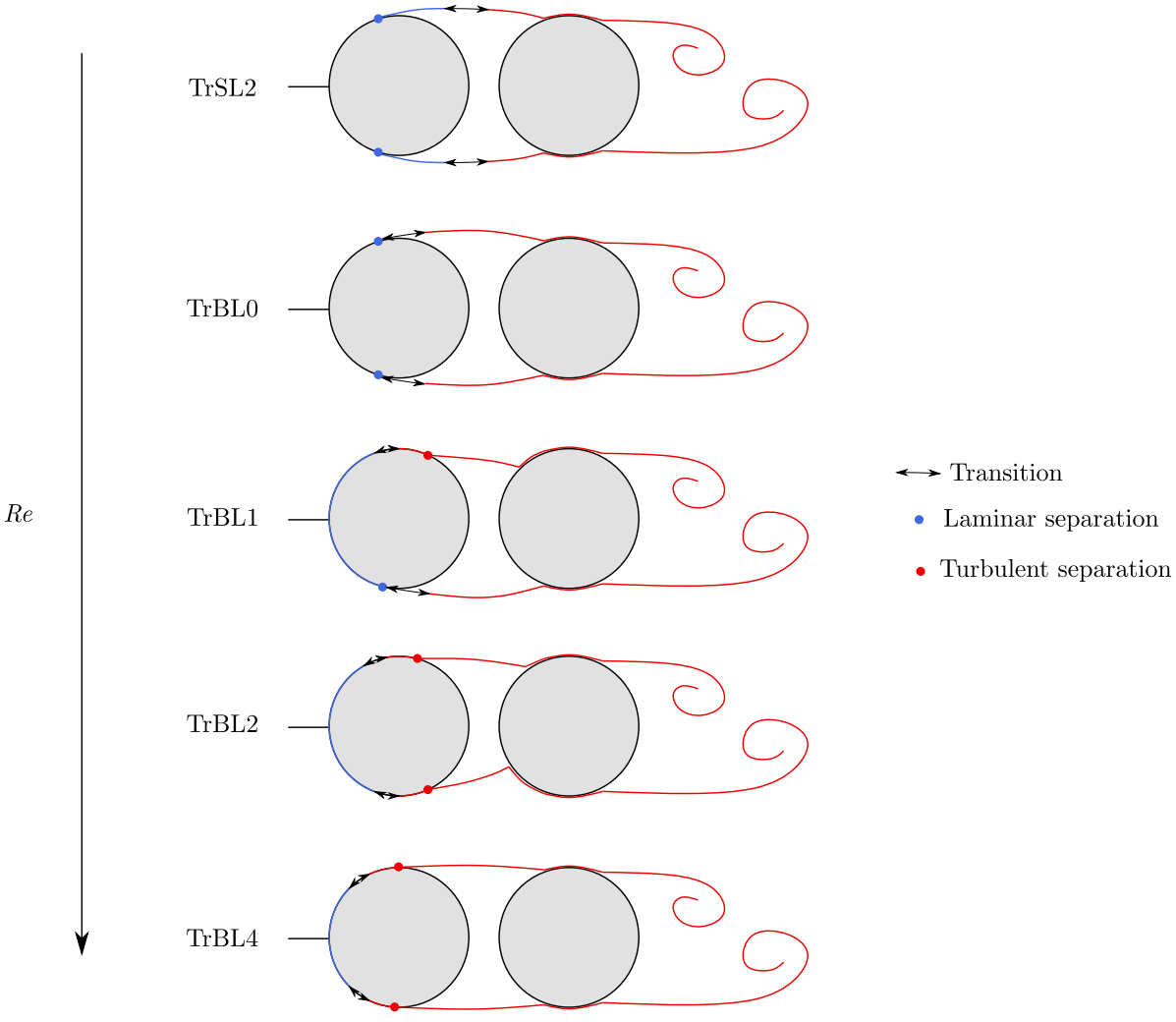

FIGURE 4.4: Flow schematics around the two tandem cylinders in the different identified flow regimes.

The distinct flow regimes are now described in details. The discussion below is supported by the flow schematics in Figure 4.4.

- **TrSL2**, *intermediate sub-critical regime* (21k < *Re* < 40k):
  The first identified flow regime is TrSL2, which belongs to the sub-critical state of flow. As suggested by the terminology, the transition from laminar to turbulence occurs in the separated shear layers from the front cylinder, as shown in Figure 4.4. In this regime, the time-averaged drag coefficient slightly increases for both cylinders and all spacing ratios when the Reynolds number increases. On the other hand, the time-averaged lift coefficients do not vary with the Reynolds number. Nevertheless, their values are not perfectly equal to zero. This non-zero value may stem from a slight misalignment of the cylinders to the incoming free-stream in the wind tunnel. TrSL2 regime extends up to $Re \approx 40$k.

- **TrBL0**, *pre-critical regime* (45k < *Re* < 65k):
  TrSL2 is followed by the so-called pre-critical TrBL0 flow regime (Morkovin, 1964). Unlike suggested by its name, the transition is not fully located in the boundary layers. The onset of transition in the shear layers has reached the separation lines onto the front cylinder, as represented in Figure 4.4. As a consequence, the shear layer in the vicinity of the laminar separation is slightly disturbed. It results in a limited decrease of the time-averaged drag coefficients, as explained in Zdravkovich (1997) for a single cylinder. Except for $L/D = 1.56$, the time-averaged lift coefficients remain almost constant (Figure 4.3). For $L/D = 1.56$, the lift coefficient of the front cylinder slightly increases while the lift coefficient of the rear cylinder decreases. The pre-critical regime suddenly terminates at $Re \approx 65$k.

- **TrBL1**, *critical regime* (65k < *Re* < 75k):
  The Reynolds number $Re \approx 65$k marks the beginning of the TrBL1 flow regime. TrBL1 is called the critical regime because of the drag crisis within its Reynolds number range, as observed in Figure 4.3(a). In this regime, the transition from laminar to turbulence is complete on one side of the front cylinder only. The resulting turbulent boundary layer separation is considerably delayed. On the other side of the front cylinder, the boundary layer remains laminar (or is not sufficiently turbulent, at least) before separation and thus separates earlier (see Figure 4.4). It leads to an asymmetry of the flow around the tandem arrangement, as observed for a single rough cylinder by Hinsberg (2015). The asymmetric flow generates a positive lift force on the front cylinder and a negative one on the rear cylinder. In contrast to the decrease in the time-averaged drag

coefficient of the front cylinder, the drag force acting on the rear cylinder increases with the Reynolds number in TrBL1.

- **TrBL2**, *asymmetric regime* (75k < *Re* < 125k):
  TrBL2 flow regime starts at $Re \approx 75$k. Around this particular Reynolds number, the transition becomes fully complete before separation on the other side of the front cylinder, i.e., where the boundary layer remained laminar at lower Reynolds numbers (see Figure 4.4). Hence, the turbulent separation is strongly delayed. The resulting flow remains asymmetric. However, Figure 4.3 shows that the asymmetry is opposite compared to the preceding flow regime. Indeed, a negative lift force is acting on the front cylinder while the rear cylinder is pushed upward. As the Reynolds number increases, the flow becomes more and more symmetric: the time-averaged lift coefficients converge towards zero. Simultaneously, the time-averaged drag coefficient of the front cylinder increases, and the time-averaged drag coefficient of the rear cylinder decreases.

- **TrBL4**, *post-critical regime* (125k < *Re* < 395k):
  The last identified flow regime is the post-critical TrBL4. It begins at $Re \approx 125$k when the flow around the tandem cylinders is symmetric again: the time-averaged lift coefficients are equal to zero within its Reynolds number range. The time-averaged drag coefficients of the front and rear cylinders are increasing and decreasing with the Reynolds number in TrBL4, respectively. The end of TrBL4 corresponds to the beginning of the fully-turbulent flow regime.

The regimes TrBL1 and TrBL2 defined in the present work differ from the namesake regimes presented by Zdravkovich (1997). Indeed, the flow regimes TrBL1 and TrBL2 around a smooth cylinder are called one-bubble and two-bubble regimes, respectively (section 2.1.3 in Chapter 2). They correspond to the formation of a laminar separation bubble on one side of the cylinder for the former regime and of a second bubble on the other side of the cylinder for the latter regime. The regimes represent an intricate combination of laminar separation, transition, re-attachment and turbulent separation of the boundary layers. Because of their sensitivity to disturbances, one-bubble and two-bubble regimes disappear if the roughness level is sufficiently large on the surface of the cylinder. This feature has already been reported in the previous chapter (see Figure 3.2). The flow regime TrBL3, also known as the super-critical regime, is also missing when using surface roughness. This regime corresponds to the disruption of the laminar separation bubbles along the span of the cylinder which leads to the disorganisation of the wake behind the front cylinder. However, no separation bubble is formed, as explained just above. Hence, the eddy shedding never ceases. Two flow regimes, namely TrBL1 and TrBL2, are nonetheless defined in this

work between the sub- and post-critical flow regimes to report the different asymmetric flows in this specific Reynolds number range.

Table 4.1 compares the time-averaged drag coefficients measured by Schewe and Jacobs (2019) and the present ones for a spacing ratio $L/D = 1.56$. The three main flow regimes are analysed: sub-critical, critical and post-critical flow regimes. Because of the different roughness levels between the work of Schewe and Jacobs (2019) and the present work, the flow regimes take place at different Reynolds numbers, as reported in Table 4.1.

Work	Cylinder	sub-critical		critical		post-critical	
Schewe and Jacobs (2019)	Front	Re=200k	1	Re=500k	0.05	Re=6M	0.5
	Rear		-0.4		0.4		-0.07
Present work	Front	Re=45k	1.25	Re=79k	0.82	Re=395k	1.08
	Rear		-0.6		-0.14		-0.46

TABLE 4.1: Comparison of $\bar{c}_d$ obtained from the work of Schewe and Jacobs (2019) (k/D=10^{-4}) and the present one (k/D=7.2×10^{-3}) in different flow regimes for a spacing ratio $L/D = 1.56$.

In the sub-critical flow regime, the absolute value of each drag coefficient increases with the relative roughness k/D, as expected for the front cylinder. Indeed, the surface roughness reduces the momentum in the boundary layers, which results in an upstream displacement of the separation points and, thus, an increase in the drag coefficient (Güven, Farell, and Patel, 1980). The upstream displacement of the separation points on the front cylinder has the effect of widening its wake. This widening of the wake increases the « shielding » effect on the rear cylinder and hence reduces its drag coefficient.

The same observations and interpretations can be made in the post-critical flow regime. One can state that the effect of the surface roughness is more significant in the post- than in the sub-critical flow regime. This statement is explained by the fact that the boundary layer thickness decreases with Re. Consequently, the protrusions on the surface become large in comparison with the boundary layer thickness. Therefore, their effect on the boundary layer characteristics is significant at high Reynolds numbers.

It is considerably different in the critical flow regime: the drag coefficient of the front cylinder is significantly higher for a high roughness level. Moreover, the drag coefficient of the rear cylinder remains negative (-0.14) while it is found positive (0.4) by Schewe and Jacobs (2019). As stated above, the surface roughness prevents the formation of the laminar separation bubbles (characterising the critical regime of a

smooth cylinder) on the front cylinder. Therefore, the turbulent separation points move significantly upstream with relative roughness in the critical regime, increasing the drag coefficient of the front cylinder. As mentioned above, the width of the wake behind the front cylinder increases, reducing the drag coefficient of the rear cylinder.

This comparison highlights the fact that the flow around the tandem arrangement is not the same for different roughness levels and Reynolds numbers, even though it is in the same flow regime.

4.2.2 Fluctuating lift coefficients

Figure 4.5 shows the variation of the fluctuating lift coefficient c_l' (standard deviation of the lift signal for each individual cylinder) with the Reynolds number.

The first observation concerns the reduction of the fluctuating lift coefficient of the front cylinder in comparison with a single cylinder (noted SC in Figure 4.5(a)). This reduction is attributed to the presence of a cylinder in its wake. As stated in the previous section, the flow behaviour either belongs to the extended-body or re-attachment one. Hence, the eddies grow and are shed behind the rear cylinder. Therefore, they have less influence on the flow around the front cylinder. In the sub-critical flow regime, the fluctuating lift coefficient of the rear cylinder is also lower than of a single

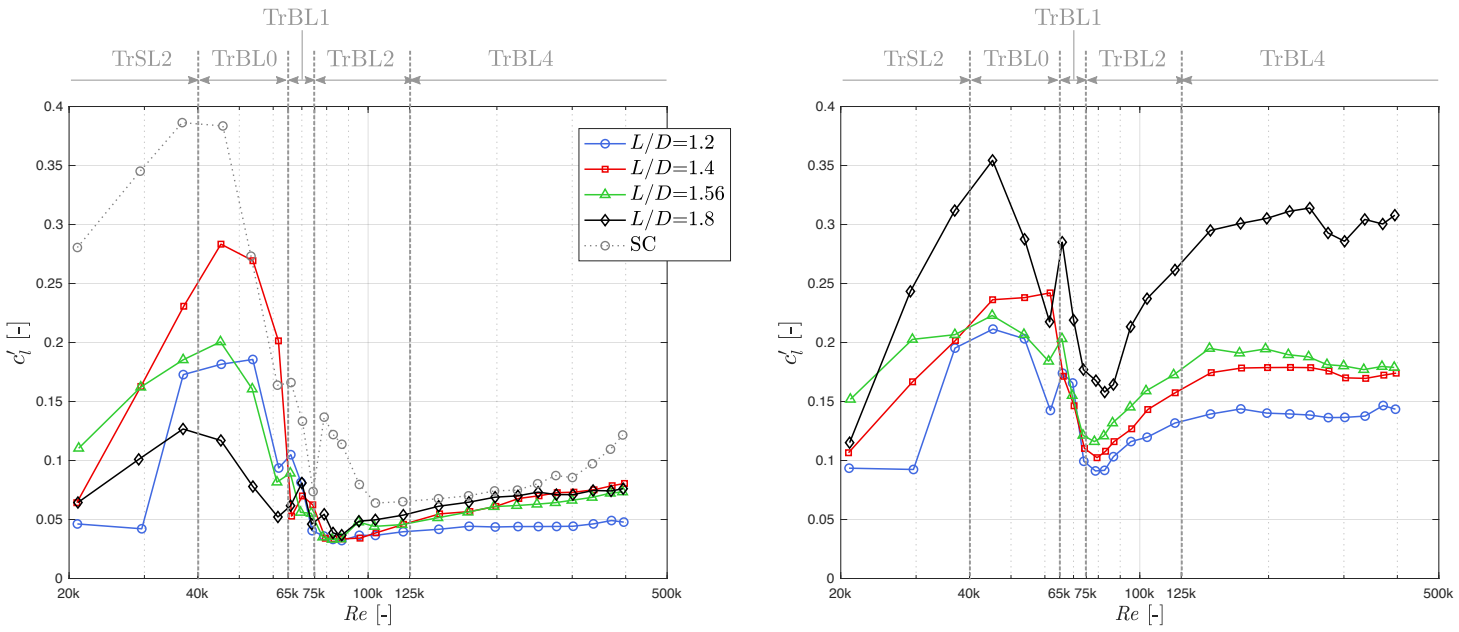

(a) Front cylinder

(b) Rear cylinder

FIGURE 4.5: Variation of the fluctuating lift coefficient c_l' with Re for different spacing ratios L/D.

cylinder. In contrast, c_l' of the rear cylinder becomes higher than the one of the single cylinder for each investigated spacing ratio in the post-critical regime (Figure 4.5(b)).

The fluctuating lift coefficients of both cylinders increase with the Reynolds number in the TrSL2 regime up to the beginning of the TrBL0 regime. This variation with the Reynolds number differs in amplitude and shape for the different spacings. It is difficult to extract a clear trend in the variation of the fluctuating lift coefficients with the spacing ratio at the lowest Reynolds numbers.

When increasing the Reynolds number further in the TrBL0 and TrBL1 regimes, the fluctuations on both cylinders drastically decrease and reach their respective minimum value at the beginning of the asymmetric TrBL2 regime. A possible explanation involves the downstream movement of the separation points on the front cylinder induced by the transition from laminar to turbulent boundary layers. This delay of separation narrows the wake of the front cylinder and stabilises the flow between the cylinders, leading to smaller fluctuations. The minimum value obtained for the rear cylinder is higher than for the front cylinder.

The lift fluctuations increase again as the Reynolds number increases in TrBL2 up to the beginning of the post-critical TrBL4 flow regime. This increase is steeper as the spacing ratio is larger, especially concerning the fluctuating lift coefficient of the rear cylinder (Figure 4.5(b)). The fluctuating lift coefficients seem to eventually converge and remain constant at the highest tested Reynolds numbers. The lift fluctuations on the front cylinder remain relatively lower than on the rear cylinder.

Figure 4.6 shows the variation of the fluctuating lift coefficient c_l' with the spacing ratio L/D in the main flow regimes, i.e., the sub-critical (Re = 45k), critical (Re = 79k) and post-critical (Re = 395k) flow regimes. The Reynolds number corresponding to the critical regime is associated with the minimum drag coefficient of the front cylinder. The results from the work of Alam et al. (2003) performed in the sub-critical flow regime on smooth cylinders are added for comparison.

In the sub-critical flow regime, the fluctuating lift coefficients of both cylinders increase when the rear cylinder is moved downstream from L/D = 1.2 to 1.4. As the rear cylinder moves further downstream, the lift fluctuations on the front cylinder decrease. On the other hand, the lift fluctuations on the rear cylinder first decrease when L/D increases from 1.4 to 1.56 but increase again between 1.56 and 1.8. Similar variations were measured by Alam et al. (2003), as shown in Figure 4.6. They observed a local maximum of the fluctuating lift coefficients at a spacing ratio of 1.4. The values of the present study are nonetheless rather different in comparison with

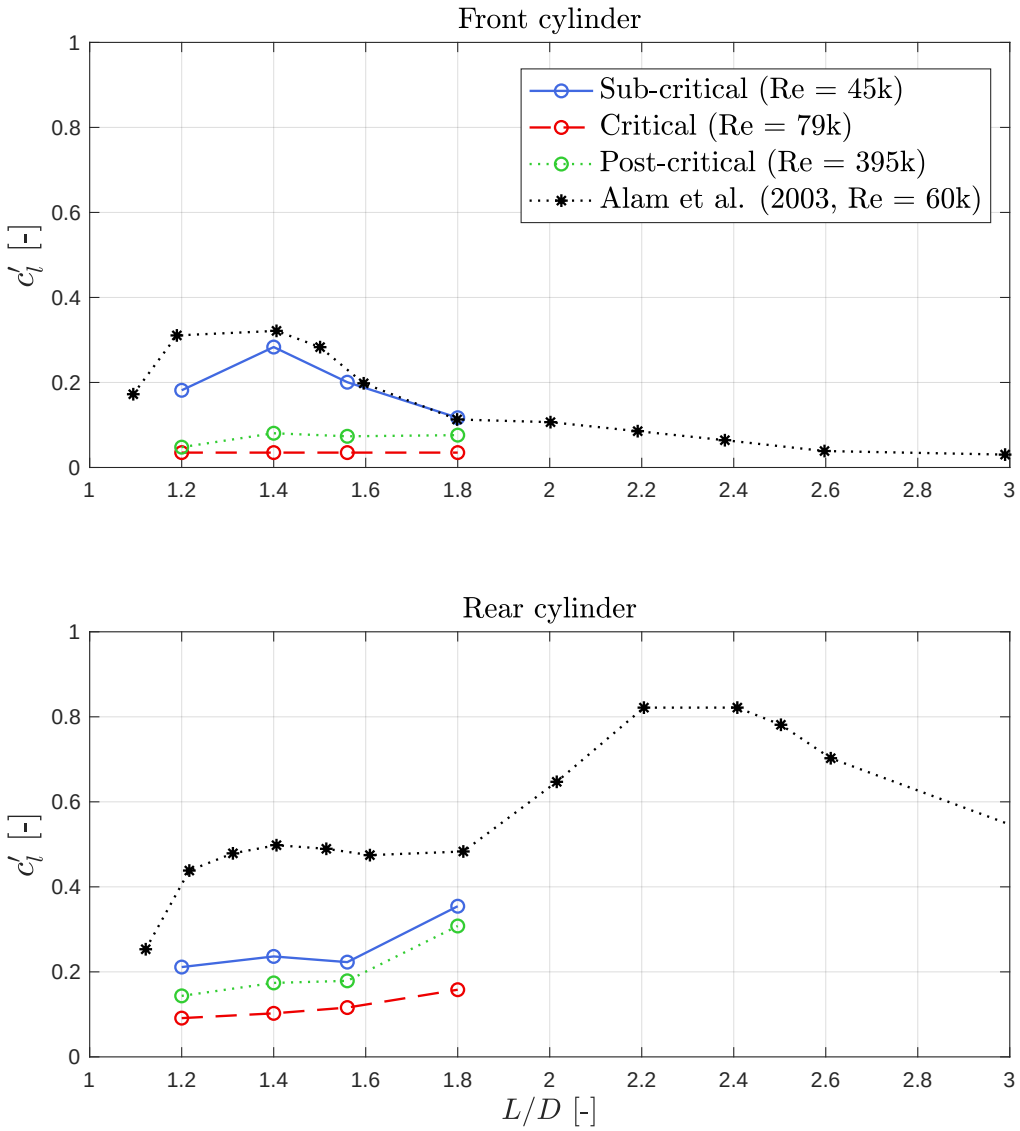

FIGURE 4.6: Variation of the fluctuating lift coefficient c_l' with the spacing ratio L/D in the three main flow regimes.

those obtained by Alam et al. (2003), especially for the rear cylinder. This discrepancy is due to the difference of Reynolds number (Re = 45k versus 60k). For a single cylinder, Zdravkovich (1997) reported the decrease in the formation length of the eddies with the Reynolds number in the TrSL2 regime. The reduction in formation length of the eddies induces an increase in fluctuating lift coefficient and a decrease in Strouhal number. In case of two tandem cylinders, this Reynolds number effect has a significant influence on the flow around the rear cylinder.

In the critical flow regime, the fluctuating lift coefficient of the front cylinder does not vary with the spacing ratio. On the other hand, the fluctuations of the lift force acting on the rear cylinder increase with the spacing ratio.

In the post-critical flow regime, the fluctuating lift coefficient of the front cylinder remains small and constant, except between $L/D = 1.2$ and 1.4, where it slightly increases. The fluctuating lift coefficient of the rear cylinder increases with the spacing ratio, and its values are smaller than the ones obtained in the sub-critical flow regime.

4.2.3 Frequency content of the lift forces

The *Power Spectral Density* (*PSD*) of the fluctuating lift forces acting on the tandem cylinders is shown in Figure 4.7 as a function of the Reynolds number. The temporal lift coefficients are initially normalised by their corresponding standard deviation. This procedure allows comparing the frequency content of the lift signal at different Reynolds numbers. Additionally, the frequency content of the lift forces at particular Reynolds numbers is plotted in Figure 4.8 to facilitate the observation of multiple peaks, as discussed hereafter. In Figure 4.8, the different Reynolds numbers are chosen to illustrate the frequency contents in the main flow regimes, i.e., the sub-critical (Re = 45k), the critical (Re = 74k and 79k: from one asymmetric flow to the other) and the post-critical (Re = 395k) flow regimes. The dimensionless Strouhal number $St = fD/U_\infty$ is used as the frequency variable. It varies in the range of $0 \leq St \leq 0.75$ in the present analysis to include potential harmonics in the spectra.

For the spacing ratios $L/D = 1.4$ to 1.8, a peak at a very low frequency ($St \approx 0.01$) is observed in the TrSL2 and beginning of TrBL0 regimes (Figure 4.7(b-d)). It also clearly appears in Figure 4.8(c-d) at Re = 45k. A physical interpretation of this peak is difficult because its corresponding frequency does not follow a common trend for the different spacing ratios. Hence, it cannot be attributed to an eddy shedding phenomenon. An attempt to explain this very low-frequency fluctuation is the meandering effect, similar to the one observed around the rotors of wind turbines. The following analyses focus on the higher frequency peaks associated with the eddy shedding phenomenon.

At the lowest Reynolds numbers, two peaks which do not correspond to harmonic frequencies can be observed in the spectra for spacing ratios $L/D \leq 1.4$ in Figure 4.7(a-b). This observation is made at Reynolds numbers $Re <$ 36k and 28k for $L/D = 1.2$ and 1.4, respectively. Igarashi (1984) also observed two peaks in the frequency content of the fluctuating velocity behind the tandem arrangement for the same spacing ratio and Reynolds number ranges. Two peaks were identified in the Reynolds number ranges 19k $\leq Re \leq$ 32k and 17k $\leq$ Re $\leq$ 25k for $L/D = 1.2$ and 1.4, respectively. He concluded that the occurrence of those two peaks stems from the intermittent re-attachment of the shear layers onto the rear cylinder. The same

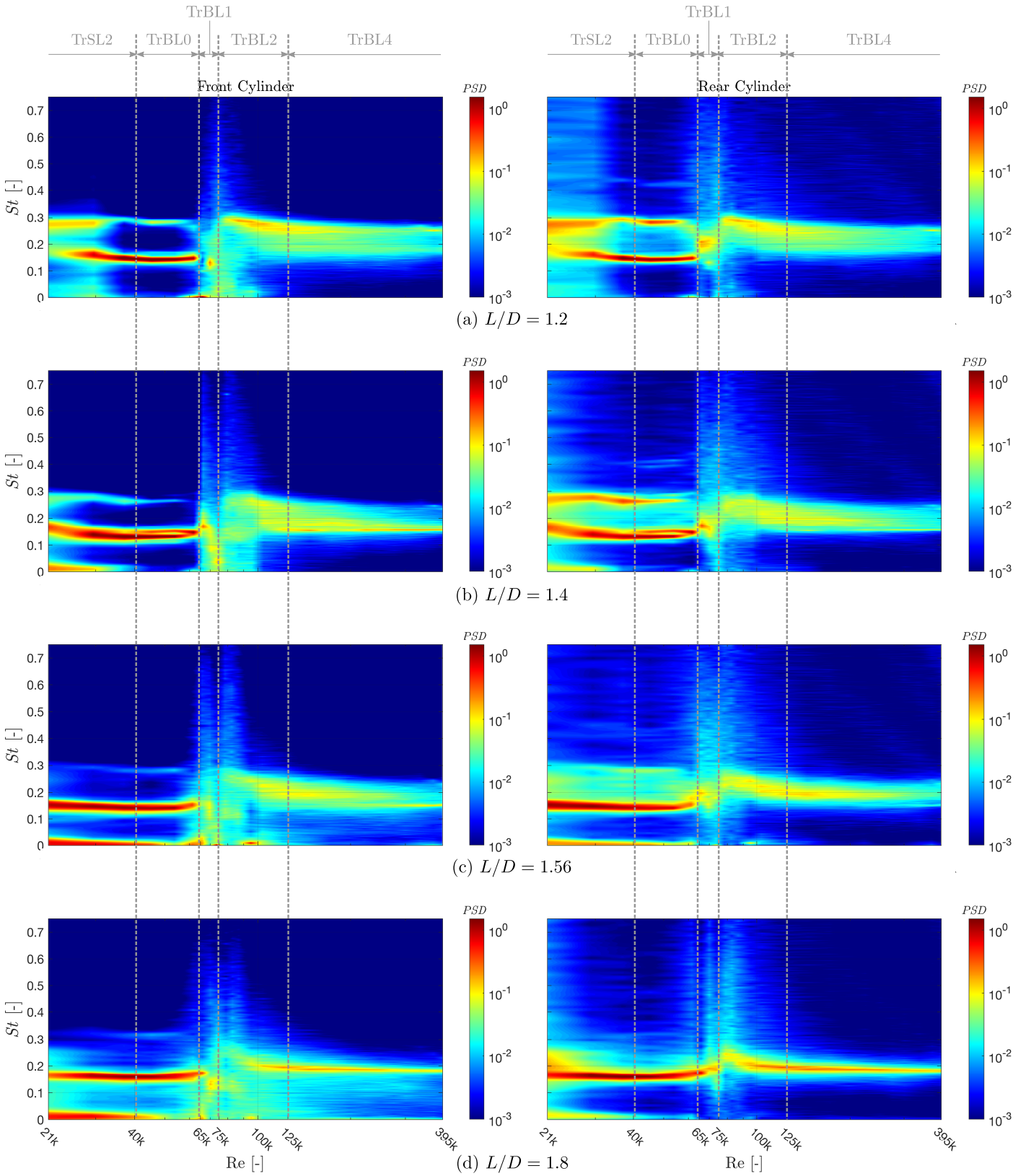

FIGURE 4.7: Variation of the frequency content of the lift force acting on the tandem cylinders with *Re* for the different spacing ratios L/D.

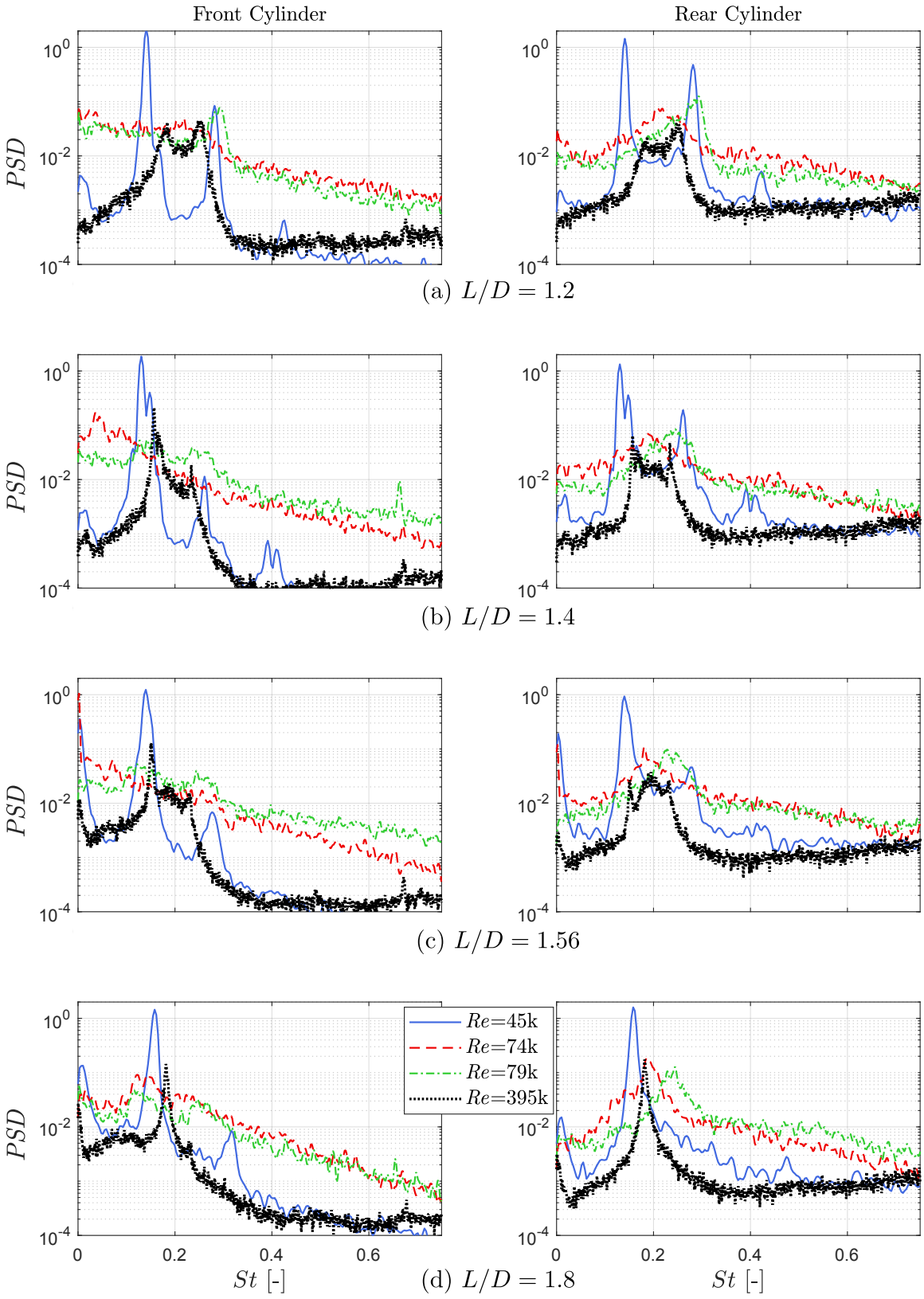

FIGURE 4.8: Frequency content of the lift force acting on the tandem cylinders at different Re for each spacing ratio L/D.

conclusion may therefore be stated in the present work. The peak at the highest Strouhal number ($St \approx 0.27$) corresponds to the extended-body behaviour, i.e., without re-attachment of the shear layers, and the other one ($0.15 \leq St \leq 0.2$) to the re-attachment behaviour. A single peak is observed for the two other spacing ratios (Figure 4.7(c-d)) and is also associated with the re-attachment behaviour. The corresponding Strouhal number decreases with the Reynolds number in TrSL2 regime (see Figure 4.7(a-d)).

As the Reynolds number increases, the peak at the highest Strouhal number ($St \approx 0.27$) disappears while the other one ($St \approx 0.15$) remains rather constant. A second peak appears at a harmonic frequency of the dominant peak. It is therefore assumed to stem from the same physical phenomenon as the one associated with the fundamental frequency and the flow pattern is not unstable anymore. This harmonic component is also present for spacing ratios $L/D = 1.56$ and 1.8 at the end of TrSL2 and TrBL0 regimes. The harmonic component clearly appears for each spacing ratio in Figure 4.8 at Re = 45k (end of the sub-critical regime). At this particular Re, a third peak can be observed at a higher harmonic frequency ($St \approx 0.4$) for $L/D = 1.2$ and 1.4 (Figure 4.8(a-b)). Note that these third peaks do not appear in Figure 4.7 because of their low energy level. In Figure 4.8, one can see that the harmonic component decreases with the spacing ratio and even seems to disappear from the spectrum of the lift force of the rear cylinder for $L/D = 1.8$. "Double" peaks ($St \approx 0.15$ and 0.4) are observed for $L/D = 1.4$ in the TrBL0 regime (Figures 4.7(b) and 4.8(b) at Re = 45k). Those peaks are due to a modulation of the temporal lift coefficient of each cylinder. Figure 4.9 shows the temporal lift coefficients of the front and rear cylinders and the respective PSDs for the different spacing ratios at Re = 45k. The results obtained for the single cylinder at the same Re have been added for comparison. In this figure, the modulation of the lift signals for the spacing $L/D = 1.4$ is important and regular compared to the other spacing ratios. The "double" peaks detected in Figure 4.8(b) are a consequence of this modulation and do not bring any information on the physical phenomena taking place around the cylinders. Instead, they can be used to calculate the frequencies of two phenomena: (i) the vortex shedding taking place in the wake of the rear cylinder at $St = 0.13$ and (ii) a low-frequency component at 0.39 Hz ($St \approx 0.009$) for which no physical explanation is found.

In the critical flow regime, the spectra become broad, and the peaks are flattened so that a clear single peak cannot be identified anymore for the front cylinder, as shown in Figure 4.8 at Re = 74k. The fluctuations of the lift coefficient of the front cylinder are thus non-periodic and weakly impacted by the eddy shedding from the rear cylinder.

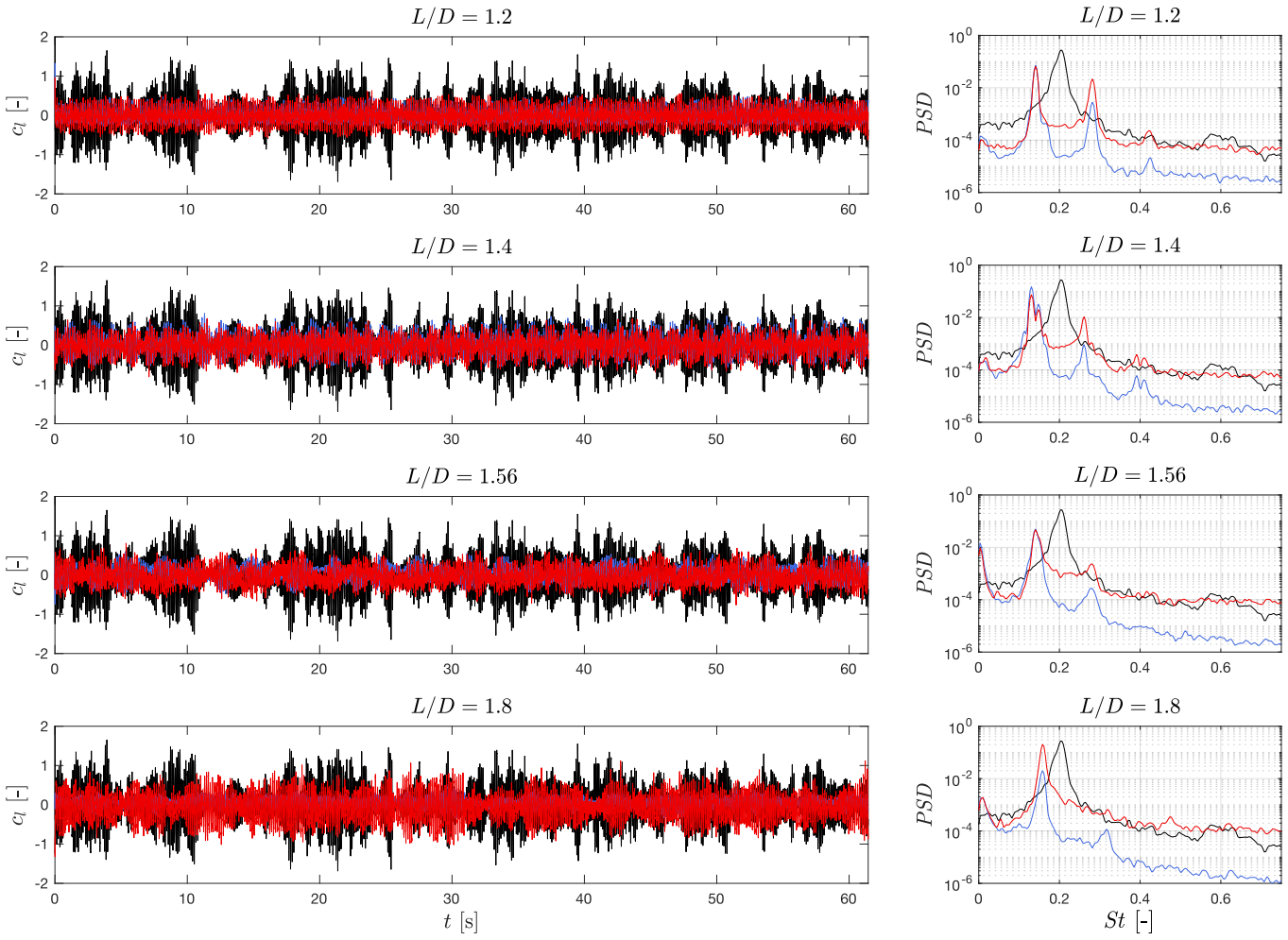

FIGURE 4.9: Temporal lift coefficients and respective *PSD*s of the single cylinder (black) and tandem cylinders (blue: front; red: rear) for the different spacing ratios at *Re* = 45k.

A peak is still identified in the frequency content of the rear cylinder for all spacing ratios. The associated Strouhal number increases with the Reynolds number in TrBL1 (see Figure 4.7) and reaches a maximum value at the end of the critical regime. One can also notice the absence of harmonic components in this regime. In the TrBL2 regime, a peak slightly re-appears for the front cylinder at the same Strouhal number as for the rear cylinder, even though the spectra remain quite broad. The Strouhal number decreases with the Reynolds number in TrBL2.

In the post-critical regime TrBL4, the spectra are sharper and peaks are easier to identify. At high Reynolds numbers, two peaks which do not correspond to harmonic frequencies are observed for spacing ratios $L/D \leq 1.56$. Those peaks appear in Figure 4.8(a-c) at *Re* = 395k. This observation is similar to the one previously made

at the lowest Reynolds numbers for spacing ratios $L/D \leq 1.4$. Therefore, a tentative explanation for the occurrence of two peaks in the post-critical flow regime is the intermittent re-attachment of the separated shear layers from the front cylinder onto the rear cylinder. For $L/D = 1.8$, the spectra present a single peak (see Figure 4.8(d)). It reflects the stable behaviour of the shear layers for this configuration: they do not re-attach intermittently anymore.

Based on the previous observations and analyses, it is pointed out that the eddy shedding phenomenon, which is the most energetic one, is identified in the range $0.13 < St < 0.32$ (by including the second harmonic components), depending on the Reynolds number and spacing ratio.

Figure 4.10 shows the Strouhal number associated with the eddy shedding as a function of the spacing ratio L/D at the three main flow regimes. Literature results for tandem cylinders are added for comparison. Additionally, the dashed-dotted lines correspond to the Strouhal numbers of a single rough cylinder. Note that the results from Igarashi (1981) and Alam et al. (2003) correspond to smooth cylinders, while the ones from Okajima (1979) correspond to rough cylinders ($k/D = 9 \times 10^{-3}$).

In the sub-critical flow regime, the Strouhal number decreases from 0.141 to 0.13 between $L/D = 1.2$ and 1.4. When the spacing ratio between the cylinders further increases, the Strouhal number increases up to 0.16 for $L/D = 1.8$. Alam et al. (2003) and Igarashi (1981) observed the same trend for the Strouhal number with the spacing ratio in the sub-critical regime, with a local minimum value in the range $1.3 < L/D < 1.4$. Nevertheless, the values of the Strouhal number measured by Alam et al. (2003) are slightly smaller. It is probably due to the difference in Reynolds number, as explained in the previous section. Okajima (1979) performed only two experiments within the spacing ratio range of interest ($1 < L/D < 2$). Therefore, it is difficult to compare the evolution of the Strouhal number in this range. The quantitative values are though in good agreement with the other experiments.

In the critical flow regime, one can see that Strouhal numbers are shown only for the rear cylinder. It is justified by the broad spectrum of the fluctuating lift force acting on the front cylinder, which flattens the peaks and makes their identification cumbersome. As it was stated earlier, the fluctuations on the front cylinder are mostly non-periodic. On the other hand, the Strouhal number of the rear cylinder monotonically decreases with the spacing ratio. It is also interesting to notice that the Strouhal number is larger than the one of a single cylinder when $L/D = 1.2$ and becomes

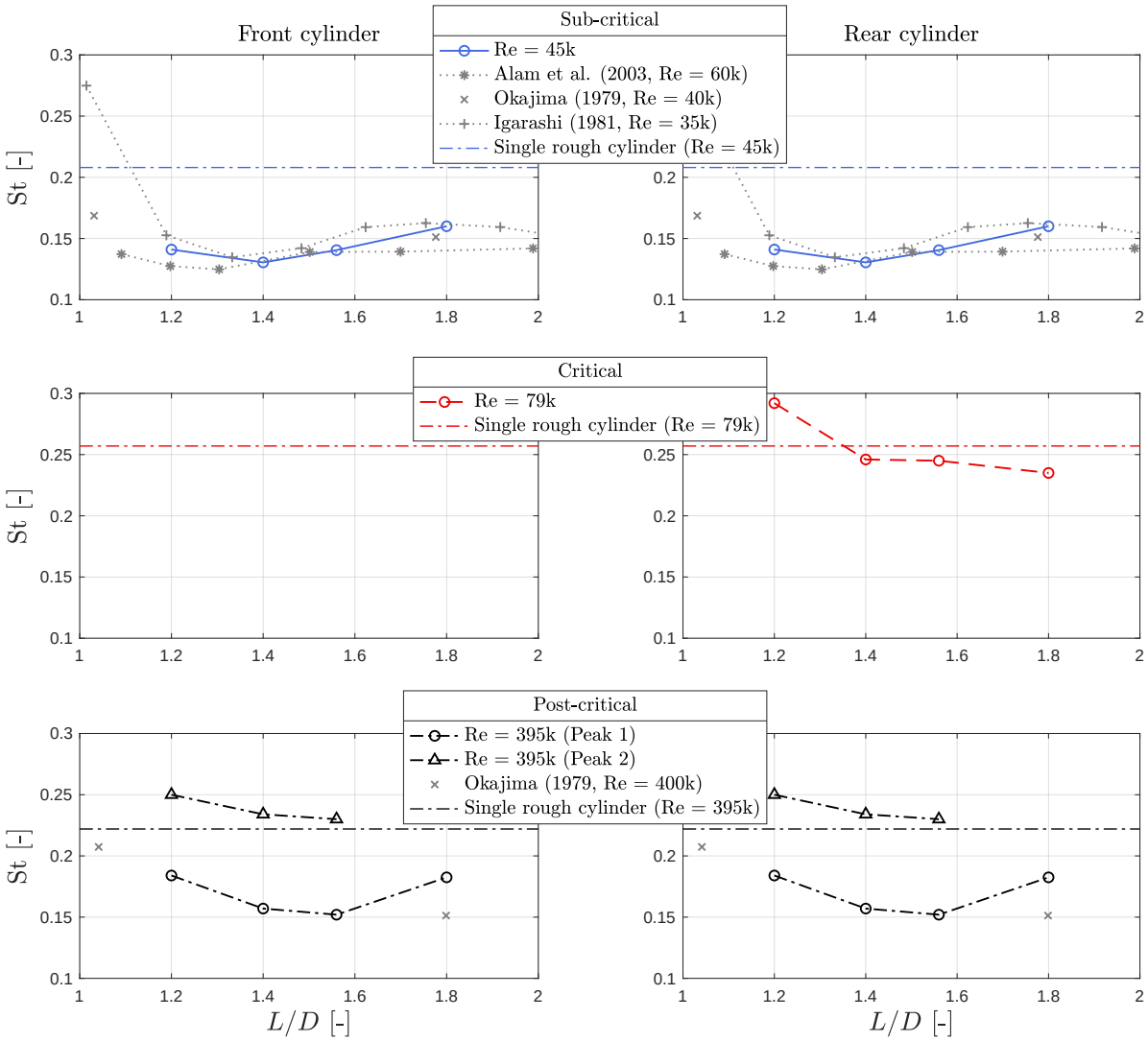

FIGURE 4.10: Variation of the Strouhal number with the spacing ratio L/D at the three main flow regimes.

smaller for the other spacing ratios. To the author's knowledge, literature data do not exist in this particular regime for comparison (similar roughness level and Reynolds number).

In the post-critical flow regime, one can observe two Strouhal numbers for $L/D \leq 1.56$ in Figure 4.10, corresponding to the two peaks identified in Figures 4.7 and 4.8. The highest Strouhal number (i.e., peak 2 in Figure 4.10) decreases with the spacing ratio and seems to converge towards the value obtained from a single cylinder. The other Strouhal number decreases from 0.184 to 0.152 between $L/D = 1.2$ and 1.56. Then, it increases to 0.183 when the spacing ratio is further increased to $L/D = 1.8$. This variation of St with L/D is quite similar to the one observed in

the sub-critical flow regime, even though the spacing ratio at which the minimum value of the Strouhal number occurs is not the same, and the values are higher in the post- than in the sub-critical regime. Okajima (1979) reported only one peak and, thus, a unique Strouhal number. As stated in the sub-critical regime, he performed only two experiments within the spacing ratio range of interest. It is thus difficult to compare the variation of the Strouhal number with his results. For $L/D = 1.8$, the value of the Strouhal number measured by Okajima (1979) is around 0.15, while it is equal to 0.183 in the present work, even though the Reynolds number and the relative surface roughness are equivalent. The only difference between the two works is the technique used to extract the Strouhal number: Okajima (1979) computed it from the fluctuating velocity in the wake, while it is computed from the fluctuating lift in the present investigation.

4.2.4 Pressure distributions

The pressure distributions measured around the tandem cylinders are presented for each spacing ratio L/D at three different Reynolds numbers representing the main flow regimes, i.e., sub-critical ($Re = 45$k), critical ($Re = 79$k) and post-critical ($Re = 395$k).

- $L/D = 1.2$:

The time-averaged pressure coefficient distributions at the three different flow regimes are plotted in polar coordinates for $L/D = 1.2$ in Figure 4.11(a). The distributions are nearly symmetric around the centreline between the cylinders at Re = 45k and 395k, i.e., in the sub- and post-critical regimes. A negligible asymmetry is observed and most likely originates from a slight misalignment of the set-up to the incoming flow, as already mentioned when analysing the time-averaged lift coefficients. At the end of the critical flow regime (Re = 79k), the $\overline{C}_p$ distribution of each cylinder is strongly asymmetric. These observations are in agreement with the ones of the time-averaged lift coefficients of both individual cylinders: the lift coefficients are found to be nearly zero in TrSL2, TrBL0 and TrBL4 regimes while they are non-zero in TrBL1 and TrBL2 (Figure 4.3). The pressure distributions around the front cylinder are similar to the ones observed around a single cylinder. The pressure distributions around the rear cylinder present two local maximum values on its forward face at angular positions, which depend on the Reynolds number. It is inferred that these angular locations correspond to the time-averaged re-attachment points of the separated shear layers from the front cylinder onto the rear cylinder, as observed by Igarashi (1981) and Alam et al. (2003). Even though they do not clearly appear in Figure 4.11(a), small

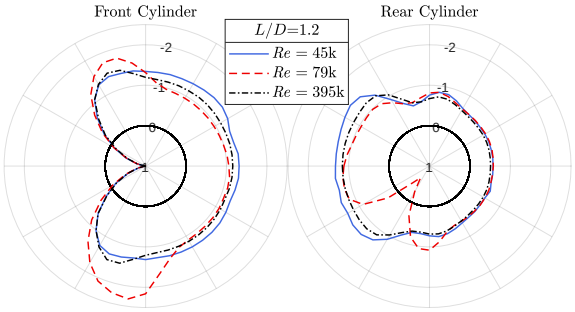

(a) Time-averaged pressure coefficient $\overline{C}_p$ distribution

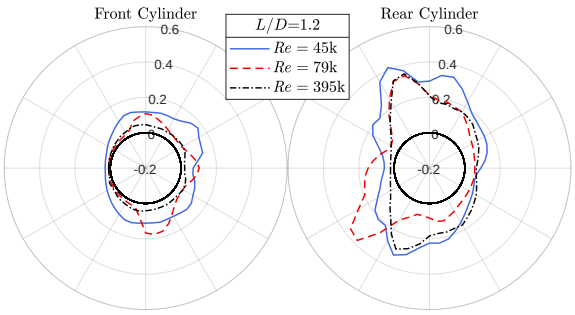

(b) Fluctuating pressure coefficient C'_p distribution

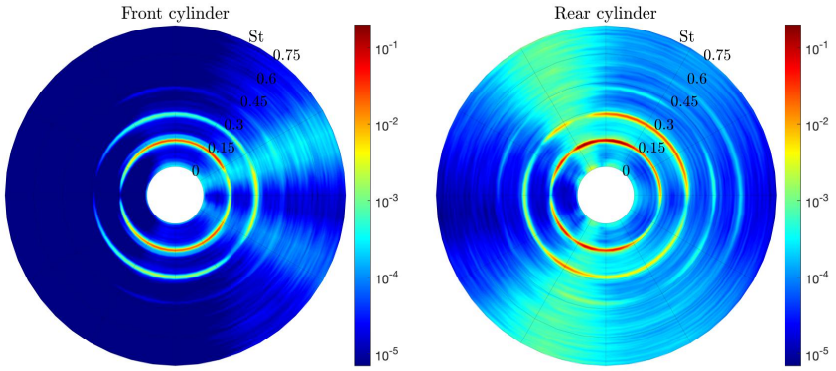

(c) *PSD* of the temporal pressure coefficients at *Re* = 45k

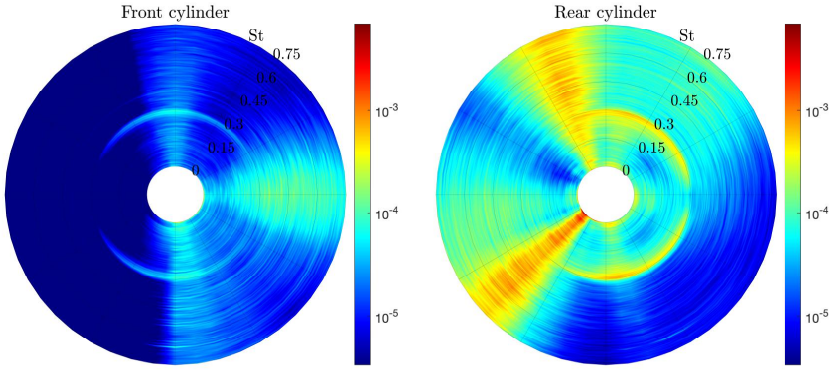

(d) *PSD* of the temporal pressure coefficients at *Re* = 79k

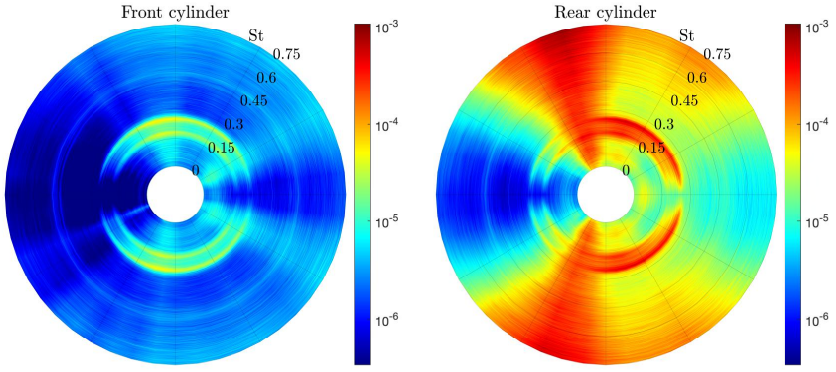

(e) *PSD* of the temporal pressure coefficients at *Re* = 395k

FIGURE 4.11: Pressure coefficient quantities around the tandem cylinders for $L/D = 1.2$ in the main flow regimes.

local maximum values are also observed on the back face of the front cylinder. This observation reveals the re-attachment of separated shear layers from the forward face of the rear cylinder onto the front cylinder.

The fluctuating pressure coefficient distributions for $L/D = 1.2$ are shown in polar coordinates in Figure 4.11(b). Similarly to the time-averaged distributions, they are nearly symmetric at Re = 45k and 395k and asymmetric at Re = 79k. Concerning the front cylinder, maximum fluctuating pressure coefficients are located between $\pm 65^\circ$ and $\pm 110^\circ$, depending on the Reynolds number. These maximum values are due to the separation of the boundary layers. Local maximum values are also observed on the back-face of the front cylinder at $\theta \approx \pm 150^\circ$ in the sub- and post-critical regimes (Re = 45k and 395k) and $\theta \approx 180^\circ$ in the critical regime (Re = 79k). As stated above, they are associated with the re-attachment of the separated shear layers from the forward face of the rear cylinder onto the front cylinder. Concerning the rear cylinder, the maximum fluctuating pressure coefficients are located around the re-attachment points of the shear layers from the front cylinder. At Re = 45k, for example, the re-attachment points are located at angular positions $\theta \approx \pm 75^\circ$ and the maximum fluctuating pressure coefficients at $\theta \approx \pm 70^\circ$. This observation highlights the significant effect of the buffeting of the shear layers on the pressure fluctuations acting on the rear cylinder. The other local maximum values observed in C'_p distributions around the rear cylinder are found downstream and are associated with the separation of the boundary layers.

Figures 4.11(c)-(e) show the spectra of the fluctuating pressure coefficients around the cylinders for $L/D = 1.2$ at the three different Reynolds numbers of interest. The radial direction corresponds to the frequency variable, represented by the dimensionless Strouhal number, and the tangential direction refers to the angular location around the cylinders. Similarly to the previous quantities, the spectra are nearly symmetric around the centreline for the cylinders in the sub- and post-critical regimes. The spectra in the critical regime are also clearly asymmetric. In the sub-critical flow regime (Re = 45k), a dominant peak is observed at $St = 0.141$ for each cylinder and the second harmonic component ($St = 0.282$) is also observable in the spectra. An interesting observation concerns the broad frequency content of the fluctuations at an energy level around 10^{-3} Hz^{-1} around the re-attachment points on the rear cylinder and at a smaller energy level around the ones on the back face of the front cylinder. This broad energy distribution in the frequency domain is characteristic of turbulent shear layers. This observation is also valid for the two other flow regimes (Figure 4.11(d)-(e)). A peak is identified at $St = 0.292$ in the critical flow regime, but its energy level is rather low compared with the sub-critical regime. Indeed, it is balanced by the broad frequency content around the re-attachment points. In the

post-critical flow regime, two peaks are identified in the spectra. The second peak ($St = 0.25$) is not a harmonic component of the first peak ($St = 0.184$). The identification of those two Strouhal numbers was previously observed in the frequency content of the fluctuating lift coefficients at the same Reynolds number (see Figure 4.8(a)). It is due to the intermittent re-attachment of the separated shear layers from the front cylinder onto the rear cylinder. This intermittent behaviour of the shear layers may explain the low energy level associated with the identified peaks in the spectra (Figure 4.11(e)).

- $L/D = 1.4$:

The different quantities of the pressure coefficients around tandem cylinders spaced by $L/D = 1.4$ are shown in Figure 4.12. The same general observations can be made on the time-averaged and fluctuating pressure coefficient distributions in comparison with the previous spacing ratio. The distributions of the different quantities are nearly symmetric in the sub- and post-critical regimes and highly asymmetric in the critical regime around the centreline between the cylinders. Local maximum values in the time-averaged pressure distributions on the forward face of the rear cylinder and the back face of the front cylinder are observed, reporting the occurrence of the re-attachment of shear layers. In the sub-critical flow regime, a dominant peak in the frequency content of the fluctuating pressure coefficients on both cylinders is found at $St = 0.13$ (see Figure 4.12(c)). The second harmonic component also contributes to the fluctuations, similarly to the previous spacing ratio. In the critical flow regime, the spectra are broader, but a small peak can be observed at $St = 0.245$ at the back of the rear cylinder. Unlike the previous spacing ratio (Figure 4.11(d)), a clear peak is not identified in the spectra around the front cylinder. In the post-critical regime, two peaks are observed at non-harmonic frequencies, similarly to the previous spacing ratio. Once again, it is attributed to the intermittent re-attachment of the shear layers. It is noticed that the peak at $St = 0.16$ is larger compared to the one at $St = 0.23$. Moreover, the highest energy levels of the second identified peak ($St = 0.23$) are mainly found at the back of the rear cylinder, while they are located near and on both sides of the re-attachment points on the rear cylinder for the first peak ($St = 0.16$). This observation supports the statement that the peak associated with $St = 0.23$ corresponds to the extended-body pattern (no re-attachment) and the one associated with $St = 0.16$ to the re-attachment pattern. It will be discussed in the next section.

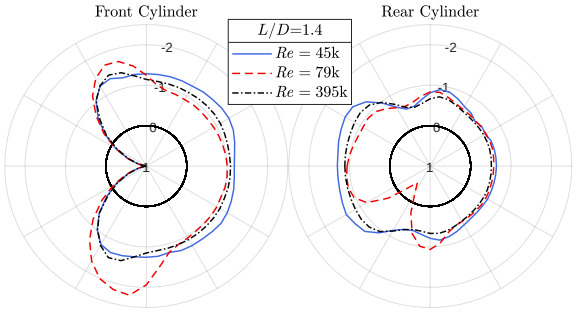

(a) Time-averaged pressure coefficient $\overline{C}_p$ distribution

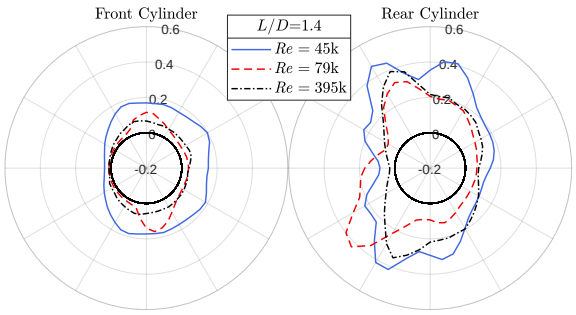

(b) Fluctuating pressure coefficient C'_p distribution

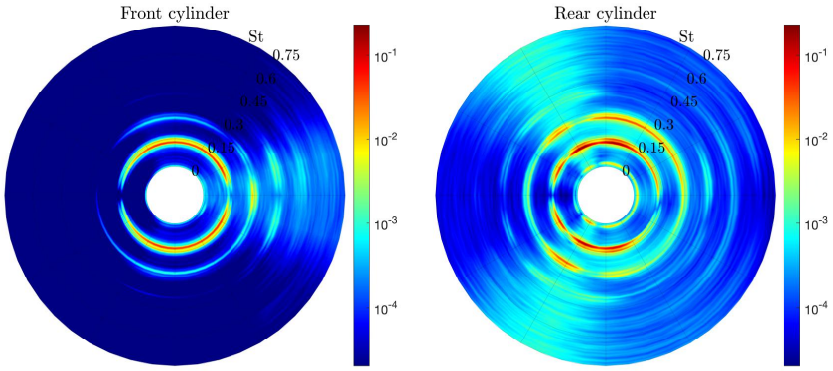

(c) *PSD* of the temporal pressure coefficients at Re = 45k

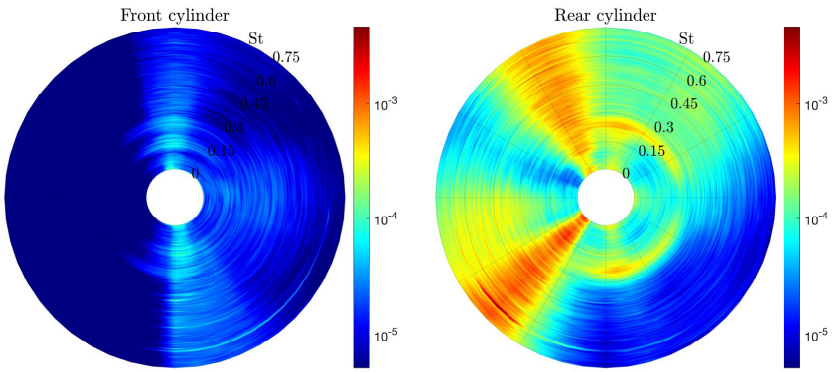

(d) *PSD* of the temporal pressure coefficients at Re = 79k

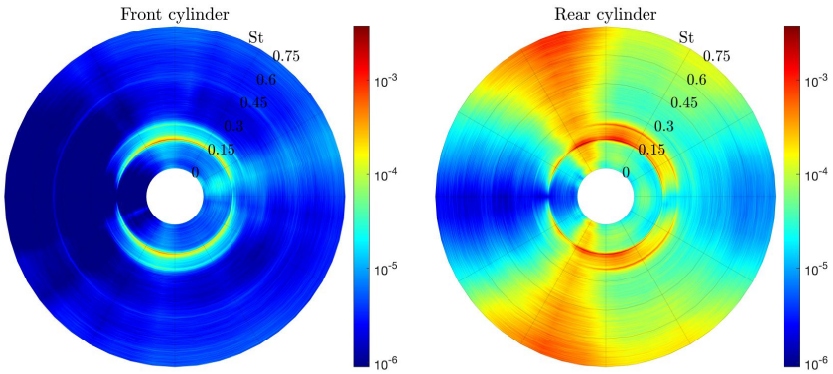

(e) *PSD* of the temporal pressure coefficients at Re = 395k

FIGURE 4.12: Pressure coefficient quantities around the tandem cylinders for $L/D = 1.4$ in the main flow regimes.

- $L/D = 1.56$:

The different quantities of the pressure coefficients around tandem cylinders spaced by $L/D = 1.56$ are shown in Figure 4.13. Similarly to the previous spacing ratios, one can observe that the distributions of the different quantities are symmetric in the sub- and post-critical regimes and highly asymmetric in the critical regime. The occurrence of the re-attachment of the shear layers onto the rear cylinder is also identified from the presence of local maximum values in the time-averaged pressure distributions on its forward face. In the sub-critical flow regime, the dominant peak is found at $St = 0.14$ in the spectra. Once again, a harmonic component to the pressure fluctuations is observed. In the critical flow regime, the observations about the spectra are the same as for the previous spacings. In the post-critical flow regime, two peaks at non-harmonic frequencies are again observed in the spectra. The pressure fluctuations around the front cylinder are mainly dominated by the Strouhal number $St = 0.15$. The frequency content is broader around the rear cylinder. Nevertheless, one can identify the second peak at $St = 0.23$ at the back of the same cylinder. The spectra near and on both sides of the re-attachment points of the shear layers onto the rear cylinder present a dominant peak at $St = 0.15$, as for the front cylinder. This is in agreement with the observation and statement made for the previous spacing ratio.

- $L/D = 1.8$:

The different quantities of the pressure coefficients around tandem cylinders spaced by $L/D = 1.8$ are shown in Figure 4.14. Again, the distributions of the different quantities are symmetric in the sub- and post-critical regimes and highly asymmetric in the critical regime. The locations of re-attachment points of the shear layers onto the rear cylinder are identified from the observation of local maximum values in the time-averaged pressure distributions. In the sub-critical flow regime, a peak is found in the spectra at $St = 0.16$, together with its second harmonic, similarly to the previous spacing ratios. The main difference with the previous spacing ratios is the observation of a single peak at $St = 0.18$ in the spectra of the pressure coefficients in the post-critical regime (Figure 4.14(e)). Multiple peaks are not observed and it is concluded that the re-attachment of the shear layers onto the rear cylinders is not intermittent anymore. Moreover, a second harmonic component is not observed, in contrast with the sub-critical flow regime.

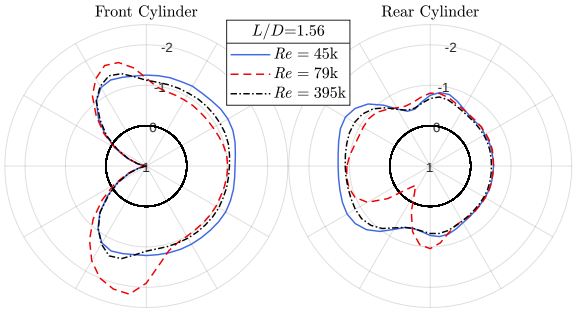

(a) Time-averaged pressure coefficient $\overline{C}_p$ distribution

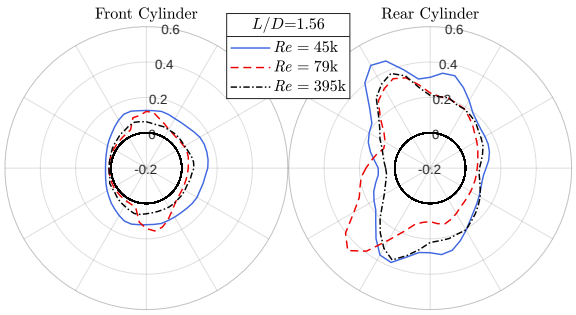

(b) Fluctuating pressure coefficient C'_p distribution

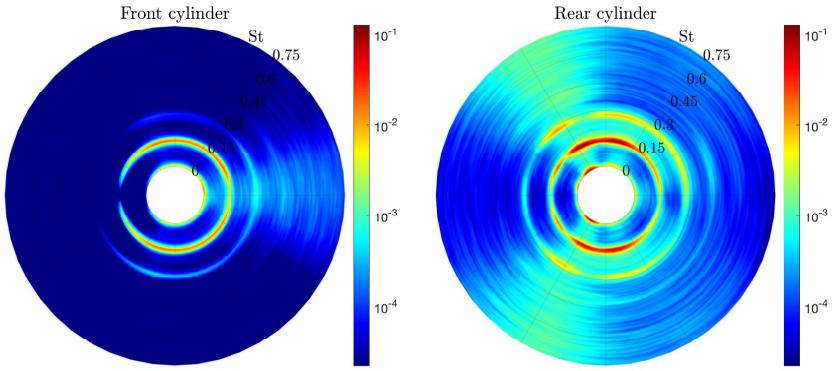

(c) *PSD* of the temporal pressure coefficients at *Re* = 45k

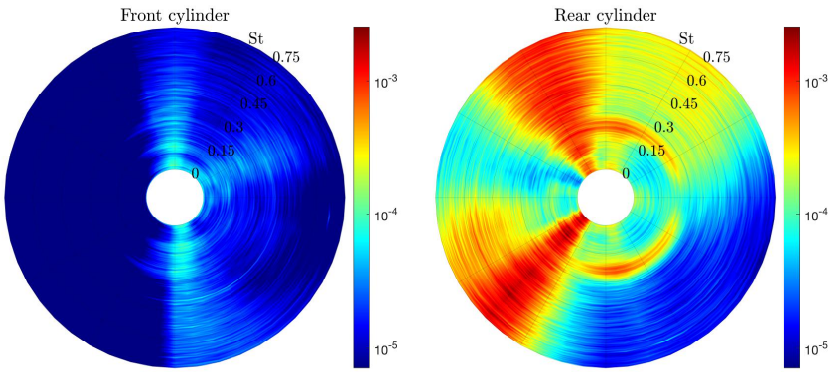

(d) *PSD* of the temporal pressure coefficients at *Re* = 79k

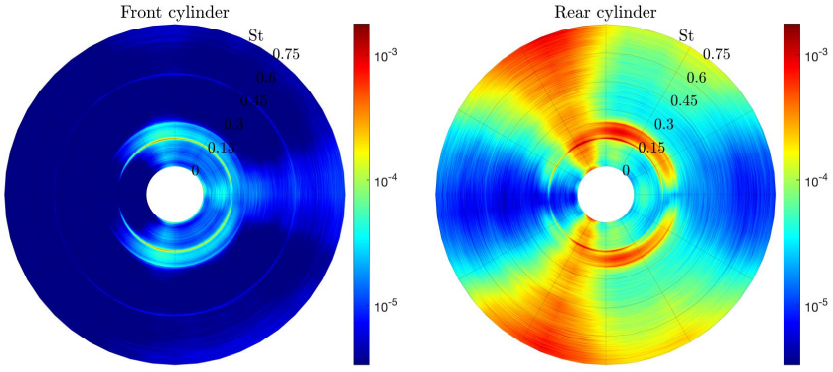

(e) *PSD* of the temporal pressure coefficients at *Re* = 395k

FIGURE 4.13: Pressure coefficient quantities around the tandem cylinders for $L/D = 1.56$ in the main flow regimes.

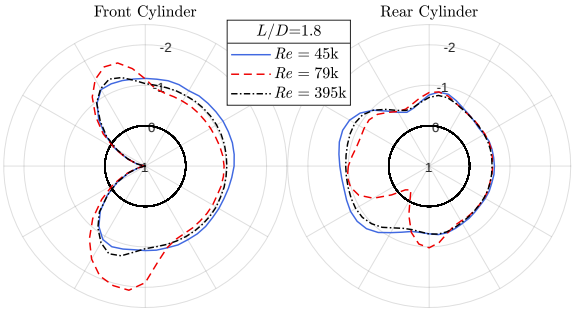

(a) Time-averaged pressure coefficient $\overline{C}_p$ distribution

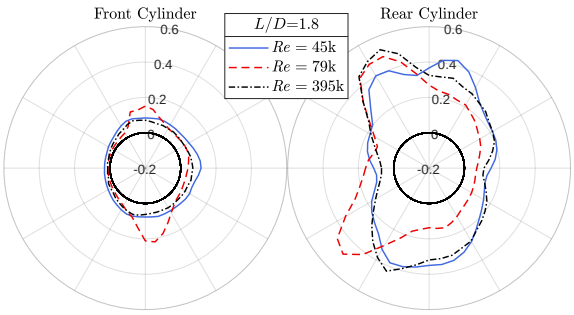

(b) Fluctuating pressure coefficient C'_p distribution

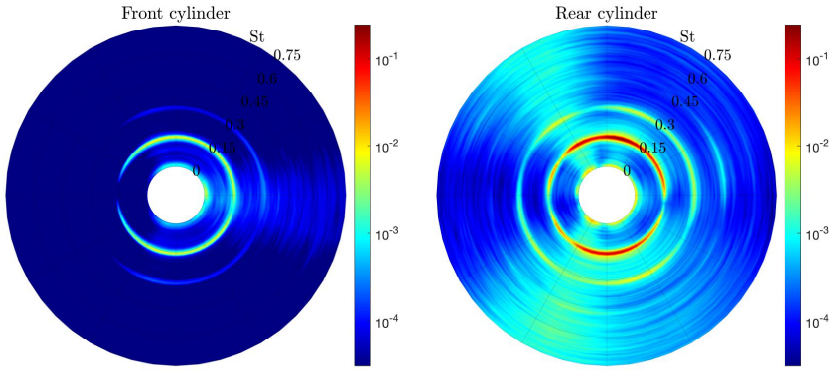

(c) *PSD* of the temporal pressure coefficients at *Re* = 45k

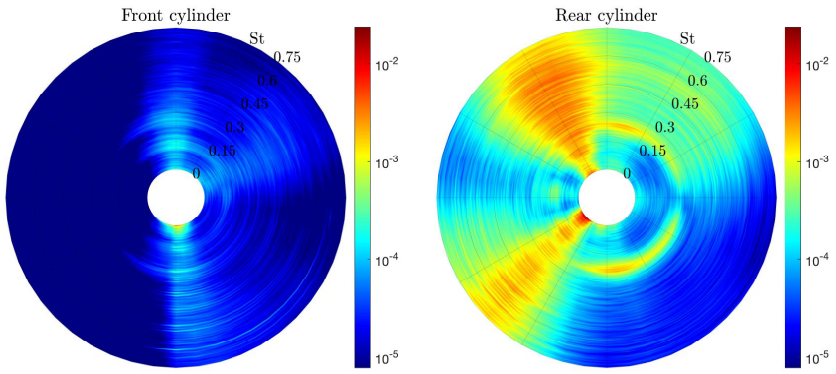

(d) *PSD* of the temporal pressure coefficients at *Re* = 79k

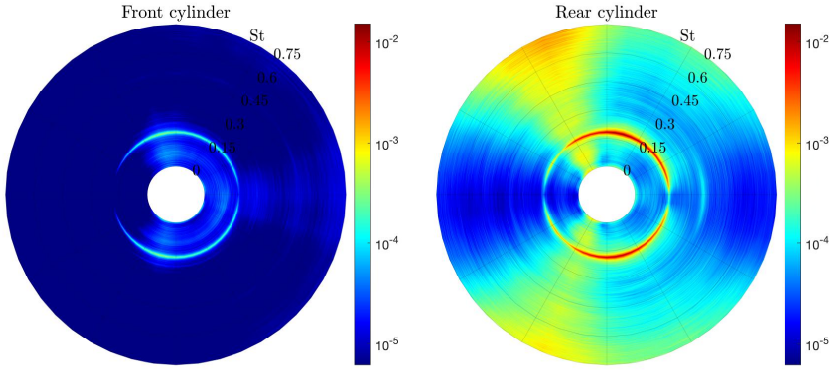

(e) *PSD* of the temporal pressure coefficients at *Re* = 395k

FIGURE 4.14: Pressure coefficient quantities around the tandem cylinders for $L/D = 1.8$ in the main flow regimes.

As a summary, Table 4.2 gathers the numerical values of the time-averaged separation and re-attachment points on the two cylinders for the different spacing ratios in the main flow regimes. They are estimated from the time-averaged pressure distributions and spectra. The different points are defined in Figure 4.15. The approximate separation angles are defined as suggested by Niemann (1971) and are obtained with a maximum angular resolution of 7.5°, i.e., the minimum angular distance between subsequent pressure taps.

Regimes	L/D	θ_{SL1} [°]	θ_{SU1} [°]	θ_{SL2} [°]	θ_{SU2} [°]	θ_{RL1} [°]	θ_{RU1} [°]	θ_{RL2} [°]	θ_{RU2} [°]	θ_{FSL} [°]	θ_{FSU} [°]
sub-critical	1.2	75	-75	120	-120	157.5	-160	78	-75	30	-22.5
	1.4	75	-75	120	-120	160	-160	72.5	-70	15	-15
	1.56	75	-75	120	-120	NR	NR	75	-72.5	7.5	-7.5
	1.8	75	-75	120	-120	NR	NR	80	-70	7.5	0
critical	1.2	105	-97.5	112.5	-120	180	-180	50	-75	-15	-37.5
	1.4	105	-97.5	112.5	-120	180	-180	52.5	-68	-22.5	-30
	1.56	105	-97.5	112.5	-120	NR	-160	52.5	-68	-22.5	-30
	1.8	105	-97.2	112.5	-120	NR	-150	50	-65	-15	-22.5
post-critical	1.2	90	-90	120	-120	157.5	-157.5	80	-80	30	30
	1.4	90	-90	120	-120	160	-160	77.5	-75	22.5	-22.5
	1.56	90	-90	120	-120	NR	NR	75	-72.5	15	-7.5
	1.8	90	-90	120	-120	NR	NR	75	-70	15	-15

TABLE 4.2: Time-averaged separation and re-attachment points on the two cylinders defined in Figure 4.15 for the different spacing ratios and flow regimes (NR: No Re-attachment of the shear layer from the rear cylinder onto the back of the front one).

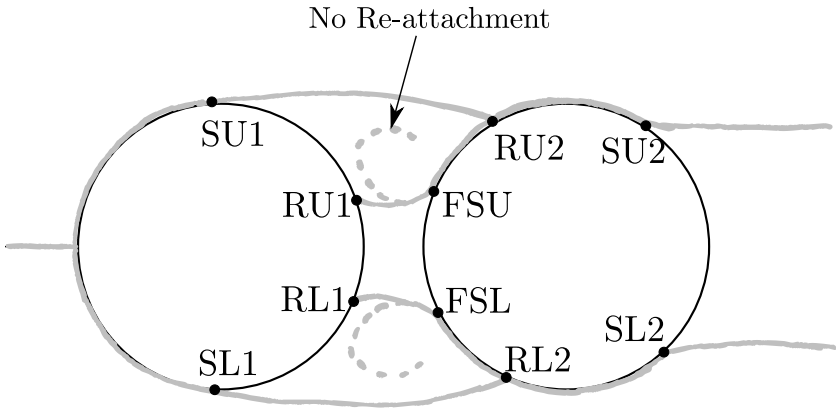

FIGURE 4.15: Definition of the separation and re-attachment points on the tandem cylinders (S: Separation; FS: Forward Separation; R: Re-attachment / U: Upper; L: Lower).

4.3 Classification of flow patterns

Figure 4.16 shows the different flow patterns around the tandem cylinders that can be observed within the tested Reynolds number and spacing ratio ranges. In this figure, the grey sketches show the time-averaged flows, while the black curves represent the instantaneous ones. The positions of the shear layers are inspired by the work of Alam et al. (2003) and Igarashi (1981). In that sense, the sketches are intended to facilitate the discussion about the flows for different configurations.

The first flow pattern is called extended-body (or no re-attachment) pattern. The separated shear layers from the front cylinder do not re-attach onto the rear cylinder, and they alternately roll up and form eddies in the near wake of the rear cylinder. The time-averaged flow of the extended-body pattern is symmetric, as represented in the top sketch of Figure 4.16. This pattern corresponds to Pattern A, identified by Igarashi (1981) (Figure 2.14).

The three other flow patterns belong to the re-attachment regime: (i) the alternate and (ii-iii) steady re-attachment patterns. For the alternate re-attachment pattern, the separated shear layers from the front cylinder re-attach alternately: the shear layer on one side re-attaches onto the rear cylinder, while the shear layer on the other side does not and rolls up behind the rear cylinder to form an eddy. Half a period later, the situation is the opposite. As for the previous flow pattern, the time-averaged flow is symmetric. This pattern corresponds to Pattern B, identified by Igarashi (1981) (Figure 2.14). For the steady re-attachment patterns, although the separated shear layers may fluctuate, they always re-attach onto the rear cylinder, as shown by the black curves in the two lower sketches of Figure 4.16. Eddies are shed behind the rear cylinder. Two different time-averaged flows can be identified for this specific behaviour of the separated shear layers: one symmetric and the other one asymmetric. The pattern corresponding to a symmetric time-averaged flow is Pattern C identified by Igarashi (1981) (Figure 2.14). Note that when a separated shear layer re-attaches onto the rear cylinder, it splits into two boundary layers: (i) one flowing in the downstream direction and (ii) the other one in the upstream direction. The former separates at the back of the rear cylinder, while the latter separates at its front. This forward separation leads to a separated shear layer going upstream, which can either re-attach on the back surface of the front cylinder or roll up between the cylinders, depending on the spacing ratio L/D. Those forward shear layers are sketched in Figure 4.16, with dotted black lines corresponding to the case of no re-attachment onto the back face of the front cylinder.

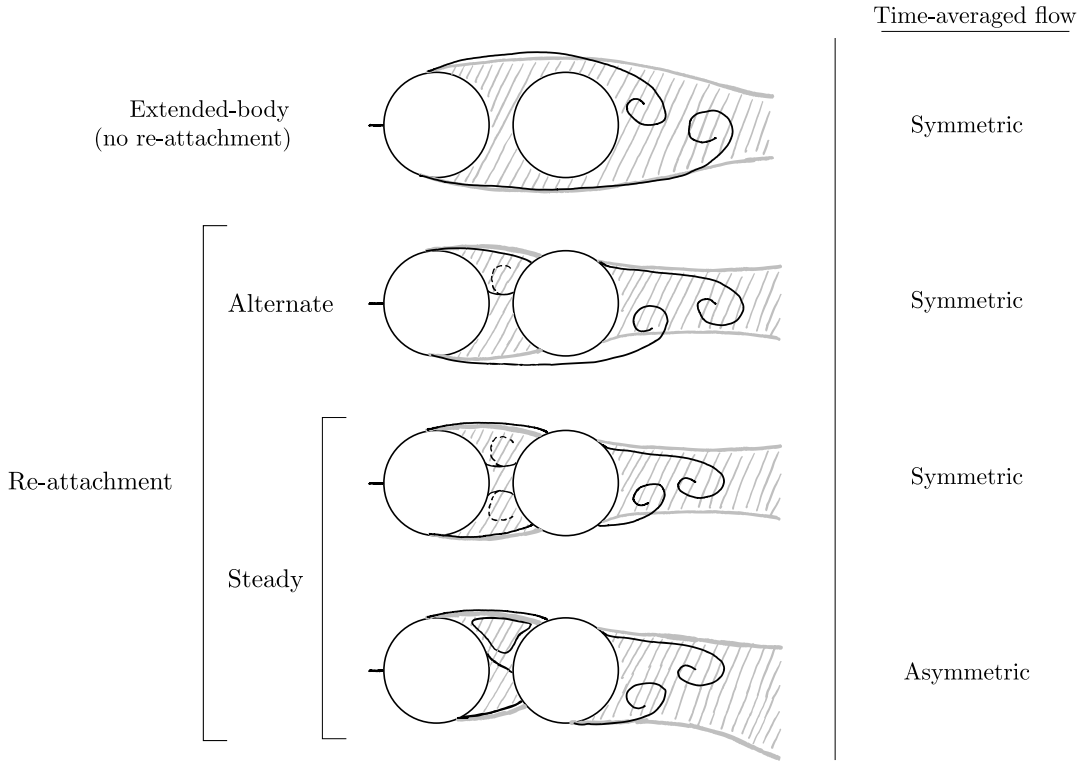

FIGURE 4.16: Sketches of the different flow patterns around tandem cylinders: time-averaged flow (in grey), instantaneous flow/shear layers (in black).

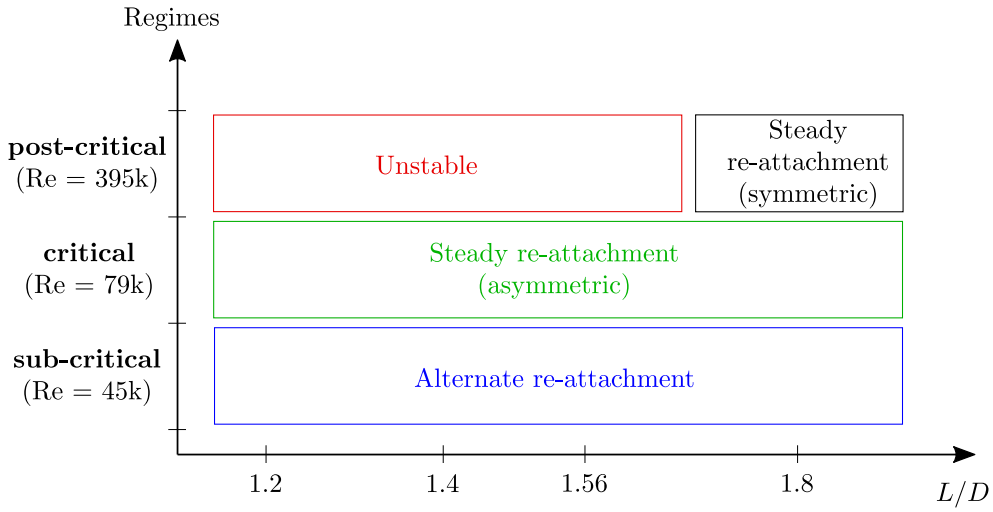

FIGURE 4.17: Identified flow patterns for each spacing ratio in the main flow regimes.

Figure 4.17 shows the identified flow patterns around the tandem cylinders for each spacing ratio at three Reynolds numbers. The Reynolds numbers were chosen to represent the main flow regimes. The flow patterns are identified based on the quantitative analyses presented in the previous sections.

In the sub-critical regime ($Re = 45$k), the time-averaged flow is symmetric around the centreline between the cylinders. The symmetry can be visualised in the time-averaged pressure distributions (Figures 4.11-4.14(a)) and lift coefficients (Figure 4.3). For each spacing ratio, the flow pattern corresponds to an alternate re-attachment of the separated shear layers from the front cylinder onto the rear cylinder. This particular flow pattern is identified by the presence of a super-harmonic frequency of twice the Strouhal frequency in the spectra of fluctuating pressure (see Figures 4.11-4.14(c)). The association of alternate re-attachment with the presence of a super-harmonic frequency in the spectra of the pressure distribution was suggested by Alam et al. (2003).

In the critical regime, the symmetry of the time-averaged flow is lost. The separation points on the front cylinder are not located at the same streamwise positions. It leads to the asymmetry of the pressure distributions (Figures 4.11-4.14(a)) and non-zero lift forces acting on the cylinders (Figure 4.3). In this regime, the resulting flows are characterised by a steady re-attachment: upper and lower shear layers fluctuate but always re-attach on the rear cylinder. As a matter of fact, no harmonic frequency can be observed in the frequency content of the pressure fields around the two cylinders. Moreover, the re-attachment points do not fluctuate at a given frequency. Instead, the frequency contents near the re-attachment points are broad, which is characteristic of non-periodic fluctuations (see Figures 4.11-4.14(d)). The eddy shedding still occurs behind the rear cylinder in the critical regime. It is confirmed by the identification of a peak in the spectra of the fluctuating pressure at the back of the rear cylinder (see Figures 4.11-4.14(d)). Nonetheless, the energy level of the corresponding peak is balanced by the region of re-attachment characterised by a broadband frequency content. Hence, the effect of the eddy shedding on the flow is significantly reduced compared to the sub-critical regime. This observation is in agreement with the drop in c_l' of both cylinders reported in the critical flow regime (see Figure 4.5). Nevertheless, the flow pattern for each spacing ratio is the steady re-attachment one with an asymmetric time-averaged flow, shown in Figure 4.16.

In the post-critical flow regime, the time-averaged flow retrieves its symmetry: the pressure distributions are symmetric around the centreline between the cylinders (Figures 4.11-4.14(a)), and the resulting lift forces are equal to zero (Figure 4.3). For the first three spacing ratios ($L/D \leq 1.56$), multiple peaks are present in the spectra of the lift coefficients, which do not appear at harmonic frequencies (see Figure 4.8).

This observation is discussed in section 4.2.3 and a tentative explanation for the occurrence of the two peaks is the intermittent re-attachment of the separated shear layers from the front cylinder onto the rear cylinder. It leads to an unstable (bi-stable) pattern, which intermittently fluctuates between the extended-body pattern and the steady re-attachment pattern shown in Figure 4.16. For the spacing ratio $L/D = 1.8$, a single peak is observed in the frequency content. The corresponding flow pattern is characterised by a steady re-attachment. It is corroborated by the absence of harmonic frequencies of the Strouhal number associated with the peak in the spectra (see Figure 4.14(e)).

4.4 Effect of the free-stream turbulence

Up to now, the incoming free-stream in the wind tunnel was low-turbulent (T_i<0.2%). In reality, the incoming flow can be highly turbulent. This is especially the case at low altitudes in the atmospheric boundary layers, where most civil engineering structures are found. The question then arises as what happens by increasing the turbulence level in the free-stream. In Chapter 2, it was pointed out that the free-stream turbulence corresponds to a flow disturbance, which may significantly affect the flow around bluff bodies.

The effect of free-stream turbulence on the flow around a single cylinder has already been investigated in the past (Fage and Warsap, 1929; Kiya et al., 1982; Bearman and Morel, 1983; Cheung and Melbourne, 1983; Norberg and Sundén, 1987). The tandem arrangement of two cylinders has received less attention, but some studies exist in the literature (Ljungkrona, Norberg, and Sunden, 1991; Zhang and Melbourne, 1992; Gu et al., 1993). The free-stream turbulence promotes the transition from the laminar to turbulent state of flow. Hence, the drag crisis takes place at lower Reynolds numbers when the turbulence level is increased.

This section investigates the effect of the free-stream turbulence on the flow around two tandem cylinders for a spacing ratio of $L/D = 1.4$. This specific spacing ratio is found to be the one generating the most energetic fluctuations on the two tandem cylinders (in the sub-critical flow regime, at least). Therefore, it seems appropriate to deal with this one. Moreover, it may be considered representative of the two tandem cylinders in close proximity.

4.4.1 Turbulence grids

The turbulence in the incoming free-stream is produced by passive grids. An example of turbulence grid is shown in Figure 4.18. Each grid is composed of wooden bars of width equal to b on a mesh of length M, as defined in Figure 4.19.

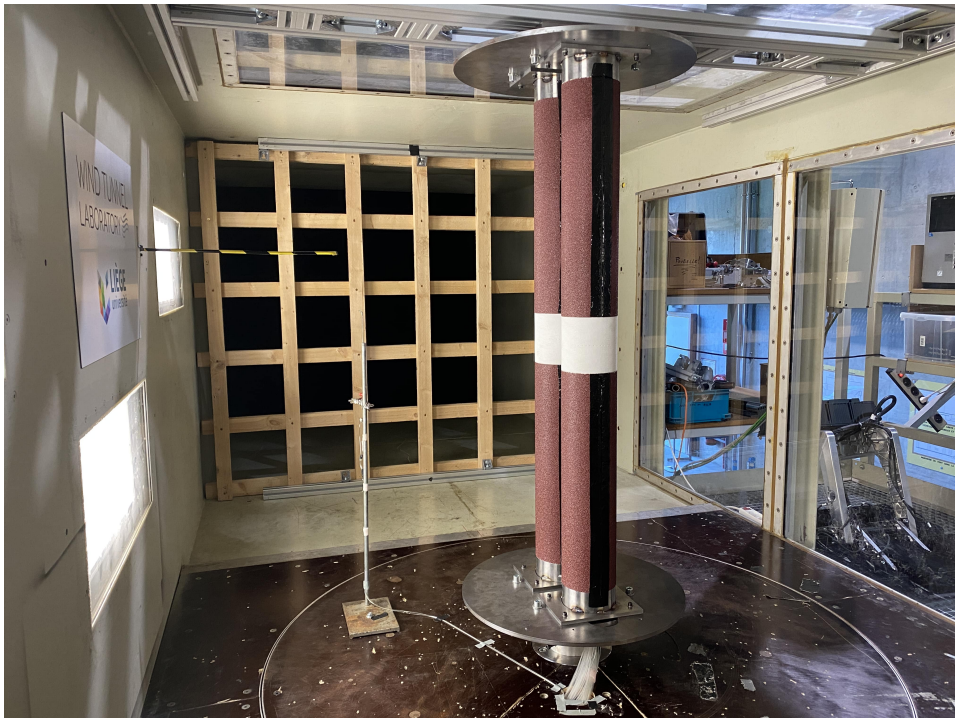

FIGURE 4.18: Experimental model together with the turbulence grid installed in the wind tunnel of ULiège.

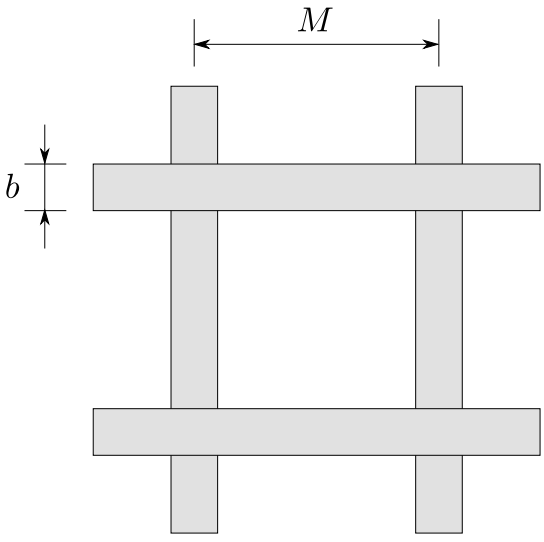

FIGURE 4.19: Schematic of the passive grid.

Configuration	b [m]	M [m]	T_i [%]	L_u [m]	Blockage [m^2]
No grid	-	-	<0.2	-	-
Grid 1	0.036	0.15	8.5	0.065	1.35
Grid 2	0.063	0.3	14.7	0.08	1.25

TABLE 4.3: Tested configurations for different levels of turbulence in the incoming flow.

The turbulence is produced by the eddy-shedding phenomenon downstream of the bars. The passive grid is placed 1.5 m upstream of the centre of the turntable, where the two cylinders are mounted. Two different grids leading to two levels of turbulence are tested. The different configurations and corresponding turbulence parameters of the incoming flow are given in Table 4.3.

The two free-stream turbulence parameters are defined as follows:

- *turbulence intensity*:

$$T_i = \frac{u'}{U_\infty} \tag{4.1}$$

  with u' being the standard deviation of the streamwise component of the incoming velocity $u(t)$. T_i represents the turbulent energy in the flow.

- *integral length scale*:

$$L_u = U_\infty \int_0^\infty \rho_u(\tau) d\tau \tag{4.2}$$

  with

$$\rho_u(\tau) = \frac{\overline{u(t)u(t+\tau)}}{u'^2} \tag{4.3}$$

  being the autocorrelation coefficient. This definition of the integral length scale relies on Taylor's hypothesis of frozen turbulence. L_u is a measure of the size of the most energetic vortices in the turbulent flow.

For additional information on the use of passive grids in the wind tunnel of ULiège, the reader is referred to the thorough investigation performed by Vita et al. (2018).

4.4.2 Time-averaged aerodynamic force coefficients

Figure 4.20 shows the variation of the time-averaged drag and lift coefficients of the front and rear cylinders with the Reynolds number for different levels of free-stream turbulence. It should be pointed out that the maximum Reynolds numbers that can be reached with different turbulence intensities are not the same. It is due to the

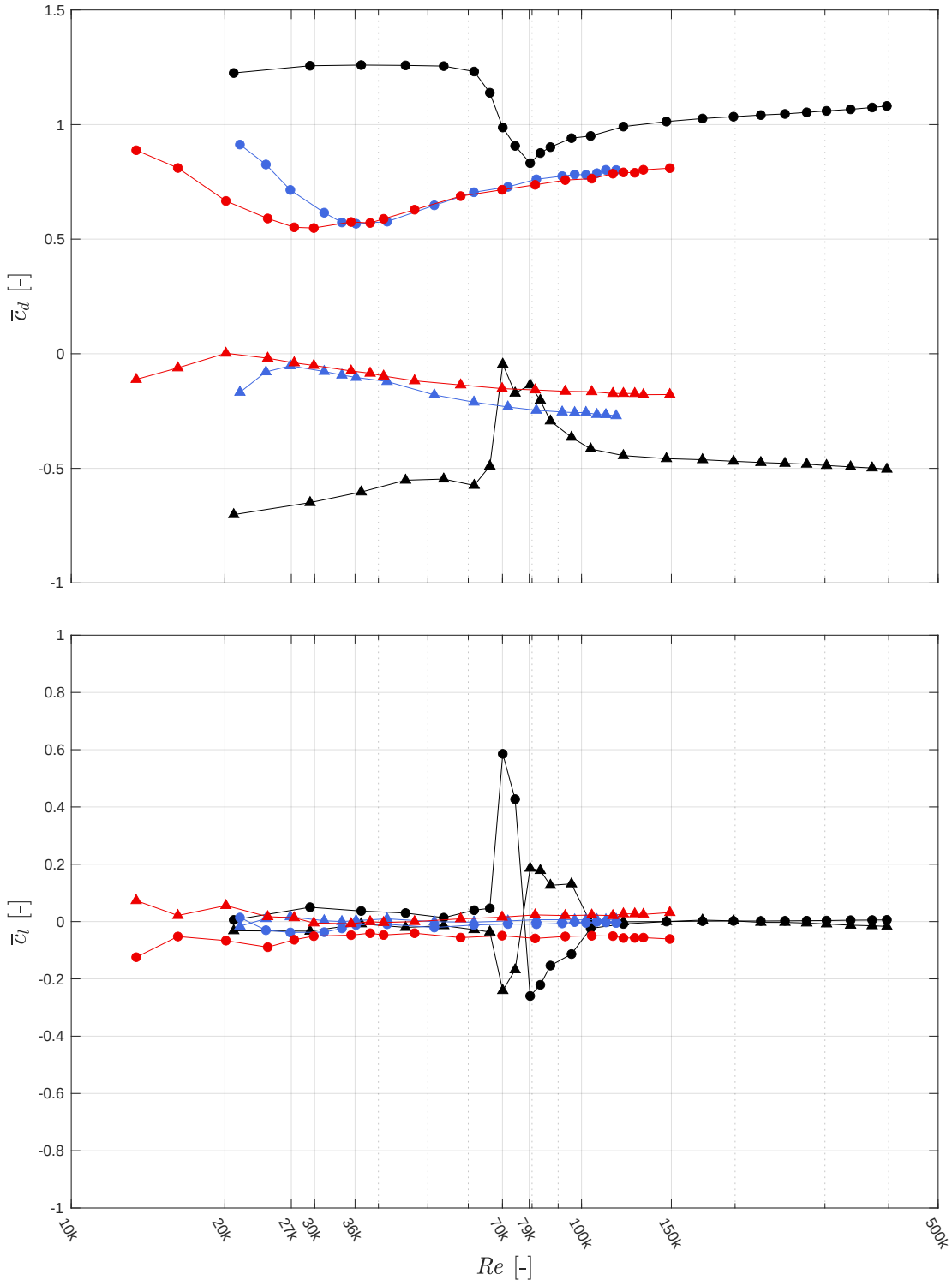

FIGURE 4.20: Time-averaged drag and lift coefficients of the tandem configuration for different levels of free-stream turbulence: T_i = (–) 0.2% (–) 8.5% (–) 15%, Cylinder: (●) front and (▲) rear.

blockage effect of the grids inside the wind tunnel. Nevertheless, the Reynolds number is sufficiently high to reach the post-critical flow regime.

Figure 4.20 shows that the Reynolds number at which the drag coefficient of the front cylinder is minimal decreases with the turbulence level. For a low-turbulent free-stream, the corresponding Reynolds number is around 79k, and it decreases to 36k and 30k when the turbulence intensity is increased to 8.5% and 14.7%, respectively. In Figure 4.20, the drag crisis seems smoother (or less sudden) in a turbulent free-stream than in a low-turbulent one. However, it is an effect of the logarithmic scale on the x-axis. Indeed, Figure 4.21 plots the time-averaged drag coefficients in a linear scale for Re. It is observed that the slope of drag crisis is the same, irrespective of the level of free-stream turbulence.

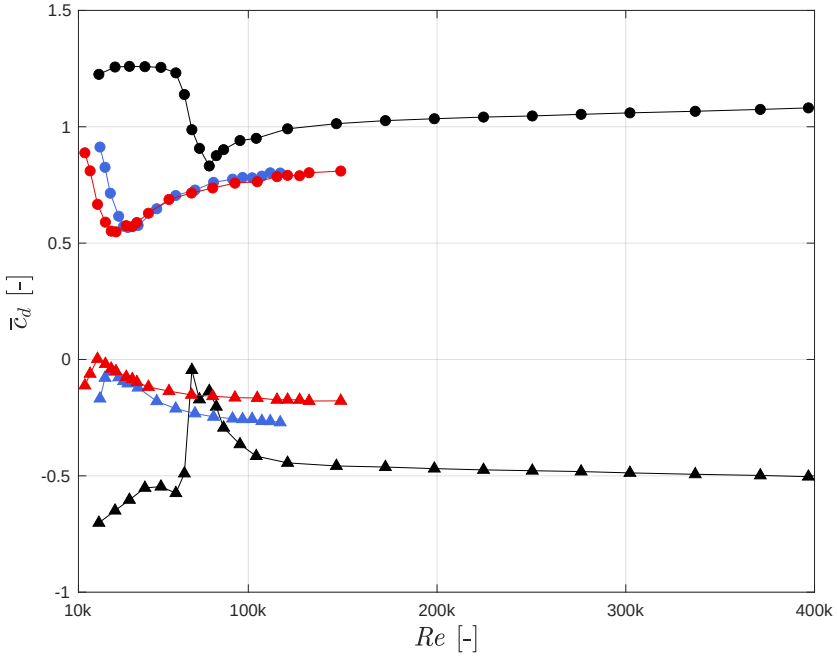

FIGURE 4.21: Time-averaged drag coefficients of two tandem cylinders for different levels of free-stream turbulence in linear scale for Re (same legend as Figure 4.20).

In the bottom plot of Figure 4.20, it is observed that the time-averaged lift coefficients of both cylinders remain almost constant and around zero in a turbulent free-stream. It can be stated that the time-averaged flow around the tandem arrangement remains symmetric within the entire tested Reynolds number range when the free-stream is turbulent. This statement remains valid even in the critical flow regime, in contrast to a low-turbulent incoming flow. In this latter case, the asymmetry of

the flow in the critical flow regime has already been explained earlier in this chapter. As a reminder, it results from the asymmetry of the onset of transition in reaching the separation lines on either side of the front cylinder. When turbulence is present in the incoming free-stream, the asymmetry is broken or significantly reduced. The free-stream turbulence randomly excites the separated shear layers and the boundary layers. Hence, it triggers the onset of transition in a similar manner on either side of the front cylinder, and the asymmetry in the critical flow regime disappears.

In the post-critical flow regime – highest Re – the absolute values of the time-averaged drag coefficients decrease with the free-stream turbulence. For the front cylinder, the time-averaged drag coefficient decreases with T_i. But it seems to converge towards a particular value since the variation becomes small when T_i is increased from 8.5% to 14.7% (see Figure 4.20). Concerning the rear cylinder, the time-averaged drag coefficient increases with T_i, and it still varies significantly when the turbulence intensity is increased from 8.5% to 14.75% (see top plot of Figure 4.20).

4.4.3 Fluctuating lift coefficients

Figure 4.22 shows the variation of the fluctuating lift coefficients of the front and rear cylinders with the Reynolds number for different levels of free-stream turbulence.

The following observations are made:

- The lift fluctuations increase on both cylinders with the level of free-stream turbulence, especially in the post-critical flow regime.

- For a low-turbulent free-stream, the largest fluctuations are identified in the sub-critical flow regime, while they become large in the post-critical regime when the turbulence intensity is increased. It seems that the fluctuations keep increasing with Re in a turbulent incoming flow.

- In the post-critical flow regime, the lift fluctuations are significantly higher on the rear cylinder than on the front one in the case of a low-turbulent free-stream. When increasing the free-stream turbulence, the difference in the level of fluctuations between the front and rear cylinders decreases. For the highest tested level of turbulence ($T_i = 14.7\%$), the fluctuations are approximately equal on both cylinders (see Figure 4.22). Those large fluctuations may emanate from a strong eddy-shedding phenomenon or more probably from the buffeting of the turbulent free-stream on the tandem arrangement.

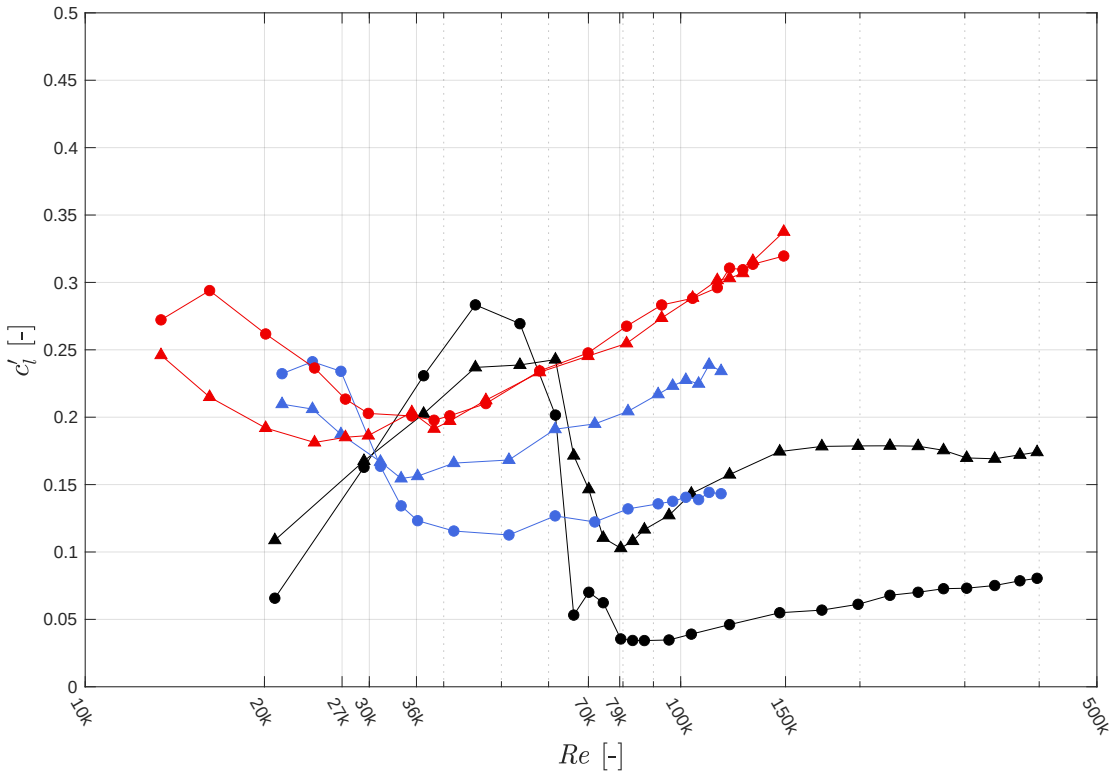

FIGURE 4.22: Fluctuating lift coefficients of the tandem configuration for different levels of free-stream turbulence: T_i = (–) 0.2% (–) 8.5% (–) 15%, Cylinder: (●) front and (▲) rear.

4.4.4 Frequency content of the lift coefficients

Figure 4.23 shows the spectra of the lift coefficient of each cylinder as a function of the Reynolds number. As done previously, the lift signals have been normalised by their respective standard deviations before computing the power spectral densities.

For a turbulent free-stream, it is observed that the energy distribution extends in a broad range of reduced frequencies in Figure 4.23(b-c). This is particularly true for the front cylinder, where the fluctuating energy distribution is rather flat and broad. This particular broad distribution is expected since it is a characteristic of the free-stream turbulence. Nonetheless, peaks can still be observed in the spectra, especially for the rear cylinder. The presence of peaks in the spectra reveals the existence of an eddy shedding process behind the two tandem cylinders, even in a turbulent flow. In comparison to the peaks identified in a low-turbulent free-stream (Figure 4.23(a)), the peaks are wide when introducing sufficient turbulence into the incoming flow. It is believed that the free-stream turbulence reduces the spanwise correlation length

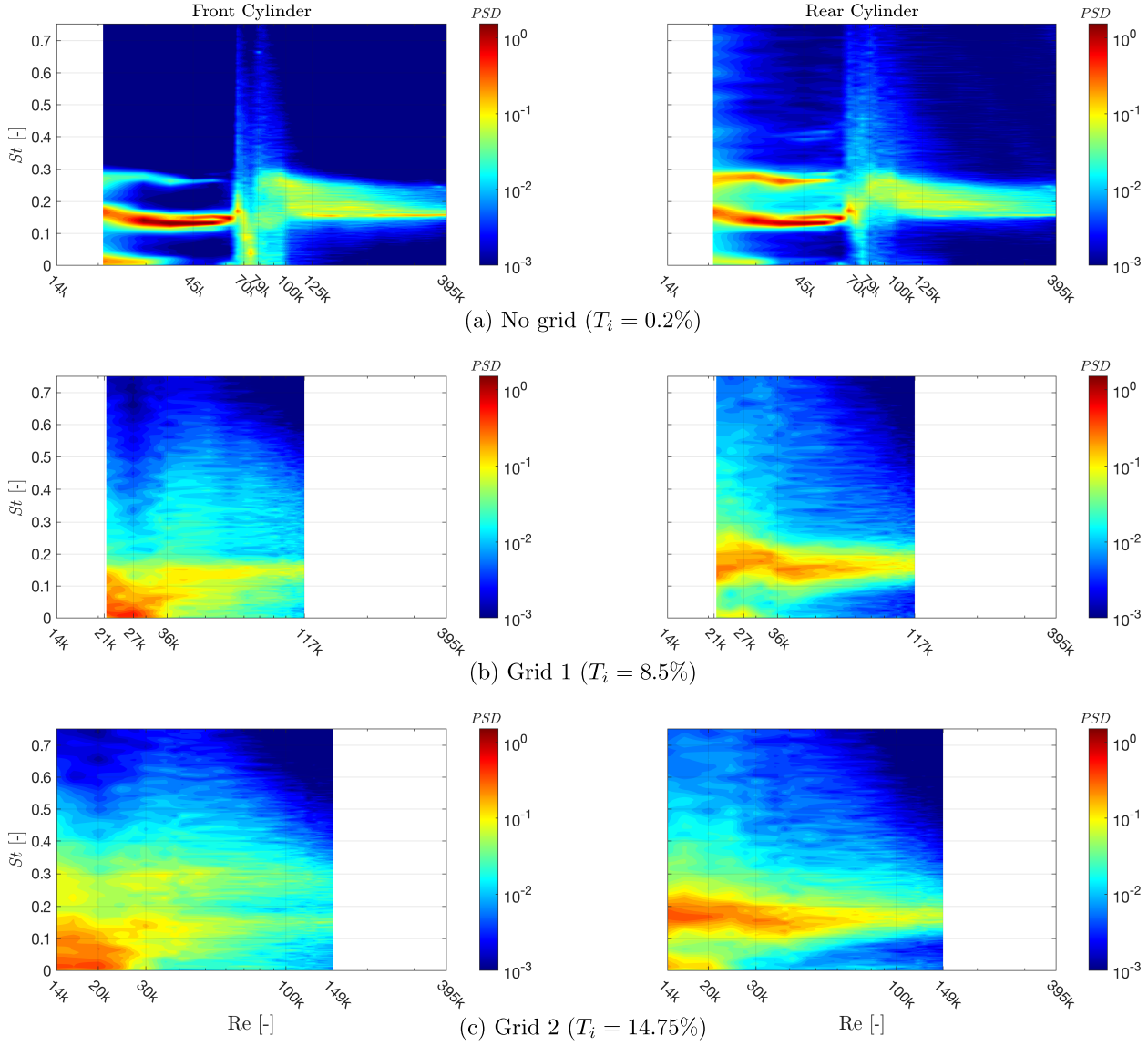

FIGURE 4.23: Frequency content of the lift coefficients as a function of *Re* for different levels of free-stream turbulence.

of the shedding process, which leads to a flatter and broader associated peak in the spectra of the lift coefficient.

In Figure 4.23(b-c), it is observed that the Strouhal number associated with the identified peak, and therefore linked to the eddy shedding frequency, is rather constant in a turbulent free-stream. In the post-critical flow regime, the Strouhal number associated with the eddy shedding is found to be $St \approx 0.15 - 0.16$. As a reminder, double non-harmonic peaks were observed in a low-turbulent flow in the post-critical flow regime. They were attributed to an instability in the behaviours of the shear layers in between the cylinders. It seems that the free-stream turbulence prevents the

latter instability from occurring, as a single peak is reported in the spectra. The resulting single Strouhal number, i.e., $St \approx 0.15 - 0.16$, is associated with the re-attachment flow pattern. Therefore, it is concluded that the free-stream turbulence disturbs the separated shear layers from the front cylinder and induces a stable re-attachment onto the rear cylinder.

4.4.5 Pressure coefficient distributions

Figure 4.24 shows the time-averaged and fluctuating pressure coefficient distributions around the two tandem cylinders for different levels of free-stream turbulence at the critical Reynolds number, i.e., when the time-averaged drag coefficient of the front cylinder reaches a minimum value.

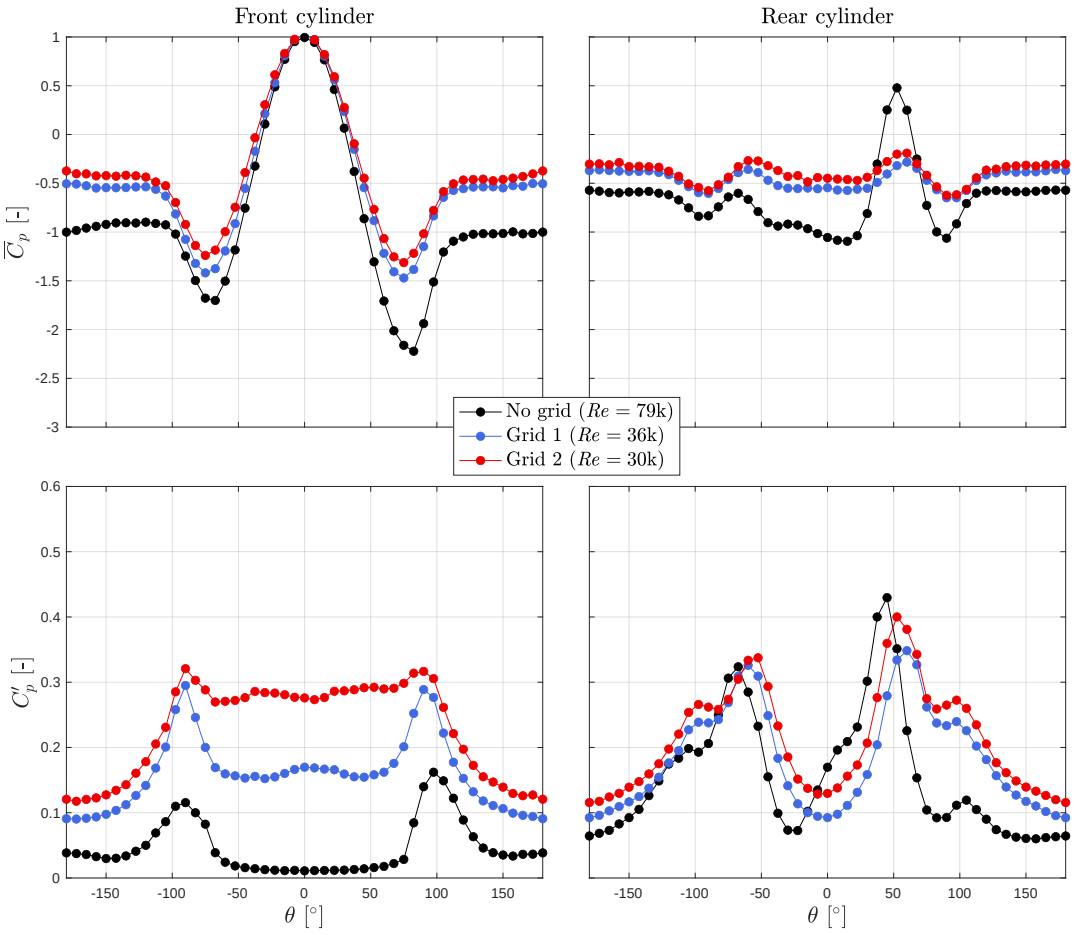

FIGURE 4.24: Time-averaged and fluctuating pressure coefficient distributions around the two tandem cylinders for different levels of free-stream turbulence at the critical Reynolds number (when $\overline{c}_d$ of front cylinder is minimum).

The first observation concerns the symmetry of the distributions of the different quantities. In a low-turbulent flow, the distributions are strongly asymmetric while they are rather symmetric when increasing the turbulence level. This is consistent with the observation made earlier about the time-averaged lift coefficients which take values close to zero when increasing the turbulence intensity in the free-stream.

Based on Figure 4.24, it can be stated that the pressure in the gap between the two tandem cylinders increases with the level of free-stream turbulence. Indeed, the time-averaged base pressure coefficient $\overline{C}_{pb}$ (at $\theta \pm 180°$) of the front cylinder and the frontal pressure coefficient $\overline{C}_{pf}$ (at $\theta = 0°$) of the rear cylinder both increase with the turbulence in the free-stream. This increase of the pressure in the gap may explain the decrease of the time-averaged drag coefficient of the front cylinder with turbulence intensity (see Figure 4.20). It is observed that the base pressure coefficient of the rear cylinder increases in a less significant way and, together with the increase of pressure in the gap, it explains the increase of its time-averaged drag coefficient with the turbulence level.

It has already been stated in this manuscript that the local maximum values in the time-averaged pressure distribution around the rear cylinder are related to the re-attachment of the separated shear layers onto the rear cylinder. It is observed in Figure 4.24 that the angular locations corresponding to the re-attachment slightly move upstream when the turbulence intensity is increased. This observation is more evident when comparing the configurations corresponding to large turbulent flows ($T_i = 8.5\%$ and 14.7%) since the time-averaged flow is symmetric in those cases.

Concerning the fluctuating pressure distributions in Figure 4.24, it is observed that the fluctuations increase with the turbulence level in the free-stream. A particularly interesting observation is the large level of fluctuations on the upstream face of the front cylinder which is directly facing the turbulent incoming flow. It is expected from an increase in the turbulence intensity and shows that the flow, and hence the boundary layers, are strongly disturbed by the free-stream turbulence in that region. As a consequence, it promotes an earlier onset of transition to turbulence in the boundary layers when increasing the free-stream turbulence.

Figure 4.25 shows the time-averaged and fluctuating pressure coefficient distributions around the two tandem cylinders for different levels of free-stream turbulence in the post-critical flow regime. The same Re is considered to focus on the effect of the free-stream turbulence only. It corresponds to the maximum tested Reynolds number with "Grid 1" ($Re \approx 120$k) and it can be stated that the post-critical flow regime is reached for every tested configurations.

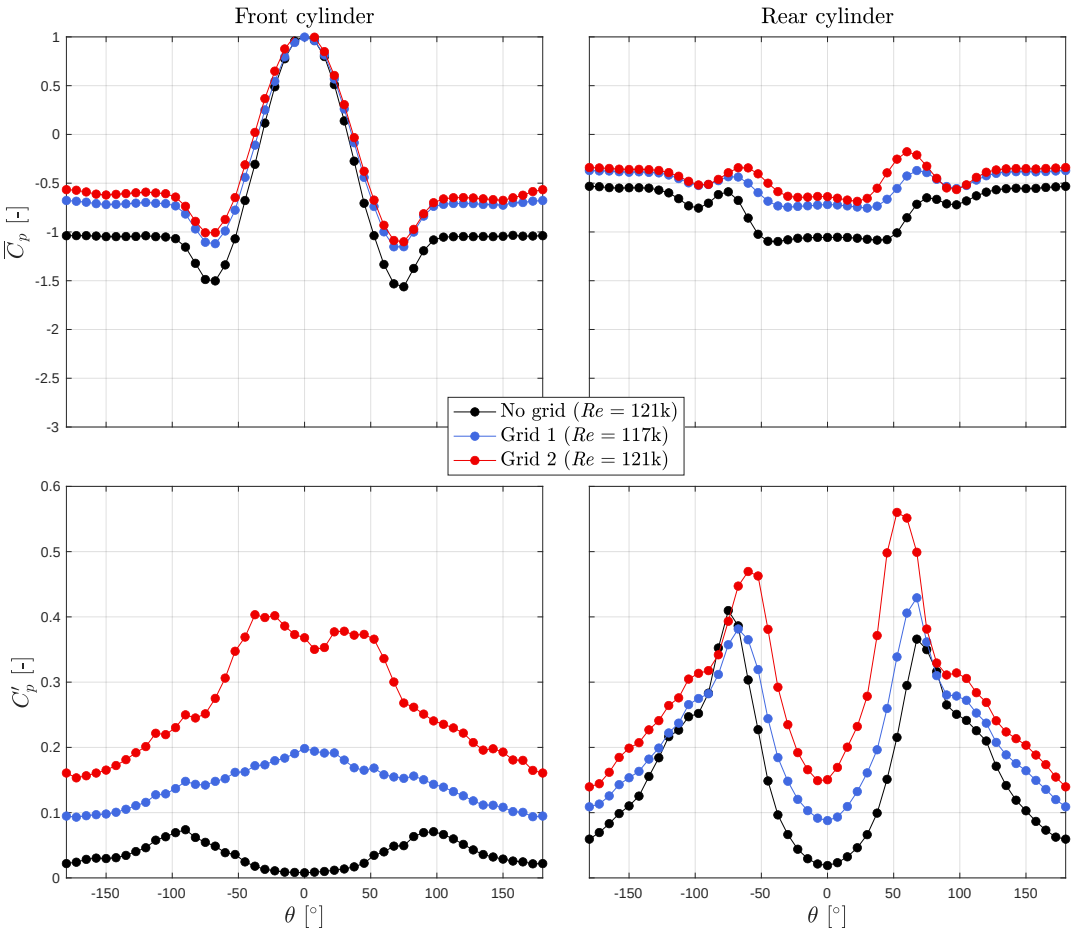

FIGURE 4.25: Time-averaged and fluctuating pressure coefficient distributions around the two tandem cylinders for different levels of free-stream turbulence in the post-critical flow regime.

In comparison with the critical regime (Figure 4.24), the different distributions around the two tandem cylinders are symmetric, even for a low-turbulent free-stream. Similar observations to those for the critical regime are made: the pressure in the gap between the cylinders increases with the turbulence intensity in the incoming flow, leading to a decrease and increase in the time-averaged drag coefficients of the front and rear cylinders, respectively. The re-attachment locations of the separated shear layers onto the rear cylinder move upstream with the turbulence level. They move from an angular location of $\theta \approx 75°$ to $60°$ when the turbulence intensity is increased from 0.2% to 14.7%.

The pressure fluctuations on the upstream face of the front cylinder are even higher than in the critical regime. The fluctuating pressure distributions around the rear cylinder are similar for the different free-stream turbulence levels. Those are shifted to larger values in a turbulent free-stream.

Based on the previous observations, it is stated that the flow pattern in a turbulent free-stream corresponds to a steady re-attachment of the separated shear layers from the front cylinder onto the rear cylinder. It is corroborated by the resulting Strouhal number related to the eddy shedding frequency equal to 0.16-0.17. With the available data (only pressure measurements), the identification of the physical phenomenon responsible for the upstream movement of the re-attachment locations of the shear layers onto the rear cylinder is complex. Nonetheless, it may be explained by the fact that the turbulence leads to enhanced mixing of the shear layers and entrainment of free-stream into the near-wake of the front cylinder. As a consequence, the length of the near-wake decreases and the shear layers thus re-attach more upstream onto the rear cylinder.

In this chapter, the tandem arrangement of two rough cylinders has been investigated in detail. The experimental results show the sensitivity of the flow to the Reynolds number through the identification of several flow regimes. Distinct flow patterns are identified around the cylinders, depending on the spacing ratio L/D and the flow regime. These distinct flow patterns may excite the structure in different manners, leading to potential aeroelastic instabilities. Furthermore, the free-stream turbulence also modifies the flow pattern around the cylinders. It highlights the complexity of the flow around two static cylinders and the necessity to investigate the effect of the different parameters (L/D, Re, T_i). For the rest of the manuscript, only low-turbulent free-stream is considered but it must be kept in mind that the free-stream turbulence may have a significant effect on the flow dynamics around two cylinders and, thus, on the potential flow-induced vibrations.

Chapter 5

Two cylinders in staggered arrangement

This chapter is dedicated to the analysis of the unsteady flow around the two cylinders by considering the variation of the flow incidence. It is performed in the sub- ($Re = 45$k) and post-critical ($Re = 275$k) flow regimes. The flow incidence α is varied from 0° (tandem arrangement) to 10° by increment of 2°. A thorough investigation is first performed for the smallest spacing ratio, i.e., $L/D = 1.2$. It corresponds to the main subject of the second published article related to the present doctoral thesis (Dubois and Andrianne, 2023). The analysis is then extended to the other spacing ratios.

5.1 Investigation of the flow for $L/D = 1.2$

5.1.1 Effect of flow incidence

Figure 5.1 focuses on the variation of the lift coefficient quantities of each cylinder with the flow incidence in the sub- and post-critical flow regimes. Sub-figures (a-b) show the time-averaged values, while sub-figures (c-f) show the *Power Spectral Density* (*PSD*) of the fluctuating lift signal of each cylinder. As done previously, the fluctuating lift signals are initially normalised by their respective standard deviation to allow the comparison of the frequency content at different flow incidences. The dimensionless Strouhal number $St = fD/U_\infty$ is used as the frequency variable. It takes values in the range $0 < St < 1$ in the present analysis. The superimposed black lines with different markers correspond to the different peaks that are not harmonic (the frequency of one peak is not an integer multiple of the other one) observed in the spectra. Within the tested range of flow incidences, three distinct behaviours can be identified in the sub- or post-critical flow regime.

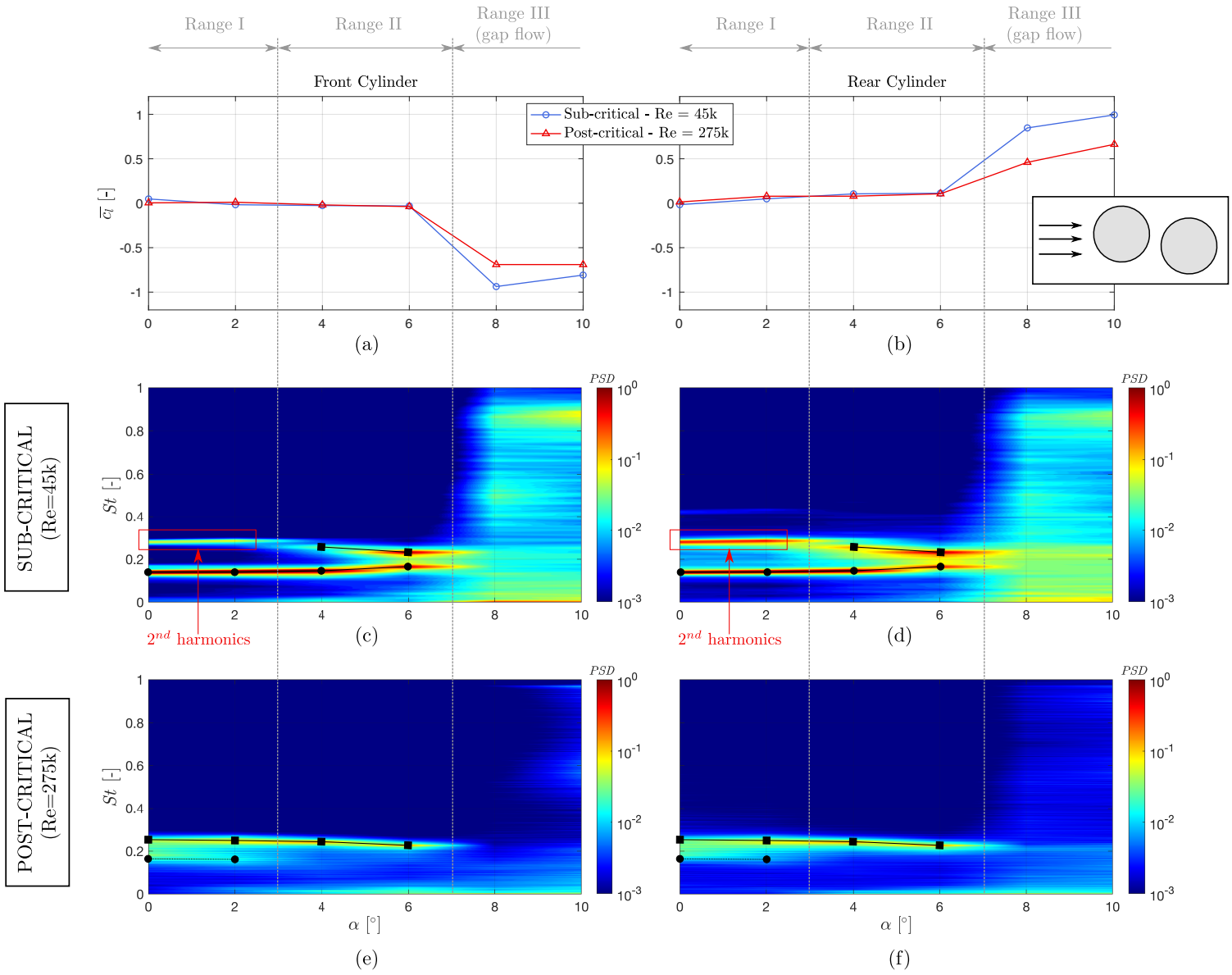

FIGURE 5.1: Variation of the time-averaged value and frequency content of the lift coefficient of each cylinder with the flow incidence in the sub- and post-critical flow regimes ($L/D = 1.2$).

The first behaviour is observed at low flow incidences (range I: $\alpha = 0°$ - $2°$). In both flow regimes, the time-averaged lift coefficient of each cylinder remains close to zero, as shown in Figure 5.1(a-b). Nevertheless, it can be observed that the lift coefficient of the front cylinder becomes slightly negative, while the one of the rear cylinder becomes positive when increasing the flow incidence. The two flow regimes differ in the frequency content of the lift signals. In the sub-critical flow regime, a strong peak is observed at $St \approx 0.14$. A second and weaker peak is also identified at a harmonic frequency of the fundamental one, $St \approx 0.28$ (see Figure 5.1(c-d)). This observation was already done in the tandem arrangement of cylinders ($\alpha = 0°$) in

the previous chapter (see Figure 4.8(a)). The presence of harmonic components was attributed to the alternate re-attachment of the separated shear layers from the front cylinder onto the rear cylinder, as suggested by Alam et al. (2003) (see flow pattern in Figure 4.16). In the post-critical flow regime, the frequency content also reveals two peaks (see Figure 5.1(e-f)). However, the second peak does not correspond to a harmonic component of the first one. Again, this observation was already done in the tandem arrangement (see Figure 4.8(a)), and it was concluded that it corresponds to a bi-stability due to the intermittent re-attachment of the separated shear layers from the front cylinder onto the rear cylinder.

A second behaviour is observed at intermediate flow incidences (range II: $\alpha = 4°$ - 6°). Similarly to the low flow incidences, the lift coefficient of each cylinder remains small in both flow regimes. When increasing the flow incidence, the lift coefficient of the front cylinder slightly decreases and the one of the rear cylinder slightly increases. In the sub-critical flow regime, two peaks are still present in the spectra of the lift signals (see Figure 5.1(c-d)). Unlike the previous range of flow incidences, the peaks are identified at non-harmonic frequencies ($St \approx 0.14$ and 0.25). It is therefore assumed that they stem from two distinct processes: a bi-stability between two flow patterns takes place, leading to two different Strouhal numbers. The lowest identified Strouhal number increases when the flow incidence is increased from 4° to 6° while the other Strouhal number decreases. In the post-critical flow regime, a single peak is observed in the spectra at $St \approx 0.24$ (Figure 5.1(e-f)). This peak corresponds to the highest Strouhal number identified in the previous sub-range of flow incidences. Thus, it is stated that only the eddy-shedding process related to this Strouhal number remains present in this configuration.

A third behaviour is observed at higher flow incidences (range III: $\alpha = 8°$ - 10°). The time-averaged lift coefficients of the front and rear cylinders take large negative and positive values, respectively. The appearance of these large lift forces has already been observed in previous studies in the sub-critical flow regime (Zdravkovich, 1987 or Sumner, Richards, and Akosile, 2005, among others) and is referred to as the "inner" lift force. These large lift forces are induced by a strong gap flow, which establishes between the two cylinders. The gap flow takes place in both sub- and post-critical flow regimes, as shown in Figure 5.1(a-b). Based on the absolute values of the lift coefficients, it can be stated that the gap flow is stronger in the sub- than in the post-critical flow regime. The exact flow incidence at which the gap flow appears is not identified, but it is expected between $\alpha = 6°$ and 8° in both flow regimes. Concerning the frequency content of the lift signals, it is observed that it becomes broad

within this range of flow incidences (see Figure 5.1(c-f)). In both flow regimes, the occurrence of the broad spectra coincides with the establishment of a strong gap flow. Hence, it is stated that the gap flow strongly impacts the eddy-shedding process behind the twin-cylinder configuration.

5.1.2 Bi-stability analysis

This section focuses on the analysis of the bi-stability of the flow, previously revealed in the frequency content of the lift forces. For this purpose, a methodology is suggested to extract the two stable flow patterns. The resulting flow modes are presented hereafter for a particular configuration, i.e., $\alpha = 4°$ in the sub-critical flow regime (Re = 45k). This specific configuration is chosen because the two modes are easily decoupled based on the observation of the lift signals, as will be shown below, while it is not the case for the other flow regimes or flow incidences. The suggested methodology is then applied to the other flow regimes and incidences.

Mode decomposition from lift signals

Figure 5.2(a,c) shows typical time signals of the lift coefficient measured on the two cylinders. Their respective wavelet transforms - calculated using Morlet wavelet - are shown in Figure 5.2(b,d). A wavelet transform allows a time-frequency analysis of the signal. Hence, this tool allows detecting local events in time, such as variation of the dominant frequency of the flow. In the time signals, two time intervals are highlighted. The lift coefficients do not fluctuate at the same frequency in these two intervals, while the flow conditions (velocity and incidence) are unchanged. The lift coefficients of the two cylinders do fluctuate at a lower frequency in the first time interval (Mode 1 : $t \approx 49 - 53$ s) than in the second one (Mode 2 : $t \approx 57.5 - 59.5$ s). This observation is corroborated by the corresponding wavelet transforms. In Figure 5.2(b,d), it is observed that Modes 1 and 2 are associated with Strouhal numbers of 0.14 and 0.25, respectively.

The selected lift coefficients in each time interval are phase-averaged to ease the analysis of the modes. The same number of cycles (22) is selected in both modes to perform the phase-averaging. The lift coefficient of the front cylinder is taken as the reference signal. It means that the different cycles within the time interval are separated by locating the minima of the lift coefficient of the front cylinder. The resulting cycles are averaged at 40 equally spaced time instants within the period. The resulting phase-averaged lift coefficients are shown in Figure 5.3.

The time-averaged and fluctuating values of the phase-averaged lift coefficients are summarised in Table 5.1 for each mode. The lift force fluctuations are higher

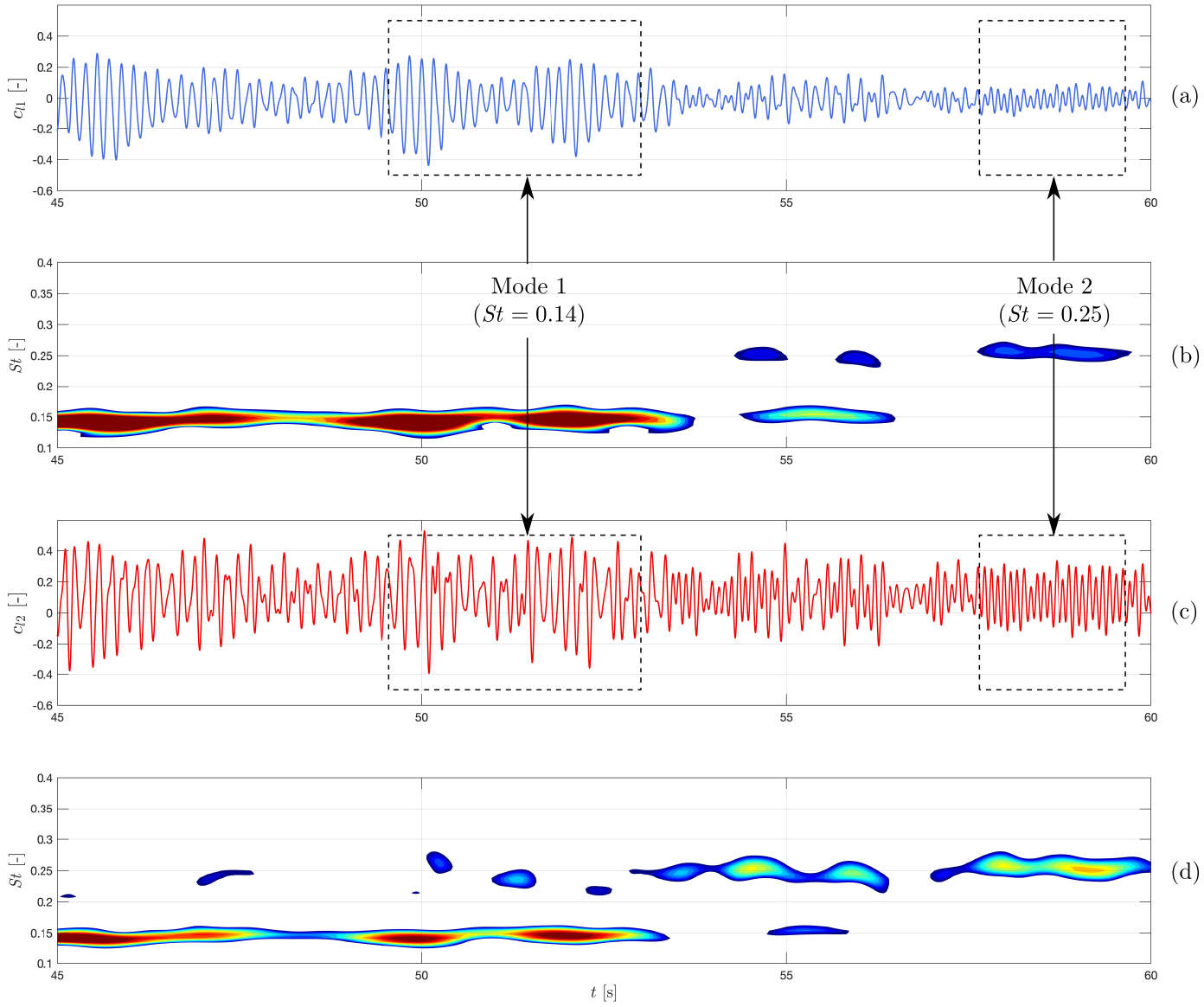

FIGURE 5.2: Time-frequency analysis of the lift coefficient of each cylinder: (a) signal c_{l1} (front), (b) wavelet norms of c_{l1}, (c) signal c_{l2} (rear) and (d) wavelet norms of c_{l2} (sub-critical: Re = 45k; $\alpha = 4°$; $L/D = 1.2$).

in the first mode than in the second one, especially for the front cylinder, while the time-averaged values do not change significantly. Another interesting observation is the phase lag between the lift coefficients of the front and rear cylinders. Figure 5.3 shows that the lift force coefficients on both cylinders are in phase in the second mode ($St = 0.25$), while they are not in phase in the first mode. For mode 1, the lift signal of the rear cylinder is characterised by a super-harmonic component. Based on these observations, it can be stated that the fluctuating mechanisms of the two modes are not the same and correspond to two distinct flow patterns.

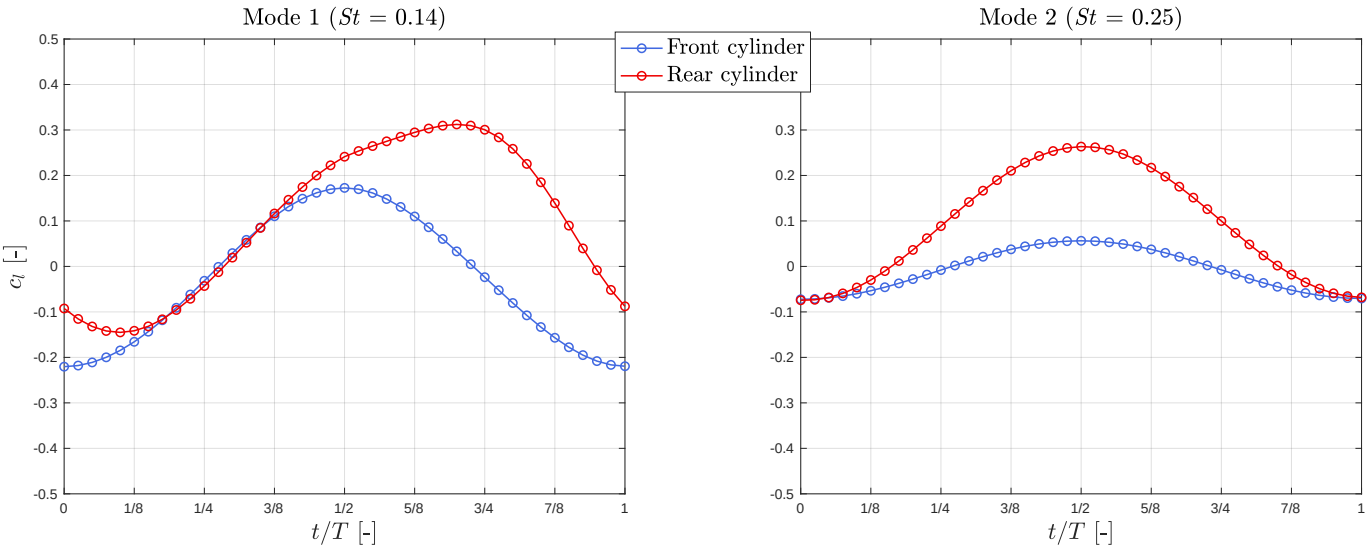

FIGURE 5.3: Phase-averaged lift coefficients of each cylinder in the identified modes for a particular configuration (sub-critical: Re = 45k; $\alpha = 4°$; $L/D = 1.2$).

Mode	Cylinder	$\bar{c}_l$	c_l'
1	Front	-0.04	0.15
	Rear	0.10	0.17
2	Front	-0.01	0.05
	Rear	0.09	0.12

TABLE 5.1: Time-averaged and fluctuating lift coefficients of each mode computed from the phase-averaged lift coefficients shown in Figure 5.3 (sub-critical: Re = 45k; $\alpha = 4°$; $L/D = 1.2$).

Phase-averaged pressure distributions

The two modes are analysed in further detail by means of the pressure coefficient distributions around the cylinders. To do so, the pressure coefficients are phase-averaged following the same procedure as previously done for the lift coefficients. Figure 5.4 shows the variation of the phase-averaged pressure distribution on each cylinder within both modes. As a reminder, $\theta > 0°$ corresponds to the lower surface of the cylinder and $\theta < 0°$ to the upper surface (see Figure 4.1). Figure 5.5 also shows sketches of the flow patterns to help the reader throughout the analysis and discussion.

The analysis first focuses on the pressure coefficient distributions at $t/T = 0$. For the front cylinder, a pressure coefficient equal to 1 is observed at $\theta \approx 4°$ in both modes (see Figure 5.4). This maximum value in the pressure coefficient distribution

corresponds to the stagnation point of the incoming flow on the front cylinder. From this particular point, the flow is divided into two parts. An upper and lower boundary layers start developing. The flow accelerates in these regions before separating at $\theta \approx -67.5°$ and 75° from the upper and lower surfaces, respectively. The lower separated shear layer from the front cylinder re-attaches onto the rear cylinder (see

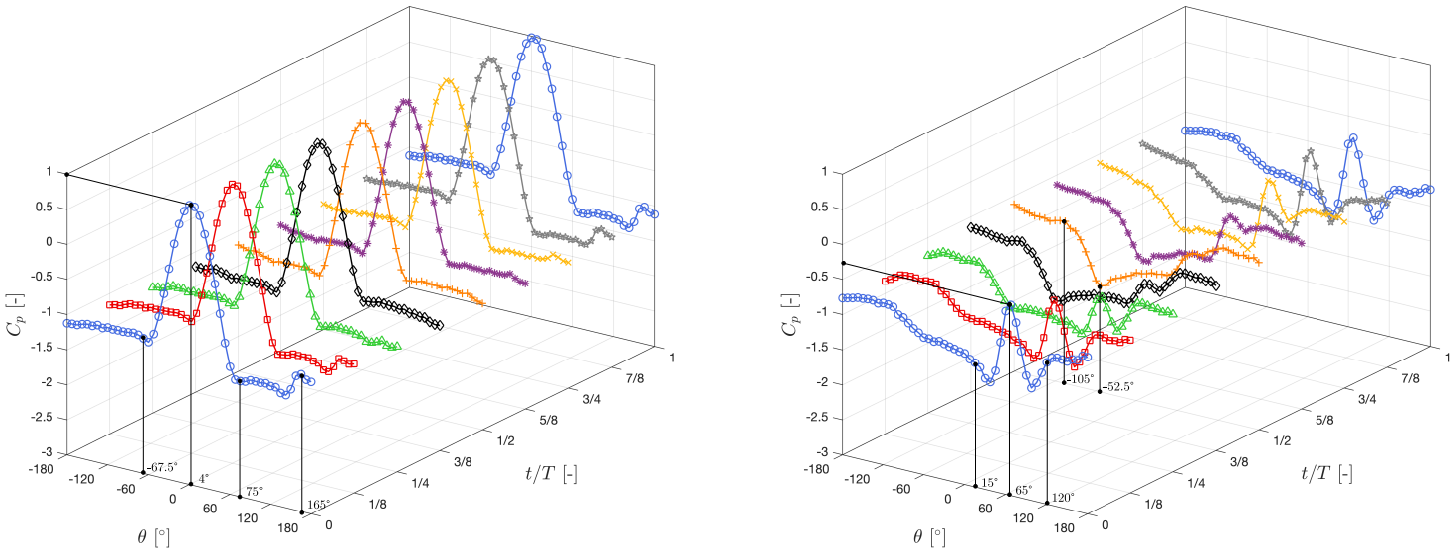

(a) Mode 1 - $St = 0.14$

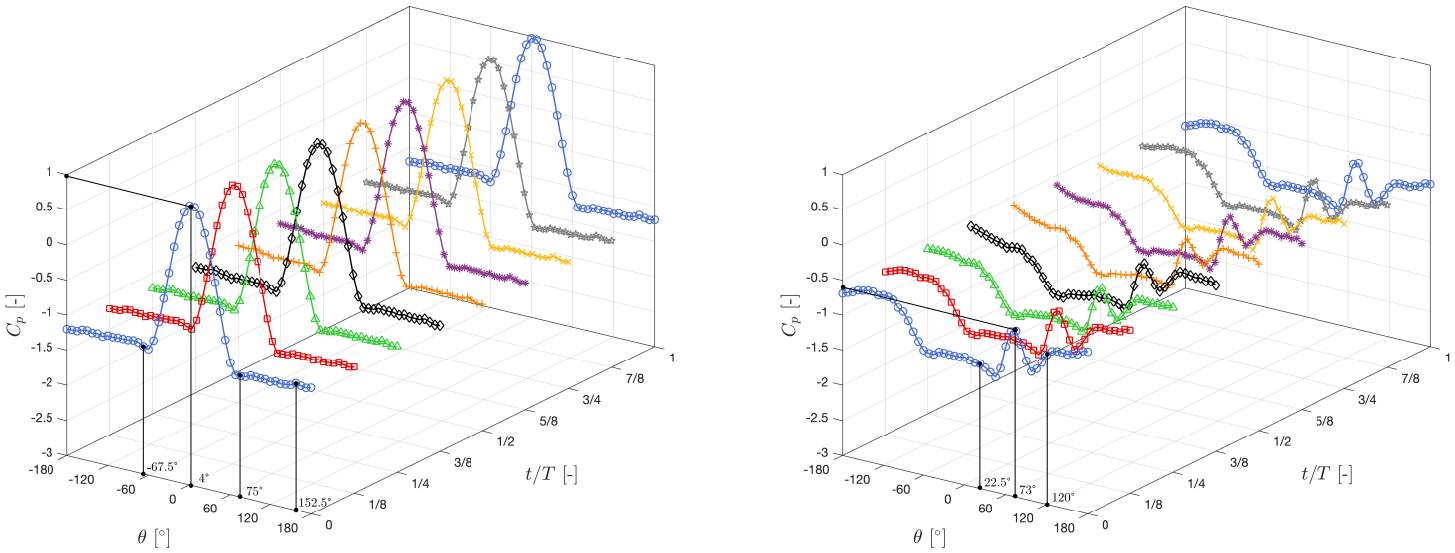

(b) Mode 2 - $St = 0.25$

FIGURE 5.4: Phase-averaged pressure coefficients around each cylinder in both modes (left: front cylinder; right: rear cylinder / sub-critical: Re = 45k; $\alpha = 4°$; $L/D = 1.2$).

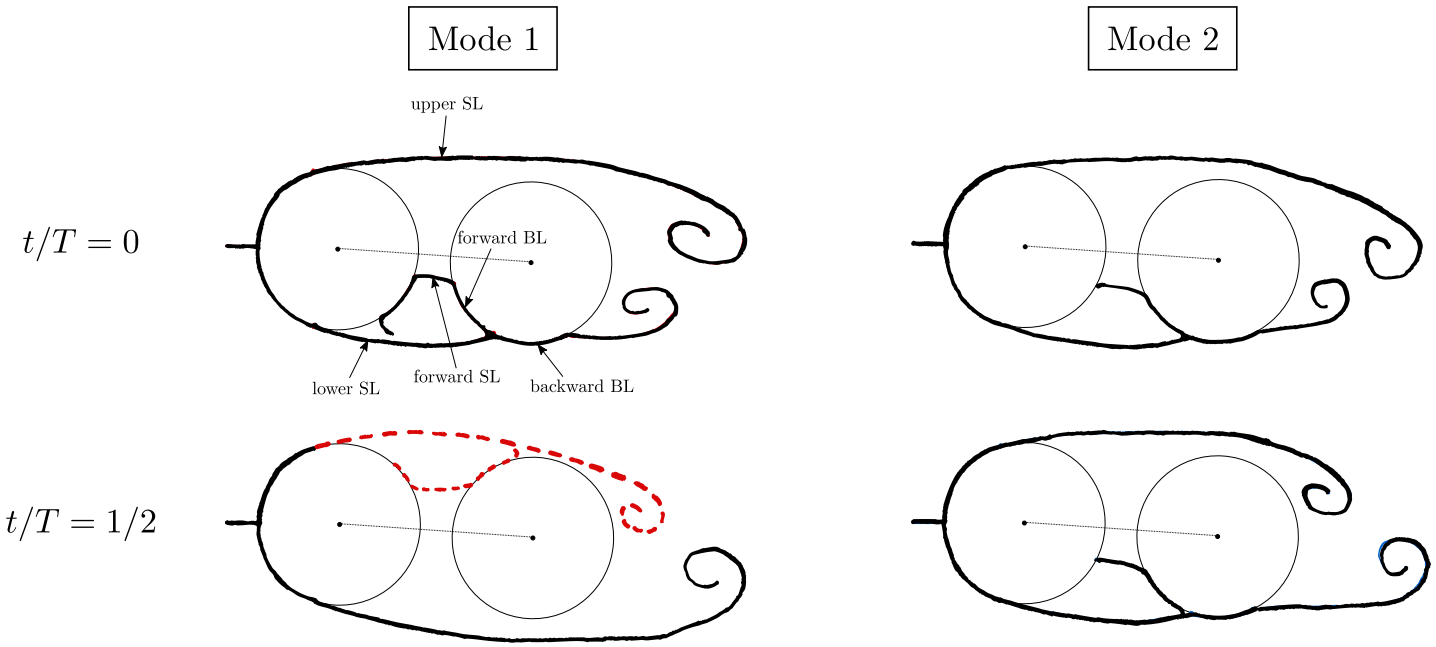

FIGURE 5.5: Flow sketches of the two modes: unclear behaviour in red dotted line (SL: shear layer; BL: boundary layer / sub-critical: Re = 45k; $\alpha = 4°$; $L/D = 1.2$).

Figure 5.5). Indeed, a local maximum value (characteristic of a re-attachment point) is observed in the pressure coefficient distribution of the rear cylinder at $\theta \approx 65°$ and 73° in modes 1 and 2, respectively. The corresponding maximum value is larger in mode 1 ($C_p \approx -0.25$) than in mode 2 ($C_p \approx -0.6$). On the other side, the upper separated shear layer from the front cylinder does not re-attach onto the rear cylinder (Figure 5.5) because no local maximum value is identified on the upper surface of the rear cylinder in either mode (Figure 5.4). The shear layer that re-attaches onto the lower surface of the rear cylinder also splits into two parts: backward and forward boundary layers, as shown in Figure 5.5. The flow accelerating in those regions leads to local minimum values in the pressure coefficient on both sides of the re-attachment point, as observed in Figure 5.4. In mode 1, the forward and backward boundary layers finally separate because of the adverse pressure gradients at $\theta \approx 15°$ and 120°, respectively. In mode 2, they respectively separate at $\theta \approx 22.5°$ and 120°. The forward separated shear layer from the rear cylinder then re-attaches onto the back face of the front cylinder (see Figure 5.5). It leads to a local maximum value in the pressure coefficient of the front cylinder at $\theta \approx 165°$ in mode 1 (see Figure 5.4(a)) and 152.5° in mode 2 (see Figure 5.4(b)). Notice that the latter local maximum value is more visible in mode 1 than in mode 2.

- Mode 1:

In mode 1 (Figure 5.4(a)), the local maximum value in the pressure coefficient of the rear cylinder, which is associated with the re-attachment point, decreases when t/T increases within the shedding cycle. It is also observed that the corresponding angular location slightly moves downstream. At $t/T = 1/2$, it disappears along with the local minimum values on both sides (Figure 5.4(a)). Based on this observation, it is stated that the lower separated shear layer from the front cylinder does not re-attach anymore onto the rear cylinder at this time instant within the shedding cycle in mode 1 (see bottom left sketch in Figure 5.5). The shear layer re-attaches back onto the lower surface of the rear cylinder at $t/T = 5/8$, as the local maximum value in the pressure coefficient distribution re-appears (see the purple curve on the right in Figure 5.4(a)). As t/T increases, the re-attachment point moves upstream, and the associated pressure coefficient increases again. This behaviour can be explained by the fact that the lower separated shear layer from the front cylinder moves downwards in the first half of the shedding cycle and, at some point, does not re-attach onto the rear cylinder anymore. In the second half of the shedding cycle, it moves upwards and re-attaches back onto the lower surface of the rear cylinder. Hence, an alternate re-attachment of the lower separated shear layer occurs onto the rear cylinder. This statement is corroborated by the fact that the re-attachment of the forward separated shear layer from the rear cylinder onto the back face of the front cylinder also disappears within the shedding cycle. Indeed, the local maximum value in the pressure coefficient at the back of the front cylinder cannot be observed when the lower separated shear layer from the front cylinder does not re-attach onto the rear cylinder (see the orange curve on the left in Figure 5.4(a)).

The analysis is more complex concerning the upper surfaces of the cylinders. It can be observed that a local minimum value in the pressure coefficient distribution of the rear cylinder appears at $\theta \approx -52.5°$ when t/T increases in the first half of the shedding cycle. A very small local maximum value is also observed at $\theta \approx -105°$. A clear physical explanation cannot be provided and the upper shear layer is therefore drawn in red dotted in Figure 5.5. Flow visualisation would be of great help in this case to identify the exact behaviour of the flow.

- Mode 2:

In mode 2 (Figure 5.4(b)), the local maximum value in the pressure coefficient of the rear cylinder ($\theta \approx 73°$) and the minimum values on both sides are always present within the entire shedding cycle. Moreover, their respective angular locations and values do not significantly vary. It is thus assumed that the lower separated

shear layer from the front cylinder always re-attaches onto the rear cylinder in this mode, and the re-attachment point only slightly moves within the shedding cycle (see sketches on the right in Figure 5.5). It corresponds to a steady re-attachment of the lower separated shear layer from the front cylinder onto the rear cylinder. It is observed in Figure 5.4(b) that the highest fluctuations of the pressure coefficient are located at the back of the rear cylinder ($|\theta| > 100°$). This observation will be more evident in the next section.

Extraction of modes from frequency contents

For the specific configuration presented above (sub-critical flow regime: Re = 45k and $\alpha = 4°$), the two modes could be decoupled by selecting two different time intervals. Unfortunately, it is not the case in the other configurations for which bi-stability is observed, as stated before. The objective of this section is thus to present a new methodology allowing the extraction and identification of the modes based on the frequency content of fluctuating pressures.

Figure 5.6 shows the spectra of the fluctuating pressure coefficients around each cylinder. The radial direction corresponds to the frequency variable, represented by the dimensionless Strouhal number, and the tangential direction refers to the angular location around the cylinders. The spectra are computed on the entire pressure signals, implying that both modes intermittently take place within the signals. Indeed, the two Strouhal numbers corresponding to the two modes are observed in Figure 5.6. Second harmonic components of the Strouhal number associated with the first mode ($St = 0.14$) are also observable. The presence of these harmonic components is attributed to the alternate re-attachment of the separated shear layer from the front cylinder onto the rear cylinder, as already stated before.

The amplitude of the PSD is associated with the energy distribution around each cylinder. The idea is to extract the energy level at specific Strouhal numbers corresponding to the two modes ($St = 0.14$ and 0.25). This procedure aims at giving an image of the fluctuating pressure coefficient distributions around the cylinders for a specific Strouhal number or, equivalently, a given mode. Figure 5.7 shows the tangential distribution of the energy associated with each mode extracted from the spectra of the pressure signals. Additionally, the fluctuating pressure distributions computed from the temporal pressure coefficients of each mode (selected time intervals in Figure 5.2) are plotted for comparison. The distributions are normalised by their corresponding maximum value on the rear cylinder. It is observed that the shape of the energy distributions compares very well with the fluctuating pressure

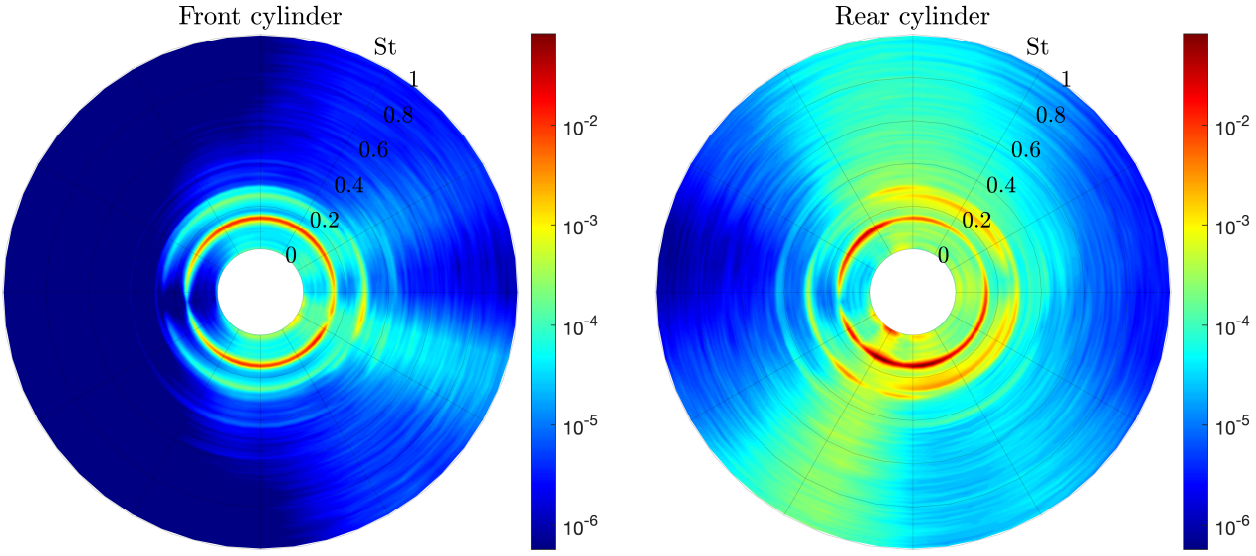

FIGURE 5.6: Frequency content of the pressure coefficients around each cylinder (sub-critical: $Re = 45$k; $\alpha = 4°$; $L/D = 1.2$).

distributions. Hence, it validates the statement above that the energy distribution around the cylinders at a specific Strouhal number corresponds to an image of the fluctuating pressure distributions of the corresponding mode. The flow dynamics of each mode is thus identified based on the frequency content of the pressure fields.

In mode 1, three peaks are present on the lower surface of the rear cylinder ($\theta > 0°$). On this cylinder, the peak at $\theta \approx 65°$ corresponds to the pressure fluctuations associated with the re-attachment point. The peaks on both sides of the re-attachment point ($\theta \approx 37.5°$ and $97.5°$) are induced by the appearance and disappearance of the backward and forward boundary layers because of the alternate re-attachment of the shear layer onto the rear cylinder (Figure 5.5). Alam et al. (2003) or Tsutsui (2012) also observed these three peaks in the fluctuating pressure distribution of the rear cylinder in case of alternate re-attachment. On the upper surface of the same cylinder ($\theta < 0°$), two peaks can be identified. The largest one is located at $\theta \approx -52.5°$, where the local minimum value appears in the pressure coefficient distribution for $1/4 < t/T < 3/4$ (see Figure 5.4(a)). The other peak is found at $\theta \approx -97.5°$. A clear physical explanation cannot be given here concerning those two peaks. Once again, it is stressed that flow visualisation would help clarifying the behaviour of the flow in this region. For the front cylinder, peaks are observed at $\theta \approx 75°$ and -67.5° in the fluctuating pressure distribution. Their location corresponds to the respective separation point of the boundary layer from the front cylinder. Two additional peaks are reported on the lower surface of the front cylinder at $\theta \approx 142.5°$ and 165°. It is assumed that the pressure fluctuations corresponding to those peaks are induced by

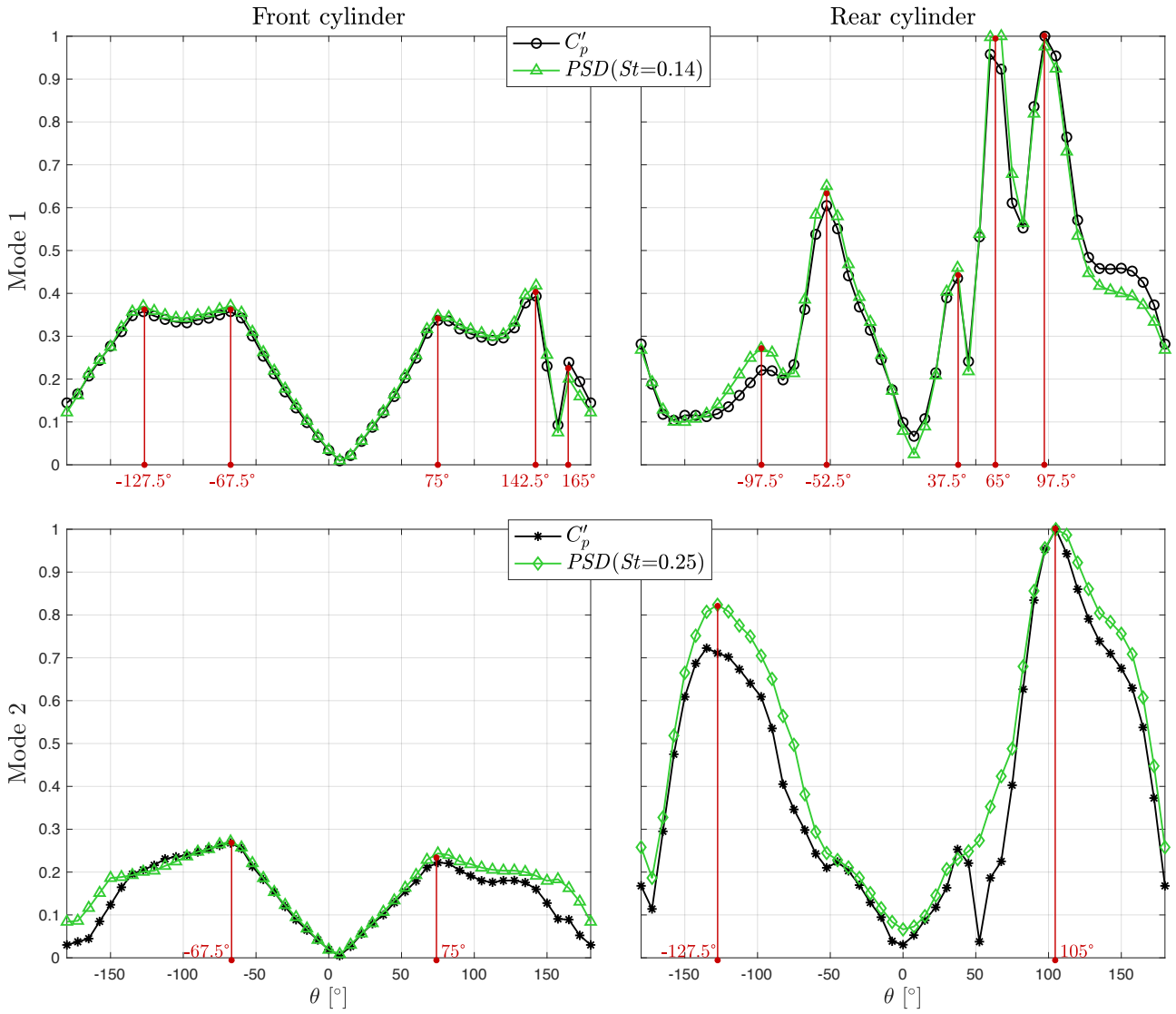

FIGURE 5.7: Extracted energy distributions of the pressure field of both modes from: (in black) time signals or (in green) *PSD* (sub-critical: Re = 45k; $\alpha = 4°$; $L/D = 1.2$).

the alternate re-attachment of the forward shear layer from the rear cylinder onto the back of the front cylinder (see Figure 5.5). A local maximum value is also observed at $\theta \approx -127.5°$ on the upper surface of the front cylinder.

In mode 2, only two peaks are observed in the fluctuating pressure distribution of the rear cylinder. One is located on the lower surface at $\theta \approx 105°$ and the other one on the upper surface at $\theta \approx -127.5°$. Fluctuations are mostly observed at the back of the rear cylinder, as noticed earlier in Figure 5.4(b). These peaks are associated with the eddy shedding behind the rear cylinder (Figure 5.5). Concerning the front cylinder, two maximum values are also observed at $\theta \approx 75°$ and -67.5° corresponding to the separation points on the lower and upper surfaces, respectively.

5.1.3 Identification of flow behaviours

The procedure presented above is applied to all the tested configurations for which no gap flow is established between the cylinders ($\alpha \leq 6°$) in the sub- and post-critical flow regimes.

Sub-critical flow regime

Figure 5.8 combines the time-averaged pressure distributions and the extracted modes for the different flow incidences in the sub-critical flow regime. To help the reader through the analysis and discussion, sketches of the identified flow patterns in the different flow incidence ranges and flow regimes are shown in Figure 5.9.

In tandem configuration ($\alpha = 0°$), it is observed that the different distributions are almost symmetric. As stated in the previous chapter, the slight asymmetry is attributed to a slight misalignment of the cylinders to the incoming free-stream inside the wind tunnel. Only mode 1 is present in this configuration, i.e., no bi-stability is observed. It shows three peaks on either the lower or upper surface of the rear cylinder (see Figure 5.8(d)). Based on the previous analysis, it is therefore stated that alternate re-attachment of the separated shear layers from the front cylinder occurs onto the lower and upper surfaces of the rear cylinder. The same conclusion has already been made in the previous chapter. When the flow incidence is increased to 2°, the asymmetry switches side: the maximum fluctuating pressure is now located on the lower surface of the rear cylinder (see Figure 5.8(d)). Three peaks in the fluctuating pressure distribution are still observed on either side of the rear cylinder (see Figure 5.8(d)), meaning that both shear layers from the front cylinder alternately re-attach onto the rear cylinder. Moreover, it can be assessed that the re-attachment of the upper separated shear layer is shorter in time and, hence, weaker than the lower shear layer. It leads to reduced fluctuating pressures around the corresponding re-attachment point. This analysis confirms the statement made before concerning the flow behaviour within this range of flow incidences: the separated shear layers from the front cylinder alternately re-attach onto the rear cylinder for $\alpha = 0°$ and 2° in the sub-critical flow regime and the associated Strouhal number is equal to 0.14. This flow pattern is sketched in Figure 5.9(a).

The configuration with $\alpha = 4°$ has already been analysed and discussed in the previous section. Because of the presence of a bi-stability, two modes can be extracted at $St = 0.14$ and 0.25, respectively. In mode 1, the lower separated shear layer from the front cylinder alternately re-attaches onto the lower surface of the rear cylinder while

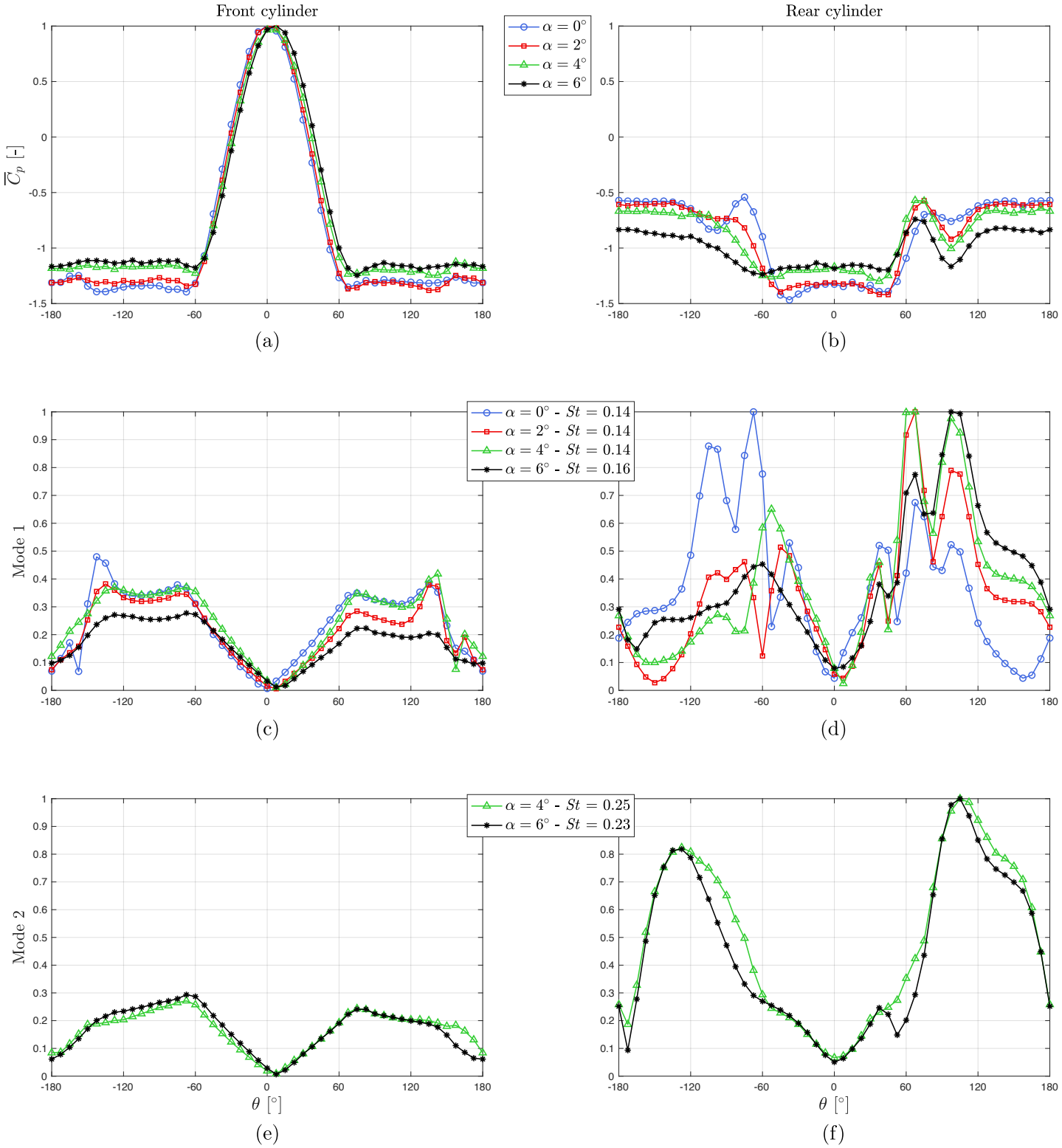

FIGURE 5.8: Time-averaged pressure coefficients and fluctuating modes around each cylinder at different flow incidences in the sub-critical flow regime (Re = 45k; $L/D = 1.2$).

the behaviour of the upper separated shear layer remains unexplained (red dotted line in Figure 5.9(b)). In mode 2, the lower separated shear layer always re-attaches onto the rear cylinder. On the other hand, the upper separated shear layer does not re-attach and rolls up to form an eddy behind the rear cylinder. The high pressure fluctuations are mostly located on the back face of the rear cylinder, where eddies are shed. The corresponding flow pattern is sketched in Figure 5.9(c). At $\alpha = 6°$, a bi-stability also exists (see Figure 5.1(c-d)) and the associated Strouhal numbers are 0.16 and 0.23. Mode 2, associated with $St = 0.23$, is very similar in shape in comparison to the second mode at $\alpha = 4°$ (see Figure 5.8(e-f)). Based on this observation, it can be stated that the flow pattern is the same: the lower separated shear layer from the front cylinder always re-attaches onto the rear cylinder while the upper shear layer does not re-attach and rolls up behind the rear cylinder where eddies are alternately shed from both sides (Figure 5.9(c)). The decrease of the associated Strouhal number between $\alpha = 4°$ and 6° may be attributed to a widening of the wake due to the increase of the frontal area of the twin-cylinder configuration. Mode 1, associated with $St = 0.16$, is more difficult to analyse. Three peaks in the distribution of fluctuating pressure are still present on the lower surface of the rear cylinder. The larger peak is not associated with the re-attachment point anymore but with the backward boundary layer (see Figure 5.8(d)). The peak on the upper surface of the same cylinder, observed at $\theta \approx -52.5°$ for $\alpha = 4°$, has slightly moved downstream to $\theta \approx -60°$ at $\alpha = 6°$.

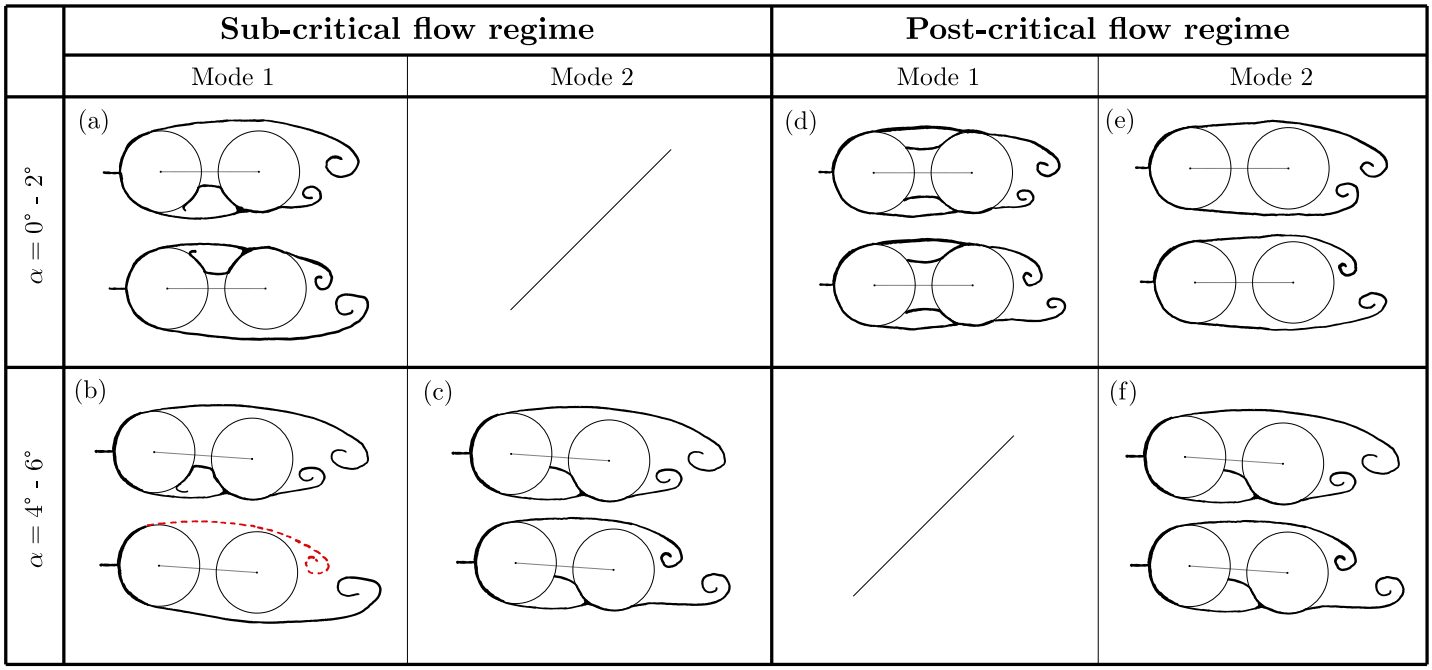

FIGURE 5.9: Sketches of the flow patterns identified at different flow incidences in the sub- and post-critical flow regimes: unclear behaviour in red dotted line.

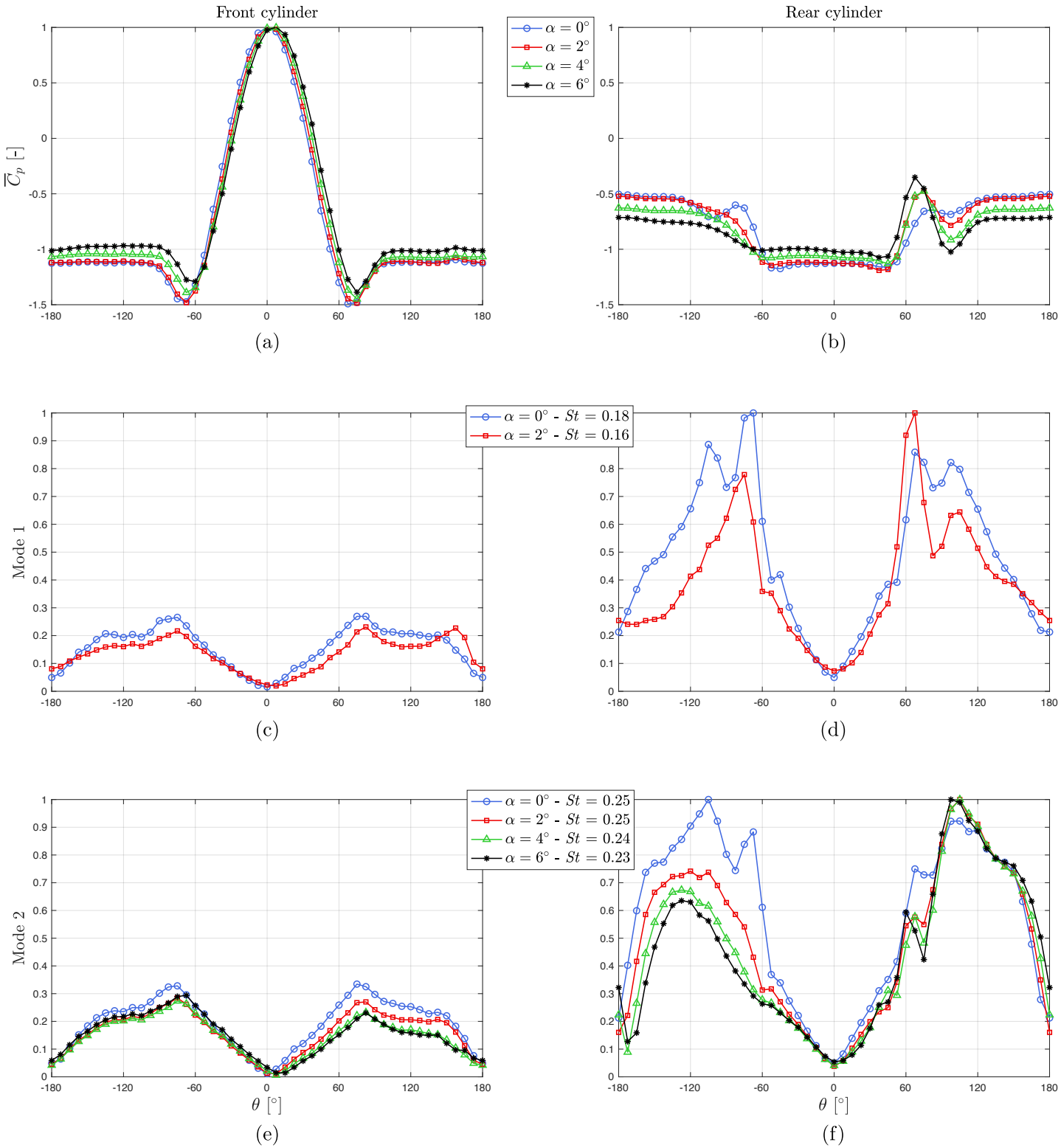

FIGURE 5.10: Time-averaged pressure coefficients and fluctuating modes around each cylinder at different flow incidences in the post-critical flow regime (Re = 275k; $L/D = 1.2$).

Post-critical flow regime

Figure 5.10 shows the time-averaged pressure distributions and the extracted modes for the different flow incidences in the post-critical flow regime. In this regime, mode 1 (associated with the lowest Strouhal number) only occurs for $\alpha = 0°$ and 2° since bi-stability is observed in this range of flow incidences (see Figure 5.1(e-f)). For the tandem configuration ($\alpha = 0°$), it was concluded that this mode corresponds to the steady re-attachment of the separated shear layers from the front cylinder onto the rear cylinder (see Figure 5.9(d)). Similarly, it is stated that the same flow behaviour occurs in this mode when the wind incidence is increased to 2° (see Figure 5.10(c-d)).

The second mode (associated with the highest Strouhal number) occurs for all flow incidences before the appearance of the gap flow, as shown in Figures 5.1(e-f) and 5.10(e-f). For the tandem configuration, it was stated that this mode corresponds to the extended-body flow pattern, meaning that the separated shear layers do not re-attach onto the rear cylinder (Figure 5.9(e)). This statement was based on the work about tandem cylinders made by Igarashi (1984). When the flow incidence increases, the lower separated shear layer does re-attach onto the rear cylinder (Figure 5.9(f)), and the fluctuating pressure distributions of mode 2 are very similar to the ones of the second mode observed in the sub-critical flow regime (see Figures 5.8(e-f) and 5.10(e-f)). The Strouhal number associated with mode 2 decreases with the flow incidence. Similarly to the sub-critical flow regime, this decrease may be explained by the widening of the wake due to the increase of the frontal area of the twin-cylinder configuration.

5.1.4 Gap flow between the cylinders

Figure 5.11 shows the time-averaged pressure coefficients around each cylinder when the strong gap flow is established at $\alpha = 8°$ and 10°. A sketch of the gap flow is also shown in Figure 5.12 to facilitate the understanding of the analysis once again. Note that the wake behaviour is not represented (e.g., no eddy) because a clear peak cannot be identified in the frequency content of the lift coefficients (Figure 5.1(c-f)). The main observation concerns the difference in the pressure distributions between the sub- and post-critical flow regimes, especially in the gap between the cylinders.

In both flow regimes, a stagnation point ($\overline{C}_p = 1$) is identified on the lower surface of the rear cylinder at $\theta \approx 45°$ in Figure 5.11(b,d). From this stagnation point, the flow divides into two parts: a backward and forward boundary layer. The flow in the forward boundary layer accelerates to large velocities, leading to lower pressure values. Depending on the flow incidence, the pressure coefficient reaches a minimum value

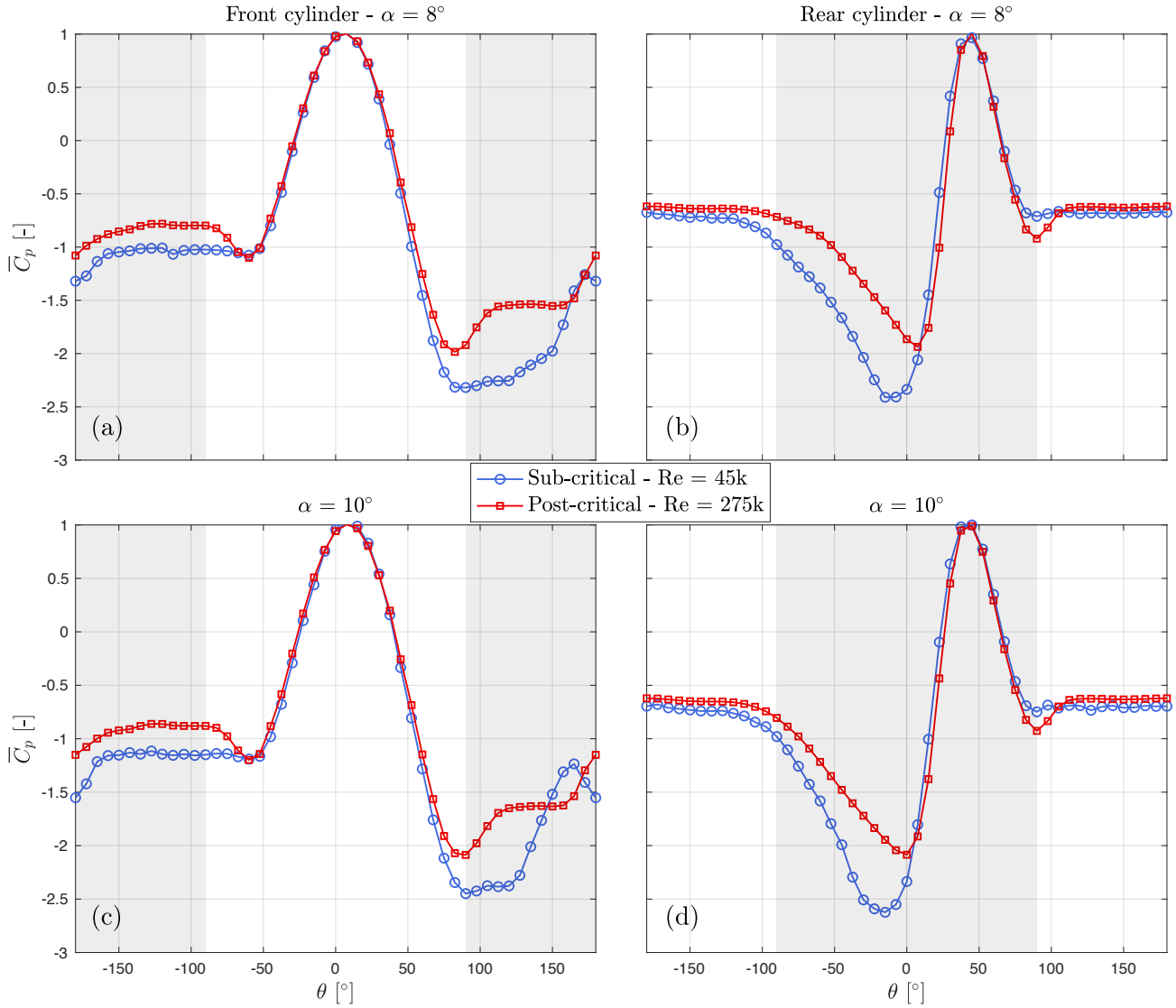

FIGURE 5.11: Time-averaged pressure coefficients around each cylinder with the occurrence of a gap flow ($\alpha = 8°$ and 10°) in the sub- and post-critical flow regimes (inter-cylinder region is shown as grey zones).

of -2.4–2.6 and -1.9–2.1 in the sub- and post-critical flow regimes, respectively. The minimum value is followed by a large pressure recovery, leading to the separation of the boundary layer. The flow in the backward boundary layer also accelerates, but to lower velocities, and then separates because of the adverse pressure gradient. It is observed that the pressure recovery before separation is larger in the post-critical flow regime than in the sub-critical one. This phenomenon is due to the difference in state of flow in the boundary layer before separation: laminar and turbulent in the sub- and post-critical flow regimes, respectively.

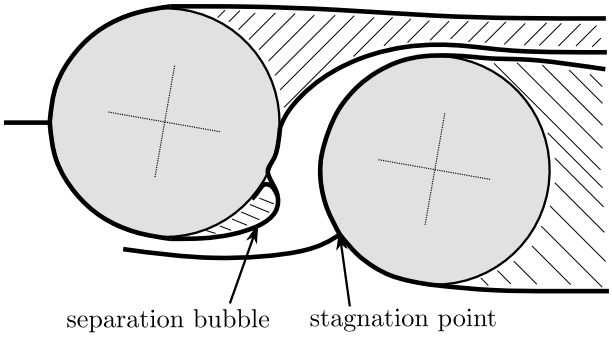

(a) Sub-critical ($Re = 45$k)

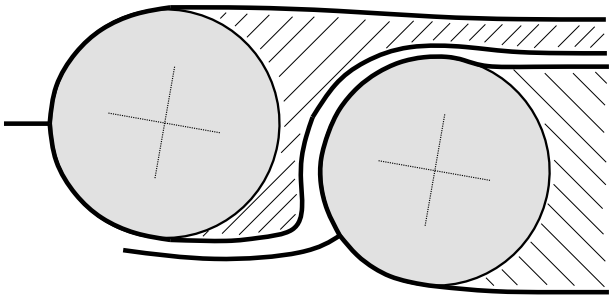

(b) Post-critical ($Re = 275$k)

FIGURE 5.12: Sketch of the gap flow between the two cylinders.

The upper boundary layer on the front cylinder separates at $\theta \approx -67.5°$ and -75° in the sub- and post-critical flow regimes, respectively. In the sub-critical flow regime, the lower boundary layer first separates at $\theta \approx 100°$, followed by a short plateau in the pressure coefficient distribution (see Figure 5.11(a,c)). This short plateau is characteristic of a separation bubble: the separated shear layer re-attaches onto the surface of the front cylinder. Unfortunately, the exact angular location associated with this re-attachment is difficult to identify. It is followed by a pressure recovery up to $\theta \approx 172.5°$ or 165° whether the flow incidence is 8° or 10°, respectively. After this particular angular location, the flow accelerates as the pressure coefficient decreases up to $\theta \approx 180°$ and then it eventually separates from the surface of the front cylinder after another pressure recovery. In the post-critical flow regime, a plateau in the pressure coefficient distribution is also observed following the separation of the lower boundary layer from the front cylinder. This plateau is large in comparison with the one observed in the sub-critical flow regime ($120° < \theta < 160°$). Moreover, no local peak in pressure distribution is observed on the back face of the front cylinder. Hence, the shear layer going through the gap between the cylinders does not re-attach onto the front cylinder in the post-critical flow regime. The plateau in pressure coefficient is most likely due to a quasi-stationary eddy. It is then followed by a second pressure

recovery through the centreline between the cylinders ($\theta \approx 180°$). The flow patterns identified in the two flow regimes are shown in Figure 5.12. The difference is thus the occurrence of a separation bubble on the front cylinder in the sub-critical flow regime (Figure 5.12(a)), while it is not the case in the post-critical regime (Figure 5.12(b)). This difference explains why the time-averaged lift coefficients take larger absolute values in the sub- than in the post-critical regime, as pointed out above in Figure 5.1.

5.2 Investigation of the ($L/D - \alpha$) plane

As stated at the beginning of the chapter, a thorough investigation has been performed for cylinders distant of $L/D = 1.2$. The analysis is now extended to the other tested spacing ratios with the objective to obtain a general classification of the flow patterns around two cylinders in a given range of values in the ($L/D - \alpha$) plane. For the sake of conciseness, only the main outcomes or new observations of the analysis are reported in this section. However, the reader should keep in mind that the same methodology as described previously for $L/D = 1.2$ is followed to analyse the flow for other spacing ratios.

5.2.1 New type of bi-stable flow

A new type of bi-stability appears when increasing the spacing ratio. It is highlighted in Figure 5.13, showing temporal drag and lift coefficients of both cylinders for $\alpha = 10°$ and $L/D = 1.8$ in the post-critical flow regime. The bi-stability differs from the one observed earlier in section 5.1.2 by the significant change in the time-averaged value of the force coefficients. Those values are reported in Table 5.2. Hence, this type of bi-stability corresponds to an intermittent switch from one time-averaged flow to another. On the other hand, the bi-stability investigated earlier for $L/D = 1.2$ is due to the intermittent switch from one fluctuating behaviour to another, while conserving the same time-averaged flow (Table 5.1).

Flow	**Cylinder**	$\overline{c}_l$	$\overline{c}_d$
A	Front	-0.03	1.03
	Rear	0.64	-0.08
B	Front	-0.12	1.00
	Rear	0.46	0.14

TABLE 5.2: Time-averaged lift and drag coefficients of each flow highlighted in Figure 5.13 (post-critical: Re = 275k; $\alpha = 10°$; $L/D = 1.8$).

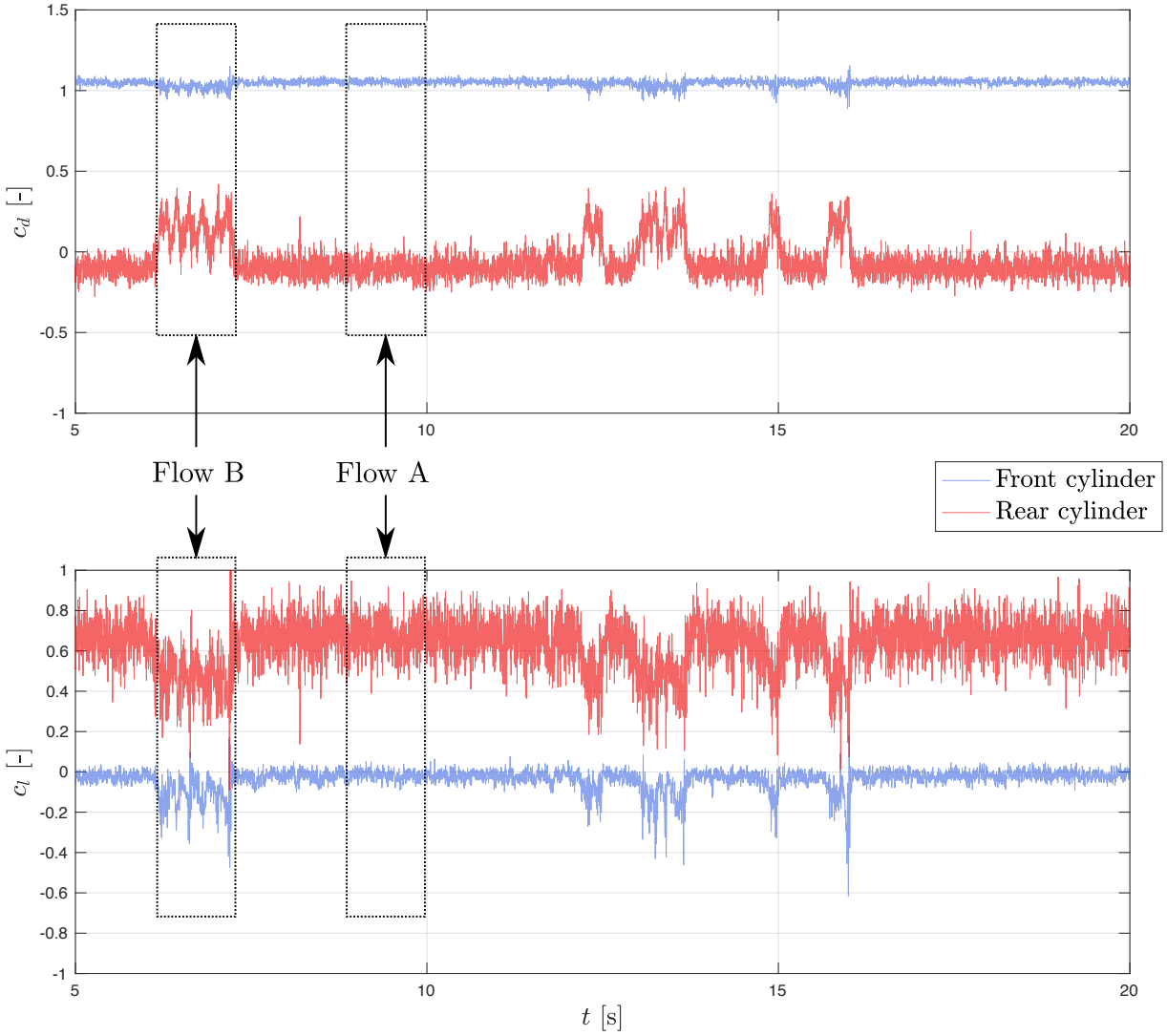

FIGURE 5.13: Signals of the drag and lift coefficients of both cylinders at $\alpha = 10°$ and $L/D = 1.8$ in the post-critical regime ($Re = 275$k).

The two distinct flows of the present bi-stability can be easily decoupled from the time signals, as shown in Figure 5.13. The resulting time-averaged pressure distributions around the two cylinders for each flow are plotted in Figure 5.14. It is observed that the pressure coefficient on the rear cylinder reaches a value of 1 at $\theta \approx 37.5°$, corresponding to the stagnation point, in both flows. It reveals the establishment of a gap flow (entrainment of a small amount of the free-stream) between the two cylinders. It is observed that the pressure distribution downstream of the stagnation point ($\theta > 45°$) is very similar in both flows. It means that the separation of the backward boundary layer, which develops downstream of the stagnation point, occurs at the same angular location in flow A or flow B. The main difference between the two flows is found on the upper front surface of the rear cylinder (-90°$< \theta <$ 0°). It is

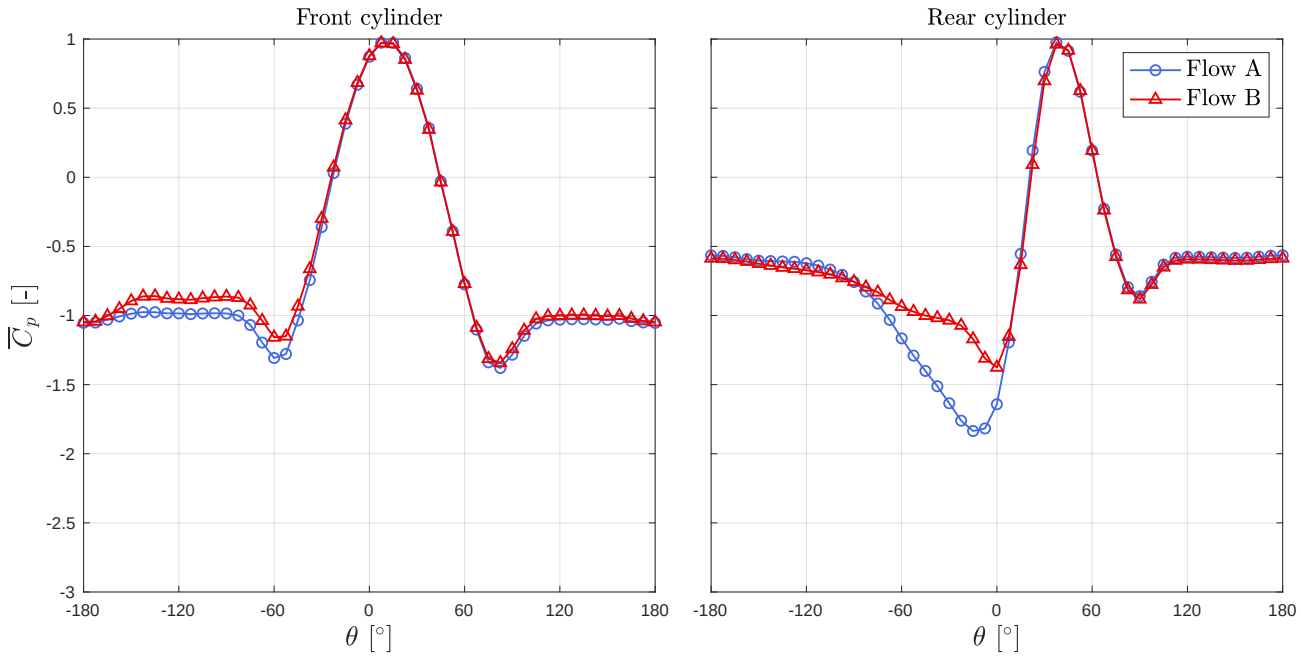

FIGURE 5.14: Time-averaged pressure coefficient distributions on both cylinders at $\alpha = 10°$ and $L/D = 1.8$ in the post-critical regime ($Re = 275$k).

observed that flow A leads to a minimum value of -1.9 (at θ = -15°) while it is equal to -1.4 (at θ = 0°) for flow B.

Alam, Sakamoto, and Zhou (2005) observed the same bi-stable nature of flow in the sub-critical flow regime with similar pressure distributions on the rear cylinder. With the help of surface oil-flow visualisations, they could identify that the separation of the forward boundary layer developing from the stagnation point occurs earlier in flow B than in flow A. In other words, the forward boundary layer sweeps along the surface of the rear cylinder for a longer peripheral length in flow A, which leads to a higher suction pressure (the flow is more accelerated). This change of flow behaviour in the gap between the cylinders also impacts the flow on the upper surface of the front cylinder ($\theta < 0°$). Figure 5.14 shows that the pressures in this region are larger in flow B than in flow A. Figure 5.15 shows schematics of the two identified flows to help visualise the differences stated above.

The same type of bi-stability is observed for other particular configurations ($L/D - \alpha$) in the post-critical flow regime. On the other hand, all bi-stabilities identified in the sub-critical flow regime – whatever the configuration ($L/D - \alpha$) – correspond to a change of the fluctuating process, like the one analysed in the previous sections, meaning that the time-averaged flow does not change significantly.

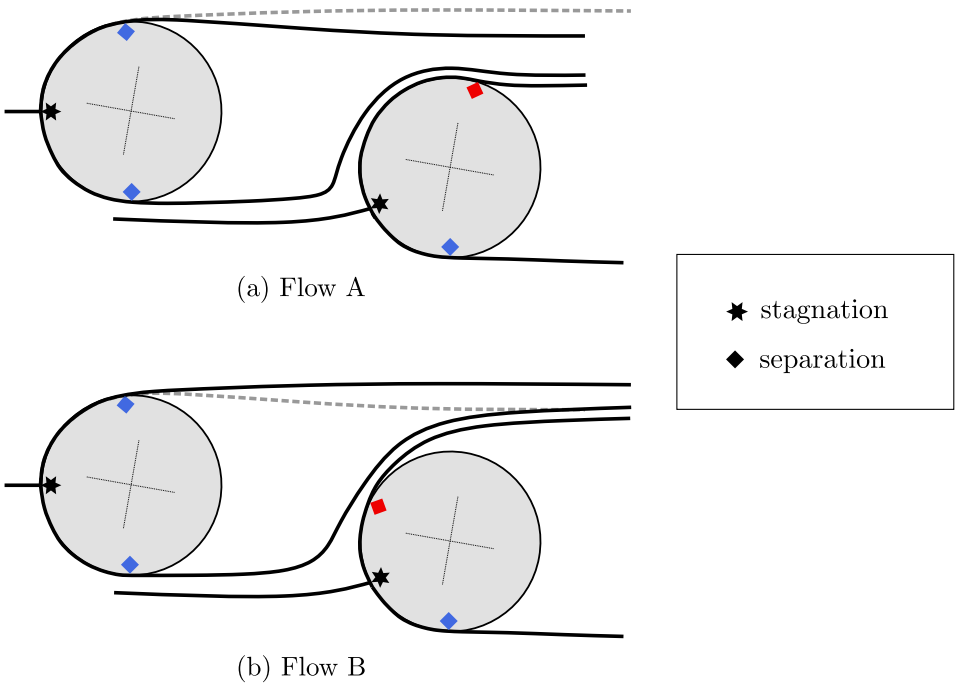

FIGURE 5.15: Schematics of the flow around two cylinders at $\alpha = 10°$ and $L/D = 1.8$ in the post-critical regime ($Re = 275$k).

5.2.2 General classification of flow patterns

After a thorough investigation of the aerodynamic forces and pressure fields on the two cylinders, 8 distinct flow patterns have been identified in the sub- and post-critical flow regimes.

Schematics of the flow patterns are shown in Figure 5.16. The different flow patterns are basically identified based on the behaviour of the separated shear layers from the front cylinder:

(i) The two separated shear layers may not completely re-attach onto the rear cylinder. It leads to the first flow pattern, *No Re-attachment* (NR).

(ii) One or two separated shear layer(s) may re-attach onto the rear cylinder, and the respective *one-sided* or *two-sided* re-attachment may either alternate (AR1 or AR2) or remain steady (SR1 or SR2).

(iii) One separated shear layer may completely go through the gap between the cylinders. It leads to the occurrence of a strong gap flow (entrainment of free-stream between the cylinders). Three different types of gap flow can be identified:

- GF1: the separated shear layer, which goes through the gap, is forced to re-attach onto the back face of the front cylinder, and the forward boundary layer on the rear cylinder, which develops from the stagnation point, separates at the back of the cylinder.
- GF2: the separated shear layer, which goes through the gap, does not re-attach onto the back face of the front cylinder anymore, and the flow around the rear cylinder remains similar to flow pattern GF1. It corresponds to Flow A, shown in the previous section.
- GF3: the forward boundary layer on the rear cylinder separates earlier (on the front face) from the surface compared to flow pattern GF2. It corresponds to Flow B, shown in the previous section.

The occurrence of a flow pattern or the other highly depends on the location in the $(L/D - \alpha)$ plane and the flow regime. Classification maps of the occurrence of the different flow patterns in the $(L/D - \alpha)$ plane are presented in Figure 5.17 for the sub- and post-critical regimes. The dots in the maps represent the different configurations that have been tested during the wind tunnel campaign. Based on that, it should be emphasised that the boundaries separating one flow pattern/behaviour from the other are not perfectly defined in the $(L/D - \alpha)$ plane. Nonetheless, it has the merit of roughly showing how the flow dynamics evolves as a function of L/D and α.

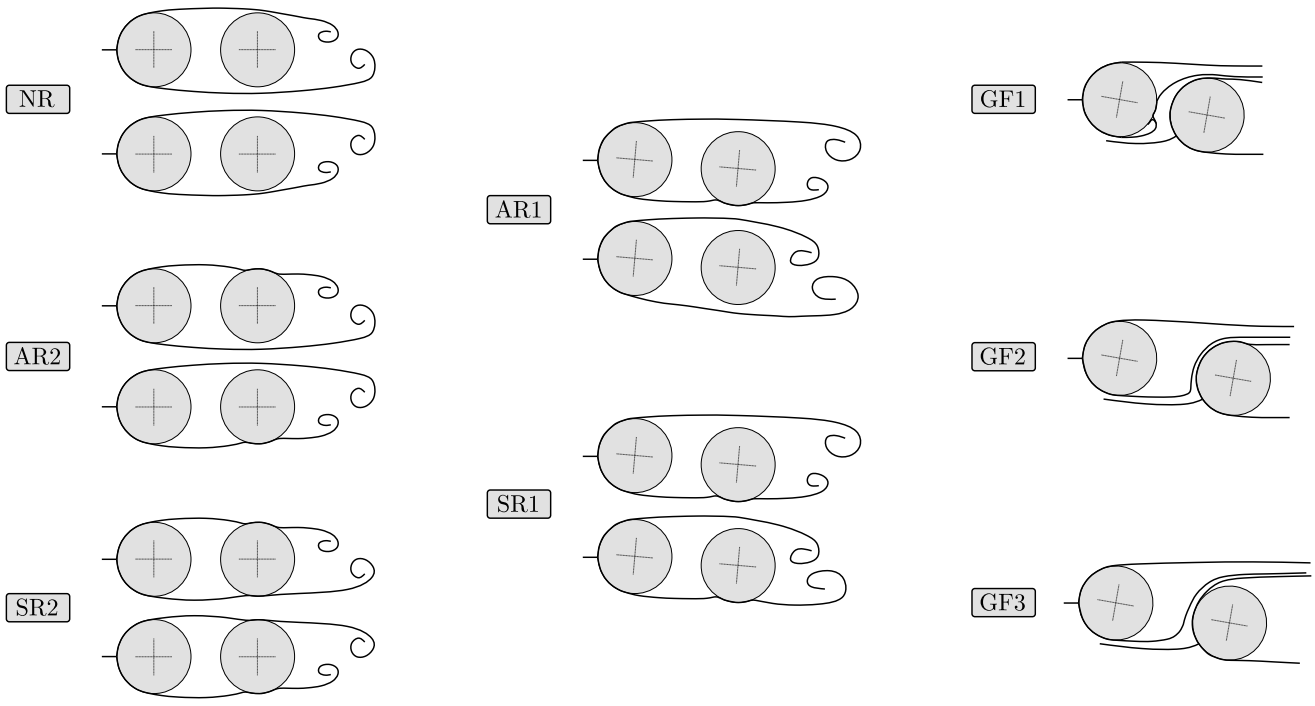

FIGURE 5.16: Schematics of the distinct flow patterns around the two cylinders identified in the sub- and/or post-critical regimes.

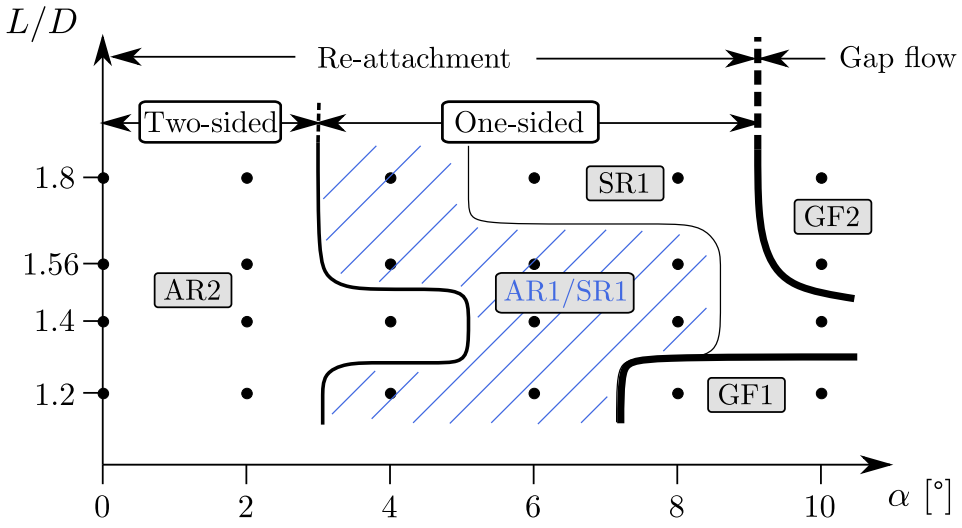

(a) Sub-critical ($Re = 45$k)

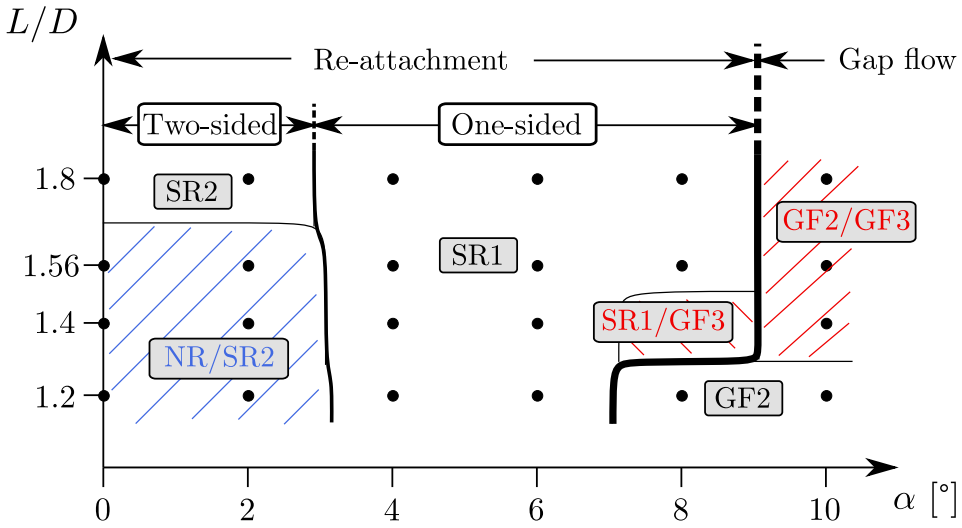

(b) Post-critical ($Re = 275$k)

FIGURE 5.17: Classification of the flow patterns defined in Figure 5.16 around the two cylinders in the $(L/D - \alpha)$ plane in the (a) sub- and (b) post-critical regimes (the hatched zones report bi-stable behaviours of the flow: (in blue) first type and (in red) second type; the dots represent the different tested configurations).

In Figure 5.17, the hatched zones correspond to regions where a bi-stability is observed. The first type of bi-stability – intermittent switch from one fluctuating behaviour to the other characterised by different Strouhal numbers – and the second one – intermittent switch from one time-averaged flow to the other characterised by different force coefficients – are reported in blue and red, respectively.

- **Sub-critical flow regime** (Figure 5.17(a)):

  At low flow incidence, the flow pattern AR2 occurs for each spacing ratio: the two shear layers from the front cylinder alternately re-attach onto the rear cylinder. This finding was already obtained for the tandem arrangement in the previous chapter. As the flow incidence increases, a bi-stable flow is observed between the flow patterns AR1 and SR1: the re-attachment occurs onto one side of the rear cylinder only and may be either alternate or steady. This behaviour was discussed in detail when analysing the flow around the two cylinders with $L/D = 1.2$. It is interesting to note that the flow becomes bi-stable at $\alpha = 4°$ for each L/D except for $L/D = 1.4$, where it is observed at $\alpha = 6°$. It is believed that the flow between the cylinders is strongly unstable for this particular spacing ratio and therefore the large fluctuations of the separated shear layers lead to their re-attachment on both sides for larger flow incidences. This explanation is supported by the observation of a local maximum value in the fluctuating lift coefficient of the front cylinder at $L/D = 1.4$ in the tandem arrangement (see Figure 4.6). When the flow incidence is increased further, the bi-stability disappears and only the flow pattern SR1 is observed. It is identified at $\alpha = 6°$ and $8°$ for $L/D = 1.8$ and at $\alpha = 10°$ for $L/D = 1.4$. Finally, a strong gap flow is established between the two cylinders at the largest tested flow incidences. It is observed that the gap flow appears between $\alpha = 8°$ and $10°$ for $L/D \geq 1.56$ while it appears between $\alpha = 6°$ and $8°$ for $L/D = 1.2$. It is also noticed that the gap flow is not occurring for $L/D = 1.4$. For $L/D = 1.2$, the flow pattern GF1 is observed: the separated shear layer which goes through the gap re-attaches at the back of the front cylinder. This induces a strong acceleration of the flow between the cylinders and creates an asymmetry in the flow, leading to a large non-zero value of the lift coefficients. For $L/D = 1.56$ and 1.8, the flow pattern GF2 is observed: the separated shear layer does not re-attach onto the front cylinder anymore. It results in a reduction of the absolute value of the time-averaged lift coefficients, especially on the front cylinder.

- **Post-critical flow regime** (Figure 5.17(b)):

  At low flow incidence, the flow has a bi-stable nature for $L/D \leq 1.56$. The two separated shear layers intermittently re-attach onto the rear cylinder and the flow pattern switches from NR to SR2. It must be pointed out that for $L/D = 1.2$ the flow pattern NR is the most dominant one, but as the spacing ratio increases, SR2 becomes more dominant. Only the flow pattern SR2 is observed when the spacing ratio is increased to $L/D = 1.8$. The unstable and stable natures of the flow for $L/D \leq 1.56$ and $L/D = 1.8$, respectively,

were already analysed for the tandem arrangement in the previous chapter. As the flow incidence is increased, the flow remains stable for all spacing ratios. The corresponding flow pattern is SR1 — irrespective of the value of L/D — which means that one shear layer from the front cylinder steadily re-attaches onto the rear cylinder while the other one does not. A bi-stability is observed at $\alpha = 8°$ for $L/D = 1.4$. In this particular configuration, the separated shear layer which re-attaches onto the cylinder sometimes completely goes through the gap between the cylinders. It results in the occurrence of a gap flow. Thus, the flow pattern is mostly SR1 but sometimes switches to GF3. Similarly to the sub-critical flow regime, a strong gap flow is established between the cylinders at the largest tested flow incidences, but in this case, for all spacings. Again, it is observed that the gap flow appears at $\alpha = 8°$ and 10° for $L/D = 1.2$, while it appears at $\alpha = 10°$ for $L/D \geq 1.4$. Moreover, the nature of the flow is bi-stable for $L/D \geq 1.4$ and the flow pattern switches from GF2 to GF3. As a reminder, those flow patterns differ from each other by the behaviour of the forward boundary layer on the rear cylinder: it separates earlier in GF3 compared to GF2. For $L/D = 1.2$, the flow pattern is GF2 when a gap flow is established.

An additional statement has to be made on the boundaries shown in Figure 5.17. The reader may believe by analysing the maps that the flow pattern might switch from one to the other at a given value of α or L/D. However, the switching process is most likely taking place within a specific range of values of these parameters in which an unstable nature between the flow patterns occurs. It explains the existence of the bi-stabilities reported in Figure 5.17, but the latter are not exhaustive. This comment on the switching process between flow patterns was already discussed and emphasised by Gu and Sun (1999).

A comment must also be addressed concerning the duration of measurements when assessing the occurrence of bi-stability. Indeed, the duration of the signals has to be long enough to allow the switching from one stable state to the other one in case of bi-stability. In the present work, the measurement time is set to 61.44 seconds. In the sub-critical flow regime (Re = 45k), it implies that 366 or 655 shedding cycles are measured with a Strouhal number of 0.14 or 0.25, respectively. In the post-critical flow regime (Re = 275k), 2230 or 3982 shedding cycles are respectively measured. One can thus wonder if the measurement time is sufficiently long to ensure the observation of bi-stability, especially in the sub-critical flow regime. Longer measurements in time would have increased the probability to observe bi-stability (if it exists), but it was not done unfortunately.

The discussion above on the classification of flow patterns around the two cylinders as a function of $(L/D - \alpha)$ in the sub- and post-critical flow regimes reveals the sensitivity and complexity of the flow around twin cylinders. Hence, the aerodynamic quantities ($\overline{c}_d$, $\overline{c}_l$, c'_l, St, etc.) are also highly dependent on L/D, α and the flow regime. The highly non-linear behaviour of the flow can lead to fluid-structure instabilities. Additionally, it must be kept in mind that the vibrations of the two cylinders may favour the occurrence of one particular flow pattern over the others. Indeed, the structural vibrations can be considered as disturbances on the flow dynamics, as discussed in Chapter 2 when introducing the influencing parameters.

Chapter 6

Aeroelastic behaviours of twin cylinders

The flow around two static cylinders has been thoroughly investigated up to now. In this chapter, we consider the flexibility of the structure and analyse the aeroelastic responses of twin cylinders, which is ultimately the main objective of this doctoral thesis. Physical explanations are given based on the flow physics identified around static cylinders in the previous chapters. An extensive experimental campaign is first performed to identify the potential aeroelastic instabilities. The possibility to mathematically model the observed phenomena is then investigated.

6.1 Introduction

Because of the flexibility of the structure, new important parameters have to be defined when dealing with dynamic aeroelastic phenomena. Indeed, the fluid-structure interaction strongly depends on the structural properties in addition to the fluid and flow characteristics.

From a mathematical point of view, an aeroelastic system is represented in the form

$$\mathbf{M}\ddot{\mathbf{y}} + \mathbf{C}\dot{\mathbf{y}} + \mathbf{K}\mathbf{y} = \mathbf{f}_a(U_\infty, \dot{\mathbf{y}}, \mathbf{y}) + \mathbf{f}_e(U_\infty) \tag{6.1}$$

where $\mathbf{y}$ is the displacement vector of the structure and the operator $\dot{(\,)}$ denotes the time derivative. The matrices $\mathbf{M}$, $\mathbf{C}$ and $\mathbf{K}$ represent the structural properties of the system in terms of mass, damping and stiffness, respectively. The right-hand side terms of equation (6.1) correspond to the aerodynamic excitation. The term $\mathbf{f}_a(U_\infty, \dot{\mathbf{y}}, \mathbf{y})$ denotes the aeroelastic loads acting on the structure, which depend on the flow velocity U_∞ and the motion of the structure $(\dot{\mathbf{y}}, \mathbf{y})$. The term $\mathbf{f}_e(U_\infty)$ denotes the external forces that are independent of the structural motion, such as the buffeting loads due to the turbulent components of the incoming free-stream.

In a still fluid ($U_\infty = 0$), the structural dynamics can conveniently be described by its modal properties:

- natural frequency(ies) f_0 [Hz],
- damping ratio(s) ζ [-],
- structural mass per unit length m_s [kg/m].

For a structure composed of two identical cylinders, the aeroelastic response is a function of the parameters describing the characteristics of the flow (U_∞), the fluid (ρ and μ) and the structure (D, L, α, m_s, f_0 and ζ). In a general form, we have the following relation

$$\mathbf{y}(t) = \text{function}\big(\rho, \mu, U_\infty, D, L, \alpha, m_s, f_0, \zeta\big). \tag{6.2}$$

Using Buckingham-π theorem, the dimensionless form of the same relation is obtained and reads

$$\mathbf{Y}(\tau) = \text{Function}\big(Re, L/D, \alpha, U_r, m_r, \zeta\big) \tag{6.3}$$

where the new dimensionless parameters are

- the *dimensionless time*:
$$\tau = \omega_0 t = 2\pi f_0 t, \tag{6.4}$$
- the *reduced velocity*:
$$U_r = \frac{U_\infty}{f_0 D}, \tag{6.5}$$
- the *mass ratio*:
$$m_r = \frac{m_s}{m_f} = \frac{m_s}{\rho \pi D^2/4}, \tag{6.6}$$
m_f being the mass per unit length of the displaced fluid.

In fluid-structure interaction, the damping and mass ratios are usually combined to obtain the well-known *Scruton number*:

$$Sc = \pi^2 m_r \zeta = \frac{4\pi m_s \zeta}{\rho D^2}. \tag{6.7}$$

Assuming a harmonic motion of each cylinder when an aeroelastic instability occurs, the structural response can be written

$$y_1(t) = A_1 \sin(2\pi f_s t), \tag{6.8a}$$
$$y_2(t) = A_2 \sin(2\pi f_s t + \phi), \tag{6.8b}$$

where A_i is the amplitude of vibration of the ith cylinder, f_s is the common structural frequency and ϕ is the phase lag between the motions of the two cylinders. Hence, the structural response may be described by the following dimensionless variables: A_i/D, f_s/f_0 and ϕ, which depend on the dimensionless parameters defined above (see equation (6.3)).

6.2 Experimental set-up

The first part of this chapter is dedicated to the experimental investigation of the flow-induced vibrations of slightly staggered twin cylinders. The wind tunnel tests are performed in low-turbulent conditions ($T_i < 0.2\%$).

The experimental aeroelastic model is shown in Figure 6.1. It consists of two cylinders supported by flexible elements. Parts of the static set-up (see Figure 4.2) are kept: the end-plates at both extremities of the cylinders are used to clamp the flexible elements, allowing to vary the spacing ratio L/D by means of new pre-defined fixation holes. The investigated spacing ratios L/D are 1.2, 1.4, 1.56 and 1.8, as previously. The set-up is still mounted on the turn-table to accurately adjust the initial flow incidence. Once the desired value of flow incidence is reached, the rotation of the upper end-plate connected to the ceiling through a ball bearing is blocked to avoid spurious oscillations.

Both cylinders are hollow, made of PVC, with an external diameter $D = 0.125$ m and span length $S = 1.25$ m. Each cylinder is supported by four extension springs so that it vibrates with a rigid-body motion. A close-up view of the extension springs, which correspond to the flexible elements of the set-up, is shown in Figure 6.2. Their installation on the set-up is designed so that they operate in the crosswise direction with respect to the centreline between the cylinders, as shown in Figure 6.3. Although the cylinders are free to oscillate along the 6 degrees of freedom, the resulting motion due to the interaction with the flow is mainly in the spring-operating direction. The extension springs have a linear range of motion up to 3.2 cm, leading to a maximum amplitude of vibration A/D of 12.5%. Beyond this maximum value, structural non-linearities appear in the system. All the wind tunnel tests are thus performed by ensuring to remain in the linear range of motion.

The surface of the cylinders is covered with sandpaper P40 ($k/D = 6.7 \times 10^{-3}$) to reach the post-critical flow regime before the occurrence of aeroelastic instabilities. The choice of this roughness level is based on the thorough investigation reported in Chapter 3.

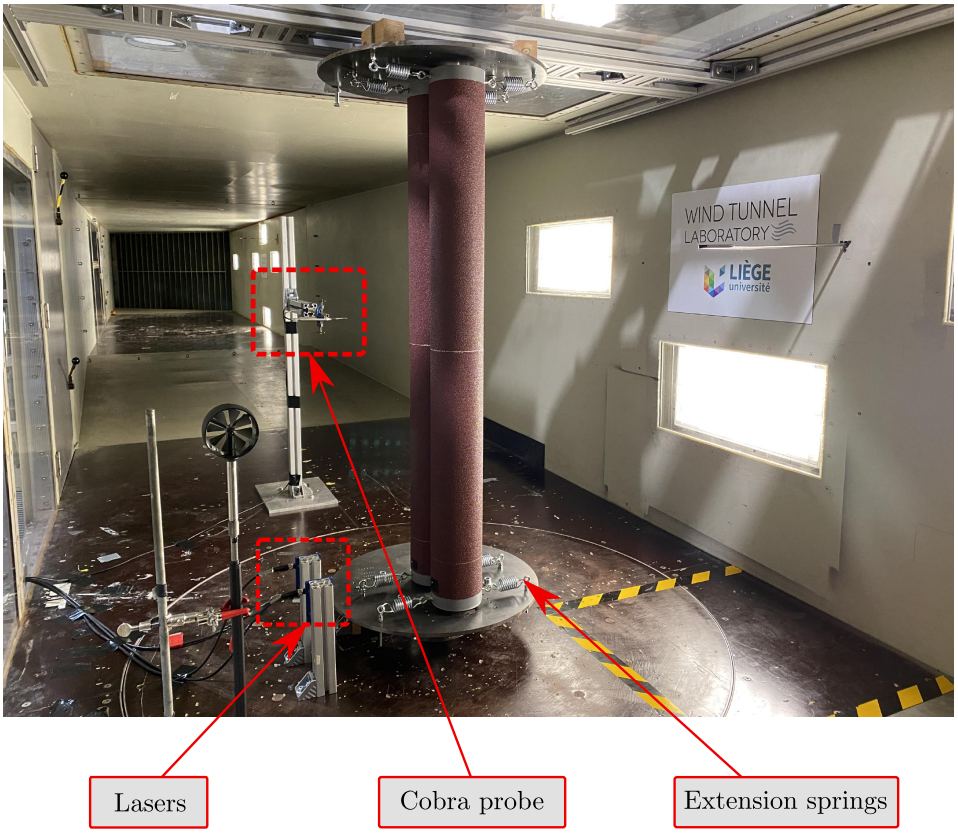

FIGURE 6.1: Experimental aeroelastic model installed in the wind tunnel of ULiège.

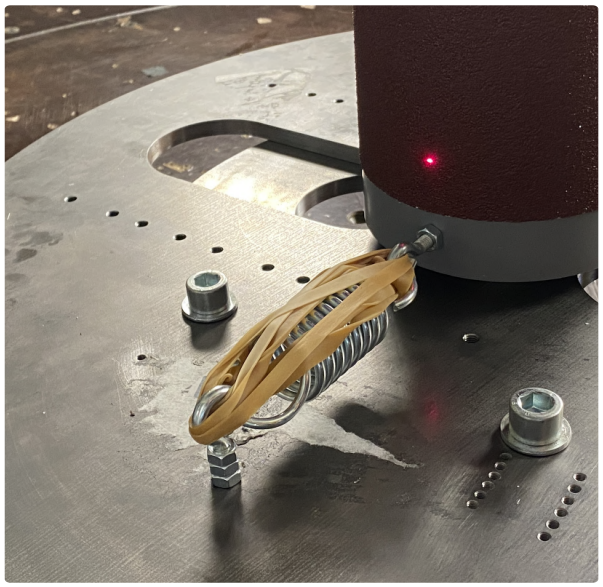

FIGURE 6.2: Flexible element of the aeroelastic model: extension spring with the addition of elastomers.

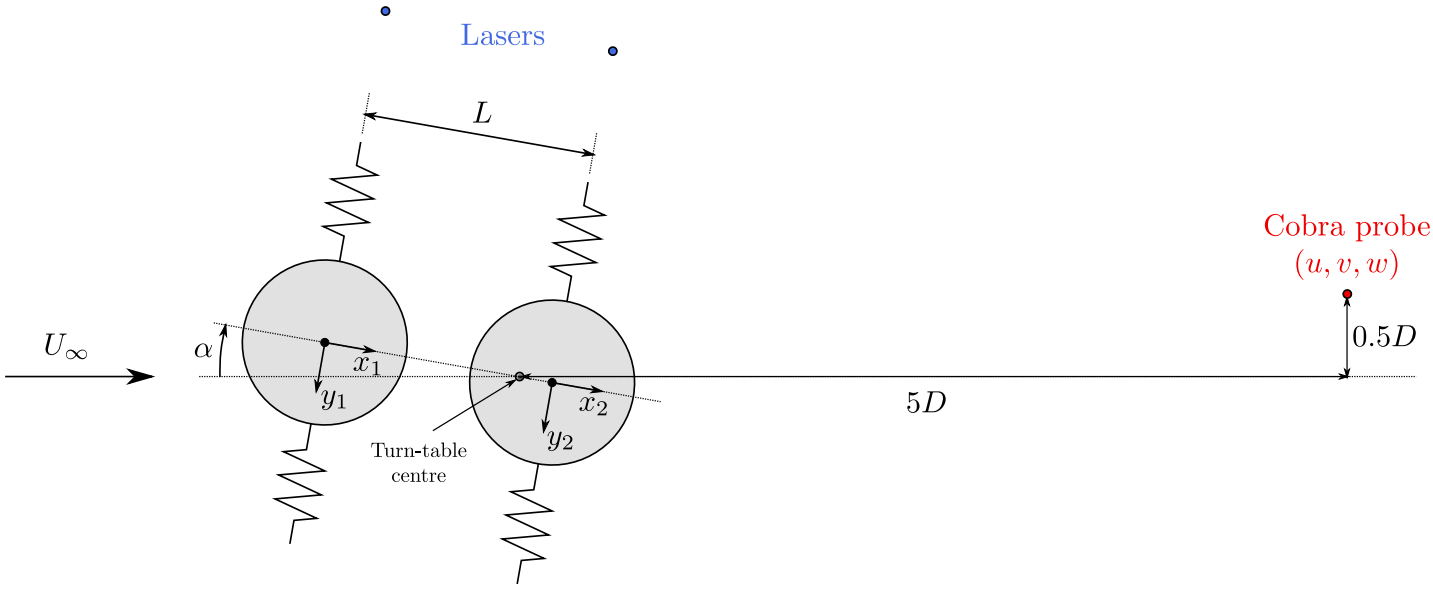

FIGURE 6.3: Schematic of the experimental set-up and definition of parameters.

Figure 6.2 shows that elastomers are added to the extension springs. It allows for a change in the value of the structural damping ratio ζ. The latter is an important parameter when dealing with aeroelastic phenomena. It must be emphasised that the addition of elastomers also slightly increases the structural stiffness and, hence, the natural frequencies of the system (see Appendix A).

The displacements of the front and rear cylinders y_1 and y_2 are measured using laser distance sensors (OD2-P300W200IO, from SICK), capable of resolving a displacement of 0.1 μm. Additionally, a Cobra probe (from Turbulent Flow Instrumentation Pty Ltd) is placed behind the twin-cylinder arrangement, as shown in Figures 6.1 and 6.3. The Cobra probe measures the three components of the flow velocity at its location and, hence, gives access to the frequency content of the wake. The sampling frequency and duration of each measurement are set to 1 kHz and 20 seconds, respectively.

6.3 Characteristics of the structure

An extensive modal analysis with six accelerometers and an impact hammer is first performed to identify the modal characteristics of the structure in a still fluid. The experimental set-up is shown in Figure 6.4, in which the sandpaper is not present to ease the installation of accelerometers on the cylinders. The removal of sandpaper leads to a change of mass in the system: the total vibrational mass of each cylinder M

FIGURE 6.4: Picture of the experimental set-up to perform the modal analysis of the structure.

decreases from 2.582 kg to 2.146 kg. Hence, the resulting natural frequencies of the system are higher in comparison with rough cylinders.

During the test campaign, it was observed that the two cylinders have a slight mechanical coupling: the vibrations of one cylinder induce vibrations of the other one. This mechanical coupling is expected since the two cylinders have an identical natural frequency and are supported on a flexible structure. A transfer of energy is observed between the cylinders when generating an impulse on them, as shown in Figure 6.5. Consequently, two peaks are observed in the frequency response function at very close frequencies. An example is shown in Figure 6.6. From the measurements, the following modal properties are identified:

- **Mode 1**: $f_{01} = 21.3$ Hz and $\zeta_1 = 0.33\%$;
- **Mode 2**: $f_{02} = 21.5$ Hz and $\zeta_2 = 0.20\%$.

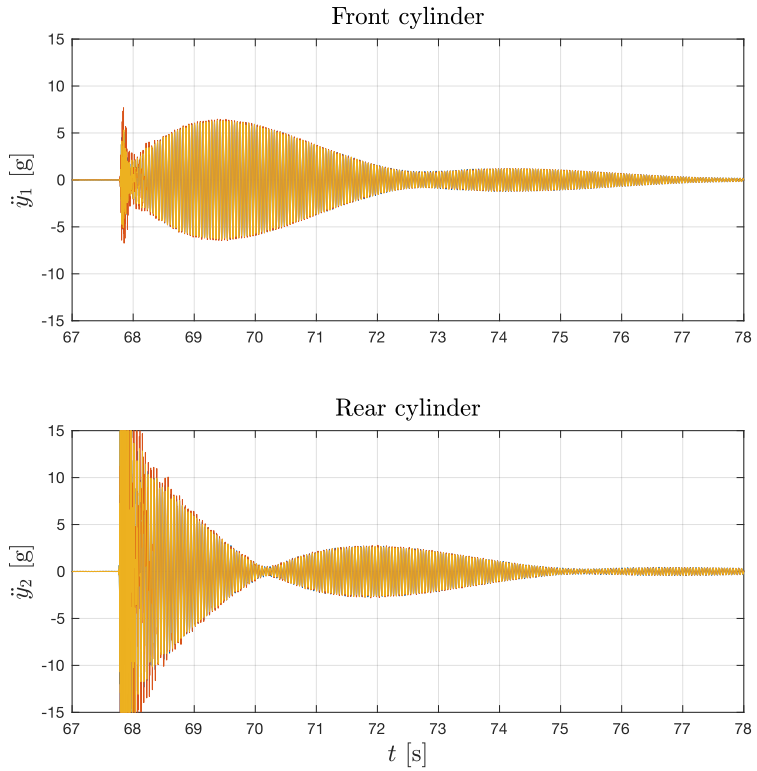

FIGURE 6.5: Signals of accelerations of both cylinders measured during the extensive modal tests (impact on rear cylinder at mid-span).

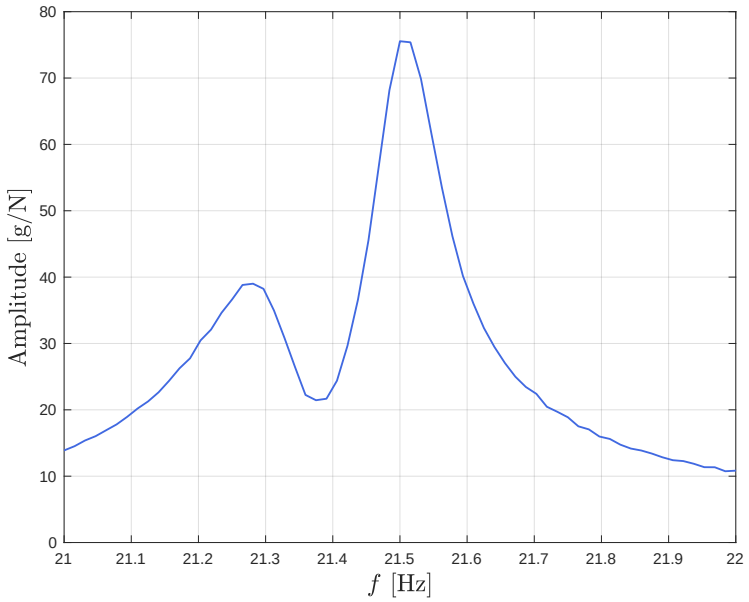

FIGURE 6.6: Frequency Response Function (FRF) of the front cylinder when exciting the same cylinder.

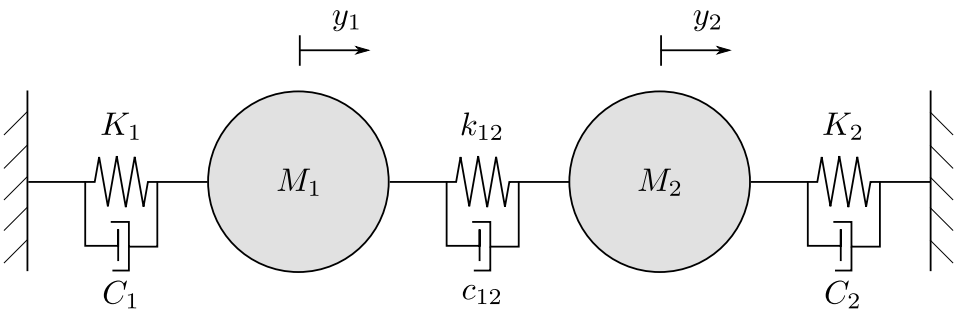

FIGURE 6.7: Schematics of the mathematical model of the structure.

The structural system of two cylinders, which are mechanically coupled, is sketched in Figure 6.7. In this representation, it is assumed that the mass, damping and stiffness are identical for the two cylinders ($M_1 = M_2 = M$, $C_1 = C_2 = C$ and $K_1 = K_2 = K$). This assumption is supported by the fact that the two cylinders have identical modal properties when tested independently. The corresponding equations of motion are written as

$$M\ddot{y}_1 + C\dot{y}_1 + Ky_1 = -k_{12}(y_1 - y_2) - c_{12}(\dot{y}_1 - \dot{y}_2), \tag{6.9a}$$
$$M\ddot{y}_2 + C\dot{y}_2 + Ky_2 = -k_{12}(y_2 - y_1) - c_{12}(\dot{y}_2 - \dot{y}_1). \tag{6.9b}$$

Making use of the following change of variables $\varphi_1 = y_1 + y_2$ and $\varphi_2 = y_1 - y_2$, the two following uncoupled equations of motion are obtained

$$M\ddot{\varphi}_1 + C\dot{\varphi}_1 + K\varphi_1 = 0, \tag{6.10a}$$
$$M\ddot{\varphi}_2 + (C + 2c_{12})\dot{\varphi}_2 + (K + 2k_{12})\varphi_2 = 0, \tag{6.10b}$$

which can further be re-written as

$$\ddot{\varphi}_1 + 2\zeta_1\omega_{01}\dot{\varphi}_1 + \omega_{01}^2\varphi_1 = 0, \tag{6.11a}$$
$$\ddot{\varphi}_2 + 2\zeta_2\omega_{02}\dot{\varphi}_2 + \omega_{02}^2\varphi_2 = 0 \tag{6.11b}$$

where

$$\omega_{01} = \sqrt{K/M}, \tag{6.12a}$$
$$\zeta_1 = C/2\omega_{01}M, \tag{6.12b}$$
$$\omega_{02} = \sqrt{(K + 2k_{12})/M}, \tag{6.12c}$$
$$\zeta_2 = (C + 2c_{12})/2\omega_{02}M. \tag{6.12d}$$

The procedure of identification is then to (i) measure the mass M, (ii) identify the modal properties ω_{0i} and ζ_i, and (iii) compute the values of K, C, k_{12} and c_{12} through the following relations obtained from equations (6.12):

$$K = \omega_{01}^2 M, \tag{6.13a}$$

$$C = 2\zeta_1 \omega_{01} M, \tag{6.13b}$$

$$k_{12} = (\omega_{02}^2 - \omega_{01}^2) M/2, \tag{6.13c}$$

$$c_{12} = (\zeta_2 \omega_{02} - \zeta_1 \omega_{01}) M. \tag{6.13d}$$

The following values are finally identified (without elastomer):

$$\begin{aligned} K &= 38449 \text{ [N/m]}, \\ C &= 1.8958 \text{ [N.s/m]}, \\ k_{12} &= 364.5 \text{ [N/m]}, \\ c_{12} &= -0.368 \text{ [N.s/m]}. \end{aligned}$$

In this work, it is assumed that the addition of elastomers on the extension springs (Figure 6.2) only modifies the values of K and C, while k_{12} and c_{12} remain the same. This assumption is relevant for the structural coupling values introduced in the structural model (dimensionless quantities). But, it was not checked experimentally.

Modal test during aeroelastic campaign

During the aeroelastic test campaign, the modal properties (ω_0, ζ) of both cylinders are determined at wind-off conditions for each configuration (L/D, α, number of elastomers) from laser measurements. The modal test consists in generating an impulse on the cylinder at mid-span in the crosswise direction to excite the mode of interest, and the free response of the structure is measured, as shown in Figure 6.8(a). It is performed by blocking the displacement of the other cylinder to avoid the beating phenomenon due to the mechanical coupling investigated above. The natural frequency is extracted from the frequency content of the displacement signal (Figure 6.8(c)), and the associated damping ratio is calculated from the free decay responses. Figure 6.8(b) shows the free-decaying amplitude of vibrations with time: the blue curve is the extracted amplitude from the measurements, while the red curve is a decaying exponential fit to the former. A logarithmic decrement δ is thus identified, and the damping ratio can be estimated as $\zeta = (\delta/2\pi)/\sqrt{1 + (\delta/2\pi)^2}$. The values obtained by following this methodology for each configuration are reported in Appendix A.

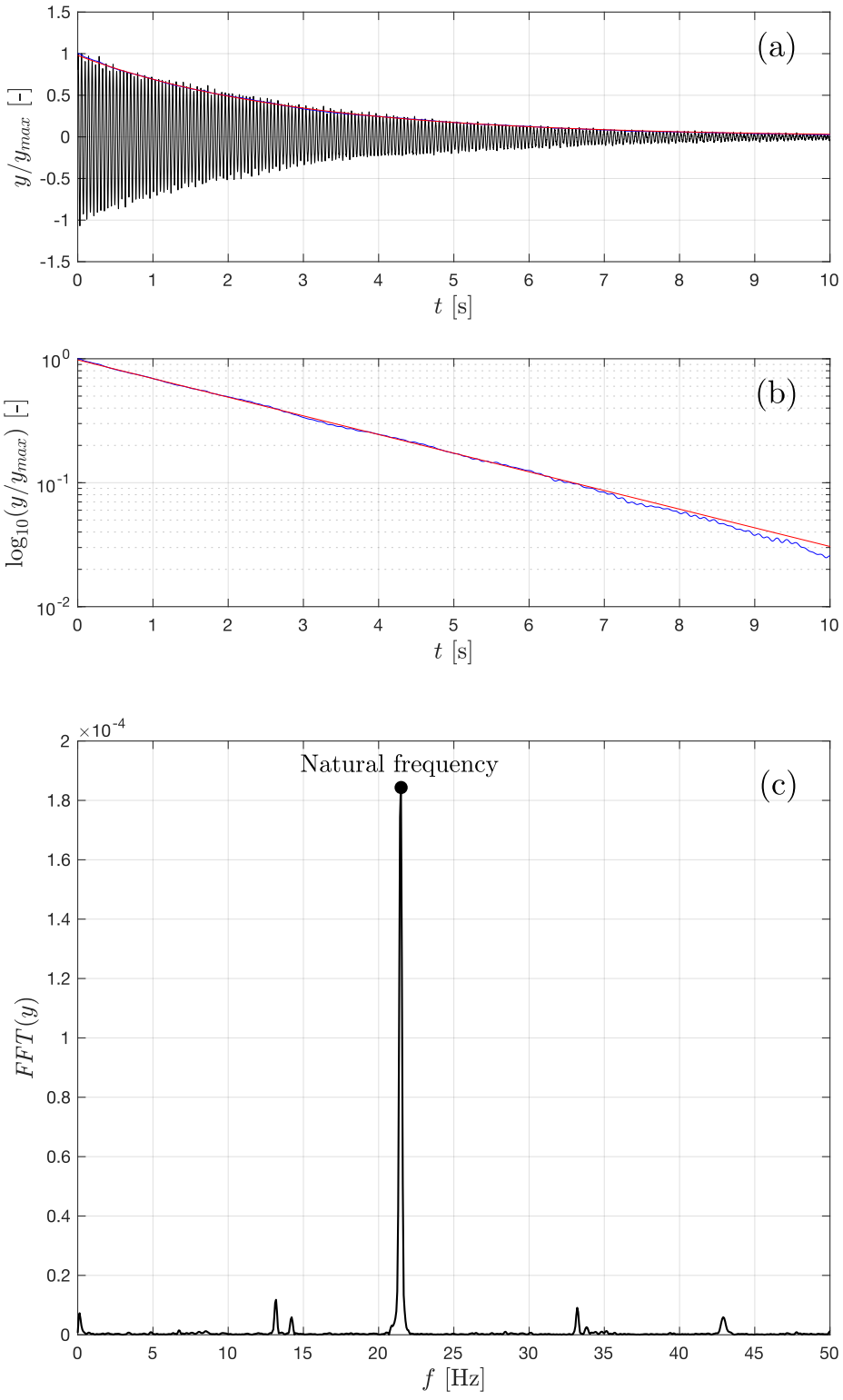

FIGURE 6.8: Example of a modal analysis at wind-off conditions: (a) free response, (b) variation of the amplitude of vibration with time and (c) frequency content of the displacement signal.

6.4 Aeroelastic responses

The experimental aeroelastic test procedure is the following for each tested configuration (L/D, α, number of elastomers): (i) a modal test as described just above is performed at wind-off conditions; (ii) the flow velocity is incremented; (iii) the displacements of the cylinders and the velocity in the wake are measured when the aeroelastic response of the system is stable in time (i.e., constant amplitude of vibration).

The amplitude of vibration is computed as $A_i/D = \sqrt{2}\, Y_i'$, where Y_i' is the standard deviation of the displacement $y_i(t)/D$ (sinusoidal equivalent amplitude). The structural (f_s) and eddy shedding (f_{vs}) frequencies are extracted from the frequency content of $y(t)$ and crosswise flow velocity $v(t)$, respectively.

6.4.1 Tandem arrangement

In this section, the tandem arrangement ($\alpha = 0°$) of two cylinders is investigated. The resulting vibrations of both cylinders are, thus, in the transverse direction with respect to the incoming flow, as shown in Figure 6.3. Note that no (or at least negligible) vibration was observed in the x-direction (checked with accelerometers).

Scruton number effect for $L/D = 1.2$

At first, the spacing ratio $L/D = 1.2$ is investigated in detail for different values of damping ratio and, hence, of the Scruton number. The latter is the correct dimensionless parameter to address the problem because it takes into account the mass ratio parameter, which has a significant effect on the fluid-structure interaction.

Figure 6.9 shows the variation of the amplitude of vibration of each cylinder with the reduced flow velocity U_r for different values of Sc. The dashed lines correspond to the critical reduced velocity at which the VIV instability is expected to start based on the static results, i.e., the eddy shedding frequency matches the structural frequency at $U_r^{VIV} = 1/St$. In section 4.2.3, two values of St were identified in this particular arrangement (post-critical regime, $L/D = 1.2$ and $\alpha = 0°$). Two potential critical VIV reduced velocities are thus reported in Figure 6.9.

The two cylinders start vibrating at a reduced velocity of $U_r \approx 4$ for each value of Sc. This specific reduced velocity corresponds to the critical VIV velocity associated with $St = 0.25$. Thus, the vibrations are initiated by the eddy shedding excitation. When the Scruton number increases, the amplitudes of vibration at a given reduced velocity decrease. It is also interesting to notice that the amplitude of vibration of

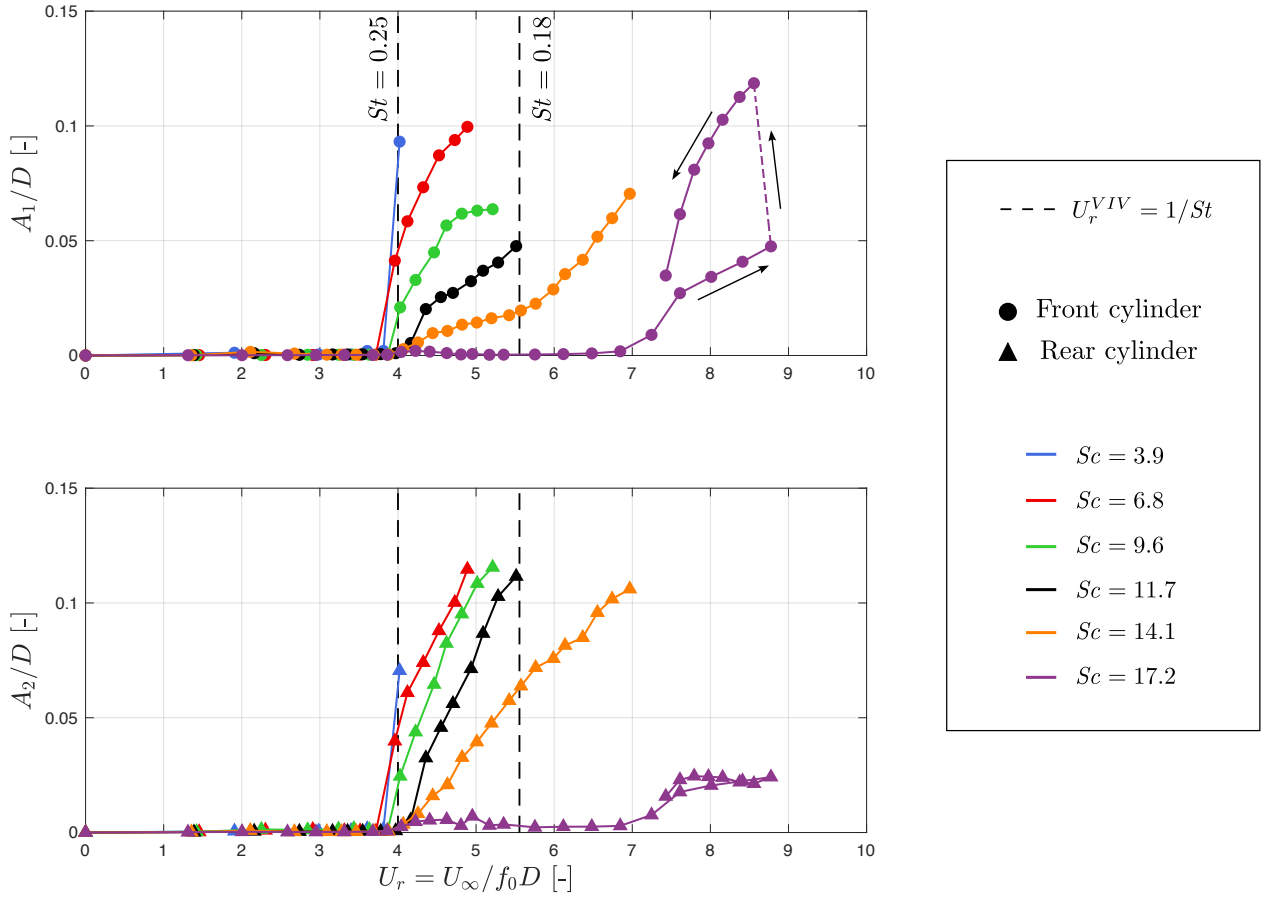

FIGURE 6.9: Variation of the amplitude of vibration of each cylinder with U_r for different values of Sc ($L/D = 1.2$ and $\alpha = 0°$).

the front cylinder is larger than the one of the rear cylinder for the lowest value of Sc (3.9), and it becomes lower for higher values of Sc.

For $Sc \leq 14.1$, the amplitude of vibration of each cylinder monotonically increases with the reduced velocity until it reaches saturation of the extension springs, i.e., $(A/D)_{max} \approx 0.125$. When the saturation is reached, the flow velocity is not further increased to ensure the integrity of the set-up.

For $Sc = 17.2$, the vibrations initiated by the eddy shedding process stop at a reduced velocity $U_r \approx 5$. It leads to the well-known clutch-shape response curves typically observed for VIV instabilities but with very low amplitudes of vibration in the present case. At larger reduced velocities, a second aeroelastic instability is observed above $U_r \approx 7$. This particular reduced velocity does not correspond to any theoretical VIV velocity. Therefore, it is believed that this second aeroelastic instability corresponds to a damping-driven phenomenon usually denoted as galloping. During this instability, the front cylinder vibrates with a larger amplitude than the rear cylinder (Figure 6.9). Since the front cylinder significantly vibrates, it is stated

that a strong flow interference effect is responsible for the instability and the latter is therefore referred to as the *interference galloping*. An interesting behaviour arises during the interference galloping instability: a *bifurcation* occurs between two stable branches at $U_r \approx 8.8$. By slightly increasing the flow velocity, the amplitude of vibration of the front cylinder jumps to a large value. This jump in amplitude resulted in saturation of the extension springs. Because of this, the flow velocity was directly decreased after the jump to remain in the linear range of structural motion. Figure 6.9 shows that the amplitude of vibration of the front cylinder remains on the upper stable branch when U_r is decreased from 8.8 to 7.4. It is interesting to note that the amplitude of vibration of the rear cylinder remains almost the same after the bifurcation (Figure 6.9). The existence of a bifurcation in the aeroelastic response reveals a highly non-linear behaviour of the aeroelastic forces acting on the cylinders (right-hand side terms in equation (6.1)).

A formula is given in the Eurocode (EN1991-1-4) to estimate the critical flow velocity of the interference galloping of two or more free standing cylinders. It is based on the work of Ruscheweyh (1983), which was performed in the sub-critical regime, and reads

$$U_r^{IG} = \sqrt{4\pi \frac{L}{D} \frac{Sc}{a_G}}, \tag{6.14}$$

where a_G is a combined stability parameter and takes a value of 3. This value was fitted by Ruscheweyh on a particular configuration ($L/D = 2.3$ and $\alpha = 10°$), and hence, the formula must be used carefully. Indeed using relation 6.14, a critical reduced flow velocity of 9.3 is estimated in our case ($L/D = 1.2$ and $Sc = 17.2$), while the instability starts at $U_r \approx 7$ experimentally. For this reason, this formula is not applicable in the present configuration (spacing and flow regime).

Figure 6.10 shows the variation of the structural frequency with U_r for different values of Sc and $L/D = 1.2$. Note that f_s/f_0 is reported only when vibrations of the cylinders occur. Because of the linearity of the structure, the variation of this quantity of interest is due to the aerodynamic stiffness, which may take negative or positive values and change (decrease or increase) the global stiffness of the system. As expected, the structural frequency is the same for the two cylinders when flow-induced vibrations occur. The most important outcome of this figure is the dependence of f_s/f_0 on U_r and A/D. The link with the former is not evident but the one with the latter is easily made when the interference galloping instability is investigated ($U_r > 7$ and $Sc = 17.2$). Indeed, the structural frequency decreases when the amplitude of vibration of the front cylinder increases (Figure 6.9), revealing a *softening* effect of the aerodynamic stiffness.

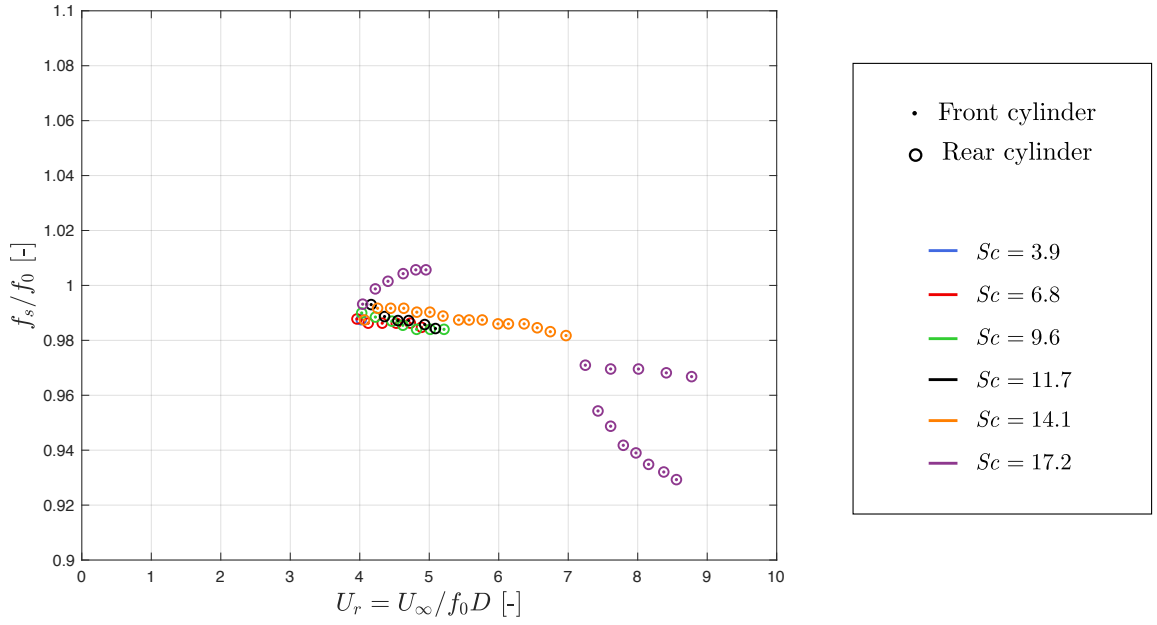

FIGURE 6.10: Variation of the frequency of vibration with U_r for different values of Sc ($L/D = 1.2$ and $\alpha = 0°$).

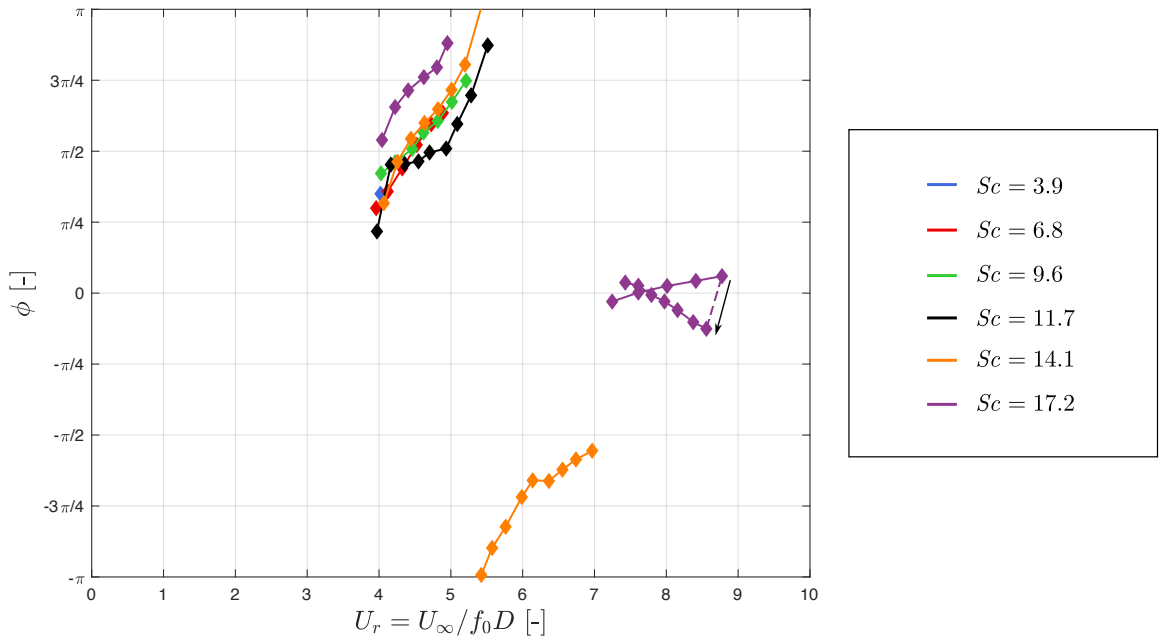

FIGURE 6.11: Variation of the phase lag between the motions of the cylinders with U_r for different values of Sc ($L/D = 1.2$ and $\alpha = 0°$).

The phase lag ϕ between the displacements of the cylinders is also an interesting quantity of the aeroelastic response to analyse. The variation of this quantity with

U_r for different values of Sc and $L/D = 1.2$ is shown in Figure 6.11. Similarly to the previous quantity (f_s/f_0), the phase lag is reported only when flow-induced vibrations occur. Figure 6.11 shows that the phase lag varies with U_r, whether VIV or galloping instability occurs. During the interference galloping instability ($U_r > 7$ and $Sc = 17.2$), the phase lag is around zero. It implies that the vibrations of the two cylinders are almost in phase during this instability. On the other hand, the phase lag is not around zero, and its variation with U_r is more pronounced during the VIV instability.

Figure 6.12 shows the variation of the eddy shedding frequency f_{vs} with the reduced velocity for different values of Sc and $L/D = 1.2$. It is reported in its dimensionless form by normalising it with the natural frequency of the structure in still fluid (f_0). The occurrence of the different main flow regimes around the tandem arrangement is added in the figure. Moreover, the dotted lines show the Strouhal laws associated with the identified St (in red: sub-critical regime; in black: post-critical regime).

- In the sub-critical flow regime, the eddy shedding frequency follows the Strouhal law associated with $St = 0.14$.

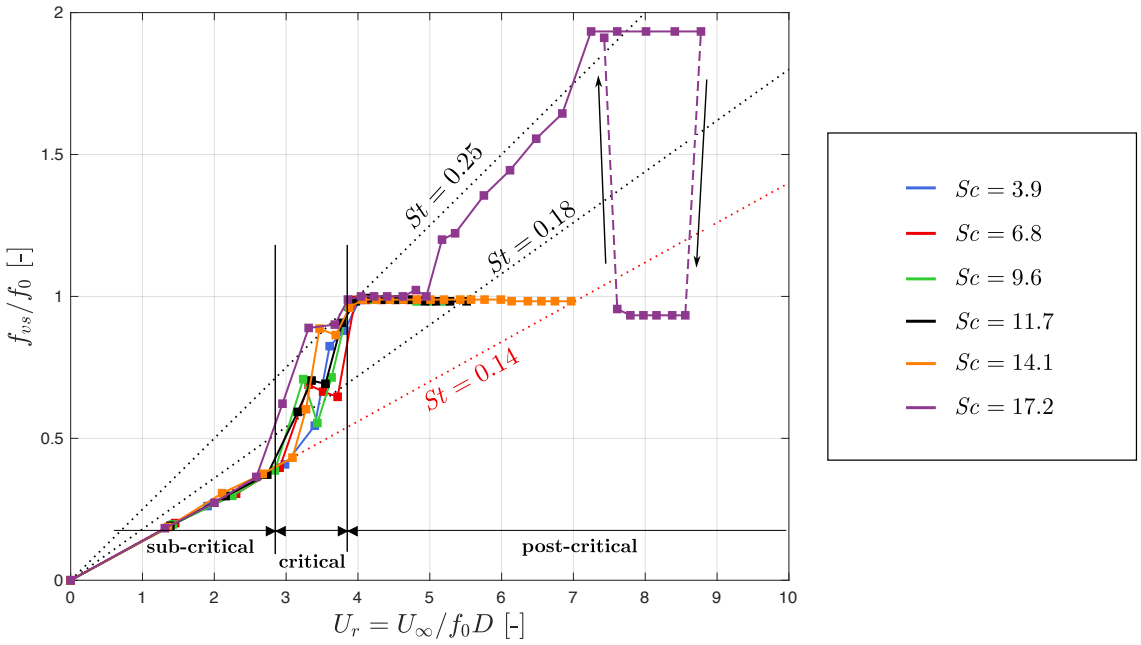

FIGURE 6.12: Variation of the eddy shedding frequency with U_r for different values of Sc ($L/D = 1.2$ and $\alpha = 0°$).

- In the critical flow regime, the eddy shedding frequency is not properly identified. It is a characteristic of the disorganised wake observed in this particular flow regime.

- At the very beginning of the post-critical flow regime, the eddy shedding frequency follows the Strouhal law with $St = 0.25$. When the reduced velocity reaches $U_r \approx 4$, corresponding to the critical VIV velocity ($1/St$), the lock-in phenomenon occurs: the eddy shedding frequency remains equal to the structural frequency as U_r increases. This observation further supports the statement made before that the vibrations of the cylinders are initiated by the eddy shedding process and hence correspond to VIV.
  The lock-in phenomenon disappears at $U_r \approx 5$ for the highest value of Sc, and the eddy shedding frequency follows the Strouhal law again. As the interference galloping instability begins at $U_r \approx 7$, the most energetic frequency in the wake corresponds to the second harmonic of the structural frequency ($2f_s$) at first, i.e., when the amplitude of vibration follows the lower stable branch (bifurcation). When the aeroelastic response jumps to the upper stable branch, the most energetic frequency in the wake becomes equal to the structural one (f_s).

Based on the above observations, it is concluded that the aeroelastic instabilities correspond to VIV-galloping interaction for low values of Sc. The VIV and interference galloping instabilities are decoupled for the largest value of Sc. During the interference galloping instability, it is interesting to emphasise that the motions of the cylinders are almost in phase and that the amplitude of the front cylinder is larger than the one of the rear cylinder. Moreover, a bifurcation between two stable branches is observed in the galloping instability. It reveals a strong non-linear behaviour of the aeroelastic forces acting on the cylinders, especially on the front cylinder.

Case of $L/D = 1.8$

The spacing ratio $L/D = 1.8$ is now investigated for different values of the Scruton number. Figure 6.13 represents the variation of the amplitude of vibration of each cylinder with the reduced velocity for this particular spacing ratio. These aeroelastic curves can be compared with the responses of Figure 6.9, corresponding to $L/D = 1.2$.

Figure 6.13 shows that the amplitude of vibration of the rear cylinder is always larger than the one of the front cylinder, irrespective of the value of Sc. It is slightly different from $L/D = 1.2$ as it was previously observed that A_1/D is greater than

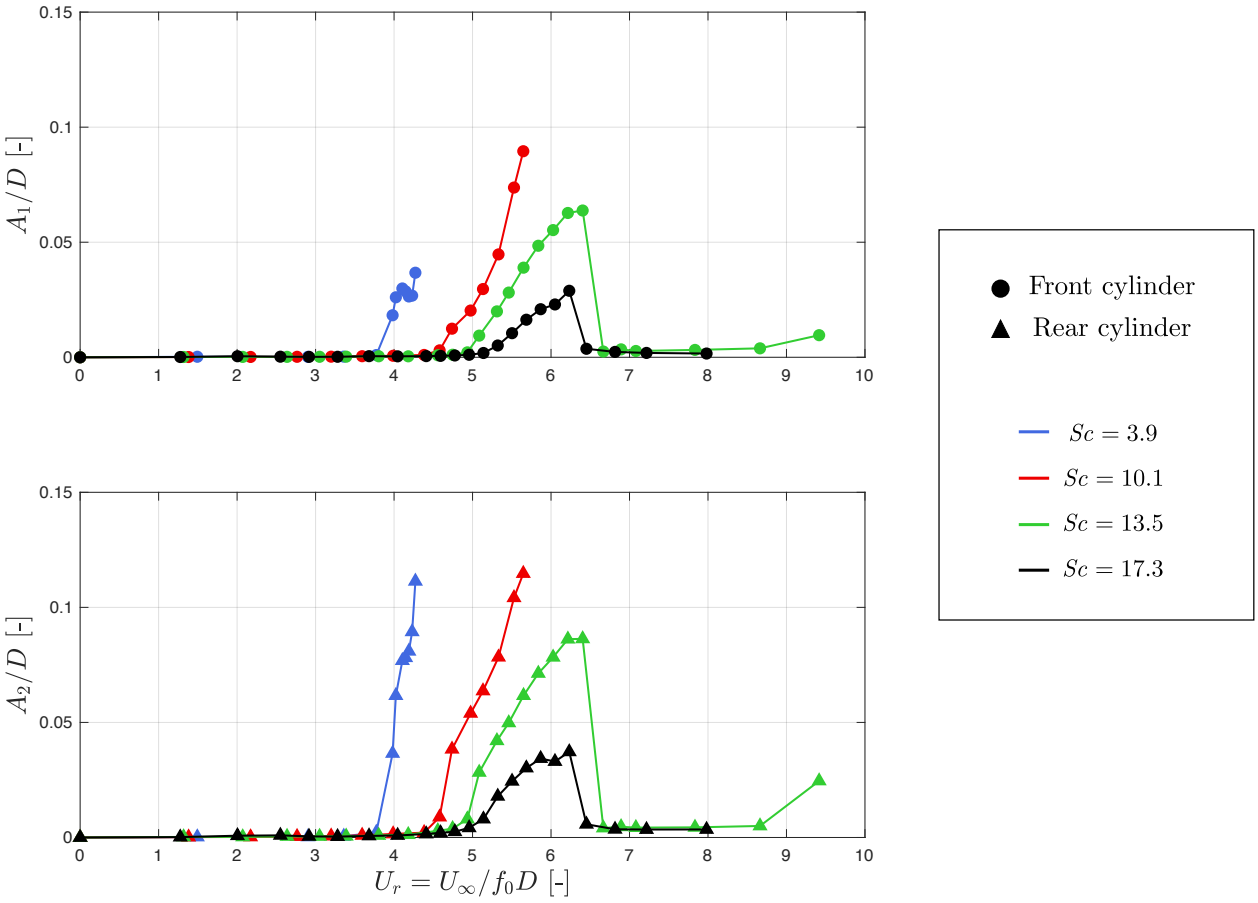

FIGURE 6.13: Variation of the amplitude of vibration of each cylinder with U_r for different values of Sc ($L/D = 1.8$ and $\alpha = 0°$).

A_2/D for the lowest value of Sc (Figure 6.9). However, an increase in the Scruton number leads to lower values of A/D at a given reduced velocity, similarly to $L/D = 1.2$.

Another difference with $L/D = 1.2$ is identified: the critical reduced velocity at which flow-induced vibrations initiate varies with the value of Sc. For a given value of the Strouhal number, the critical VIV reduced velocity ($U_r^{VIV} = 1/St$) should not change with the Scruton number. One can therefore wonder if the eddy-shedding process is responsible for the onset of those flow-induced vibrations. The explanation behind this variation of the critical reduced velocity is a Reynolds number effect due to the increase in the natural frequency f_0 when elastomers are added to the extension springs. Since the natural frequency is increased, the flow velocity has to be larger so that the eddy shedding frequency f_{vs} matches f_0 (resonance phenomenon). Hence, the Reynolds number also becomes larger before the VIV instability is triggered. It is observed from static results that the value of St decreases in this small

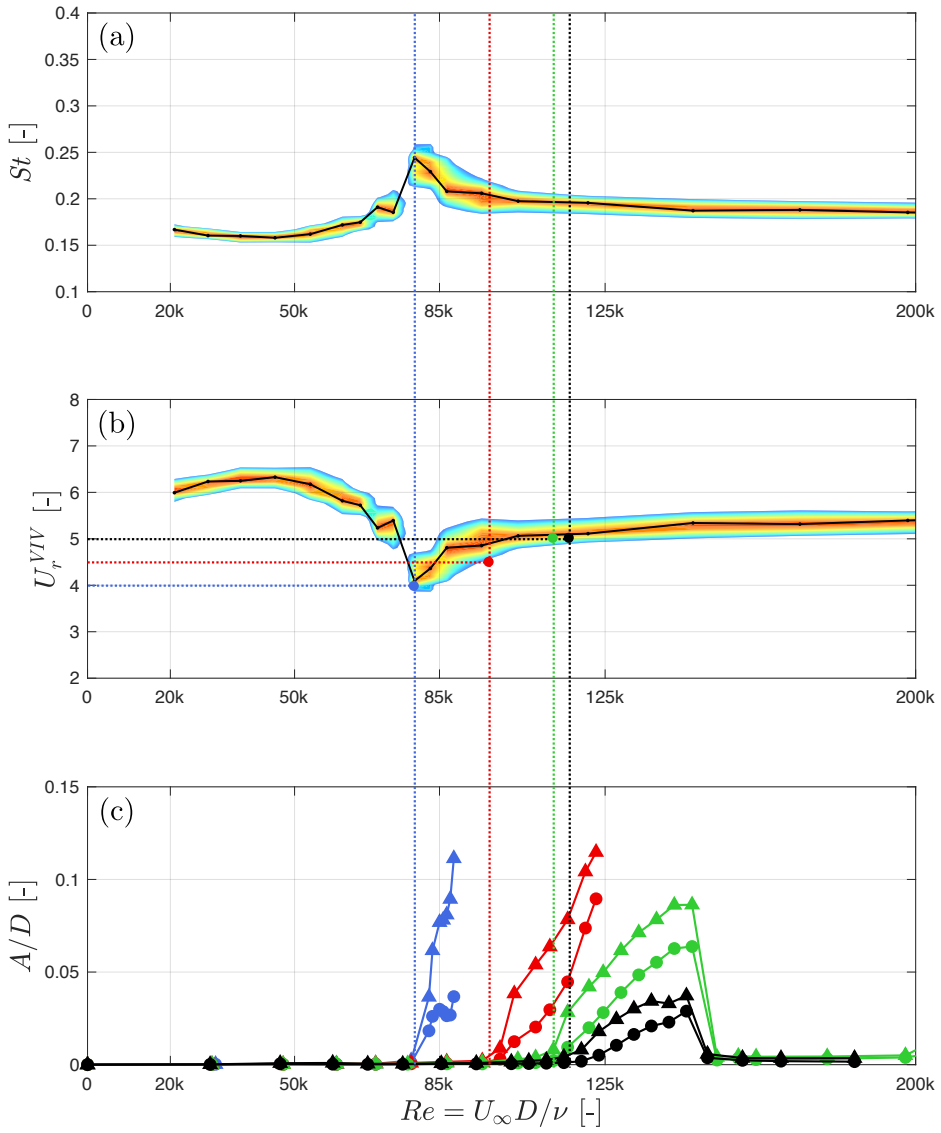

FIGURE 6.14: Variation with Re of (a) the St (from static tests), (b) the critical VIV reduced velocity and (c) the amplitude of vibration of each cylinder for different values of Sc (legend: see Figure 6.13; $L/D = 1.8$ and $\alpha = 0°$).

range of Reynolds number for $L/D = 1.8$, as shown in Figure 6.14(a). The Strouhal number decreases from 0.25 to 0.2 between $Re = 80$k and 120k. The theoretical VIV reduced velocity (Figure 6.14(b)) thus increases from 4 to 5 in the same range of Re. It is consistent with the onset of aeroelastic instabilities identified experimentally and reported in Figure 6.14 as horizontal and vertical dashed lines in terms of U_r and Re, respectively. Therefore, the increase in the critical reduced velocity with the Scruton number is attributed to a Reynolds number effect on the Strouhal number. It must be pointed out that this effect also exists for $L/D = 1.2$, but it is negligible (St remains

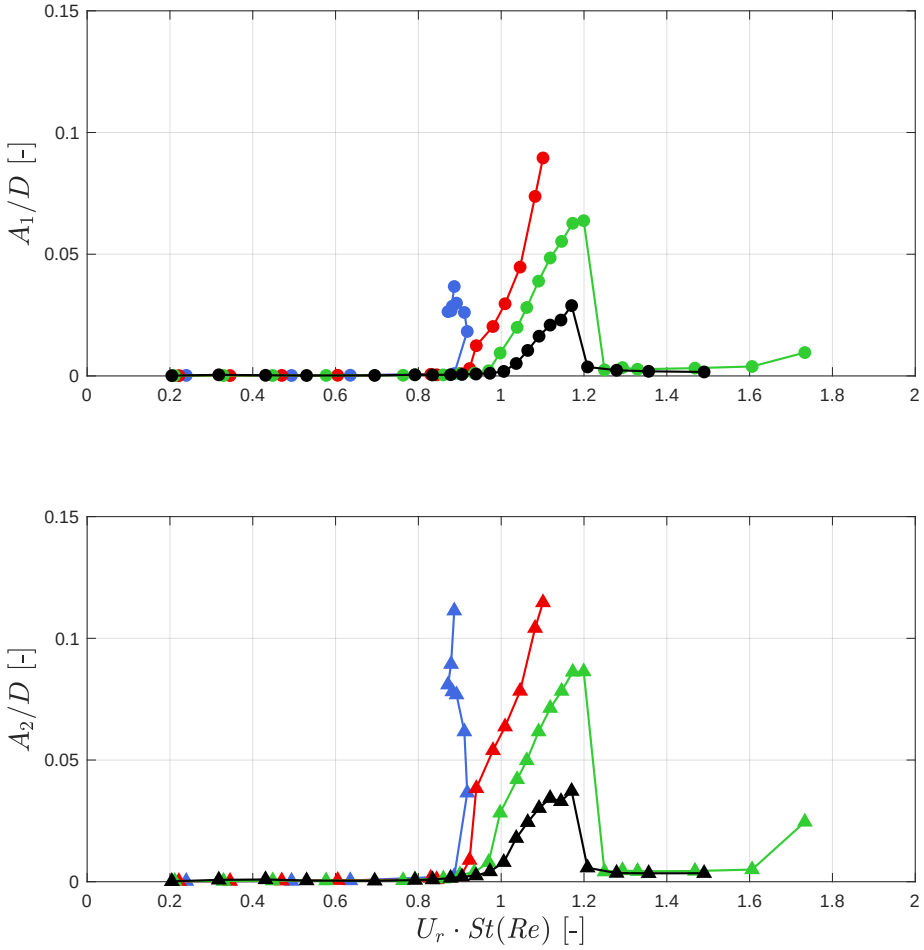

FIGURE 6.15: Variation the amplitude of vibration of each cylinder with $U_r St(Re)$ for different values of Sc (legend: see Figure 6.13; $L/D = 1.8$ and $\alpha = 0°$).

around 0.25). Figure 6.14 shows that the aeroelastic instabilities for the lowest values of Sc occur very close to the critical flow regime, where the flow varies with Re.

Figure 6.15 shows the variation of the amplitude of vibration of each cylinder with $U_r St$, where the value of St comes from measurements on static cylinders and varies with Re (see Figure 6.14(a)). When the aeroelastic responses are presented in that way, it is expected to observe an initiation of VIV instability at $U_r^{VIV} St = 1$ because its associated critical reduced velocity is $U_r^{VIV} = 1/St$. It is valid whatever the value of St, which depends on Re. In that sense, it allows to overcome the Reynolds number effect on the critical reduced velocity discussed above. Figure 6.15 shows that the vibrations of the cylinders start at $U_r St \approx 0.9 - 1$. It confirms that a resonance phenomenon between the structure and the eddy shedding is responsible for those vibrations, which correspond to VIV.

The observations above show that the variation of the Reynolds number and its

effect on the flow cannot be neglected in the identified aeroelastic responses. Therefore, it needs to be taken into account in the mathematical model that will be presented later in this work.

Other spacing ratios

Figures 6.16 and 6.17 show the amplitudes of vibration of both cylinders as a function of the reduced velocity U_r for $L/D = 1.4$ and 1.56, respectively. Similarly to the previously investigated L/D, the value of Sc is varied for the two spacing ratios.

The Reynolds number effect – discussed above for $L/D = 1.8$ – is also observed for the two spacing ratios $L/D = 1.4$ and 1.56. The critical reduced velocity corresponding to the onset of aeroelastic instabilities increases with the value of Sc. Again, it is due to the increase in the natural frequency when adding elastomers combined

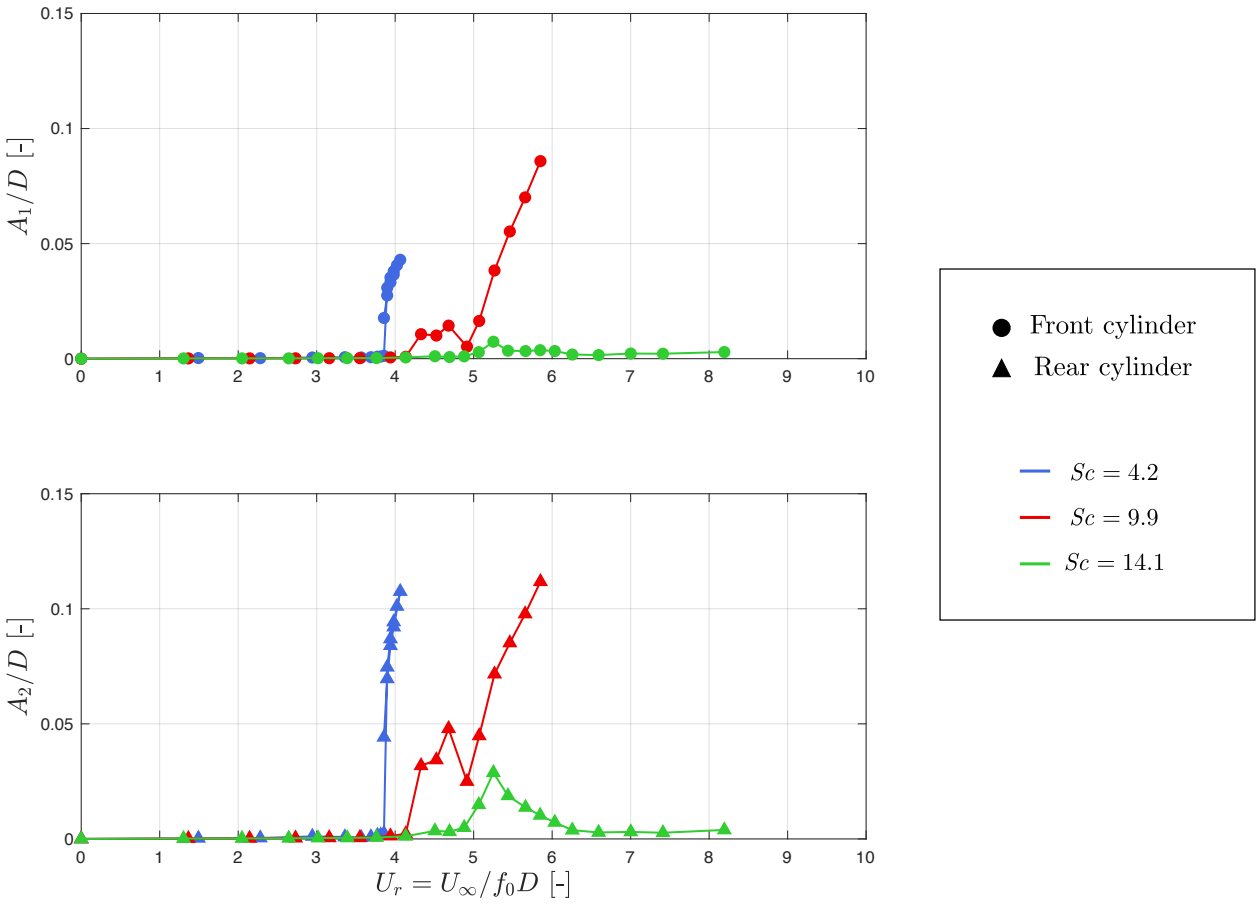

FIGURE 6.16: Variation of the amplitude of vibration of each cylinder with U_r for different values of Sc ($L/D = 1.4$ and $\alpha = 0°$).

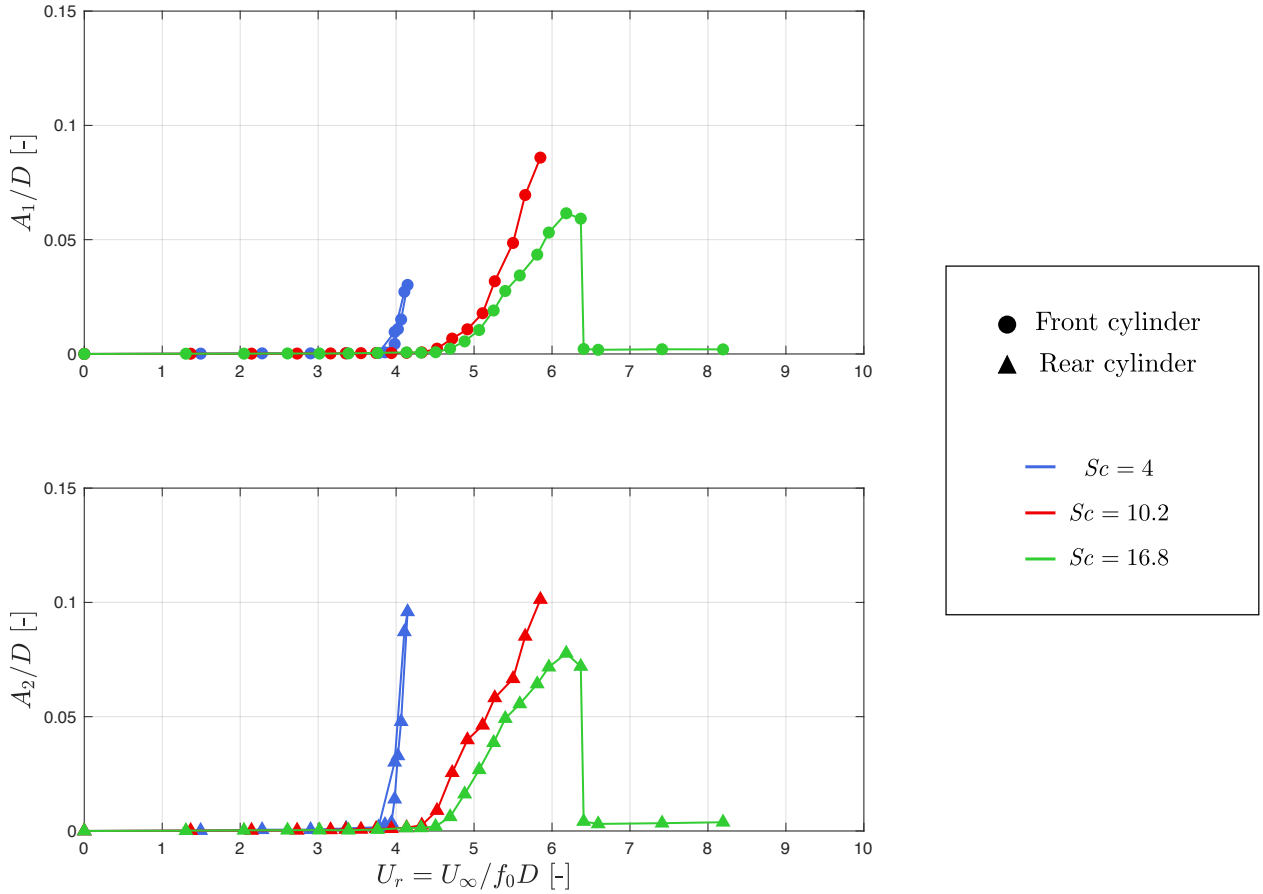

FIGURE 6.17: Variation of the amplitude of vibration of each cylinder with U_r for different values of Sc ($L/D = 1.56$ and $\alpha = 0°$).

with the decrease in the Strouhal number within the increment in Re, which is required to reach the resonance region.

For $L/D = 1.4$, a peculiar behaviour in the aeroelastic responses is observed when $Sc = 9.9$ (see Figure 6.16). The cylinders start vibrating at $U_r \approx 4.3$, and the amplitudes of vibration increase with the reduced velocity before decreasing between $U_r \approx 4.7$ and 5. The amplitudes of vibration then increase again with U_r. Unfortunately, a clear physical explanation for this behaviour cannot be identified. Two tentative explanations are given: (i) a strong Reynolds effect in this small range of the flow velocity or (ii) an interaction between VIV and interference galloping instabilities. For $L/D = 1.8$, a similar observation is made on the aeroelastic response curve of the front cylinder for $Sc = 3.9$ (see Figure 6.13).

When the value of Sc is sufficiently large, the typical VIV clutch-shape curves are observed for $L/D = 1.4$, 1.56 and 1.8. But in contrast to $L/D = 1.2$, no interference galloping instability is observed at larger reduced velocities, or at least within the tested range of U_r. Thus, it cannot be identified whether the vibrations at smaller

values of Sc (which lead to saturation of the extension springs) correspond to a pure VIV instability or a VIV-galloping interaction, as identified for $L/D = 1.2$.

Summary

The different aeroelastic instabilities identified for two tandem cylinders are summarised in Figure 6.18. They are classified as a function of the spacing ratio L/D and the Scruton number Sc. For $L/D = 1.2$, a VIV-galloping interaction occurs for low values of Sc. The two phenomena – VIV and interference galloping – are decoupled for sufficiently high values of Sc. For larger L/D, only VIV responses are observed for high values of Sc within the tested range of U_r. Because of this, it is unfortunately impossible to identify whether interference galloping occurs or not for those spacing ratios at low values of Sc. Nonetheless, the vibrations are always initiated by the vortex shedding excitation.

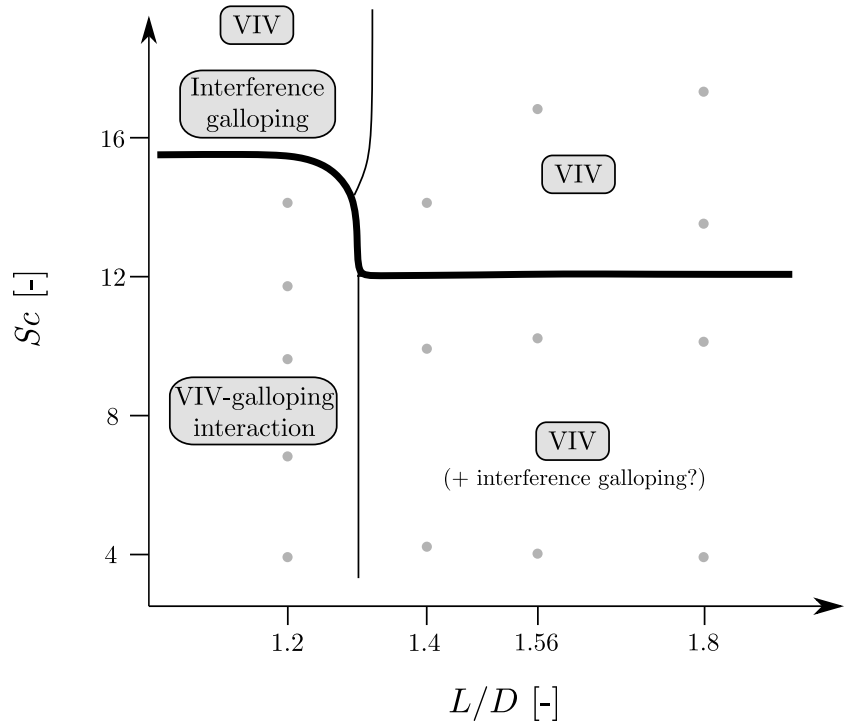

FIGURE 6.18: Classification of the identified aeroelastic instabilities of two tandem cylinders as a function of L/D and Sc.

6.4.2 Effect of the flow incidence

The effect of the flow incidence on the aeroelastic responses is now investigated in this section for a specific configuration: $L/D = 1.2$ and $Sc \approx 10$. Similarly to the experimental campaign on static cylinders, the flow incidence α is varied from 0°

to 10° by increment of 2°. It is important to note that the resulting vibrations of the cylinders are not in the crosswise direction with respect to the incoming flow anymore when a non-zero flow incidence is set, as shown in Figure 6.3.

Figure 6.19 shows the variation of the amplitude of vibration of each cylinder with the reduced velocity at different flow incidences α.
Although the amplitudes of vibration slightly decrease when the flow incidence increases from 0° to 4°, it is observed that the aeroelastic response curves remain very similar. It is thus concluded that the aeroelastic behaviour of the two cylinders remains the same in this range of α. It corresponds to a VIV-galloping interaction as previously identified for the tandem arrangement.

Figure 6.19 shows that the VIV and interference galloping instabilities are decoupled when the flow incidence is increased to 6° and 8°. Typical VIV clutch-shape

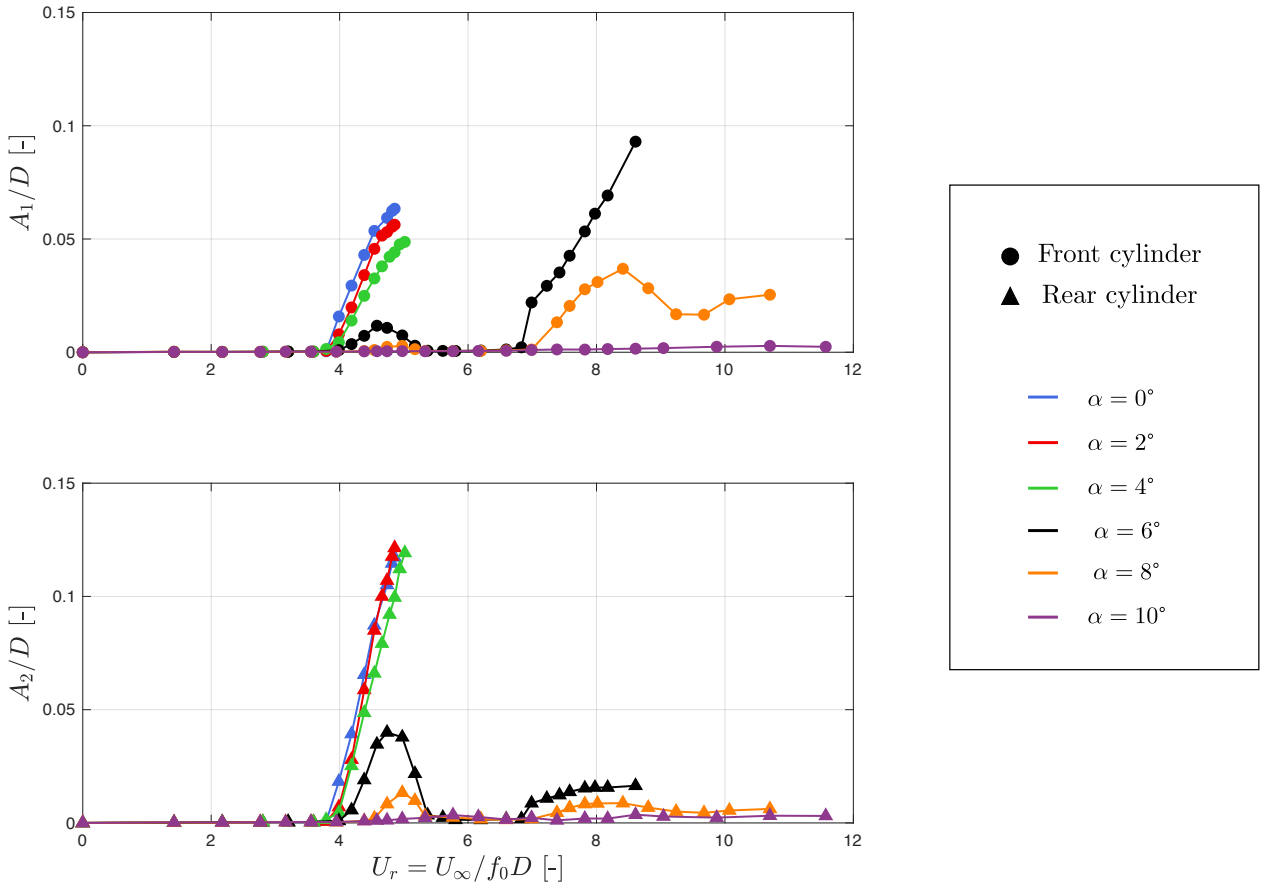

FIGURE 6.19: Variation of the amplitude of vibrations of each cylinder with U_r at different values of α ($L/D = 1.2$ and $Sc \approx 10$).

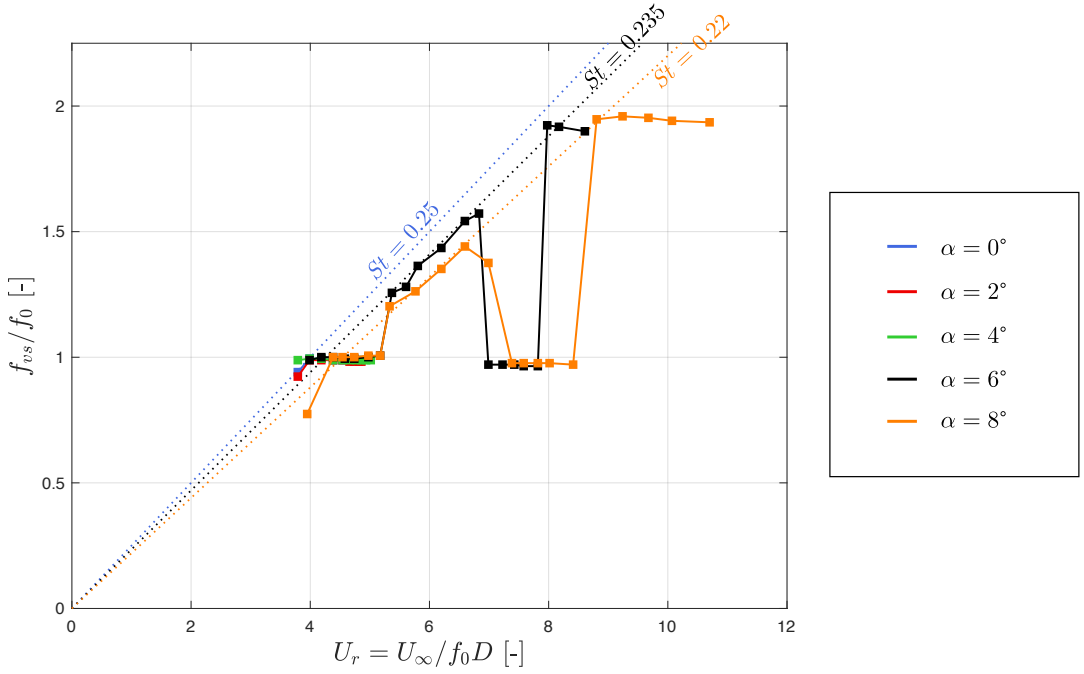

FIGURE 6.20: Variation of the eddy shedding frequency with U_r at different values of α ($L/D = 1.2$ and $Sc \approx 10$).

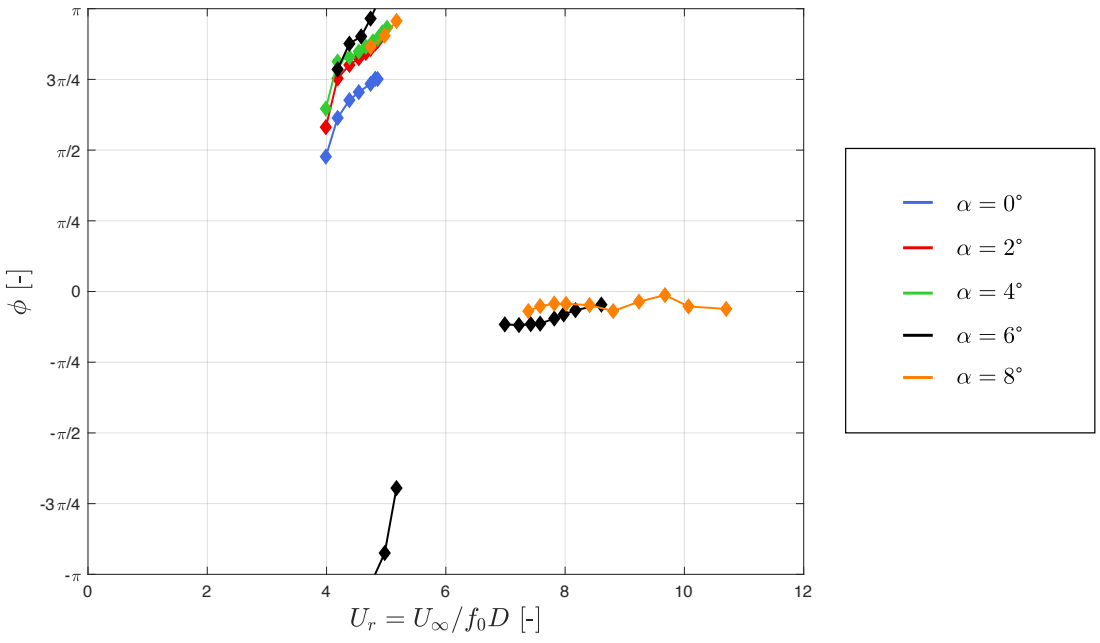

FIGURE 6.21: Variation of the phase lag between the two cylinders with U_r at different values of α ($L/D = 1.2$ and $Sc \approx 10$).

responses are observed between $U_r \approx 4$ and 5. This pure VIV response is probably due to the gap flow which modifies the aerodynamic forces (Figure 5.1(a-b)) on

the cylinders and thus limits the VIV instability at reduced velocities between 4 and 5, approximately. Furthermore, it is observed that the VIV phenomenon initiates at larger values of U_r as the flow incidence is increased. The increase of the critical VIV velocity is consistent with the decrease of the Strouhal number observed during static tests. This decrease in St is also identified and highlighted in Figure 6.20, showing the variation of the eddy shedding frequency with U_r at the different tested flow incidences. At low flow incidence ($\alpha < 4°$), the Strouhal number is approximately 0.25, as it was identified earlier when analysing the tandem arrangement (static or dynamic tests). Then, the Strouhal number decreases to 0.235 and 0.22 at $\alpha = 6°$ and 8°, respectively. At larger reduced velocities, interference galloping responses are observed in Figure 6.19. The critical reduced velocity at which these galloping vibrations start is around $U_r^G \approx 7$ and 7.4 at $\alpha = 6°$ and 8°, respectively. Similarly to the interference galloping observed at $\alpha = 0°$ and $Sc = 17.2$ (Figure 6.9), the amplitude of vibration of the front cylinder is larger than the one of the rear cylinder during this aeroelastic instability. Moreover, the phase lag between the displacements of the two cylinders is also close to zero, i.e., the cylinders oscillate in phase (Figure 6.21).

Finally, no significant flow-induced vibrations are observed when the flow incidence is increased to 10°, as shown in Figure 6.19. Based on the static measurements (Figure 5.1 in the previous chapter), it was identified that a strong gap flow is established at this flow incidence. This gap flow strongly impacts the eddy-shedding process behind the twin-cylinder configuration. Therefore, it is believed that the gap flow prevents the cylinders from vibrating.

6.5 Modelling aspects

The possibility of mathematically modelling the flow-induced vibrations in post-critical conditions of twin cylinders is now investigated. A test case is chosen and corresponds to cylinders in a tandem arrangement ($\alpha = 0°$) spaced by $L/D = 1.2$ with the highest value of $Sc = 17.2$. This specific case is chosen because the VIV and interference galloping instabilities are fully decoupled and thus can be treated separately.

The mathematical model of the structure has already been treated in Section 6.3. It corresponds to the left-hand side terms of equation (6.1). The mathematical developments hereafter focus on the right-hand side terms of the same equation. Furthermore, the external forces $\mathbf{f}_e(U_\infty)$ – due to the free-stream turbulence, for example – are neglected in the following developments. Hence, we focus on the mathematical

modelling of the aerodynamic forces

$$\mathbf{f}_a(U_\infty, \dot{\mathbf{y}}, \mathbf{y}) = \frac{1}{2}\rho U_\infty^2 DS\ \mathbf{c}_{f_a}(Re, \dot{\mathbf{y}}, \mathbf{y}) \tag{6.15}$$

where ρ is the fluid density, U_∞ is the flow velocity, D and S are the external diameter and span length of the cylinder, respectively, and $\mathbf{c}_{f_a}(Re, \dot{\mathbf{y}}, \mathbf{y})$ are the aerodynamic force coefficients which depend on the Reynolds number and the motion of the structure.

In case of two cylinders free to vibrate in the transverse direction with a rigid-body motion, the system of equations (6.1) can be re-written

$$\mathbf{M}_s\ddot{\mathbf{y}} + \mathbf{C}_s\dot{\mathbf{y}} + \mathbf{K}_s\mathbf{y} = \frac{1}{2}\rho U_\infty^2 D\ \mathbf{c}_{f_a}(Re, \dot{\mathbf{y}}, \mathbf{y}) \tag{6.16}$$

where $\mathbf{y} = [y_1, y_2]^T$ and the matrices $\mathbf{M}_s$, $\mathbf{C}_s$ and $\mathbf{K}_s$ represent the structural mass, damping and stiffness per unit length, respectively. The sign conventions for the different variables are defined in Figure 6.22.

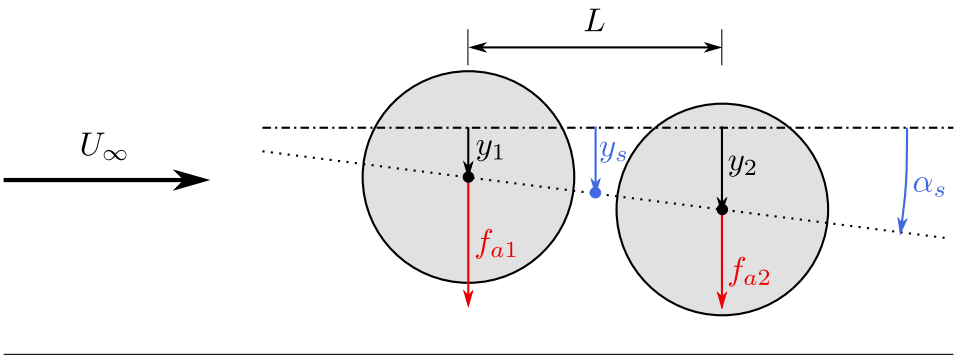

FIGURE 6.22: Definition of variables and sign conventions.

In its dimensionless form, the system of equations becomes

$$Y_1'' + 2\zeta Y_1' + Y_1 - \left(c_r Y_2' + k_r Y_2\right) = \frac{U_r^2}{2\pi^3 m_r} c_{f_{a1}}(Re, \mathbf{Y}', \mathbf{Y}) \tag{6.17a}$$

$$Y_2'' + 2\zeta Y_2' + Y_2 - \left(c_r Y_1' + k_r Y_1\right) = \frac{U_r^2}{2\pi^3 m_r} c_{f_{a2}}(Re, \mathbf{Y}', \mathbf{Y}) \tag{6.17b}$$

where the operator ($'$) denotes differentiation with respect to the dimensionless time τ (equation 6.4) and

$$Y_i = \frac{y_i}{D}, \tag{6.18a}$$

$$c_r = \frac{c_{12}}{m_s S \omega_0}, \tag{6.18b}$$

$$k_r = \frac{k_{12}}{m_s S \omega_0^2}. \tag{6.18c}$$

The aerodynamic force coefficients $c_{f_{ai}}$ in the right-hand side of equations (6.17) could be directly fitted to retrieve the aeroelastic curves observed experimentally. Nonetheless, it is not the objective of this work which aims at using physical insights to develop the model.

It was observed in the previous section that the flow-induced vibrations of the cylinders may be triggered by the eddy shedding excitation or a negative aeroelastic damping contribution in the system, which leads to a VIV or galloping instability, respectively. The aerodynamic force coefficients can conveniently be decomposed as follows

$$\mathbf{c}_{f_a} = \mathbf{c}_{f_a}^{VS} + \mathbf{c}_{f_a}^{QS} \tag{6.19}$$

where $\mathbf{c}_{f_a}^{VS}$ is the unsteady force component generated by the alternate shedding of eddies in the wake, and $\mathbf{c}_{f_a}^{QS}$ corresponds to the quasi-steady force component which emanates from a change in the effective flow incidence α_{eff} due to the motion of the structure. The force corresponding to $\mathbf{c}_{f_a}^{VS}$ fluctuates in time on static cylinders, while the one related to $\mathbf{c}_{f_a}^{QS}$ is constant unless the cylinders are in motion.

6.5.1 VIV modelling

The mathematical model of the VIV instability is considered at first. Hence, the mathematical representation of the term $\mathbf{c}_{f_a}^{VS}$ of equation (6.19) is investigated.

VIV is a low reduced velocity phenomenon and is approached with unsteady models. Several models have been developed in the literature, but the most famous one corresponds to the model of Tamura and Matsui (1979), which deals with the VIV of a single cylinder. Their model consists of two coupled differential equations: the first equation describes the motion of the structure, and the second one describes the motion of the wake. The latter is known as the *wake-oscillator* model, which considers the inclination β of the near-wake as a time-dependent variable. Following the suggestion made by Birkhoff (1953), the near-wake is reduced to a lamina of mean length $2\bar{l}$ and depth h, pivoting around the centre of the cylinder. From the Jutta-Joukowski theory and assuming small oscillations, Birkhoff obtained the following relation for

the two-dimensional lift acting on the lamina

$$F_L = \frac{1}{2}\rho U_\infty^2 2\bar{l} 2\pi\beta. \tag{6.20}$$

This force is applied at the quarter-chord length of the lamina ($\bar{l}/2$ from the centre of the cylinder). Hence, the resulting moment acting on the wake lamina around its hinge point (restoring moment) is

$$M_L = -F_L \frac{\bar{l}}{2} = -\rho U_\infty^2 \pi \bar{l}^2 \beta = -\bar{k}\beta. \tag{6.21}$$

Approximating the moment of inertia of the wake lamina by $\bar{I} = 2\rho h \bar{l}^3$ and considering the undamped wake oscillator described by the following equation

$$\bar{I}\ddot{\beta} + \bar{k}\beta = 0, \tag{6.22}$$

the eddy shedding frequency f_{vs} can be determined and the Strouhal number reads

$$St = \frac{f_{vs} D}{U_\infty} = \frac{1}{2\pi}\sqrt{\frac{\bar{k}}{\bar{I}}}\frac{D}{U_\infty} = \sqrt{\frac{1}{8\pi \bar{l}^* h^*}} \tag{6.23}$$

where $\bar{l}^* = \bar{l}/D$ and $h^* = h/D$.

Funakawa (1969) coupled the wake model described by equation (6.22) (adding a viscous damping term) with a single linear structural oscillator. He assumed that a moment is exerted on the wake lamina due to the acceleration of the body, similarly to a pendulum undergoing a motion at its hinge point. Moreover, he stated that the restoring moment (equation 6.21) acting on the lamina is proportional to the effective angle $\beta - \dot{y}/U_\infty$ to take into account the motion of the body, which changes the apparent flow incidence. Finally, he expressed the lift coefficient acting on the body through the following relation

$$C_l^{VS} = -f_m(\beta - \dot{y}/U_\infty). \tag{6.24}$$

It is proportional to the effective wake angle through a parameter f_m related to the Magnus effect. In analogy to the wake behind a rotating cylinder, which is deviated and creates a steady lift force (Magnus effect), the wake angle β is assumed to generate a transverse force similarly. The parameter f_m is extracted from flow visualisation experiments or calibrated to fit the aeroelastic response.

Tamura and Matsui (1979) introduced in the wake oscillator of Birkhoff the concept of fluctuating length of the lamina, as eddies are alternately shed in the wake.

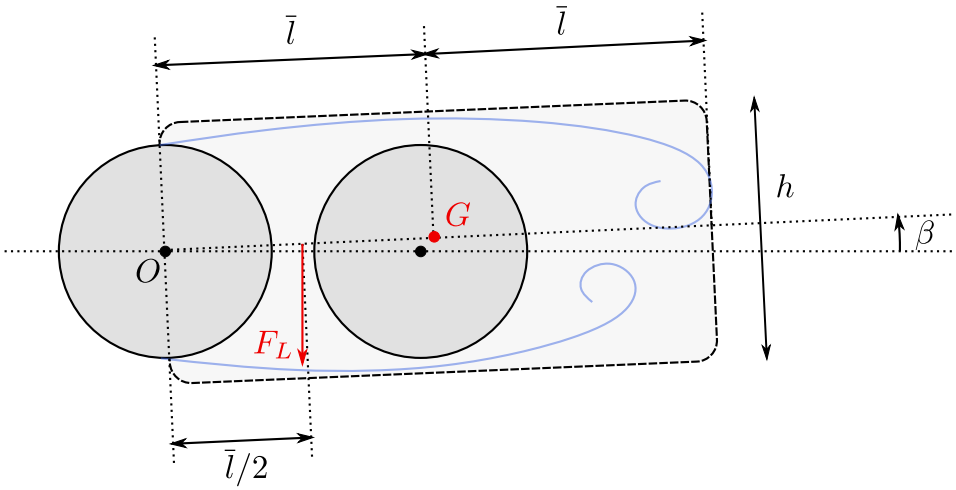

FIGURE 6.23: Schematic of the wake oscillator and definition of its parameters.

Consequently, the stiffness term in equation (6.22) became strongly non-linear. The effects of the eddies, which grow in the near-wake and discharge downstream, were also investigated. It resulted in a negative damping term, and a Van der Pol-type equation was finally obtained to describe the dynamics of the wake angle β.

For further explanations about the set-up of the mathematical VIV model for a single cylinder, the reader is referred to the recent publication of Tamura (2020).

In the present work, it is assumed that a single wake lamina pivots around the centre of the front cylinder, although two cylinders are present. This choice is based on the flow pattern occurring for the configuration of interest ($\alpha = 0°$ and $L/D = 1.2$ in the post-critical regime). It was identified in the previous chapters that the shear layers from the front cylinder do not re-attach onto the rear cylinder for that configuration when $St = 0.25$. Hence, the flow pattern corresponds to the NR one (see Figure 5.16). Moreover, it is assumed that the rear cylinder does not affect the dynamics of the wake. Its motion is, therefore, neglected in the wake-oscillator model. This strong assumption might be considered valid for small oscillations of the cylinder and the wake. However, it becomes questionable when the relative motion between the cylinders leads to the re-attachment of the shear layers onto the rear cylinder. Figure 6.23 shows a schematic of the wake oscillator considered herein. It follows the choice made by Mannini, Massai, and Marra (2018), who successfully modelled the VIV-galloping interaction of a rectangular cylinder with a side ratio equal to 1.5.

Because of the presence of the second cylinder, a change has to be made in the present model compared to a single body. Indeed, the oscillations of the wake angle β do not generate lift force coefficients of the same amplitude on the two cylinders. It

was observed for static tandem cylinders that the fluctuating lift coefficient is larger on the rear cylinder than on the front one. This makes sense since the eddies grow and are shed behind the rear cylinder, which is therefore more impacted. A unique parameter f_m is still defined, and the transverse force coefficients associated with the eddy shedding are defined as

$$\begin{aligned} c_{f_{a1}}^{VS} &= f_m\Big(\beta - \frac{\dot{y}_1}{U_\infty}\Big) \\ c_{f_{a2}}^{VS} &= f_m \frac{c_{l_{f2}}}{c_{l_{f1}}}\Big(\beta - \frac{\dot{y}_1}{U_\infty}\Big) \end{aligned} \tag{6.25}$$

where $c_{l_{fi}}$ is the fluctuating lift coefficient of the ith cylinder: $c_{l_{f2}}$ is greater than $c_{l_{f1}}$ (see Figure 4.5). Physically, it implies that the same wake angle β has a larger influence on the rear cylinder than on the front one.

Finally, the transverse displacement of each cylinder and the wake angle are described by the following non-linear system of second-order differential equations in its dimensionless form:

$$Y_1'' + 2\zeta Y_1' + Y_1 - \big(c_r Y_2' + k_r Y_2\big) = \frac{U_r^2}{2\pi^3 m_r}\left[f_m\Big(\beta - \frac{2\pi Y_1'}{U_r}\Big) + c_{f_{a1}}^{QS}\right] \tag{6.26a}$$

$$Y_2'' + 2\zeta Y_2' + Y_2 - \big(c_r Y_1' + k_r Y_1\big) = \frac{U_r^2}{2\pi^3 m_r}\left[f_m \frac{c_{l_{f2}}}{c_{l_{f1}}}\Big(\beta - \frac{2\pi Y_1'}{U_r}\Big) + c_{f_{a2}}^{QS}\right] \tag{6.26b}$$

$$\beta'' + 2\eta\nu\left(1 - \frac{4f_m^2}{c_{l_{f1}}^2}\beta^2\right)\beta' + \nu^2\beta = \lambda Y_1'' + \nu^2\frac{2\pi Y_1'}{U_r} \tag{6.26c}$$

with the new dimensionless parameters

$$\eta = \frac{4\sqrt{2}}{\pi} St^2 h^* f_m, \tag{6.27a}$$

$$\nu = \frac{\omega_{vs}}{\omega_0} = U_r St, \tag{6.27b}$$

$$\lambda = \frac{1}{\bar{l}^*} = 8\pi St^2 h^*. \tag{6.27c}$$

In the non-linear system of equations (6.26), $c_{l_{f1}}$, $c_{l_{f2}}$ and St come from static tests. However, f_m and h^* cannot be identified from the pressure measurements on static cylinders. A sensitivity study is performed to calibrate their values.

6.5.2 Quasi-steady modelling

The mathematical description of the aerodynamic forces related to the term $\mathbf{c}_{f_a}^{QS}$ of equation (6.19) is now investigated. These aerodynamic forces come from a change in the effective and apparent flow incidences seen by each cylinder, which vary in time since the latter oscillates.

The quasi-steady theory is the basis of the classical galloping model. This theory assumes that the flow dynamics is much faster than the structural one, and hence, the flow adapts almost instantaneously to a change of the structural state ($\dot{\mathbf{y}}$,$\mathbf{y}$). It is often considered valid for large values of the reduced velocity U_r ($U_r > 10$).

The objective is to reproduce the motion dependence of the quasi-steady transverse force coefficient through effective and apparent flow incidences. The latter are

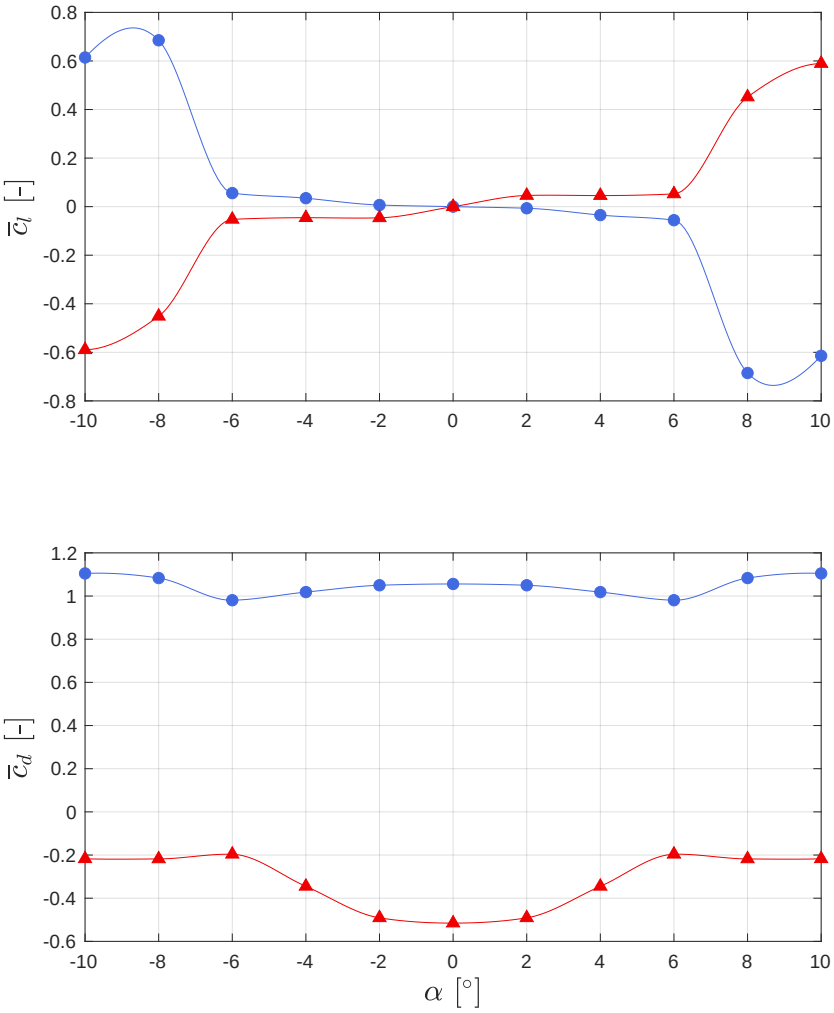

FIGURE 6.24: Time-averaged lift and drag coefficients as a function of the flow incidence α (in blue: front, in red: rear; $L/D = 1.2$ at $Re = 175$k).

combined with the time-averaged force coefficients measured during the static test campaign (previous chapters) to retrieve the quasi-steady forces acting on the cylinders. An example of the variation of $\bar{c}_l$ and $\bar{c}_d$ with α is shown in Figure 6.24. As a reminder, those curves depend on the Reynolds number within the reduced velocity range of interest. This dependency must be included in the mathematical model. The main difficulty when considering two cylinders is to find the appropriate definitions of the effective flow incidence α_{eff} and the apparent flow incidence α_a in order to find a static equivalence to the "relative" motions of the cylinders. Note that the apparent flow incidence only depends on the motion velocity of the cylinder, while the effective flow incidence also takes into account the relative position between the cylinders.

Similarly to the well-known pitch-plunge problem used to demonstrate the flutter of an airfoil, it is convenient to define a transverse displacement y_s and a pitch angle α_s (see Figure 6.22)

$$y_s = \frac{1}{2}(y_1 + y_2), \tag{6.28}$$

$$\alpha_s = \text{atan}\Big(\frac{y_2 - y_1}{L}\Big). \tag{6.29}$$

The variable y_s represents a transverse motion of the cylinders as if they were rigidly connected, while variable α_s represents the relative motion between the cylinders.

It is evident that a change in the pitch angle α_s directly contributes to the variation of the effective flow incidence. On the other hand, a change in the displacement value of y_s does not have any effect on the flow around the two cylinders and, hence, on the aerodynamic forces. Based on that, the aerodynamic stiffness of the system is related to the value of the pitch angle α_s only.

The velocity $\dot{y}_s$ leads to a change in the apparent flow incidence seen by the twin-cylinder configuration equal to $\dot{y}_s/U_\infty$, as it is classically considered in transverse galloping of a single body (see Figure 6.25).
The pitching angular velocity $\dot{\alpha}_s$ also affects the flow. The consideration of the latter is the basis of torsional galloping (or flutter). The difficulty with torsional galloping is that the apparent flow incidence induced by $\dot{\alpha}_s$ varies from point to point of the structure. As a result, an equivalent static configuration cannot be defined and one cannot apply the quasi-steady theory in the same way as for transverse galloping. Unfortunately, no fully satisfactory solution has been found to this difficulty, and hence, analytical models make approximations going further than the quasi-steady

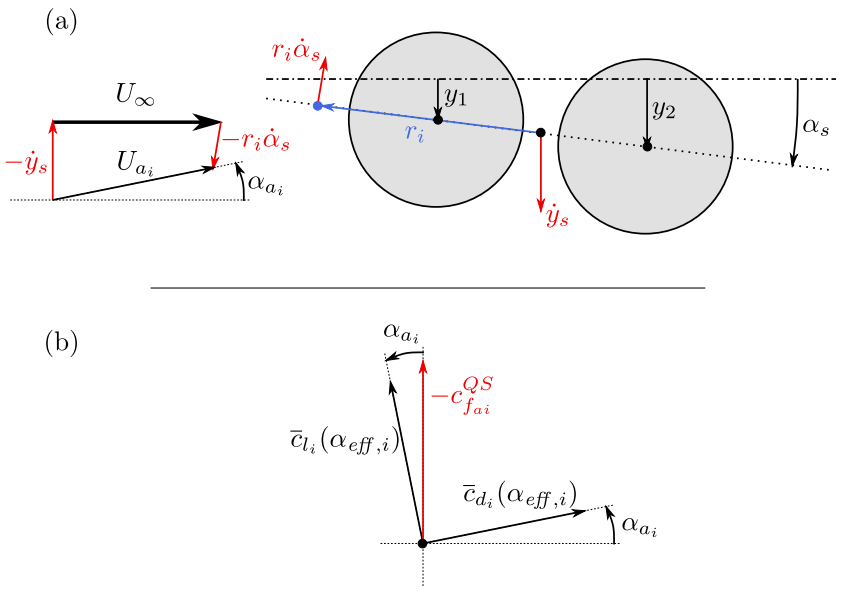

FIGURE 6.25: Schematics of (a) the definition of the apparent flow incidence α_{a_i} and (b) the resulting aeroelastic force coefficients.

assumption. The classical approach to overcome the difficulty is to define a reference radius from the rotation point r_i such that there is a unique value of transverse velocity $-r_i\dot{\alpha}_s$ with angle α_s, as shown in Figure 6.25(a). This approach has been inspired by the use of the three-quarter chord point in the flutter analysis of airfoils, although its applicability to separated flows is debatable. Two reference radii (r_1 and r_2) are defined for the two cylinders to remain as general as possible in the present work. It is believed that the pitch angular velocity may have different effects on them.

Referring to Figure 6.25(a), one obtains the apparent flow incidence for the ith cylinder

$$\alpha_{a_i} = \text{atan}\left(\frac{\dot{y}_s - r_i\dot{\alpha}_s\cos\alpha_s}{U_\infty - r_i\dot{\alpha}_s\sin\alpha_s}\right), \tag{6.30}$$

which changes the direction of application of the aerodynamic forces (lift and drag), as represented in Figure 6.25(b).

It must be emphasised that the choice of r_i is not obvious and rather arbitrary. For rectangular sections oscillating around its geometric centre, Nakamura and Mizota (1975) chose r to be the half of the chord of the rectangle, meaning that α_a corresponds to the instantaneous flow incidence seen by the leading edge. Hence, a parametric analysis is performed between $r_i = -8D$ and $4D$ to calibrate the values in the present work.

An additional difficulty is encountered for twin-cylinder structures: a time delay between fluid-dynamic forces acting on the cylinders and their respective motion is reported (Ruscheweyh, 1983; Dielen and Ruscheweyh, 1995). This time delay can be interpreted as a "fluid memory" effect and stems from the inherent unsteady behaviour of the viscous flow when the cylinders move. It depends on the flow velocity. Similarly to the parameters r_1 and r_2, two distinct time delays (τ_1 and τ_2) are considered for the two cylinders to remain as general as possible. The time delay of the ith cylinder can be expressed as

$$\tau_i = \mu_i \frac{D}{St\, U_\infty}, \tag{6.31}$$

where μ_i is a dimensionless parameter and should not be confused with the fluid dynamic viscosity. This expression is similar to the one suggested by Price and Paidoussis (1984).
From expression (6.31), one can see that the time delay is inversely proportional to the flow velocity and the Strouhal number. Using the definition of the Strouhal number, it is found that the fractional term corresponds to the inverse of the eddy shedding frequency ($1/f_{vs}$). Hence, the time delay τ_i is directly proportional to the period of eddy shedding – which is a characteristic time of the flow dynamics – through the parameter μ_i. This expression therefore introduces the time delay simply and intuitively.

It must be pointed out that τ_i may depend on the relative position between the cylinders during the vibrations, as shown experimentally by Dielen and Ruscheweyh (1995). It implies that the parameter μ_i in expression (6.31) may be a function of the relative positions of the cylinders. This aspect was investigated by Hémon (1999) for flow-induced vibrations of a cylinder in the wake of a static cylinder with $L/D = 3$. He defined a convection velocity between the cylinders, which depends on their relative position. However, the expression that he suggested cannot be applied in the present case because of the distinct values of L/D. In his work, the flow belongs to the co-shedding behaviour, while it belongs to the extended-body one in the present investigation. For the sake of simplicity, the parameters μ_i are assumed constant in this work. Nevertheless, one should keep in mind that it is potentially a point of improvement. A parametric analysis is performed between $\mu_i = 0$ and 1 to calibrate the values in the present work.

Finally, the following relation is obtained for the transverse aerodynamic force coefficient of the ith cylinder

$$c_{f_{ai}}^{QS} = -\left(\bar{c}_{l_i}(\alpha_{eff,i}) \cos\alpha_{a_i} + \bar{c}_{d_i}(\alpha_{eff,i}) \sin\alpha_{a_i}\right) \tag{6.32}$$

where $\overline{c}_{l_i}$ and $\overline{c}_{d_i}$ are the time-averaged lift and drag coefficients from static measurements, respectively (see Figure 6.24). These coefficients are evaluated from the static curves $\overline{c}_i(\alpha)$ (Figure 6.24) at the effective flow incidence $\alpha_{eff,i}$, defined as

$$\alpha_{eff,i}(t) = \alpha_s(t - \tau_i) + \alpha_{a_i}(t). \tag{6.33}$$

They are projected in the y-direction with the apparent flow incidence α_{a_i}, as represented in Figure 6.25(b).

The mathematical model is fully described by the equations (6.26) to (6.33). The model is a non-linear system of equations, which is numerically solved using an explicit Runge-Kutta method. In practice, the ODE45 Matlab function, which employs the Dormand-Prince algorithm, is used.

6.5.3 Parametric analysis

In the mathematical model, some parameters cannot be identified from the static force measurements: f_m, h^*, r_i and μ_i. The former two are crucial in modelling VIV, hence the wake lamina dynamics, while the others are used to compute the effective and apparent flow incidences for the calculation of the quasi-steady force coefficients $c^{QS}_{f_{ai}}$.

Quasi-steady parameters

A parametric analysis is first performed on the parameters r_i and μ_i. To do so, the eddy shedding excitation and the wake lamina dynamics are neglected in order to focus on the aeroelastic responses at large reduced velocities ($U_r > 6$). This gives the following non-linear system of equations:

$$Y_1'' + 2\zeta Y_1' + Y_1 - \left(c_r Y_2' + k_r Y_2\right) = \frac{U_r^2}{2\pi^3 m_r} c^{QS}_{f_{a1}}, \tag{6.34a}$$

$$Y_2'' + 2\zeta Y_2' + Y_2 - \left(c_r Y_1' + k_r Y_1\right) = \frac{U_r^2}{2\pi^3 m_r} c^{QS}_{f_{a2}}. \tag{6.34b}$$

In these equations, the non-linearity comes from the quasi-steady force coefficients ($c^{QS}_{f_{ai}}$) on the right-hand side. The system of equations is first linearised by assuming small oscillations ($\mathbf{Y} \ll 1$), so that it can be written in the form

$$\mathbf{Y}'' + \mathbf{D}\mathbf{Y}' + \mathbf{S}\mathbf{Y} = \frac{U_r^2}{2\pi^3 m_r}\left[\mathbf{D}_a(r_i, \mu_i)\mathbf{Y}' + \mathbf{S}_a(r_i, \mu_i)\mathbf{Y}\right] \tag{6.35}$$

where matrices $\mathbf{D}_a$ and $\mathbf{S}_a$ are associated with the aerodynamic damping and stiffness, respectively. The elements of $\mathbf{D}_a$ are given by

$$(D_a)_{i1} = -\left(\frac{\partial \overline{c}_{l_i}}{\partial \alpha} + \overline{c}_{d_i}\right)\left[\frac{D}{L}\sin\left(\mu_i \frac{2\pi}{StU_r}\right) + \frac{2\pi}{U_r}\left(\frac{1}{2} + \frac{r_i}{L}\right)\right], \tag{6.36a}$$

$$(D_a)_{i2} = -\left(\frac{\partial \overline{c}_{l_i}}{\partial \alpha} + \overline{c}_{d_i}\right)\left[-\frac{D}{L}\sin\left(\mu_i \frac{2\pi}{StU_r}\right) + \frac{2\pi}{U_r}\left(\frac{1}{2} - \frac{r_i}{L}\right)\right], \tag{6.36b}$$

and the elements of $\mathbf{S}_a$ are

$$(S_a)_{i1} = -\left(\frac{\partial \overline{c}_{l_i}}{\partial \alpha} + \overline{c}_{d_i}\right)\left[-\frac{D}{L}\cos\left(\mu_i \frac{2\pi}{StU_r}\right)\right], \tag{6.37a}$$

$$(S_a)_{i2} = -\left(\frac{\partial \overline{c}_{l_i}}{\partial \alpha} + \overline{c}_{d_i}\right)\left[\frac{D}{L}\cos\left(\mu_i \frac{2\pi}{StU_r}\right)\right]. \tag{6.37b}$$

The linear system of equations (6.35) is further written in the first order state space form

$$\mathbf{Z}' = \mathbf{Q}\mathbf{Z} \tag{6.38}$$

where

$$\mathbf{Z} = \begin{pmatrix} \mathbf{Y}' \\ \mathbf{Y} \end{pmatrix}, \tag{6.39a}$$

$$\mathbf{Q} = \begin{pmatrix} -\mathbf{D} + \frac{U_r^2}{2\pi^3 m_r}\mathbf{D}_a & -\mathbf{S} + \frac{U_r^2}{2\pi^3 m_r}\mathbf{S}_a \\ \mathbf{I} & \mathbf{0} \end{pmatrix}. \tag{6.39b}$$

The stability of this linear system can, therefore, be assessed from the eigenvalues of matrix $\mathbf{Q}$:

- all eigenvalues have negative real parts: the system is *stable*;
- at least one eigenvalue is purely real and is positive: the system undergoes *static divergence*;
- at least one pair of complex conjugate eigenvalues has a positive real part: the system is *unstable*.

The critical reduced velocity U_{rc} at which the system becomes unstable depends on the parameters r_1, r_2, μ_1 and μ_2.

The values of parameters r_i are varied from -8D to 4D, and the values of parameters μ_i from 0 to 1, leading to a large number of combinations (r_1, r_2, μ_1, μ_2). This large number of combinations is reduced by keeping the ones which result in a value of U_{rc}

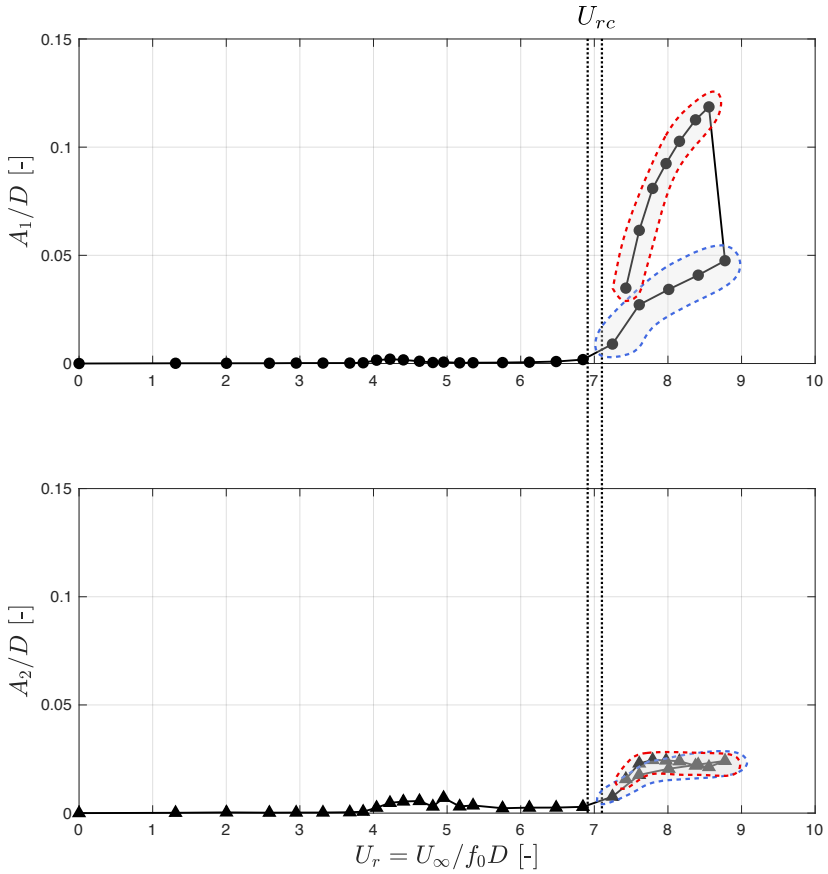

FIGURE 6.26: Selection of constraints in the procedure of identification of the best combination of parameters (r_1, r_2, μ_1, μ_2) for $L/D = 1.2$ and $Sc = 17.2$.

between 6.9 and 7.1. It corresponds to the range of values around the critical reduced velocity reported for the case ($L/D = 1.2$, $Sc = 17.2$), at which interference galloping is initiated (see Figure 6.26).

In the second step, the non-linear system of equations (6.34) is numerically solved for each remaining combination of parameters at five post-critical values of U_r. These values are highlighted in blue and red dashed curves in Figure 6.26. They correspond to the lower and upper branches observed experimentally. The objective of these simulations is to obtain the amplitudes of vibration of the cylinders during the interference galloping.

The combination of parameters (r_1, r_2, μ_1, μ_2), which minimises the error

$$err(r_1, r_2, \mu_1, \mu_2) = \frac{1}{5}\sum_{j=1}^{5}\sqrt{\sum_{i=1}^{2}\left[\frac{A_i^{exp}(U_{r,j}) - A_i^{num}(U_{r,j})}{A_i^{exp}(U_{r,j})}\right]^2} \tag{6.40}$$

is finally retained. In relation (6.40), A_i^{exp} and A_i^{num} represent the amplitude of vibration of the ith cylinder obtained experimentally and numerically, respectively. Figure 6.26 shows that the error can be computed with respect to either the lower (blue dashed lines) or upper (red dashed lines) stable branch identified in experimental results. Hence, the two stable branches are considered in the following analysis.

Applying the identification procedure described above, the best combination of parameters for each fitted branch ($L/D = 1.2$ and $Sc = 17.2$) is reported in Table 6.1. As expected, two distinct combinations of parameters are obtained for the lower and upper branches. It is observed that the error values obtained from relation (6.40) for these combinations are quite large: 43% and 72% when fitting the lower and upper branches, respectively. It implies that the fitting method does not perform very well. Since the error value is larger when using the upper branch to fit the values of parameters in comparison with the lower branch, it means that the fitting method is even worse in that case.

Fitted branch	r_1	r_2	μ_1	μ_2	err
Lower	$-4.8D$	$0.8D$	0.8	0.7	0.43
Upper	$-5.4D$	$1.4D$	0.5	0.7	0.72

TABLE 6.1: Value of parameters when minimising *err* for each stable branch.

Figure 6.27 shows the aeroelastic responses as a function of U_r obtained from the non-linear quasi-steady model described by equations (6.34) with the two identified combinations of parameters (Table 6.1). The statement made just above is highlighted in this figure: the fitting method does not perform well, especially for the upper stable branch. The amplitudes of vibration of the front cylinder are clearly underestimated in the model, which is the reason for the large error values reported in Table 6.1. Nevertheless, the amplitudes of vibration of the rear cylinder are in better agreement with the experimental results for both combinations of parameters.

One can thus wonder why the fitting procedure does not perform well. The present procedure actually results in a compromise to fit the aeroelastic responses of both cylinders. It is not a direct fit of the aerodynamic forces in the right-hand side of equations (6.34) but rather an indirect fit via the effective and apparent flow incidences. In addition, the error variable defined by relation (6.40) takes into account the amplitude errors of both cylinders. By minimising this error variable, the resulting combination of parameters corresponds to a compromise between the errors made on the front and rear cylinders. Thus, the large discrepancies between the numerical

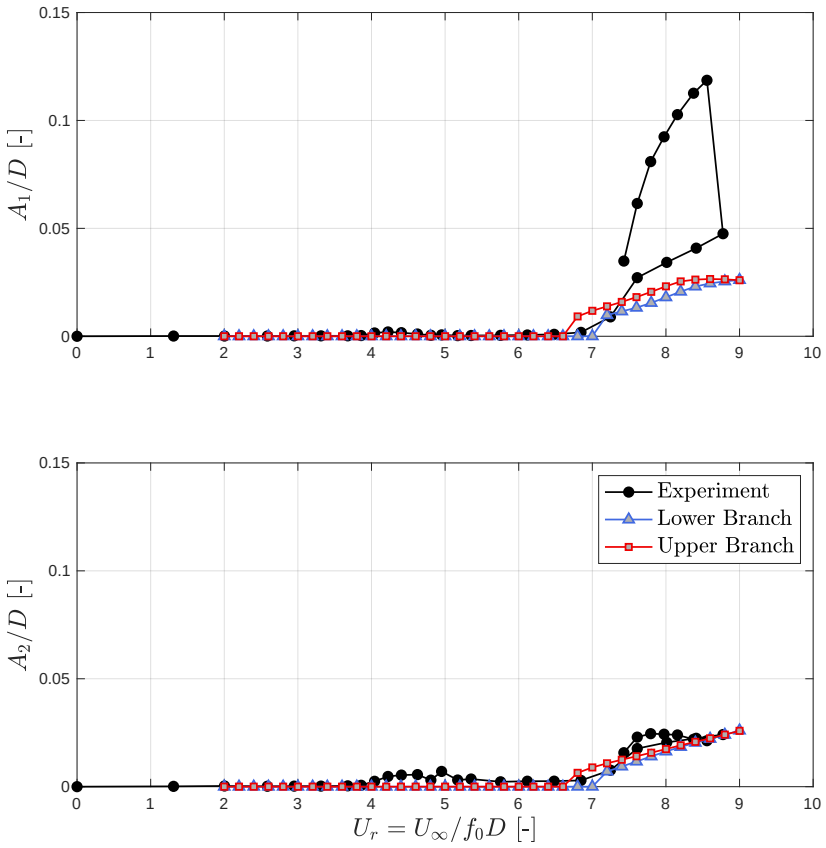

FIGURE 6.27: Numerical aeroelastic responses as a function of U_r obtained from the non-linear quasi-steady model described by equations (6.34) with combinations of parameters reported in Table 6.1 ($L/D = 1.2$ and $Sc = 17.2$).

aeroelastic responses and the experimental results in Figure 6.27 imply that the quasi-steady model is unable to fit the experimental results of the front and rear cylinders simultaneously.

To support the discussion above, it is decided to push further the parametric analysis by defining the following error:

$$errS_i(r_1, r_2, \mu_1, \mu_2) = \frac{1}{5}\sum_{j=1}^{5}\sqrt{\left[\frac{A_i^{exp}(U_{r,j}) - A_i^{num}(U_{r,j})}{A_i^{exp}(U_{r,j})}\right]^2}. \tag{6.41}$$

This relation differs from (6.40) by the absence of the summation term applied on the two cylinders inside the square root. Hence, $errS_i$ corresponds to the error made on the aeroelastic response of the ith cylinder obtained from the quasi-steady model with respect to the experimental results. These error variables are minimised independently to set values of parameters: (i) when minimising $errS_1$, only the aeroelastic

response of the front cylinder is used to fit the parameters; (ii) when minimising $errS_2$, only the aeroelastic response of the rear cylinder is used to fit the parameters. In either case, the lower or upper stable branch of the interference galloping instability can be used to compute the error (Figure 6.26).

The resulting combinations of parameters are shown in Table 6.2. In this table, values of the parameters obtained when minimising *err* are recalled, together with the corresponding values of $errS_1$ and $errS_2$, to facilitate the comparison and discussion. Table 6.2 shows that the values of parameters (r_1, r_2, μ_1, μ_2) depend on the error variable which is minimised and on the fitted branch. The minimum values of each error variable are highlighted in blue in Table 6.2. It is interesting to note that the amplitude error of the rear cylinder $errS_2$ is around 10% when it is minimised, which can be considered satisfactory. On the other hand, the amplitude error of the front cylinder $errS_1$ remains large when it is minimised: 22% and 59% for the lower and upper branches, respectively.

Minimised error	Fitted branch	r_1	r_2	μ_1	μ_2	*err*	$errS_1$	$errS_2$
err	Lower	$-4.8D$	$0.8D$	0.8	0.7	0.43	0.40	0.13
	Upper	$-5.4D$	$1.4D$	0.5	0.7	0.72	0.69	0.19
$errS_1$	Lower	$-3.2D$	$4.0D$	0.5	0.9	0.69	0.22	0.56
	Upper	$-3.4D$	$4.0D$	0.4	0.9	1.84	0.59	1.62
$errS_2$	Lower	$-6.0D$	$0.2D$	0.7	0.6	0.49	0.47	0.09
	Upper	$-6.6D$	$1.8D$	0.4	0	0.82	0.80	0.12

TABLE 6.2: Value of parameters when minimising *err* or $errS_i$ for each stable branch.

Figure 6.28 shows the numerical aeroelastic responses obtained with the sets of parameters identified when minimising the error variable $errS_1$, i.e., when fitting the response curve of the front cylinder only. It is observed that the model is unable to properly fit the aeroelastic response of the front cylinder, in particular the upper branch. Moreover, this fitting procedure is detrimental to the aeroelastic response of the rear cylinder: the amplitude of vibration A_2/D jumps at $U_r \approx 8$. It leads to a large error value of $errS_2$, as reported in Table 6.2. The divergent behaviour in amplitude can be explained based on the maximum effective flow incidences used in the quasi-steady model (equation (6.33)). The latter is plotted as a function of U_r in Figure 6.29. It is observed that the effective flow incidence of the rear cylinder $\alpha_{eff,2}$ takes value around 13°-14° at $U_r > 8$, which goes beyond the range of α from the static measurements (-10°$< \alpha <$10°). The model thus extrapolates the quasi-steady force curves (Figure 6.24), which leads to erroneous values. As a result, these

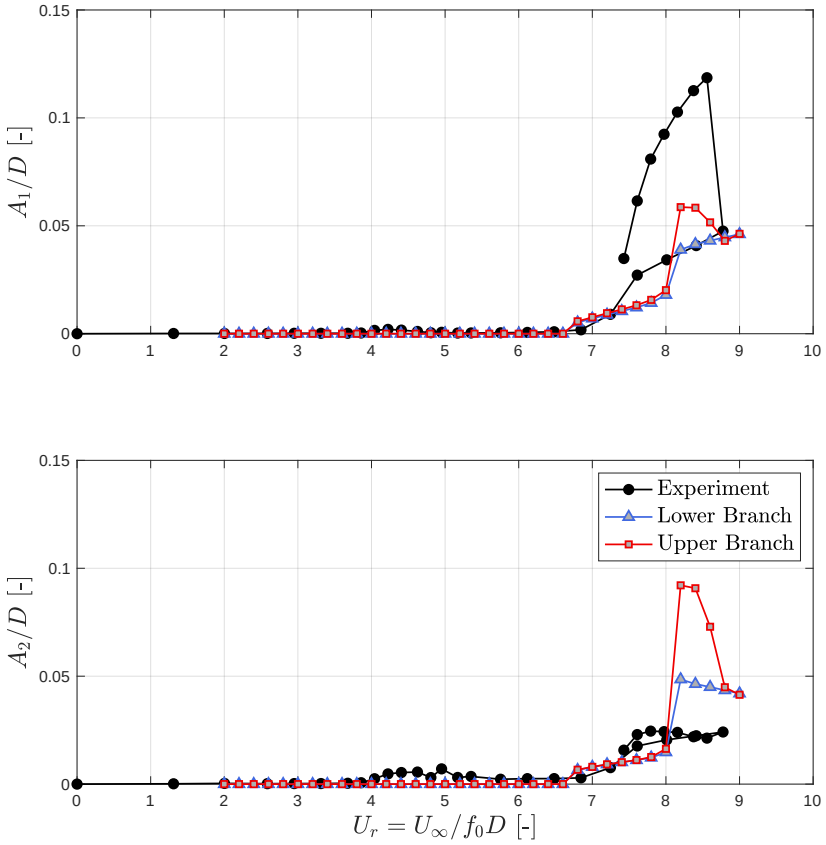

FIGURE 6.28: Numerical aeroelastic responses as a function of U_r obtained from the non-linear quasi-steady model described by equations (6.34) (values of parameters when minimising $errS_1$; $L/D = 1.2$ and $Sc = 17.2$).

numerical results must be discarded because the inputs of the model are not valid anymore.

To conclude the parametric analysis of the quasi-steady model described above, it has been demonstrated that the experimental response curve of the front cylinder cannot be properly fitted with appropriate values of (r_1, r_2, μ_1, μ_2) in the current quasi-steady model. When minimising the error variable $errS_1$, the value of the latter remains large (22% or 59%). Moreover, it has been shown that the quasi-steady force values introduced in the model are not valid anymore because the effective flow incidence of the rear cylinder goes beyond 10°. Unfortunately, it is impossible to predict the outputs of the fitting procedure if the range of α in static measurements is extended to larger values since no data is available. This specific point represents potential further works on the subject of this thesis. Nonetheless, it is believed that the excitation mechanism which leads to the upper branch is not taken into account

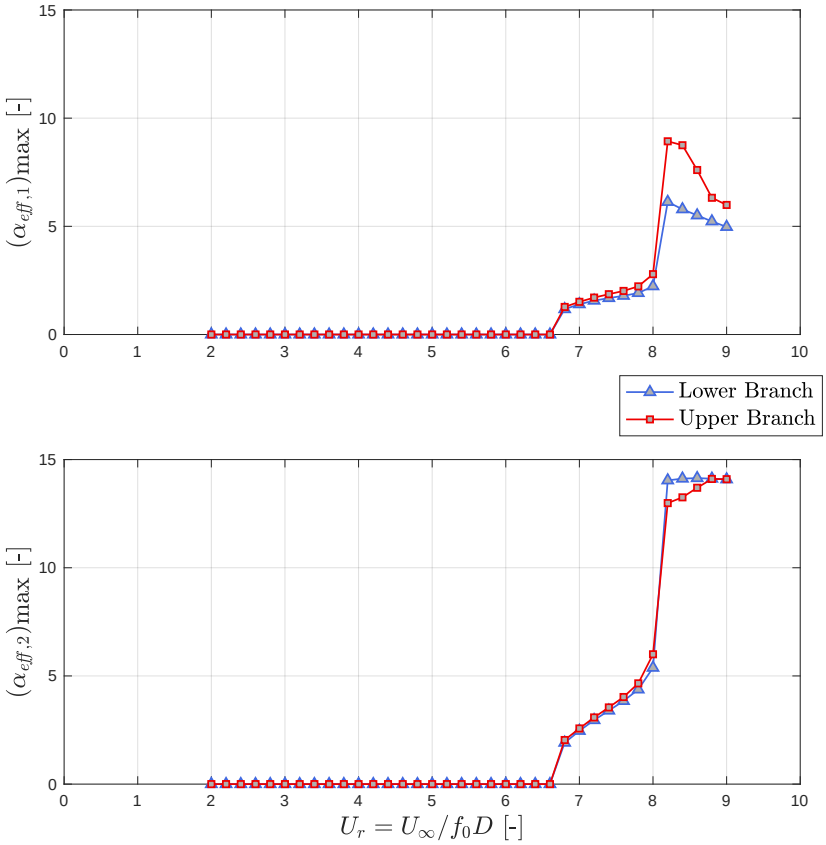

FIGURE 6.29: Maximum effective flow incidences as a function of U_r obtained from the non-linear quasi-steady model described by equations (6.34) (values of parameters when minimising $errS_1$; $L/D = 1.2$ and $Sc = 17.2$).

in the model. The unsteady flow dynamics in the gap between the cylinders must have a significant effect on the aeroelastic forces acting on the cylinders when they are closely spaced. The quasi-steady assumption completely neglects this flow dynamics, even though a time delay parameter is introduced in the model.

For the rest of this work, the set of parameters (r_1, r_2, μ_1, μ_2) obtained when minimising *err* with the lower branch is retained (first line in Table 6.2). This particular set is chosen because it leads to the best compromise by taking into account the responses of both cylinders simultaneously.

VIV parameters

Parameters h^* and f_m correspond to purely aerodynamic quantities that are usually determined by means of flow visualisation techniques. For a single cylinder, Funakawa (1969) assumed $h^* = 1.25$ based on his experimental results. He also derived

the value of 1.16 for parameter f_m, in analogy to the Magnus effect of a rotating cylinder. However, this analogy is questionable in the case of two tandem cylinders and the identification of f_m is thus not as straightforward as for a single cylinder.

Since no flow visualisation is available in the present work, a sensitivity study is performed to calibrate the values of f_m and h^*. It is based on the experimental aeroelastic responses measured in the case of pure VIV instability.

Parameter f_m is varied in the range $0.5 < f_m < 1.5$, and Figure 6.30 shows the resulting aeroelastic responses obtained by the numerical simulation of the full nonlinear mathematical model described by equations (6.26) to (6.33). It is observed that the amplitude of vibration of the rear cylinder compares well with the experimental results. On the other hand, the amplitude of vibration of the front cylinder is overestimated. The parameter f_m has a negligible effect on the peak amplitude of the VIV response. In contrast, the range of U_r associated with the VIV instability is strongly influenced by the value of f_m. For the largest value ($f_m = 1.5$), the instability even never stops within the reduced velocity range of interest. It is observed experimentally that the VIV instability disappears at $U_r > 5$. Hence, $f_m = 1.16$ appears to be

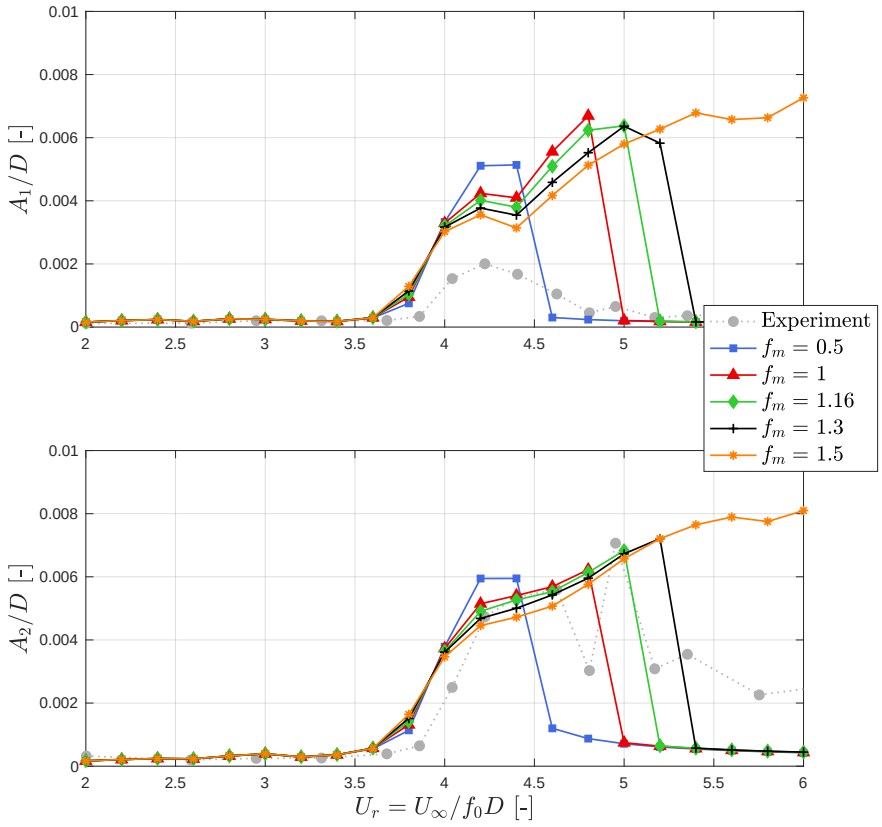

FIGURE 6.30: Numerical results obtained for different values of parameter f_m ($L/D = 1.2$, $Sc = 17.2$ and $h^* = 1.1$).

the best value and is retained for this configuration. It is interesting to note that this value is the same as the one derived for a single cylinder.

Parameter h^* is varied in the range $1< h^* <2$. Figure 6.31 shows the numerical results of the mathematical model for different values of h^*. For $h^* \leq 1.25$, it is observed that this parameter has a negligible effect on the results. Larger values of h^* lead to an increase in range of U_r associated with the VIV instability. Based on those results, the value $h^* = 1.1$ is arbitrarily retained for this configuration.

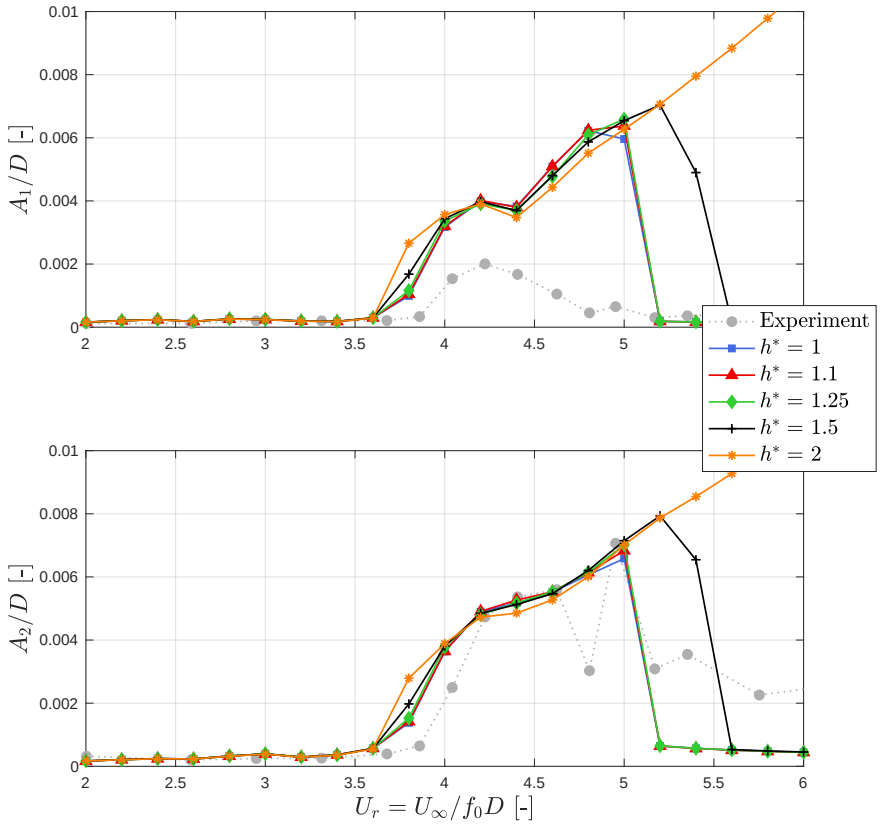

FIGURE 6.31: Numerical results obtained for different values of parameter h^* ($L/D = 1.2$, $Sc = 17.2$ and $f_m = 1.16$).

6.5.4 Results

The non-linear mathematical model fully described by the equations (6.26) to (6.33) is now numerically solved by increasing U_r from 2 to 9 with the identified parameters $f_m = 1.16$, $h^* = 1.1$ and $(r_1, r_2, \mu_1, \mu_2) = (-4.8D, 0.8D, 0.8, 0.7)$.

Figure 6.32 shows the numerical results together with the experimental ones for the selected test case $L/D = 1.2$ and $Sc = 17.2$. Since a parametric analysis and sensitivity study were performed in the previous section in order to calibrate the parameters of the model for this particular configuration, it is not surprising to observe that the numerical results show a satisfactory agreement with the experimental ones. During the VIV instability ($4 < U_r < 5$), the amplitudes of vibration are of the same order of magnitude as the ones observed experimentally, even though it is slightly overestimated for the front cylinder. The interference galloping instability is initiated at $U_r \approx 6.8$. The amplitude curve of the front cylinder follows rather well the lower stable branch observed in the experiments, while it is a bit underestimated for the rear cylinder. As a reminder, a set of parameters that leads to numerical results which fit the upper branch of the bifurcation could not be found with the current model.

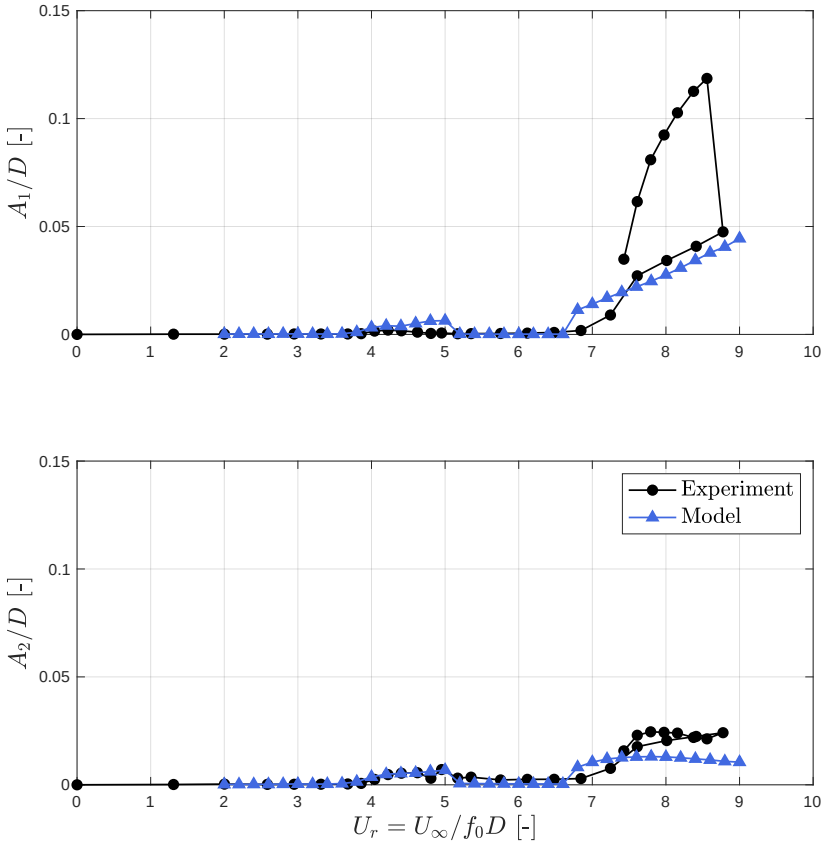

FIGURE 6.32: Numerical aeroelastic responses as a function of U_r obtained from the non-linear model fully described by equations (6.26) to (6.33) for $L/D = 1.2$ and $Sc = 17.2$ ($f_m = 1.16$; $h^* = 1.1$; $r_1 = -4.8D$; $r_2 = 0.8D$; $\mu_1 = 0.8$; $\mu_2 = 0.7$).

Other values of Sc

The mathematical model is now used to predict the aeroelastic responses of the cylinders for lower values of Sc and $L/D = 1.2$. Figure 6.33 shows the variation of A/D of each cylinder with U_r obtained numerically and experimentally for $Sc = 9.6$ and 14.1. As expected, aeroelastic instabilities start at $U_r \approx 4$ for both values of Sc and are triggered by the alternate eddy shedding excitation.

Similarly to the experiments, VIV-galloping interaction is observed for $Sc = 9.6$ (Figure 6.33(a)). However, the amplitudes of vibration in post-critical conditions are significantly underestimated. In Figure 6.33(a), the numerical curves also show a peculiar behaviour at the last four simulated reduced velocities ($8.4 < U_r < 9$): A_1/D and A_2/D suddenly drops and jumps, respectively. This behaviour comes from the fact that the effective flow incidence of the rear cylinder goes beyond 10° and hence the quasi-steady model is not valid anymore, as discussed above when trying to fit

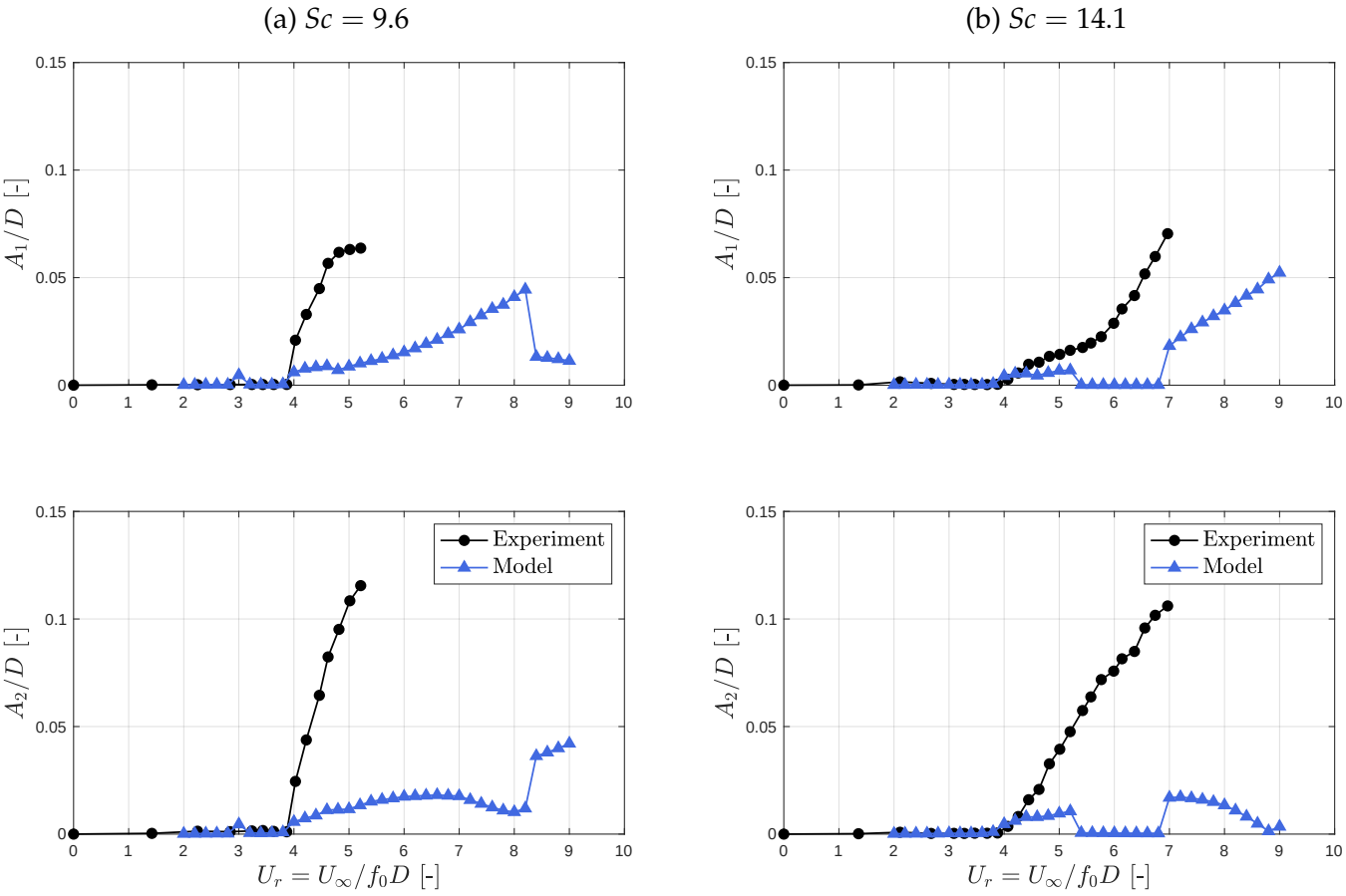

FIGURE 6.33: Numerical aeroelastic responses as a function of U_r obtained from the non-linear model fully described by equations (6.26) to (6.33) for different values of Sc and $L/D = 1.2$ ($f_m = 1.16$; $h^* = 1.1$; $r_1 = -4.8D$; $r_2 = 0.8D$; $\mu_1 = 0.8$; $\mu_2 = 0.7$).

the upper branch. These numerical results must therefore be discarded.

For $Sc = 14.1$ (Figure 6.33(b)), the VIV and galloping instabilities are still decoupled in the model which is in contradiction with the experimental results. Moreover, the amplitudes of vibration are also significantly underestimated.

Other value of L/D

The model is finally used to predict the VIV instability observed in the case of $L/D = 1.8$ and $Sc = 17.3$. Figure 6.34 shows the results of the numerical simulation in comparison with the experimental data. It is observed that the amplitudes of vibration from simulations and experiments are of the same order of magnitude. Moreover, the lock-in range of U_r is the same. Additionally, the shapes of the numerical curves are in rather good agreement with the experimental ones. Even though L/D is increased, the parameters (r_1, r_2, μ_1, μ_2) are kept the same compared with the

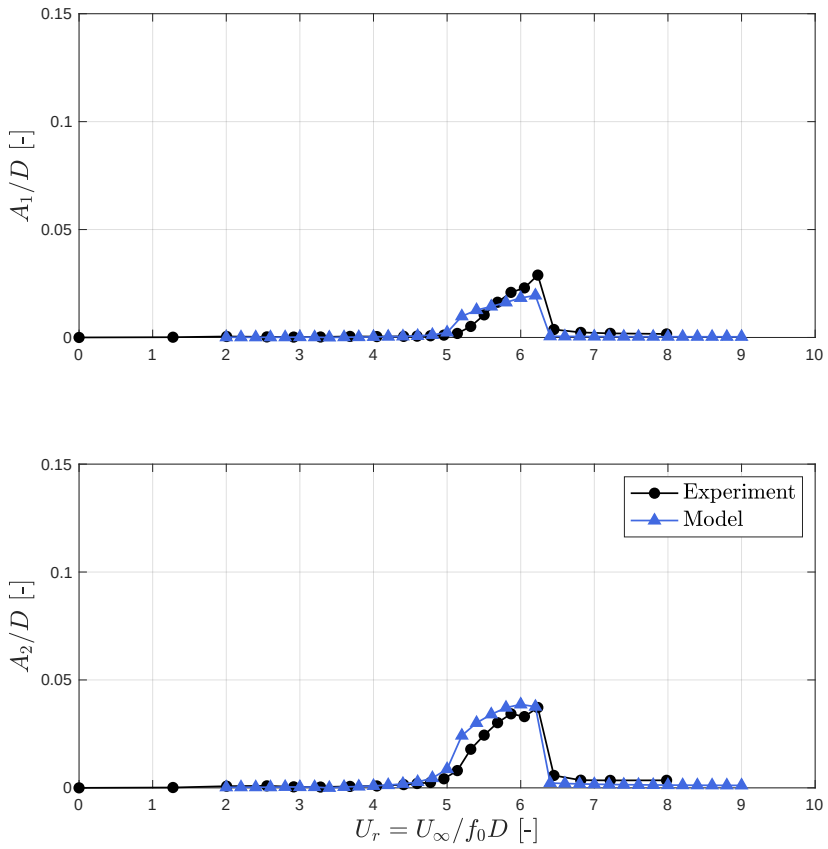

FIGURE 6.34: Numerical aeroelastic responses as a function of U_r obtained from the non-linear model fully described by equations (6.26) to (6.33) for $L/D = 1.8$ and $Sc = 17.3$ ($f_m = 1.16$; $h^* = 1.1$; $r_1 = -4.8D$; $r_2 = 0.8D$; $\mu_1 = 0.8$; $\mu_2 = 0.7$).

previous simulations ($L/D = 1.2$) because no pure interference galloping, which allows to identify the values of these parameters, is observed for $L/D = 1.8$. This may be erroneous because the spacing ratio is somehow linked to the values of those parameters, or inversely. Note that the aeroelastic responses do not change much when the quasi-steady terms $c_{f_{ai}}^{QS}$ are removed from the system of equations.

6.5.5 Discussion

A mathematical model has been developed in the present work by modifying and adapting existing VIV and galloping models to the case of two tandem cylinders. The numerical results show a satisfactory agreement with the experimental ones for the VIV instability with low amplitudes of vibration. Nevertheless, the parametric analysis and the results presented in the previous section demonstrate some limitations of the current mathematical model. The model does not properly reproduce vibrations with large amplitudes, whether in the VIV-galloping interaction or the pure interference galloping. Therefore, it is believed that the modelling approach used in the present work is not adapted, or incomplete at least, to deal with flow-induced vibrations of twin cylinders, where interference effects are important.

The mathematical model developed in this work takes into account the eddy shedding excitation and the motion-dependent forces acting on the cylinders with the following assumptions:

- *Single wake lamina for two bodies*: a single wake lamina is considered in this work, even though two cylinders are present. This simplification may be valid for small oscillations, where the shear layers from the front cylinder do not re-attach onto the rear cylinder. However, it becomes questionable when re-attachment takes place because the dynamics of the flow between the cylinders cannot be neglected anymore.

- *Effect of the rear cylinder on the wake dynamics*: the presence of the rear cylinder is expected to change the properties of the wake oscillator but it is completely neglected in this work. The effect of the motion of the rear cylinder on the wake dynamics could be investigated in further works.

- *Quasi-steady approach*: it is assumed that the flow instantaneously adapts to a change of the structural state $(\dot{\mathbf{y}}, \mathbf{y})$. This assumption is usually made for large values of U_r around a single body. In the case of two cylinders in close proximity, the quasi-steady assumption is questionable. Indeed, it requires that the flow adapts instantaneously around the front cylinder, the rear cylinder and

in the gap between them. It is doubtful that the flow in the gap, which is determined by the behaviour of the shear layers from the front cylinder around the rear cylinder, instantaneously changes. Furthermore, the interference aerodynamic forces acting on the cylinders strongly depend on the flow behaviour between the cylinders. Therefore, it is believed that the unsteady effects cannot be neglected in the case of two cylinders. An attempt to overcome this unsteady effect is made by introducing a time delay in the quasi-steady model. However, this time delay only shifts the quasi-steady forces in time and does reproduce the unsteadiness of the flow. Unsteady flow phenomena may be responsible for the large vibrations observed experimentally.

- *Constant parameters* r_i: the parameters r_i associated with the reference radii in the quasi-steady model are assumed to be constant, irrespective of the values of U_r, the relative motion between the cylinders or the Reynolds number. Unfortunately, this assumption cannot be validated with the available data. Moreover, it is impossible to find physical meanings to the values of these parameters (i.e., $r_1 = -4.8D$ and $r_2 = 0.8D$) obtained from the identification procedure presented in this work.

- *Time delay with constant parameters* μ_i: it was discussed when introducing the time delay that the related parameters μ_i may depend on the relative motion between the cylinders. In this work, μ_i is assumed constant because no data can be analysed to assess their variation with the relative motion.

The discussion above reveals the limitations of the current mathematical model and some points of improvement. Nevertheless, the main outcome is the need for more research to identify and understand the physical excitation mechanism which leads to large amplitudes of vibration of the two cylinders. It is believed that unsteady effects are responsible for the latter but additional experimental measurements are required to confirm this statement.

Chapter 7

Conclusions and Perspectives

7.1 Conclusions

The objective of this thesis is to provide a better understanding of the aerodynamics and aeroelastic instabilities of two cylinders in close proximity. A particular focus is made on the post-critical flow regime, in which the different regions of the flow around the cylinders are turbulent. This flow regime is usually reached for civil engineering structures which become larger and larger in size and thus lead to high Reynolds numbers. Despite this, only a few literature results on two static cylinders are available in the post-critical flow regime and none on aeroelastic instabilities. Hence, the novelty of this research consists in the development of a complete methodology to analyse two interacting bodies with a particular focus on the post-critical regime. In this thesis, an experimental approach is used to investigate the aeroelastic system.

In an atmospheric wind tunnel, the difficulty is to reach the post-critical flow regime because of the size and flow velocity limitations inside the test sections. Indeed, it is shown that the experimental model cannot be too large to avoid (or minimise at least) the wall blockage effect on the flow. Consequently, the maximum Reynolds number that can be reached is $Re = 395$k in this work. However, the post-critical flow regime starts at $Re = 3.4$M to 6M for a smooth cylinder. Appropriate roughness level is therefore applied on the surface of the cylinders to trigger the transition from laminar to turbulent state inside the boundary layers at lower Reynolds numbers. It allows to reach the post-critical flow regime within the tested range of Re. This methodology is investigated and validated in Chapter 3. An important outcome of this investigation concerns the effect of surface roughness on the post-critical flow. It is identified that different roughness levels lead to different post-critical flow behaviours: an increase in k/D induces a larger momentum deficit in the boundary layers which thus separate earlier from the surface of the cylinder. As a result, the wake behind the cylinder widens with k/D in the post-critical flow regime, leading to an increase in

time-averaged drag coefficient and a decrease in Strouhal number associated with the eddy shedding process. It reveals that the observations regarding the flow or aeroelastic responses in this work for rough cylinders most likely differ from the ones that would be made for smooth cylinders in the same flow regime.

Distinct flow regimes are identified and described around two static cylinders in tandem arrangement in Chapter 4. The aerodynamic quantities are analysed in detail as a function of the Reynolds number and the spacing ratio L/D. This thorough analysis highlights the strong sensitivity of the flow around the two static cylinders to the Reynolds number. Distinct flow patterns are identified and classified as a function of the spacing ratio L/D in the sub-critical, critical and post-critical regimes.

In Chapter 5, the analysis of the flow around static twin cylinders is extended by varying the flow incidence α from 0° to 10° in the sub- and post-critical regimes. Bi-stable flows are identified for specific configurations. A new methodology in the frequency domain is suggested to investigate the bi-stability of the flow when an intermittent switch between two Strouhal numbers is observed. The flow patterns around the two cylinders are finally classified as a function of L/D and α in the sub- and post-critical regimes. The classification reveals the sensitivity and complexity of the flow around twin cylinders. Therefore, the aerodynamic quantities ($\overline{c}_d$, $\overline{c}_l$, c'_l, St, etc.) are highly dependent on L/D, α and Re. It is concluded that the strong non-linear behaviour of the flow can lead to several fluid-structure instabilities.

The aeroelastic behaviour of twin cylinders is finally analysed in Chapter 6. From the wind tunnel experiments, different fluid-structure instabilities are identified depending on the spacing ratio L/D, the flow incidence α and the Scruton number Sc. VIV and interference galloping instabilities are observed for $L/D = 1.2$ and these instabilities interact with each other for $Sc \leq 14.1$. For larger L/D, only the VIV instability is identified. The possibility to mathematically model the aeroelastic instabilities observed experimentally is then investigated. The model developed in this work follows the usual approaches to deal with VIV and galloping instabilities. It is demonstrated that the quasi-steady approach does not properly reproduce the large vibrations observed during the interference galloping instability. Moreover, the model dealing with the eddy shedding excitation may be too simple in comparison with the flow dynamics identified in static measurements.

7.2 Perspectives

The experimental results presented in this thesis shed some light on the flow around twin cylinders and the potential flow-induced vibrations of such structures in the post-critical regime. As stated above, the use of surface roughness has a non-negligible influence on the flow in the post-critical regime. Hence, the case of smooth cylinders necessitates a dedicated investigation to assess the potential aeroelastic risks.

Nevertheless, the experimental set-ups and analysis tools developed in this thesis could be extended to the following investigations:

- The effect of the free-stream turbulence on the aeroelastic behaviour of the twin cylinders: it is believed that the free-stream turbulence has a strong influence on the aeroelastic responses of the two cylinders. An aeroelastic test campaign could be carried on with the existing passive grids to vary the free-stream turbulence level.

- The extension of the range of α in static measurements: it was pointed out in the modelling considerations that the quasi-steady model leads to effective flow incidences which go beyond the tested range of α from static measurements. Hence, the quasi-steady model is not valid anymore in that case. It would be interesting to extend this range of α to avoid this issue. Furthermore, it would complete the set of data to analyse the flow at larger flow incidences.

- The three-dimensionality of the flow around the cylinders: the experimental set-up could be instrumented along the span to assess the three-dimensional effect (e.g., correlation length of the eddies from static cylinders) which is usually considered as a second order effect in most studies, including this thesis.

The existing set-ups could be easily adapted to allow the suggestions above.

The limitations of the quasi-steady approaches to model the aeroelastic responses of the cylinders support the need for more research to identify the physical excitation mechanism which leads to large amplitudes of vibration. Therefore, it would be of great interest to design new experimental set-ups to measure the aerodynamic forces (or pressures) on oscillating cylinders. It could be performed through **free** vibration tests, as done within the framework of this thesis (with springs and elastomers), or **forced** vibration tests by means of a new actuated apparatus with imposed motions (amplitudes, phases and frequencies). It would allow to identify the effect of the structural motion on the aeroelastic forces and help to develop a new mathematical model. Furthermore, PIV (Particle Image Velocimetry) measurements would also

be beneficial because it would provide the physical insights into the flow dynamics responsible for the large vibrations. It is believed that this methodology is required to completely understand and successfully model the interference effect between two flexible bodies.

At last, numerical simulations could be considered in the future. CFD (Computational Fluid Dynamics) simulations could be performed to investigate in details the flow dynamics around static cylinders. The numerical results from a validated model could be compared with the outcomes of the present work (e.g., the flow patterns). In a second step, FIV (Flow-Induced Vibrations) could be simulated by coupling a CFD solver with a mechanical solver. The difficulty with these simulations mostly concerns the high Reynolds number in the post-critical regime. It leads to a wide range of scales, and hence, necessitates fine mesh resolution which becomes very expensive in CPU time. Moreover, an appropriate meshing technique must be introduced to deal with the relative motion between the cylinders (e.g. adaptive mesh or immersed boundary method). These numerical considerations go beyond the expertise of the author. Nevertheless, the experimental data base built in the scope of this thesis would be valuable for validation purpose.

Publications

The list below reports the journal publications related to this doctoral thesis:

Journal publications

1. Dubois, R. and Andrianne, T. (2022). “Flow around tandem rough cylinders: Effects of spacing and flow regimes”. In: Journal of Fluids and Structures 109, p. 103465. ISSN: 0889-9746.

2. Dubois, R. and Andrianne, T. (2023). “Identification of distinct flow behaviours around twin rough cylinders at low wind incidence”. In: Journal of Fluids and Structures 117, p. 103815. ISSN: 0889-9746.

Appendix A

Aeroelastic tests - Modal properties

This appendix reports the modal properties of the aeroelastic set-up used in the experimental campaign and presented in section 6.2. The different values are shown in Table A.1. They are obtained by following the methodology described at the end of section 6.3 (sub-section entitled "Modal test during aeroelastic campaign").

L/D [-]	# elastomers/spring	f_0 [Hz]	ζ [%]	Sc [-]
1.2	0	19.50	0.28	3.9
	1	20.02	0.48	6.8
	2	20.50	0.68	9.6
	3	20.99	0.83	11.7
	4	21.48	1.00	14.1
	5	21.97	1.22	17.2
1.4	0	19.50	0.30	4.2
	2	20.51	0.70	9.9
	4	21.48	1.00	14.1
1.56	0	19.41	0.285	4
	2	20.50	0.725	10.2
	4	21.48	1.195	16.8
1.8	0	19.41	0.275	3.9
	2	20.51	0.72	10.1
	4	21.48	0.96	13.5
	5	21.97	1.23	17.3

TABLE A.1: Modal properties of the aeroelastic set-up at wind-off conditions for the different tested configurations.

Based on the variation of the natural frequency f_0 with the number of elastomers added to the springs, the stiffness of the elastomers can be estimated as

$$K_{elast} \approx 2090 \text{ [N/m]}.$$

This means that the total stiffness of one cylinder increases by K_{elast} when one elastomer is added to each spring.

Appendix B

Uncertainty analysis

This appendix analyses the uncertainties stemming from the measurements. Knowing the experimental uncertainty to a measurement allows the comparison with the same measurement taken under different circumstances (e.g., different facility or atmospheric conditions).

In general, measurements of several parameters are combined to evaluate other flow properties of interest. For example, a Pitot tube measures the dynamic pressure to obtain the flow velocity by knowing the fluid density. Hence, it is important to understand how the measurement errors affect the determination of these properties. In that purpose, we consider the property of interest R that is represented by

$$R = R(X_1, X_2, X_3, ..., X_N), \tag{B.1}$$

where X_i are properties measured during the experiment, which have uncertainties of $\pm\delta X_i$. The objective is then to assess the uncertainty in the calculated property R. The effect of the uncertainty in one measurement on the calculated result would be

$$\delta R_{X_i} = \frac{\partial R}{\partial X_i}\delta X_i. \tag{B.2}$$

The partial derivative of R with respect to X_i is the sensitivity coefficient for the result R with respect to the measurement X_i. When several independent measurements are used in the function R, the overall uncertainty becomes

$$\delta R = \left[\sum_{i=1}^{N}\left(\frac{\partial R}{\partial X_i}\delta X_i\right)^2\right]^{1/2} \tag{B.3}$$

which is the basic equation of uncertainty analysis.

Uncertainty in pressure coefficient

The pressure coefficient is an important flow variable reported in this work. As a reminder, it is defined as

$$C_p = \frac{p - p_\infty}{1/2\rho U_\infty^2} = \frac{p_{rel}}{q_\infty} \tag{B.4}$$

where the measured quantities are the relative pressure p_{rel} and the dynamic pressure q_∞. These quantities are measured by means of the pressure scanner DPMS from Turbulent Flow Instrumentation (TFI). The seller specifies an uncertainty around 0.1% of full-scale range (i.e., 2.7 Pa), but comparison with other instruments of the lab allowed estimating the uncertainty to $\delta p = \pm 0.3$ Pa.

Using relation (B.3), the uncertainty in the pressure coefficient is

$$\delta C_p = \frac{\delta p}{q_\infty}\left[1 + C_p^2\right]^{1/2} \tag{B.5}$$

which thus depends on the dynamic pressure q_∞, and hence, the Reynolds number. It also depends on the value of the pressure coefficient C_p. At $Re = 45$k (sub-critical), the estimated uncertainty is $\delta C_p = \pm 0.0175$ to 0.06 (for $|C_p|$ ranging from 0 to 3). At $Re = 275$k (post-critical), the estimated uncertainty is $\delta C_p = \pm 0.0005$ to 0.0015 (for $|C_p|$ ranging from 0 to 3 as well).

Uncertainty in aerodynamic force coefficient

The aerodynamic force coefficients are other quantities reported in this work. The forces are integrated from the pressure measurements. Using the trapezoidal method for integration, we have

$$F_x = \sum_{i=1}^{48}\left(p_i(\theta_i)\cos\theta_i \frac{D\Delta\theta}{2}\right), \tag{B.6a}$$

$$F_y = \sum_{i=1}^{48}\left(p_i(\theta_i)\sin\theta_i \frac{D\Delta\theta}{2}\right), \tag{B.6b}$$

where $p_i(\theta_i)$ is the pressure measured at the ith tap with an angular position of θ_i, and $\Delta\theta$ is the angle between two consecutive taps. The force coefficients are given by

$$C_x = \frac{F_x}{q_\infty D} = \frac{1}{q_\infty} \sum_{i=1}^{48} \left(p_i(\theta_i) \cos\theta_i \frac{\Delta\theta}{2} \right), \tag{B.7a}$$

$$C_y = \frac{F_y}{q_\infty D} = \frac{1}{q_\infty} \sum_{i=1}^{48} \left(p_i(\theta_i) \sin\theta_i \frac{\Delta\theta}{2} \right). \tag{B.7b}$$

Using relation (B.3), the uncertainties in the force coefficients are

$$\delta C_x = \frac{\delta p}{q_\infty} \left[\sum_{i=1}^{48} \left(\cos\theta_i \frac{\Delta\theta}{2} \right)^2 + C_x^2 \right]^{1/2} \tag{B.8a}$$

$$\delta C_y = \frac{\delta p}{q_\infty} \left[\sum_{i=1}^{48} \left(\sin\theta_i \frac{\Delta\theta}{2} \right)^2 + C_y^2 \right]^{1/2} \tag{B.8b}$$

Therefore, if a maximum (conservative) value of 1.5 is considered for the force coefficient, the estimated uncertainty is $\delta C_x = \delta C_y = \pm 0.03$ or ± 0.0008 at $Re = 45$k or 275k, respectively. The drag and lift coefficients are calculated as follows

$$c_d = C_x \cos\alpha + C_y \sin\alpha, \tag{B.9a}$$

$$c_l = -C_x \sin\alpha + C_y \cos\alpha, \tag{B.9b}$$

where α is the flow incidence, for which an uncertainty $\delta\alpha$ also exists. The value of this uncertainty is set to $\delta\alpha = \pm 1°$ to be conservative. Using again relation (B.3), the uncertainties in the drag and lift coefficients are

$$\delta c_d = \left[\left(\cos\alpha\, \delta C_x \right)^2 + \left(\sin\alpha\, \delta C_y \right)^2 + \left(c_l\, \delta\alpha \right)^2 \right]^{1/2}, \tag{B.10a}$$

$$\delta c_l = \left[\left(\sin\alpha\, \delta C_x \right)^2 + \left(\cos\alpha\, \delta C_y \right)^2 + \left(c_d\, \delta\alpha \right)^2 \right]^{1/2} \tag{B.10b}$$

Taking values of 1.5 for c_d and c_l to be very conservative, we obtain maximum uncertainties equal to $\delta c_d = \delta c_l = \pm 0.0375$ or 0.0275 at $Re = 45$k or 275k, respectively.

Bibliography

Achenbach, E. (1971). "Influence of surface roughness on the cross-flow around a circular cylinder". In: *Journal of Fluid Mechanics* 46.2, pp. 321–335.

Achenbach, E. and Heinecke, E. (1981). "On vortex shedding from smooth and rough cylinders in the range of Reynolds numbers 6×10^3 to 5×10^6". In: *Journal of Fluid Mechanics* 109, pp. 239–251.

Adachi, T. (1997). "Effects of surface roughness on the universal Strouhal number over the wide Reynolds number range". In: *Journal of Wind Engineering and Industrial Aerodynamics* 69, pp. 399–412.

Alam, M.M. (2014). "The aerodynamics of a cylinder submerged in the wake of another". In: *Journal of Fluids and Structures* 51, pp. 393–400.

Alam, M.M. and Meyer, J.P. (2011). "Two interacting cylinders in cross flow". In: *Phys. Rev. E* 84 (5), p. 056304.

Alam, M.M., Moriya, M., Takai, K., and Sakamoto, H. (2003). "Fluctuating fluid forces acting on two circular cylinders in a tandem arrangement at a subcritical Reynolds number". In: *Journal of Wind Engineering and Industrial Aerodynamics* 91.1-2, pp. 139–154.

Alam, M.M., Rastan, M.R., Wang, L., and Zhou, Y. (2022). "Flows around two non-parallel tandem circular cylinders". In: *Journal of Wind Engineering and Industrial Aerodynamics* 220, p. 104870.

Alam, M.M., Sakamoto, H., and Zhou, Y. (2005). "Determination of flow configurations and fluid forces acting on two staggered circular cylinders of equal diameter in cross-flow". In: *Journal of Fluids and Structures* 21.4, pp. 363–394.

Bearman, P.W. (1969). "On vortex shedding from a circular cylinder in the critical Reynolds number regime". In: *Journal of Fluid Mechanics* 37.3, pp. 577–585.

Bearman, P.W. and Morel, T. (1983). "Effect of free stream turbulence on the flow around bluff bodies". In: *Progress in aerospace sciences* 20.2-3, pp. 97–123.

Bénard, H. (1908). "Formation de centres de giration à l'arrière d'un obstacle en mouvement". In: *Comptes Rendus de l'Académie Sciences, Paris, France* 147, p. 839.

Bergh, H. and Tijdeman, H. (1965). "Theoretical and experimental results for the dynamic response of pressure measurement systems". In: *National Aero-and Astronautical Research Institute (Netherlands), Report NLR-TR F* 238.

Biermann, D. and Herrnstein, W.H. (1933). *The interference between struts in various combinations. National Advisory Committee for Aeronautics*. Tech. rep. Tech. Rep. 468.

Birkhoff, G. (June 1953). "Formation of Vortex Streets". In: *Journal of Applied Physics* 24.1, pp. 98–103. ISSN: 0021-8979.

Buresti, G. (1981). "The effect of surface roughness on the flow regime around circular cylinders". In: *Journal of Wind Engineering and Industrial Aerodynamics* 8.1, pp. 105–114. ISSN: 0167-6105.

Cheung, J.C.K. and Melbourne, W.H. (1983). "Turbulence effects on some aerodynamic parameters of a circular cylinder at supercritical numbers". In: *Journal of Wind Engineering and Industrial Aerodynamics* 14.1-3, pp. 399–410.

Couregelongue, J. (1929). "On the existence of two families of eddies behind immersed solids". In: *Comptes Rendus Académie Sciences* 189, pp. 972–974.

Dielen, B. and Ruscheweyh, H.P. (1995). "Mechanism of interference galloping of two identical circular cylinders in cross flow". In: *Journal of Wind Engineering and Industrial Aerodynamics* 54-55. Third Asian-Pacific Symposium on Wind Engineering, pp. 289–300. ISSN: 0167-6105.

Dubois, R. and Andrianne, T. (2022). "Flow around tandem rough cylinders: Effects of spacing and flow regimes". In: *Journal of Fluids and Structures* 109, p. 103465. ISSN: 0889-9746.

Dubois, R. and Andrianne, T. (2023). "Identification of distinct flow behaviours around twin rough cylinders at low wind incidence". In: *Journal of Fluids and Structures* 117, p. 103815. ISSN: 0889-9746.

Fage, A. and Warsap, J.H. (1929). *The effects oft turbulence and surface roughness on the drag of a cylinder*. Tech. rep. HM Stationery Office.

Funakawa, M. (1969). "The Vibration of a Cylinder Caused by Wake Force in a Flow". In: *Bulletin of JSME* 12.53, pp. 1003–1010.

Gu, Z. and Sun, T. (1999). "On interference between two circular cylinders in staggered arrangement at high subcritical Reynolds numbers". In: *Journal of Wind Engineering and Industrial Aerodynamics* 80.3, pp. 287–309. ISSN: 0167-6105.

Gu, Z.F., Sun, T.F., He, D.X., and Zhang, L.L. (1993). "Two circular cylinders in high-turbulence flow at supercritical Reynolds number". In: *Journal of Wind Engineering and Industrial Aerodynamics* 49.1-3, pp. 379–388.

Güven, O., Farell, C., and Patel, V.C. (1980). "Surface-roughness effects on the mean flow past circular cylinders". In: *Journal of Fluid Mechanics* 98.4, pp. 673–701.

Hinsberg, N.P. van (2015). "The Reynolds number dependency of the steady and unsteady loading on a slightly rough circular cylinder: From subcritical up to high transcritical flow state". In: *Journal of Fluids and Structures* 55, pp. 526–539.

Hori, E. (1959). "Experiments on flow around a pair of parallel circular cylinders". In: *Proc. 9th Japan National Congress for Applied Mech.* Pp. 231–234.

Hémon, P. (1999). "An improvement of the time delayed quasi-steady model for the oscillations of circular cylinders in cross-flow". In: *Journal of Fluids and Structures* 13.3, pp. 291–307. ISSN: 0889-9746.

Igarashi, T. (1981). "Characteristics of the flow around two circular cylinders arranged in tandem: 1st report". In: *Bulletin of JSME* 24.188, pp. 323–331.

Igarashi, T. (1982). "Characteristics of a flow around two circular cylinders of different diameters arranged in tandem". In: *Bulletin of JSME* 25.201, pp. 349–357.

Igarashi, T. (1984). "Characteristics of the flow around two circular cylinders arranged in tandem: 2nd report, unique phenomenon at small spacing". In: *Bulletin of JSME* 27.233, pp. 2380–2387.

Ishigai, S., Nishikawa, E., Nishimura, K., and Cho, K. (1972). "Experimental study on structure of gas flow in tube banks with tube axes normal to flow: Part 1, Karman vortex flow from two tubes at various spacings". In: *Bulletin of JSME* 15.86, pp. 949–956.

Kármán, T. (1912). "On the mechanism of resistance produced by moving body in liquid". In: *Nachrichtungen des Gesellschaft Wissenschaft* 19.5.

Kiya, M., Suzuki, Y., Arie, M., and Hagino, M. (1982). "A contribution to the free-stream turbulence effect on the flow past a circular cylinder". In: *Journal of Fluid Mechanics* 115, pp. 151–164.

Ljungkrona, L., Norberg, C.H., and Sunden, B. (1991). "Free-stream turbulence and tube spacing effects on surface pressure fluctuations for two tubes in an in-line arrangement". In: *Journal of Fluids and Structures* 5.6, pp. 701–727.

Mannini, C., Massai, T., and Marra, A.M. (2018). "Modeling the interference of vortex-induced vibration and galloping for a slender rectangular prism". In: *Journal of Sound and Vibration* 419, pp. 493–509. ISSN: 0022-460X.

Morkovin, M.V. (1964). "Flow around a circular cylinder – a kaleidoscope of challenging fluid phenomena". In: *Proc. ASME Symp. on Fully Separated Flows*, pp. 102–118.

Nakamura, Y. and Mizota, T. (1975). "Torsional Flutter of Rectangular Prisms". In: *Journal of the Engineering Mechanics Division* 101.2, pp. 125–142.

Niemann, H.J. (1971). "On the stationary wind loading of axisymmetric structures in the transcritical Reynolds number region". In: *Konstruktiven Ingenieurbau, Ruhr-Universitat Bochum, Report* 71-2.

Niemann, H.J. and Hölscher, N. (1990). "A review of recent experiments on the flow past circular cylinders". In: *Journal of Wind Engineering and Industrial Aerodynamics* 33.1-2, pp. 197–209.

Norberg, C. and Sundén, B. (1987). "Turbulence and Reynolds number effects on the flow and fluid forces on a single cylinder in cross flow". In: *Journal of Fluids and Structures* 1.3, pp. 337–357.

Okajima, A. (1979). "Flows around two tandem circular cylinders at very high Reynolds numbers". In: *Bulletin of JSME* 22.166, pp. 504–511.

Panton, R.L. (1984). *Incompressible Flow*. Wiley.

Price, S.J. and Paidoussis, M.P. (1984). "An improved mathematical model for the stability of cylinder rows subject to cross-flow". In: *Journal of Sound and Vibration* 97.4, pp. 615–640. ISSN: 0022-460X.

Reynolds, O. (1883). "III. An experimental investigation of the circumstances which determine whether the motion of water shall be direct or sinuous, and of the law of resistance in parallel channels". In: *Proceedings of the Royal Society of London* 35.224-226, pp. 84–99.

Ruscheweyh, H.P. (1983). "Aeroelastic interference effects between slender structures". In: *Journal of Wind Engineering and Industrial Aerodynamics* 14.1, pp. 129–140. ISSN: 0167-6105.

Schewe, G. (1983). "On the force fluctuations acting on a circular cylinder in cross-flow from subcritical up to transcritical Reynolds numbers". In: *Journal of Fluid Mechanics* 133, pp. 265–285.

Schewe, G. and Jacobs, M. (2019). "Experiments on the Flow around two tandem circular cylinders from sub-up to transcritical Reynolds numbers". In: *Journal of Fluids and Structures* 88, pp. 148–166.

Sumner, D. (2010). "Two circular cylinders in cross-flow: a review". In: *Journal of Fluids and Structures* 26.6, pp. 849–899.

Sumner, D., Price, S.J., and Païdoussis, M.P. (2000). "Flow-pattern identification for two staggered circular cylinders in cross-flow". In: *Journal of Fluid Mechanics* 411, 263–303.

Sumner, D., Richards, M.D., and Akosile, O.O. (2005). "Two staggered circular cylinders of equal diameter in cross-flow". In: *Journal of Fluids and Structures* 20.2, pp. 255–276.

Sun, T.F., Gu, Z.F., He, D.X., and Zhang, L.L. (1992). "Fluctuating pressure on two circular cylinders at high Reynolds numbers". In: *Journal of Wind Engineering and Industrial Aerodynamics* 41.1, pp. 577–588. ISSN: 0167-6105.

Szechenyi, E. (1975). "Supercritical Reynolds number simulation for two-dimensional flow over circular cylinders". In: *Journal of Fluid Mechanics* 70.3, pp. 529–542.

Tamura, Y. (2020). "Mathematical models for understanding phenomena: Vortex-induced vibrations". In: *Japan Architectural Review* 3.4, pp. 398–422.

Tamura, Y. and Matsui, G. (1979). "Wake-oscillator model of vortex-induced oscillation of circular cylinder". In: 10. Forth Collins, US, Elsevier, pp. 1085–1094.

Tsutsui, T. (2012). "Experimental study on the instantaneous fluid force acting on two circular cylinders closely arranged in tandem". In: *Journal of Wind Engineering and Industrial Aerodynamics* 109, pp. 46–54.

Vita, G., Hemida, H., Andrianne, T., and Baniotopoulos, C.C. (2018). "Generating atmospheric turbulence using passive grids in an expansion test section of a wind tunnel". In: *Journal of Wind Engineering and Industrial Aerodynamics* 178, pp. 91–104.

Wang, L., Alam, M.M., and Zhou, Y. (2018). "Two tandem cylinders of different diameters in cross-flow: Effect of an upstream cylinder on wake dynamics". In: *Journal of Fluid Mechanics* 836, pp. 5–42.

Wieselberger, C. (1921). "New data on the law of hydro and aerodynamics resistance Phys". In: *Z. Flugtech. Motorluftschiff* 22, pp. 321–328.

Williamson, C.H.K. (1996). "Vortex Dynamics in the Cylinder Wake". In: *Annual Review of Fluid Mechanics* 28.1, pp. 477–539.

Younis, M.Y., Alam, M.M., and Zhou, Y. (2016). "Flow around two non-parallel tandem cylinders". In: *Physics of Fluids* 28.12, p. 125106.

Zdravkovich, M.M. (1987). "The effects of interference between circular cylinders in cross flow". In: *Journal of Fluids and Structures* 1.2, pp. 239–261.

Zdravkovich, M.M. (1990). "Conceptual overview of laminar and turbulent flows past smooth and rough circular cylinders". In: *Journal of Wind Engineering and Industrial Aerodynamics* 33.1, pp. 53–62. ISSN: 0167-6105.

Zdravkovich, M.M. (1997). *Flow around circular cylinders, Volume 1: Fundamentals*. Oxford University Press.

Zdravkovich, M.M. and Pridden, D.L. (1977). "Interference between two circular cylinders; Series of unexpected discontinuities". In: *Journal of Wind Engineering and Industrial Aerodynamics* 2.3, pp. 255–270. ISSN: 0167-6105.

Zhang, H. and Melbourne, W.H. (1992). "Interference between two circular cylinders in tandem in turbulent flow". In: *Journal of Wind Engineering and Industrial Aerodynamics* 41.1-3, pp. 589–600.

Zhou, Y., Feng, S.X., Alam, M.M., and Bai, H.L. (2009). "Reynolds number effect on the wake of two staggered cylinders". In: *Physics of Fluids* 21.12, p. 125105.